Author:
Dixon, W A J

Title:
Strain to spectra

simulations of strain, NMR spectra and quantum memories in InGaAs quantum dots

Strain to Spectra

Simulations of Strain, NMR Spectra and Quantum Memories in InGaAs Quantum Dots

By

WILLIAM DIXON

Department of Physics
UNIVERSITY OF BRISTOL

A dissertation submitted to the University of Bristol in accordance with the requirements of the degree of DOCTOR OF PHILOSOPHY in the Faculty of Physics.

JUNE 25, 2022

Word Count: 40395

Abstract

Quantum dots have the potential to play a key role in emerging quantum technologies. Their proposed uses range from sources of single or entangled photons needed for quantum communication and photonic quantum computation, to as long term quantum memories in which qubits can be stored for later use. Understanding and characterising the properties of quantum dots is therefore of vital importance. In this thesis we investigate the impact of recent measurements of the gradient elastic tensor - a fundamental part of the strain environment of an InGaAs quantum dot, have on the properties of such a structure. We will show how the quadrupolar interaction is modified by such re-calibration, and assess the impact such changes may have for the possible applications of quantum dots. We will then investigate the advantages that more symmetrical quantum dots may possess, both in terms of nuclear quadrupolar variation and in the resulting coherence time of a trapped electron. Our work is largely computational, with some distinct advantages in run time and ease of use as compared to other simulation methods. Some simple theoretical models are discussed to aid intuitive understanding.

COVID-19 IMPACT STATEMENT

The COVID-19 pandemic had a significant impact on the research detailed in this thesis. All research was hampered by restrictions on in person work, leading to a significant reduction in contact with my supervisor and colleagues. The largest impact on the overall research was the cancellation of a planned collaboration with Professor Paul Koenraad at Eindhoven University of Technology. In March 2020 I was scheduled to visit his group to discuss the requirements on quantum dots for his group to fabricate for analysis using the tools I have developed in this thesis. These would have been analysed in light of the results shown in Chapter 4 concerning the gradient elastic tensor. This necessitated a dramatic shift in the focus of the research away from purely analysing existing structures into assessing the suitability of the dots I already have data for and in the creation of the highly symmetric reflected dots discussed in Chapter 5. The entirety of Chapter 6 came about as a result of this change in focus, and as such this thesis differs substantially from how it was planned to look at the begininning of the pandemic.

Acknowledgements

I am writing this section of my thesis last - almost exactly 5 years after I first came to Bristol to begin my PhD as part of the Quantum Engineering Centre for Doctoral Training. I could not have made a better choice than to come here and work with these people.

Firstly, I must thank Dara and Ruth, without whom this project would not exist. You have helped me achieve something I first wanted when I was 7 - I can now call myself a scientist. Andrew and Edmund, you have both stepped up far more than could be expected of someone who wasn't my official supervisor and I am so grateful for your support - and the occasional (and completely necessary) kicks up the arse. I want to also thank the rest of the quantum dots research group in Bristol, the Gary Sinclair Memorial Centre for Excellence[1] and the QECDT for providing an excellent atmosphere and many learning opportunities. Secondly, thank you to Paul Sokolov and Mikhail Petrov who have provided me with the data which makes up the foundations of this work. Your generosity is emblematic of the best of the scientific community.

Outside of the world of physics, there are innumerable people without whom I would certainly have gone mad - far too many for me to list here, so I apologise if you have been left out. Thank you to Justin, Tom and Minu for some lovely dinners and some truly awful advice; to Sam, Fergus, Peter, Janine, Andrea and the rest of UBES for welcoming me with open arms and to Sam, Jason and anyone else with whom I have ridden a bike in Bristol[2].

Finally, I thank my family, who have tolerated me chatting about maths for at least 20 years. My parents Martin and Judith, who help me up whenever I fall down, and my siblings Oliver and Emily, who have seen fit to make sure my head never grows too large - a service everyone who knows me is grateful for. And of course, Lahra, who is embarrassed at being mentioned at all - yet without whose love and support I simply could not have written all this nonsense down.

[1] A research institute which may only exist on our door, but is no less valuable for it.

[2] A special shout out to Kraa, Scryer, Lute, Mirva and Bae'bi-U'luki-Ven-Daas'na-Suni'tae. May the dice be ever in your favour.

AUTHOR'S DECLARATION

I declare that the work in this dissertation was carried out in accordance with the requirements of the University's Regulations and Code of Practice for Research Degree Programmes and that it has not been submitted for any other academic award. Except where indicated by specific reference in the text, the work is the candidate's own work. Work done in collaboration with, or with the assistance of, others, is indicated as such. Any views expressed in the dissertation are those of the author.

SIGNED: ..... DATE: .....

TABLE OF CONTENTS

List of Tables

List of Figures

CHAPTER 1

INTRODUCTION AND MOTIVATION

Quantum dots have been a staple fixture of the emerging field of quantum technologies since its inception in the latter half of the 20^{th} century [1]. They have been presented as the ideal candidate for a wide variety of applications, ranging from single or entangled photon sources to long lasting quantum memories. In this thesis we investigate the effect of recent re-measurements of phenomenological parameters that are vital to the accurate simulation of quantum dots (and other solid state structures). We develop a tool that uses strain and concentration data to characterise the properties of an InGaAs quantum dot, including the electric field gradient throughout the structure and to simulate its NMR spectrum. We go on to investigate the impact of structural and strain symmetry on the coherence time of electrons trapped in the dot, and assess the suitability of said structures for use within various quantum technologies.

1.1 Thesis Structure

The first half of this thesis concerns the fundamental concepts required to understand the second half. The latter half describes our work to characterise a specific quantum dot, and to investigate the effect of possible improvements to it's structure. Here in Chapter 1, we discuss the motivation for the work - why we want to understand the behaviour of quantum dots, how they fit into the wider field of quantum technologies, and the possible benefits of those technologies. In Chapter 2 we describe the physics of electron behaviour inside a quantum dot, and demonstrate the theory behind experimental protocols designed to produce entangled cluster states using a quantum dot. In chapter 3 we introduce the fundamental physics of quantum dots, including the hyperfine and quadrupolar interactions. We also discuss the sources and effects of electron and nuclear spin decoherence, and present experimental procedures designed to minimise said decoherence.

Chapter 4 presents our work on modelling the impact of recent re-measurement of the gradient-elastic tensor on the characteristic properties of a particular quantum dot structure. We calculate the electric field gradient felt by nuclei within the structure, and use this to find quadrupolar frequency distributions and simulate NMR spectra. Using these results we discuss how this particular quantum dot may be best used within the landscape of quantum technologies. In Chapter 5 we artificially create 2 highly symmetric structures, which we then use to investigate the effect of such symmetry on the coherence time of a trapped electron and the behaviour of the nuclear spin bath as a whole. The use of these dots as quantum memories is quantitatively analysed in Chapter 6 by investigating the effect of optical pulses of various widths on the NMR spectrum. Chapter 7 summarises our findings, and suggests how this work might best be extended.

1.2 Quantum Dots

A self-assembled semiconductor quantum dot (QD) can be thought of as an artificial atom, consisting of 10^5 atoms embedded inside a larger crystal lattice. They range in size from 5 - 50nm across, and are constrained in all 3 spatial dimensions, in contrast to quantum wells or wires, which are constrained in only 1 or 2 dimensions respectively[2]. Quantum dots are formed out of 2 distinct semiconducting materials: a substrate made of a high bandgap material (such as GaAs) which encases a thin layer of a low bandgap material (such as InGaAs) - this thin layer then forms the QD. Electron confinement occurs because the conduction band of the low bandgap material sits at a lower energy than in the high bandgap material - thus restricting the ability of conduction band electrons to move out of the central region into the wider substrate. Dots can generally be categorised according to how they were fabricated, and there are 2 main methods: the strain driven Stranski-Krastanov (SK) mode, and the largely strain free droplet epitaxy (DE) process.

Stranski-Krastanov growth [4] relies on a mismatch in lattice constant causing a strain between layers of 2 different semiconducting materials. The substrate (GaAs in our case) is laid down first using molecular beam epitaxy (MBE)[1], we then layer on InGaAs. This initially forms a wetting layer atop the GaAs substrate, but as more InGaAs is added the strain induced by the lattice mismatch (7% for these materials) leads to new layers preferentially being added atop only the InGaAs wetting layer[2] (WL). Over time, this leads to the growth of 3D islands of InGaAs, sitting on top of the GaAs substrate. A final layer of GaAs is then laid down atop these islands, in order to prevent them breaking apart, in a process known as capping. This tends to produce QDs which are wider than they are tall, and hence have a greater electronic confinement in the z direction. The SK growth method is widely used in the research community but does have some significant downsides: the WL connects all dots grown atop the same substrate, we have only

[1] More details of which can be found here [5–7].

[2] This minimises the elastic potential energy of the structure

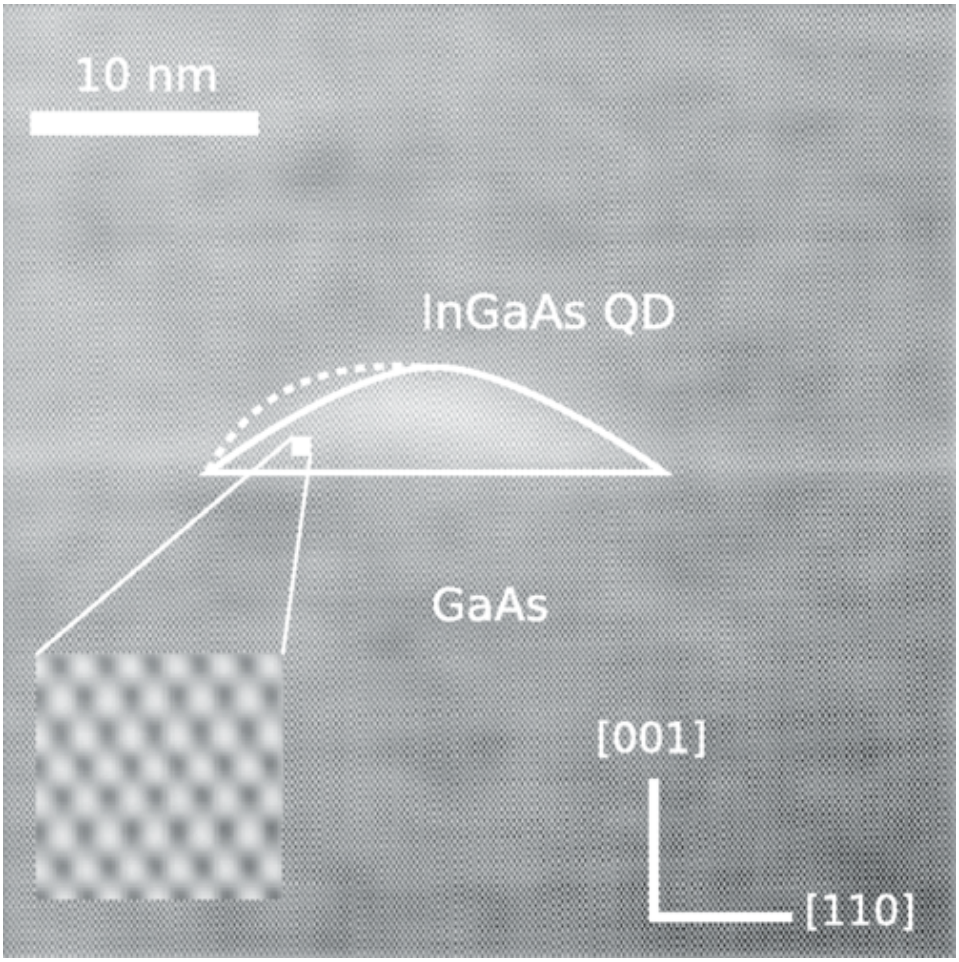

Figure 1.1: High-resolution STEM image of a single InGaAs QD embedded in the GaAs substrate. We can clearly see the QD outlined in white. The dotted line shows where the structure bulges outwards from the ideally symmetrical structure shown as a solid line. Figure reused with permission from [3].

a limited ability to choose the shape and size of the resulting QDs, and the necessity of using semiconductors with the required lattice mismatch limits the choice of materials [8]. The strain required to grow the QD also remains within the structure after it has been formed - this has both advantages and disadvantages, as we will see throughout this thesis. Nonetheless, SK dots currently are the first choice for photon emission applications [9, 10].

Droplet epitaxy fabrication on the other hand, does not rely on lattice mismatch or strain to grow the QD, and thus creates dots (and other nanostructures) which are virtually strain free [8, 11, 12]. The standard materials used in DE are GaAs, embedded in a AlGaAs, but other combinations of materials are possible [13–15]. In the first stage of DE fabrication, Ga atoms are deposited onto an AlGaAs base layer. As more Ga is added, the atoms gradually form droplets due

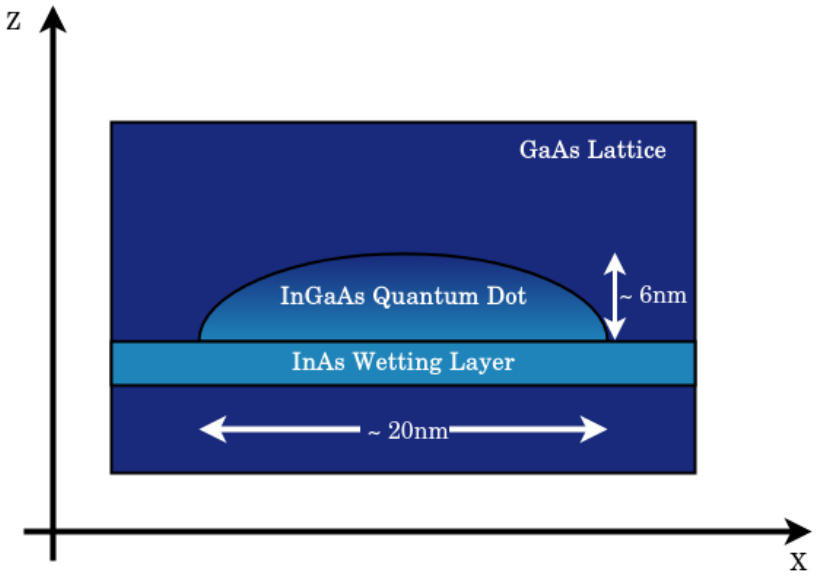

Figure 1.2: A simplified, not to scale, diagram of an InGaAs quantum dot, showing the host GaAs lattice, the InAs wetting layer and the InGaAs quantum dot.

to both their stronger attraction to each other and the desorption of As atoms[3]. Once the droplets have formed, they are crystallised in order to form the QD. This step requires the droplets to be annealed while in an atmosphere of elemental As - the As atoms are gradually absorbed into the droplet, creating a crystal structure as they bond to the Ga in the droplet. The main advantages of this method are that it allows a far greater range of materials to be used (as there is no reliance on lattice mismatch), and that the shape/size of the resulting QDs can be tightly controlled via variation of experimental parameters during both the droplet formation and crystallisation steps. However, DE QDs require post fabrication annealing in order to enhance their otherwise poor optical properties due to subtle defects in the lattice structure [18]. It should be noted there has been some success in using such annealing to fine tune such optical properties, potentially turning this into a benefit of the DE procedure [19].

In this thesis, we will focus on InGaAs quantum dots, grown via the SK method. The ideas discussed should carry over well to other dots grown using the SK method, but DE dots have a very different nuclear environment and should therefore be examined separately. In particular, we will be investigating the role of strain in determining the nuclear and optical properties of a specific InGaAs quantum dot, grown via the SK mode. For completeness, it is also possible to grow GaAs QDs by etching nano-holes in AlGaAs, an approach which has been shown to result in QDs with good optical properties [20].

[3]These processes characterise the Volmer-Weber growth mode [16, 17].

1.3 Quantum Computation

Since the famous paper by Richard Feynman [21] in 1982, the Everest of research into quantum technologies has been the universal quantum computer - a machine which uses the laws of quantum mechanics to perform calculations that would be infeasible on any classical machine[4]. Such a device has been shown theoretically to be capable of solving problems such as prime factorisation [24], function inversion [25] (and hence database searching), and of course the simulation of naturally quantum systems [26, 27] - which has uses in academic and medical research [28–30]. However, the construction of such a device poses significant practical challenge, and it is only recently that experiments have demonstrated anything close to a quantum advantage over a classical machine [31] and even then, there is no clear consensus that it has actually been achieved [32]. It should also be noted, that the problem solved in this case was one specifically designed to be easy for a quantum device, while posing an incredible challenge for a classical one, we are still some way off from solving *useful* problems with a quantum computer.

1.3.1 The Gate Model

The base element of most (though not all) quantum computing schemes is the qubit, a quantum analogue of the classical bit. While a classical bit is defined at all times to be in either the 0 or 1 state, a qubit behaves quantum mechanically and is thus allowed to exist in a superposition of classical states. We represent a qubit as $|\Psi\rangle = \alpha|0\rangle + \beta|1\rangle$, with α and β the probability amplitude of a particular state, subject to the normalisation condition that $|\alpha|^2 + |\beta|^2 = 1$. We see that we can capture classical behaviour by setting α (β) to be 1 and hence our state becomes the classical 0 (1). However, we are not restricted to only these states, and in the case of n qubits we are able to access 2^n states in superposition - allowing for the manipulation of significantly more information than a classical machine.

In much the same was as the qubit is the quantum equivalent of the bit, we can also define quantum logic gates, which act on qubits much as classical logic gates act on classical bits. This model of computation is unsurprisingly termed the 'gate model' of quantum computation, and is the one most platforms use to model computation. In order to perform quantum information processing (and hence computation) in this model, we can apply a series of these gates to our qubits in sequence, and then measure the final state. Measurement will of course force our qubits to collapse to a classical state, with probabilities dictated by the probability amplitudes of each of the 2^n states in can be in a superposition of. For this reason, many quantum algorithms are probabilistic and must be run multiple times to be sure of a correct result[5]. Such an operation

[4] A machine which does better than any classical computer is often said to have achieved 'quantum supremacy' [22]. I will be using the term 'quantum advantage' instead, due to the political connotations of the word supremacy [23].

[5] Though the potentially exponential speed advantage they can have still renders them faster than classical machines.

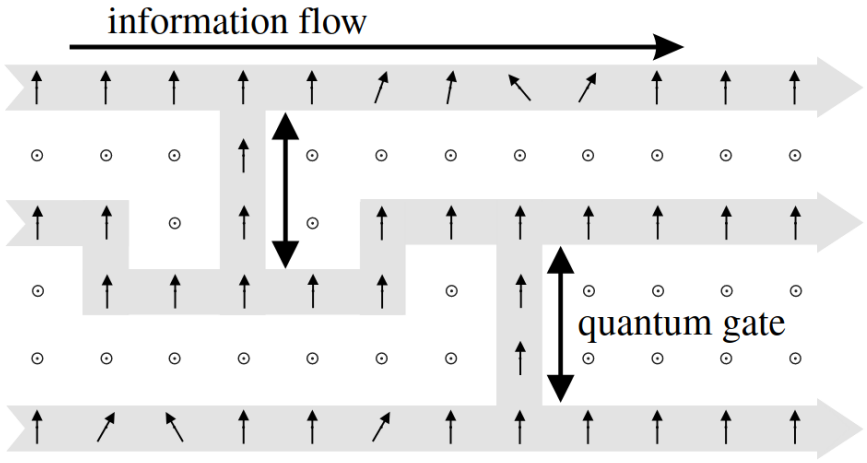

FIGURE 1.3. Cluster state measurement based quantum computation. Each point in the grid represents a measurement on a qubit (circles for σ_z, vertical arrows for σ_x and angled arrows for measurements in the x-y plane). Which measurements are taken is dependant on the outcomes of prior measurements, and hence quantum information is propagated through the lattice. Reproduced with permission from [37].

can be represented by applying a series of unitary operators ($U(t_f, t_i)$, with each gate represented by a different unitary operator) to our quantum state $|\Psi\rangle$, such that:

$$|\Psi(t_f)\rangle = U_a(t_f, t_{f-1})...U_b(t_1, t_i)|\Psi(t_i)\rangle\,. \tag{1.1}$$

At the end of this process, the state $|\Psi(t_f)\rangle$ holds the answer to the question we asked via our series of unitary quantum gates[6]. In principle, a quantum dot can be used as one of the qubits in a system such as this - the central electron spin forms a 2-level system and thus can act as a qubit. However, we do not believe this is the best use for quantum dots in quantum information processing. For that, we need to look at measurement based quantum computing (MQC).

1.3.2 Measurement Based Quantum Computing

Measurement based quantum computing is a completely different way of thinking about quantum computation than the gate model, though the two are equivalent in terms of computational power[34, 35]. Within the world of MQC, there are 2 schemes: teleportation based [36] and one-way/cluster state based [37]. We shall focus on the latter, as it is in the creation of cluster states that quantum dots may come play to a key role.

Cluster state based MQC[7] functions by taking a large 'resource state' and selectively perform-

[6] We have skipped over the incredibly important role that entanglement plays in this model (without it, this paradigm would be no more powerful than classical computation). For a more detailed look, please see works such as *Quantum Computation and Quantum Information* by Nielsen and Chuang [33]

[7] Also known as 'one way' quantum computing

ing measurements on it. The precise sequence of measurements performed encode the algorithm, with the results of the final set of measurements giving us the answer to our encoded question. The nature of the resource state is thus of paramount importance. It has been shown that a 2D lattice of particles, each entangled with their 4 nearest neighbours, is sufficient to perform any quantum algorithm and work is ongoing as to find out exactly how much this lattice can be distorted before it stops being suitable for computation [38, 39]. The key advantage of this method of MQC is that the measurements needed are only performed on a single qubit at a time, and thus may be much easier to practically perform than the multi-qubit operations needed in the gate model. That said, the preparation of a large, entangled cluster state is no easy task - in some sense we have simply moved the experimental difficulty to a different stage of the calculation!

The production of a sufficiently large and well-entangled resource state then becomes the principle challenge of experimentally implementing MQC. Several experiments have successfully created such states, across a variety of platforms, including: atomic lattices [40, 41], photonics [42–49] and trapped ions [50], though all at very small scales. We will focus in particular on photonics as our platform of choice, as it is here that quantum dots are expected to play a key role.

1.3.3 Physical Implementations

In order to implement gate-based quantum computation, any physical system must meet 5 criteria[8], initially put forward by DiVincenzo in 2000 [51]. These criteria are:

1. A well characterised qubit, which can be replicated en mass. Making a single good qubit isn't enough, we must be able to make many of them in order to do anything useful.

2. It must be possible to reliably initialise the qubits to a known quantum state. This is completely analogous to the initialisation of registers in a classical computer. It also has implications for error correction, which typically requires a large amount of qubits in known states [52, 53].

3. Long coherence times. A qubit must be able to retain quantum information long enough that we can perform multiple operations on it, and read out the results.

4. Implementation of a universal set of gates. In much the same way as Turing completeness matters for a classical gate set, a quantum gate set must be sufficiently powerful perform any possible quantum computation. Which precise set of gates is chosen is likely to depend on the specific physical system.

5. The ability to measure each qubit to a high degree of accuracy. The calculation is obviously pointless if we cannot read out the results.

[8] 2 additional criteria are put forward in the paper, each having to do with the communication of quantum information, rather than computation itself.

Every physical system currently being investigated for use in quantum computation will be well suited to some of these criteria, and less so for others. The list of possible platforms is almost constantly expanding, but for now the leading candidates (beside QDs) seem to be: superconducting circuits [31], ion traps [54], atomic lattices [55], linear optics [56], continuous variable quantum optics [57] and various topological implementations [58]. Each of these platforms is at a different stage of research, and there is currently no clear consensus which (if any) will emerge as the dominant implementation.

1.4 Dots for Quantum Information

As we have seen in previous sections, there remain a multitude of challenges before we can achieve reliable, useful quantum information processing and computing. The question now becomes, how can QDs help us solve any of these challenges?

First, let us look at how QDs might be used as the qubit in a gate based quantum computer, with reference to the criteria defined above. Criterion 1 is met is the sense that qubits in dots are well characterised, but we cannot yet fabricate multiple identical QDs - each is subtly different, and these differences can have huge impacts on qubit performance. Meeting criterion 2 has been possible for many years, and presents few barriers to a QD based system [59]. Criterion 3 remains a significant problem in the field, despite good progress in recent years [60, 61], and we will later discuss some of the mechanisms behind this. Criteria 4 has also been well addressed - ultrafast optical rotations have been possible in QD systems for over a decade [62–65]. Criterion 5 is also well understood, with techniques such as resonance fluorescence achieving fidelities of at least 96% [66–70]. We are therefore left with 2 main problems: an inability to manufacture identical QDs, and the issue of decoherence. In this thesis, we shall concentrate on decoherence processes - the effects they have and how those effects can be mitigated.

Now, we shall consider the role QDs could play in other aspects of a quantum computer. Quantum dots have long been known to be exceptional single photon sources, as they seem to meet all of the key criteria for such a device: single-photon purity, indistinguishability, brightness and reliability. That is to say, the ideal single photon source should be a button that one presses, which with 100% probability then emits a photon with well defined properties that do not change if the button is pressed again. Quantum dots perform very well in all of these categories [10]. In addition, QDs have also been suggested as a good source of linear cluster states [71, 72], which are a key resource necessary for the generation of the entangled resource states needed for linear optical quantum computing [73]. In this way, QDs seem to be a natural partner of optical quantum computing schemes, and it is in this context that we shall examine and characterise them in this thesis.

CHAPTER 2

ELECTRON ENERGY LEVELS AND ENTANGLEMENT GENERATION PROTOCOLS

In this chapter, we will explain the fundamental physics of quantum dots and how they can be used as a 2 level quantum system. We will then discuss recent proposals for the generation of entangled linear cluster states of photons, and how those states can be used to create the resource states necessary for measurement based quantum computation.

2.1 Electrons in Quantum Dots

The parallels between quantum dots and atoms are very useful to understand the basic behaviour of a QD - we can reasonably expect them to have a series of discrete energy levels, and we can therefore use them to absorb and emit photons with well-defined energies. However, in contrast to atoms, the energy levels in a QD come about as a result of their shape, size and semiconductor composition, rather than mainly the number and distribution of electrons as in an atom. By tweaking our fabrication procedures we can produce QDs in a huge range of sizes and shapes [74], and hence with vastly different electron confinement potentials and photon emission properties. The energy levels themselves come about as a result of the QD inheriting the band structure of the semiconductors it is made from.

2.1.1 Band Structure in Semiconductors

When atoms are bound together to form a lattice, their atomic orbitals overlap [75]. However, due to Pauli exclusion it is impossible for more than 2 electrons to occupy exactly the same orbital. In a crystal environment, where there might be of the order 10^{20} atoms and electrons, this forces the orbitals to be spaced incredibly close together. Hence we see the formation of energy bands,

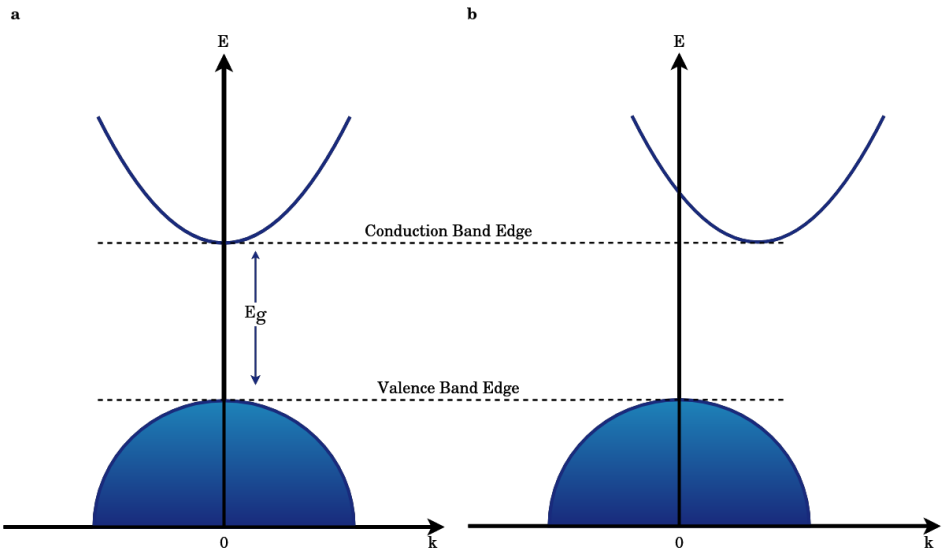

Figure 2.1: Simplified diagram of the band structure of direct (a) and indirect (b) band gap semiconductors. E_g is the same in both instances, but the bottom of the conduction band is offset in the indirect bandgap material, and hence a transfer of angular momentum is needed to excite an electron from the valence band.

which appear to be continuous regions in energy space capable of accommodating huge numbers of electrons. In a crystal made up of only a small number of atomic species (as in the case of GaAs and InGaAs), there will be gaps present in this continuum of levels, simply as a reflection of the spacing between the energy levels of the atoms that make up the lattice. The arrangement of the lattice also impacts the energy level distribution, any asymmetry present will distort the shape of the band structure and so electrons travelling in different directions (and hence having different wavevectors $\mathbf{k}$) will behave differently.

For semiconductor applications the important bands are those that are closest to the Fermi level (FL) of the material: the band immediately below the FL is the valence band (VB), and the one immediately above is the conduction band (CB). When discussing the bandgap of a crystal, we are referring to the spacing between the VB and the CB. The size of the bandgap (E_g) will vary depending on the composition of the lattice, and it can be the case that some transfer of angular momentum (in the form of a phonon) is needed to transfer electrons from the VB to the CB. This is the difference between direct and indirect bandgap semiconductors (see Fig. 2.1). When a semiconductor crystal absorbs a photon, an electron is excited from the VB to the CB, leaving behind a hole. This process is reversed for the emission of a photon, with an electron and hole recombining as the electron rejoins the VB, though this can only happen when the total angular momentum of the electron/hole pair is equal to a possible value of photon angular momentum (0 or ± 1).

We now turn our attention to GaAs and InGaAs specifically, both are direct bandgap materials,

and as such phonon processes (though still in existence) are not required to understand their basic behaviour, we can mainly concern ourselves with the strong zero phonon line transitions. In bulk, the CB of both materials is formed by the overlap of s-shell orbitals, and therefore has orbital angular momentum $L = 0$ and electron spin angular momentum $S = \frac{1}{2}$ for a total angular momentum $J = L + S = \frac{1}{2}$. These have the same spin projections as an isolated electron in an atomic orbital, and hence we will label them as $|\uparrow\rangle$ and $|\downarrow\rangle$ for $s_z = \frac{1}{2}$ and $s_z = -\frac{1}{2}$ respectively. The VB on the other hand is formed by the overlap of p-shell orbitals, and thus has orbital angular momentum $L = 1$. This means that the VB has a total angular momentum of $J = L+S = \frac{1}{2}+\frac{3}{2}$, and by adding these angular momenta we are left with states of total angular momentum $J = \frac{1}{2}$ and $\frac{3}{2}$. The $J = \frac{1}{2}$ split-off band has a very large energy separation from the rest of the VB, and hence can be ignored. The $J = \frac{3}{2}$ band has 2 sub-bands, split according to the possible spin projections $j_z = \pm\frac{1}{2}, \pm\frac{3}{2}$. These are referred to as light holes (LH) and heavy holes (HH) respectively due to the differences in their effective masses [76]. In a bulk semiconductor, the LH and HH bands are mixed, however in a QD the effects of confinement and in-plane strain cause a small splitting between these bands[1], though it is not large enough to prevent all mixing from occurring [77]. This splitting can be intuitively understood as being similar to the increase in band separation when a simple particle in a box model is horizontally shrunk. In a bulk semiconductor the equivalent box is essentially infinite in width, and thus has a continuum of bands, while when confined in a quantum dot the box is of finite (and small) width and thus energy levels (bands) emerge. The HH band is shifted less, and so has a smaller bandgap than the LH band and so is treated as the dominant band with regard to coupling to the CB. The possible spin projections of the HH are $s_z = \frac{3}{2}$ and $s_z = -\frac{3}{2}$, which we will label $|\Uparrow\rangle$ and $|\Downarrow\rangle$ respectively. Further complications in the band structure arise from the wetting layer, which consists entirely of InGaAs (which has a smaller bandgap than GaAs), but lacks the confinement effects which cause sub-band splitting. The resulting energy structure is shown in Fig. 2.2.

2.1.2 Photons and Excitons

The process of absorbing a photon necessities the movement of an electron from the valence band to the conduction band, as it gains energy equal to that of the absorbed photon. In doing so, it leaves behind a positively charged heavy hole in the valence band. This hole, due to its positive charge, can form a bond with a conduction band electron - such a pairing is called an exciton. Excitons are relatively stable, with lifetimes of a few nanoseconds [78] and generally resemble a hydrogen atom - the light electron orbits the much heavier hole. As such, there is a Coulomb binding energy E_χ associated with exciton formation, which in a bulk material is given by:

$$E_\chi = -\frac{\mu e^4}{32\pi^2\hbar^2\epsilon_r^2\epsilon_0^2} \tag{2.1}$$

[1] Referred to as sub-band splitting

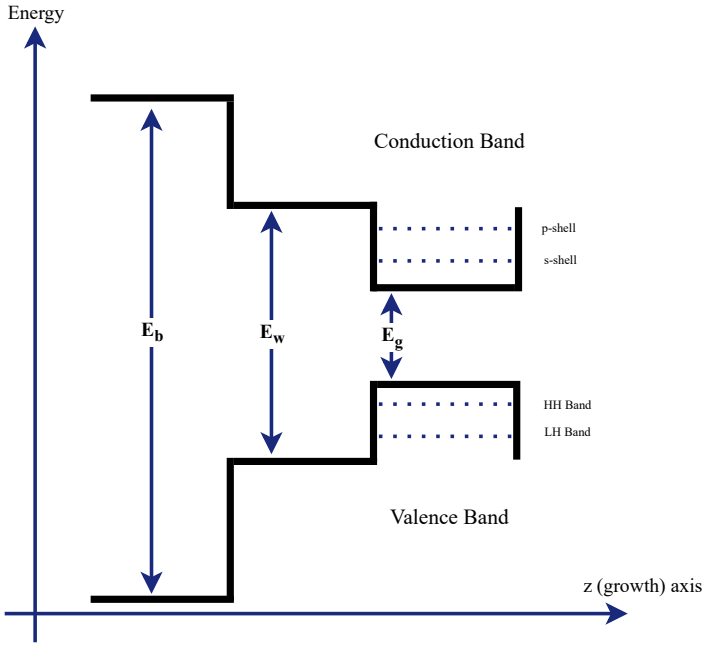

Figure 2.2: The band structure of an InGaAs/GaAs quantum dot. E_b is the band gap in bulk GaAs, E_w the band gap in the InGaAs wetting layer, and E_g the band gap in the quantum dot. There is also sub-band splitting into light and heavy holes in the valence band, and into s and p shells in the conduction band.

where ϵ_0^2 and ϵ_r^2 are the vacuum and relative permittivity, and μ is the reduced mass of the electron-hole pair, given by:

$$\frac{1}{\mu} = \frac{1}{m_e^*} + \frac{1}{m_h^*}. \tag{2.2}$$

As a result of the binding energy, the exciton sits at an energy level just below that of the conduction band, effectively slightly reducing the band gap of the structure. This leads to there being 2 methods of exciton formation - resonant and non-resonant. In resonant excitation, a photon with energy $E_\gamma = \hbar\nu = E_g - E_\chi$ excites an electron and directly creates an exciton, this is in contrast to non resonant excitation in which a photon with energy $E_\gamma = \hbar\nu > E_g$ excites an electron to a higher level inside the conduction band. This electron then binds with a lower energy hole to again form an exciton.

In a quantum dot, the confinement imposed by the structure modifies the exciton energy structure significantly [79]. The Hamiltonian of an exciton in a quantum dot is of the form [80]

$$\hat{H} = \frac{p_e^2}{2m_e} + \frac{p_h^2}{2m_h} + V_c(\mathbf{r_e}) + V_c(\mathbf{r_h}) - \frac{e^2}{4\pi\epsilon_0\epsilon_r}\frac{1}{\sqrt{(\mathbf{r_e}-\mathbf{r_h})^2 + a^2}}. \tag{2.3}$$

Here, the first 2 terms are the electron and hole kinetic energies, V_c are the relevant confinement potentials and the final term modifies the standard Coulomb interaction to account for the size of the electron and hole wavefunctions in the growth direction, characterised by a - the mean-square

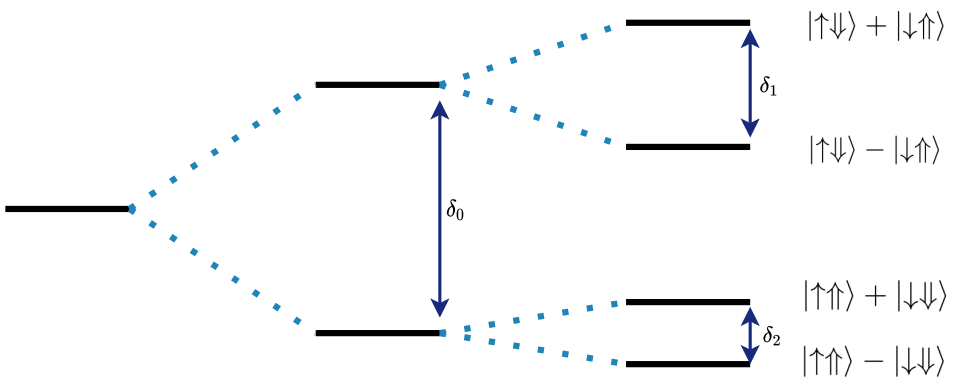

Figure 2.3: The fine structure splitting of a neutral exciton. Split first by the exchange interaction δ_0, and then by asymmetry in the dot structure δ_1, δ_2. These splittings vary as a magnetic field is applied, but are typically measured in meV or μeV [81].

separation of the electron and hole in the z direction. The exact form of V_c depends on the shape of the confining potential, a standard parabolic confinement of the electron yields

$$V_c(\mathbf{r_e}) = \frac{1}{2} m_e^2 \omega_e^2 r_e^2, \tag{2.4}$$

with the equivalent term for the hole confinement potential found by simply replacing the relevant parameters. By finding the eigenstates of Eq. 2.3, we can find the exciton binding energy of any particular quantum dot. It has been shown [80] that dots with a small radius and steep confinement potentials have the highest exciton binding energies. A tall dot (with height approaching the radius) will have a much lower exciton binding energy than a shorter dot of the same lateral size.

The exact energy structure of an exciton depends on the charge state of the quantum dot it is found in. A neutral quantum dot is one in which the ground state of the system has no electrons in the CB, whereas in a charged dot extra electrons have been injected to force the ground state to contain 1 or more electrons in the CB. In a neutral quantum dot, there are 4 possible exciton spin states, corresponding to combinations of the possible spin states of the electron and hole: $|\uparrow\Downarrow\rangle \pm |\downarrow\Uparrow\rangle$ and $|\uparrow\Uparrow\rangle \pm |\downarrow\Downarrow\rangle$. These are arranged in doublets (see Fig. 2.3), with angular momentum projections of $m = \pm 1$ referred to as bright states, and $m = \pm 2$ as dark states. These doublets are then split by the strain present in the dot, leading to fine structure splitting (FSS). FSS results in the pair of bright states having a higher energy than the pair of dark states. As such, transitions are possible between the 2 bright states, and between the 2 dark states via optical transitions to the ground state, but are much less common between the 2 pairs. As there is no change in angular momentum within the doublets, we can excite these transitions with linearly polarised photons. The exact size of the FSS (δ) depends on the strain characteristics of the structure, and as such varies significantly between dots.

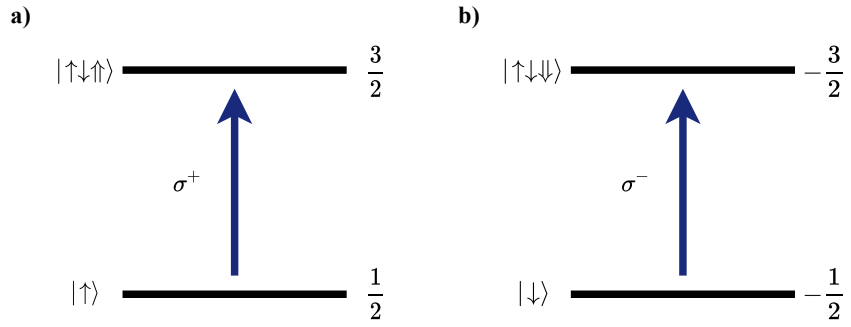

Figure 2.4: The allowed transitions of a charged QD. Each initial electron state can only be excited by the corresponding circular polarisation of light - σ^+ for spin $\frac{1}{2}$ and σ^- for spin $-\frac{1}{2}$

Charging a quantum dot is accomplished by the application of a small voltage V_g over the dot or by injecting excess electrons in a process known as doping. Both result in an electron entering the conduction band of the dot without creating a corresponding hole, and so not forming an exciton. This effect can be observed by measuring the corresponding change in capacitance [82]. When we optically excite a second electron into the conduction band, Pauli exclusion requires that it enters the opposite spin state to the one already present. This results in there being only 2 possible excited states: $|\uparrow\downarrow\Uparrow\rangle$ and $|\uparrow\downarrow\Downarrow\rangle$ with spin $\frac{3}{2}$ and $-\frac{3}{2}$ respectively, these are called trion states. As each trion state differs only by the orientation of the hole spin, which one we arrive at depends on the initial spin of the VB electron. Therefore, in the absence of any HH-LH mixing, a spin up initial state will transition to a positive spin trion, and a spin down initial state will result in a negative spin trion. These transitions require a photon with unit angular momentum, as they take a spin $\pm\frac{1}{2}$ electron to a spin $\pm\frac{3}{2}$ trion and hence can only be excited by circularly polarised light with $J_p = 1$ and $j_p = \pm 1$. To allow other transitions to occur in a charged dot, we must apply a magnetic field.

It is useful at this point to briefly discuss the polarisation of light. The polarisation of a wave is the direction of the oscillation of its component electric field[2]. This of course allows for infinite possibilities in principle, however these can all be treated as linear combinations of pairs of orthogonal polarisations. The standard convention is to label horizontal and vertical polarisation as $|H\rangle$ and $|V\rangle$ respectively, and then define diagonal and anti-diagonal polarisations as $|D\rangle = \frac{1}{\sqrt{2}}|H\rangle + \frac{1}{\sqrt{2}}|V\rangle$ and $|D\rangle = \frac{1}{\sqrt{2}}|H\rangle - \frac{1}{\sqrt{2}}|V\rangle$. Circular polarisation is the steady rotation of this linear polarisation state. This gives rise to 2 further useful states of polarisation - right handed and left handed, which we write as $|R\rangle$ and $|L\rangle$ respectively. These circular polarisations carry angular momentum $J_p = 1$ and $j_p = \pm 1$, and this is why they are used to create spin $\frac{3}{2}$ trions from spin $\frac{1}{2}$ electrons in a quantum dot.

[2]Which is obviously perpendicular to the direction of travel.

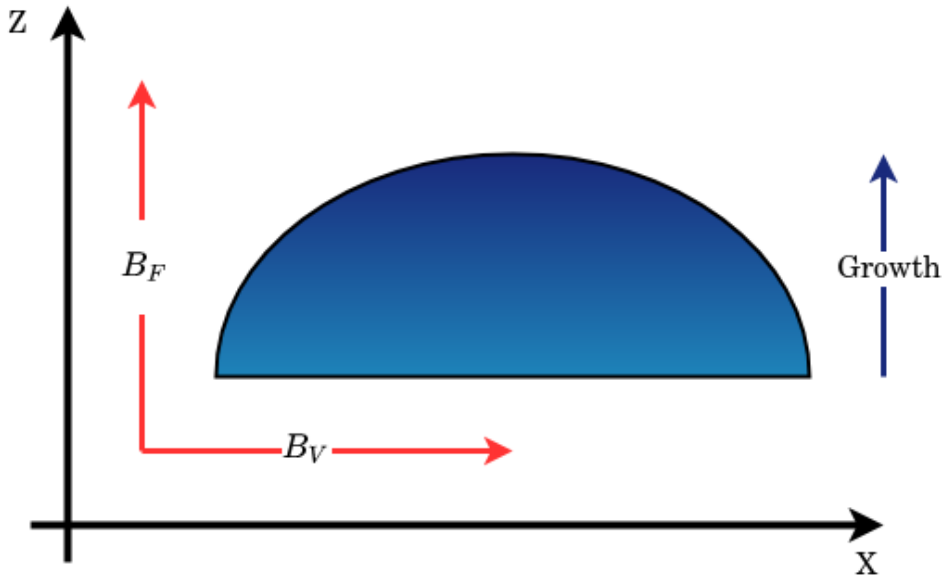

Figure 2.5: Defining the orientations of applied magnetic fields, relative to the quantum dot growth axis along z. A Faraday field B_F is parallel to z, whereas a Voigt field B_V is perpendicular, and defines the x axis (as the ideal dot is cylindrically symmetric).

2.1.3 Faraday and Voigt Geometries

The choice of along which axis to orient an applied magnetic field has a significant impact on the energy level structure of a QD. Here we shall concentrate on the effect on a charged quantum dot, as these are the type needed for generating entangled states, and those that most strongly feel the effect of nuclear interactions[3].

In a Faraday field, we describe the system using the Hamiltonian:

$$\hat{H}_F = (g_e^z + g_h)\frac{\mu_B B_z}{2}\sigma_z, \tag{2.5}$$

with g_e (g_h) the electron (heavy hole) g-factor[4], and σ_x, σ_y, σ_z the standard Pauli matrices. The lowest energy eigenstates are those comprised of only the electron spin: $|\uparrow\rangle$ and $|\downarrow\rangle$, with eigenvalues $\lambda_e = \pm\frac{g_e\mu_B B_z}{2}$ respectively. The trion state is also split, with each spin becoming a superposition along z, resulting in the eigenstates

$$\begin{aligned} |T_{\Downarrow}\rangle &= \frac{1}{\sqrt{2}}(|\uparrow\downarrow\rangle - |\downarrow\uparrow\rangle)|\Downarrow\rangle \\ |T_{\Uparrow}\rangle &= \frac{1}{\sqrt{2}}(|\uparrow\downarrow\rangle - |\downarrow\uparrow\rangle)|\Uparrow\rangle, \end{aligned} \tag{2.6}$$

which have eigenvalues of $\lambda_t = \hbar\nu \mp \frac{g_h\mu_B B_z}{2}$. We can see that the effect of a Faraday field is to keep the eigenstates along z, while lifting the degeneracy of the ground state.

[3]For a detailed description of the fine structure of InGaAs quantum dots in all configurations, please see [81].

[4]The g-factor of of both electrons and holes is different along the x and z axes [83], and care should be taken to use the correct value. In this case, each g should be treated as having the same subscript as σ.

Our analysis of the Voigt orientation proceeds in much the same way, we begin with the Hamiltonian[5]

$$\hat{H}_V = (g_e + g_h)\frac{\mu_B B_x}{2}\sigma_x. \tag{2.7}$$

The eigenstates of this system are along the x axis, but we shall write them as superpositions of z spin states

$$|e_{g\pm}\rangle = \frac{1}{\sqrt{2}}(|\uparrow\rangle \pm |\downarrow\rangle) \tag{2.8}$$

with eigenvalues

$$\lambda_g = \pm\frac{g_e \mu_B B_x}{2}. \tag{2.9}$$

which are identical in form to the eigenstates of the ground state in a Faraday geometry, but along the x axis instead of z. However, the behaviour of the trion state is more complicated, and in general depends on the splitting between the LH and HH states. In general, they are of the form

$$|e_{t\pm}\rangle = (a\,|\Uparrow\rangle + b\,|\Downarrow\rangle)|\uparrow\downarrow\rangle \tag{2.10}$$

with a and b dependent on the LH-HH splitting. In the case where the splitting is large, and hence the system cannot easily shift between the 2 HH states, we approach the state $a = b = \frac{1}{\sqrt{2}}$. The exact nature of the eigenstate depends on the HH-LH splitting, the g-factors in that material and the strength of the applied field. The associated eigenvalues are

$$\lambda = \hbar\nu \mp \frac{g_h \mu_B B_x}{2}. \tag{2.11}$$

From this we see that in a Voigt orientated field, the eigenstates will remain along the z axis even though this is no longer the energy eigenbasis. This results in a set of allowed transitions that are different from those in a charged dot that isn't in a magnetic field. In a Voigt field, the vertical transitions show in Fig. 2.4 are instead excited by vertically polarised light, and the previously forbidden cross transitions are excited by horizontally polarised light. As such, left or right circularly polarised light will now excite into *both* excited states, whereas without a Voigt field only a single transition was allowed.

2.2 Entangled State Generation

The generation of large entangled states is a necessity for the implementation of measurement based quantum computation. However, the creation of such states is a significant challenge. Here we outline proposals and some early experimental results for the creation of photonic cluster states, using quantum dot emitters.

[5]Again, we note that the electron and hole g-factors are now in the x direction and suitable values should be used.

2.2.1 The Cluster State Machine Gun

The cluster state machine gun (CSMG), as proposed by Lindner and Rudolph [71], is a procedure designed to produce a string of photons, each entangled with the preceding and following ones in the chain. If the entanglement is structured such that individual links can be broken without disentangling the entire structure, then the state is referred to as a cluster state. The three qubit cluster state, written in the computational basis and ignoring normalisation, is:

$$|\psi\rangle = |000\rangle + |100\rangle + |010\rangle - |110\rangle + |001\rangle + |101\rangle + |-011\rangle + |111\rangle \tag{2.12}$$

The CSMG produces 1D cluster states, and it has been shown that many such states can then be combined using 'fusion' gates to create the 2-dimensional entanglement necessary for MQC[6] [73, 84, 85]. This has been proposed as the basis for a photonic quantum computer, in which QDs would play a key role [56].

The CSMG relies on a system with a degenerate ground state with the standard spin projections $|\uparrow\rangle$ and $|\downarrow\rangle$, and an excited state with spin eigenvalues of $j = \pm\frac{3}{2}$. Fortunately for us, as we have seen in Section 2.1, this is exactly the energy level structure present in a charged QD. Referring to the states $|\uparrow\downarrow\Uparrow\rangle$, $|\uparrow\downarrow\Downarrow\rangle$ as $|\Uparrow\rangle$ and $|\Downarrow\rangle$, as only the exciton spin state is relevant, we know that if we excite the $|\uparrow\rangle$ ($|\downarrow\rangle$) state, we end up in the $|\Uparrow\rangle$ ($|\Downarrow\rangle$) excited state and from here decay back down via the emission of a right (left) circularly polarised photon - which we shall label $|R\rangle$ ($|L\rangle$). If instead we had started with an initial state of $|\psi_i\rangle = |\uparrow\rangle + |\downarrow\rangle$,[7] and then excited it with linearly polarised light[8] and waited for the system to decay, the electron spin/emitted photon pair would end up in the state $|\psi_f\rangle = |\uparrow, R\rangle + |\downarrow, L\rangle$, which is an entangled Bell state. While we could entangle another photon by repeating this procedure, this would create 3 photon GHZ states, instead of the desired 3 photon cluster state [86]. Both are fully entangled 3-photon states, but a single measurement will collapse all the entanglement in a GHZ state, whereas the entanglement of 2 photons in a cluster state is not affected by measurements of other entangled pairs in the state.

Instead, we shall first apply a $\frac{\pi}{2}$ rotation to the spin, around the Y axis[9]. By doing this, we evolve our 2 particle state from

$$|\uparrow\rangle, |R_1\rangle + |\downarrow\rangle, |L_1\rangle, \tag{2.13}$$

where the subscripts are labelling specific photons, to the state

$$(|\uparrow\rangle + |\downarrow\rangle), |R_1\rangle + (-|\uparrow\rangle + |\downarrow\rangle), |L_1\rangle. \tag{2.14}$$

[6] It should be noted here that fusion gates are inherently probabilistic, and so do not entirely solve the problem of *deterministically* generating 2D cluster states.

[7] Here, and for the rest of this section, we will ignore normalisation in an attempt to keep the fundamental physics clear.

[8] Remembering that linear polarisation is a superposition of left and right circular polarisation.

[9] This has the effect of taking $|\uparrow\rangle \rightarrow (|\uparrow\rangle + |\downarrow\rangle$ and $|\downarrow\rangle \rightarrow (-|\uparrow\rangle + |\downarrow\rangle)$ [33]

From here we can again excite the system, and it will decay into a spin/2-photon state of the form

$$\begin{aligned}&(|\uparrow\rangle|R_2\rangle+|\downarrow\rangle|L_2\rangle)|R_1\rangle+(-|\uparrow\rangle|R_2\rangle+|\downarrow\rangle|L_2\rangle)|L_1\rangle\\&=|\uparrow\rangle|R_2\rangle|R_1\rangle+|\downarrow\rangle|L_2\rangle|R_1\rangle-|\uparrow\rangle|R_2\rangle|L_1\rangle+|\downarrow\rangle|L_2\rangle|L_1\rangle.\end{aligned} \tag{2.15}$$

After another $\frac{\pi}{2}$ pulse, we will have the state

$$\begin{aligned}&|\uparrow\rangle|R_2\rangle|R_1\rangle+|\downarrow\rangle|R_2\rangle|R_1\rangle-|\downarrow\rangle|L_2\rangle|R_1\rangle+|\uparrow\rangle|L_2\rangle|R_1\rangle\\&-|\uparrow\rangle|R_2\rangle|L_1\rangle-|\downarrow\rangle|R_2\rangle|L_1\rangle-|\downarrow\rangle|L_2\rangle|L_1\rangle+|\uparrow\rangle|L_2\rangle|L_1\rangle.\end{aligned} \tag{2.16}$$

Now, if we label our states according to

$$\begin{aligned}|R\rangle,|\uparrow\rangle&=|0\rangle\\|L\rangle,|\downarrow\rangle&=|1\rangle\end{aligned} \tag{2.17}$$

we can see that this state is equivalent to

$$|0\rangle|0\rangle|0\rangle+|1\rangle|0\rangle|0\rangle-|1\rangle|1\rangle|0\rangle+|0\rangle|1\rangle|0\rangle-|0\rangle|0\rangle|1\rangle-|1\rangle|0\rangle|1\rangle-|1\rangle|1\rangle|1\rangle+|0\rangle|1\rangle|1\rangle \tag{2.18}$$

which is local unitary equivalent to the 3-qubit linear cluster state shown in Eq. 2.12.

From here, repeated application of an excitation pulse, followed by decay and then a $\frac{\pi}{2}$ rotation of the spin will add 1 photon at a time to the cluster state. When a state of sufficient size has been made, the electron spin can be disentangled by measuring the polarisation of the most recently produced photon. In order to experimentally implement this scheme, we must have a dot with a LH-HH splitting large enough that we can neglect the mixing between the states. We then take this dot and place it in constant magnetic field, aligned along the Y axis [10]. This has the effect of continually rotating the central spin, at a frequency of $\omega_B=\frac{g_e\mu_B B_y}{2}$, which therefore completes a $\frac{\pi}{2}$ rotation with a period $T=\frac{\pi}{2\omega_B}$. So long as the optical excitation and exciton decay are both faster than this time, we can generate cluster states. Recent experiments have shown that optical excitation of quantum dots can be done in the ps regime [65], and trion lifetimes are of the order of ns [87]. Taking reasonable values of $g_e=0.25$ [88] and $\mu_B=9.3\times10^{-24}\text{JT}^{-1}$ [89], we can rearrange the above to see that in order for the rotations to happen on a timescale of 10s of ns, we require a field of the order

$$B=\frac{\pi\hbar}{g_e\mu_B T}=\frac{\pi\hbar}{0.25\times9.3\times10^{-24}\times10^{-8}}\approx0.01\text{T}. \tag{2.19}$$

Increasing the field will lessen the time taken per cycle, meaning that fields much larger than a few 10s of mT will not allow enough time for exciton decay to occur. It is possible to increase the field size by using an optical cavity, though even to get to the 100s of mT regime would require a cavity with a Purcell factor of 10 - it is clear that this procedure requires low external fields in order to work well.

Experimentally, the CSMG has been demonstrated using a quantum dot source [48], though this particular implementation used a dark exciton transition, rather than the standard one originally proposed.

[10] In the plane of the dot.

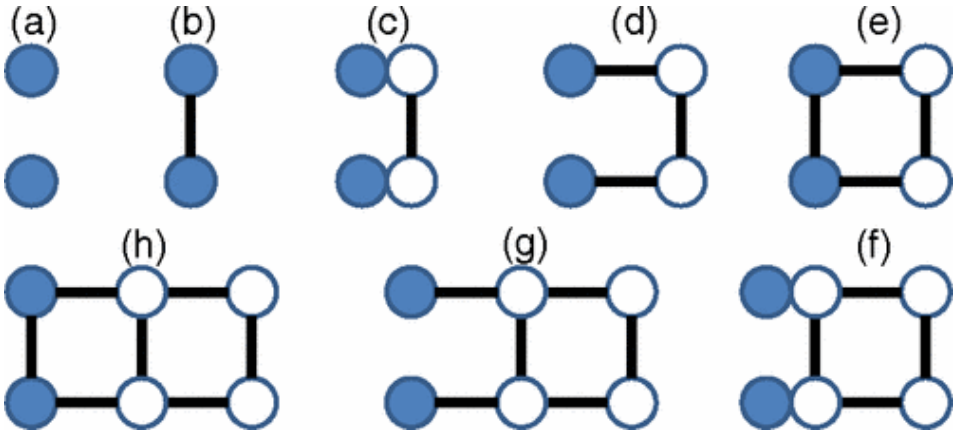

Figure 2.6: An outline of the first few cycles of 2D cluster state generation using 2 QDs. The coloured dots represent spins contained within a pair of quantum dots, while the empty dots are generated photons. In step (a) the spins are initialised, in (b) they are entangled via a CZ gate, in (c) and (d) photons are produced as per the CSMG, and then in (e-h) the steps are repeated to produce larger states. Reused with permission from [91].

2.2.2 Other Entanglement Schemes

The cluster state machine gun is not the only protocol proposed for producing entangled states using quantum dots, though it may be the most widely discussed. Other protocols have been suggested, nearly all of which build on the CSMG in some way.

2.2.2.1 2D Cluster State Generation

The CSMG proposes to generate 1D cluster states, and then use optical fusion gates to form the 2D states necessary for quantum computation. A fusion gate probabalistically combines multi-photon cluster states (for example GHZ or W states) into larger states of the same type [73, 90]. The probabilistic nature of this combination creates implementation problems, and thus other solutions are being sought.

By using 2 quantum dots, it is possible to generate 2D states without the need for fusion gates [91]. This is done by entangling 2 QDs before each cycle of the CSMG, leading to the production of a 2D cluster state. The procedure for entangling the dots is as follows: first they are initialised to the $|\uparrow\rangle|\uparrow\rangle$ state[11], and then a $\frac{\pi}{2}$ rotation is applied to give the state $(|\uparrow\rangle+|\downarrow\rangle)(|\uparrow\rangle+|\downarrow\rangle)$, this is then entangled via the use of a controlled-z (CZ) gate to give the state $|\uparrow\rangle|\uparrow\rangle+|\uparrow\rangle|\downarrow\rangle+|\downarrow\rangle|\uparrow\rangle-|\downarrow\rangle|\downarrow\rangle$, which is entangled. From here, the standard CSMG pulses are applied to both dots, but with an additional re-entanglement step before each CSMG cycle. This results in a ladder of entangled states - a 2D cluster state, as shown in Fig. 2.6.

The question remains of how to implement the required CZ gate in a pair of QDs. It has been shown that it is possible to optically implement quantum logic gates on spins by taking

[11]This can be done using repeated circularly polarised pulses, without an external magnetic field [92].

advantage of the electron-hole exchange interaction [93], and this protocol builds on that idea. By exciting the pair of QDs to higher energy trion states, we create an additional electron which is delocalised across the QDs, and a hole which can be confined to one of them. This system of 3 electrons and a hole has 16 possible states, and it is shown in [91] that they are sufficiently far apart in energy such that a σ^+ pulse couples *only* the $|\downarrow\downarrow\rangle$ state to this higher manifold, and thus a resonant 2π pulse with σ^+ polarisation will implement the CZ gate. This implementation of a CZ gate has been demonstrated experimentally [94–96], though the full procedure discussed here has not yet been implemented.

2.2.2.2 Decoherence Resistant Generation

DiVencenzo's 3rd criteria states that any qubit must have a sufficiently long coherence time, which is achieved by isolating it from its environment. The same idea holds true for the generation of cluster states, whatever physical system we use to create entanglement must have a lifetime long enough to do so. Here we are defining lifetime in a loose way to mean something like: 'the time for which the system is useful for the purpose of generating high quality entangled photons'. In the case of QDs, this system is an electron trapped in a quantum dot, and the markers of 'usefulness' are the T_1, T_2 and T_2^* times. Chapter 3 discusses in detail the mechanisms within a dot that affect these times, but we will introduce them here in order to introduce another proposal for entanglement generation. The T_1 time of a QD measures the amount of time needed for the electron spin to lose energy, causing it to flip from the state $|\uparrow\rangle \rightarrow |\downarrow\rangle$. This is typically as a result of phonon emission, and T_1 times are typically of the order of at least ms [65, 97], and potentially ranging to seconds [98]. Both the T_2 and T_2^* times measure the time taken for the spin to lose coherence - the information represented as the phase difference between possible states of a superposition. The T_2 time is this measurement for a single quantum dot in a single experiment, and has been found to be of the order of ns [99, 100]. The T_2^* time is more complicated, it tries to capture the average behaviour of an ensemble[12] of quantum dots rather than the snapshot of behaviour characterised by T_2. As such, the T_2* of a system will always be less than or (in the best case) equal to the T_2. Procedures such as Hahn echo experiments have been shown to increase T_2 and T_2^* times to the μs regime [99] - though this can be thought of as merely revealing a longer T_2 by refocussing the nuclear spin bath. It should be noted that the concepts of T_1, T_2 and T_2^* are not unique to electrons - the same ideas apply to any single spin and we shall see later on that the nuclear coherence time plays a key role in determining the behaviour of a QD.

In order to counteract the effects of spin dephasing, Denning *et al* [72] proposed a protocol which relies on off-resonant scattering from a quantum dot in an optical cavity. By exciting the system with horizontally polarised light (H), we create a superposition between 2 possible photon

[12] An ensemble can be either a group of many dots each measured concurrently or a single dot measured many times in succession.

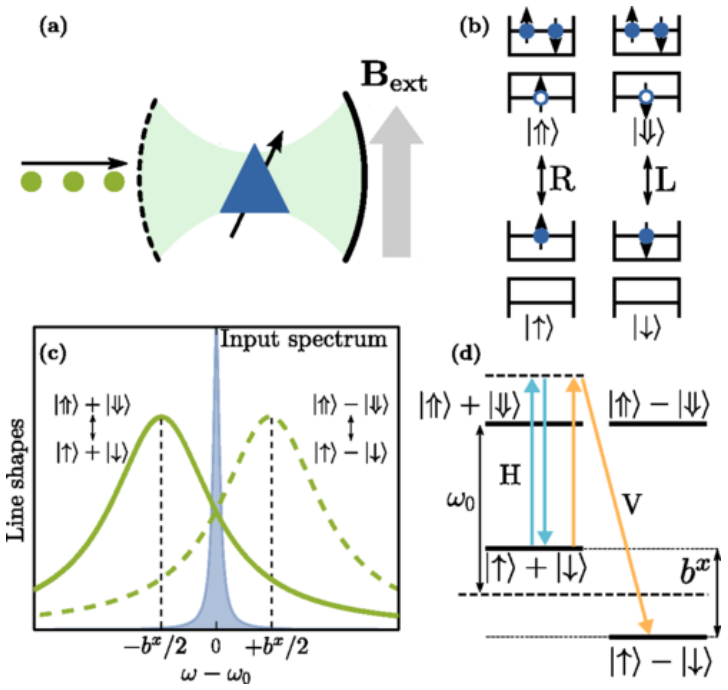

Figure 2.7: An outline of a dephasing resistant entanglement generation protocol. (a) QD sitting inside a single sided optical cavity, with a field perpendicular to the cavity. (b) Simplified band structure of the QD, showing the transitions under Right and Left circularly polarised light. (c) Incidence of a narrow photon, resonant with the 0 field transition, overlapping with the transition energies split by the applied field. (d) The possible transitions are shown in blue (a coherent transition which leaves the spin and photon states unchanged) and orange (Raman scattering, which flips the spin state and photon polarisation). Reused with permission from [72]

excitation modes (see Fig. 2.7), by repeating the photon scattering, we create a state of the form

$$\begin{aligned}|\psi\rangle = &\frac{1}{2}(|H,\omega_0\rangle_1(|H,\omega_0\rangle_2|\phi_+\rangle - i|V,\omega_+\rangle_2|\phi_-\rangle)\\ &+|V,\omega_+\rangle_1(|H,\omega_0\rangle_2|\phi_+\rangle - i|V,\omega_+\rangle_2|\phi_-\rangle)),\end{aligned} \tag{2.20}$$

where H and V refer to photon polarisation (horizontal or vertical), $\omega_{0/+}$ to photon energy, $\phi_\pm$ to spin energy and state subscripts label successive photons. This state is equivalent to the 3 qubit linear cluster state, and has the additional advantage of both terms having the same total energy. We can see this by noting that an initial Raman spin-flip will transfer energy b^x from the dot to the scattered photon, while the second will do the opposite. Thus, each term has energy $E = 2\omega_0 + \frac{b^x}{2}$ and will only pick up global phases as they evolve in time. In addition, fluctuations in the Overhauser field[13] will not cause dephasing either. States of n photons can then be created by simply repeating the cycle for as long as needed. It should be noted that such states are no longer equivalent to the n qubit linear cluster state, but are still highly entangled and provide a good resource for fusion.

[13] See Section 3.1

2.2.3 Entanglement Using Dots

We can clearly see that quantum dots are of great value in the production of photons for use in quantum computation. In principle, they are the ideal single photon source, and can be used to generate complex entangled states without the need for a great many additional optical elements. However, we have also seen that experimental implementation of suggested protocols lags behind the theoretical work, and this is largely due to the impact of spin decoherence. The first 2 protocols presented here take advantage of the complex band structure of a dot to generate entanglement, however they neglect the other complexities present in the system. The third protocol does attempt to rectify this, but it has not seen the experimental success of the cluster state machine gun, and requires the state to be modified after creation in order to be as useful for quantum computation. We have also seen that the machine gun imposes an upper limit on the possible applied magnetic field. In the next chapter, we will dive deeper into the world of spin decoherence in quantum dots, and see how the presence of $\approx 10^5$ nuclear spins causes an electron to behave somewhat differently to the ideal cases we have considered thus far.

CHAPTER 3

STRUCTURE OF THE NUCLEAR SPIN BATH

Quantum dots, though often referred to as artificial atoms, differ in a key way from individual atoms or spins - they are composed of tens of thousands of individual atoms, each with their own nuclei and electrons. The discussion in Chapter 2 treated the electron spin as though it was only under the influence of the crystal lattice and the external field. However, such a spin is navigating a far more complicated environment and the impact of the nuclear spin bath must be understood.

The fundamental physics that governs the behaviour of both electrons and nuclei in a quantum dot is that of a spin in a magnetic field. Classically, a charged, spinning particle of mass m, angular momentum $\boldsymbol{S}$ and charge q has a magnetic dipole moment of

$$\boldsymbol{\mu} = \frac{q}{2m}\boldsymbol{S}. \tag{3.1}$$

When considering a quantum spin, it becomes necessary to introduce a dimensionless g-factor g, which differs both between particles and between spin and orbital angular momentum, to relate the angular momentum quantum number to the observed magnetic moment. This results in

$$\boldsymbol{\mu} = g\frac{q}{2m}\boldsymbol{S} = g\frac{q\hbar}{2m}\frac{\boldsymbol{S}}{\hbar}, \tag{3.2}$$

as the standard equation describing a quantum spin in a magnetic field. The factor $\frac{q\hbar}{2m}$ has the units of JT^{-1}, and thus is the magnetic dipole moment of the particle in question. For an electron this is termed the Bohr magneton, and has the value $\mu_B = 9.27\times10^{-24}\mathrm{JT}^{-1}$ which is approximately 2000 times larger than the nuclear magneton of $\mu_N = 5.05\times10^{-27}\mathrm{JT}^{-1}$ [101]. Applying a magnetic field $\boldsymbol{B}$ to a generic spin, defining $\gamma = \frac{gq}{2m}$ and setting $\hbar = 1$ for convenience, we arrive at a system with Hamiltonian

$$\hat{H} = -\boldsymbol{\mu}\cdot\boldsymbol{B} = -\gamma\boldsymbol{B}\cdot\boldsymbol{S}. \tag{3.3}$$

If we simplify to the case of a magnetic field along only the z axis ($\hat{H}_z = -\gamma B \hat{S}_z$) and use the Schödinger equation we find the time evolution operator

$$\hat{U}(t,0) = \exp\left(-i\hat{H}t\right) = e^{(-iB_z\hat{S}_z t)}, \tag{3.4}$$

which we recognise as a rotation acting on the spin. To see the effect of this, we take a spin state initially aligned with the angles (θ_0, ϕ_0),

$$|\psi\rangle(t=0) = \cos\frac{\theta_0}{2}|+\rangle + \sin\frac{\theta_0}{2}e^{i\phi_0}|-\rangle, \tag{3.5}$$

where $|\pm\rangle$ are the eigenstates of $\hat{H}_z$ obeying $\hat{H}_z|\pm\rangle = \mp\frac{\gamma B}{2}|\pm\rangle$. We can apply the time evolution operator $\hat{U}_z(t,0) = \exp(-i(-\gamma B t\hat{S}_z))$ to obtain the state after time t

$$\begin{aligned} |\psi\rangle(t) &= \cos\frac{\theta_0}{2}e^{\frac{i\gamma Bt}{2}}|+\rangle + \sin\frac{\theta_0}{2}e^{i\phi_0}e^{\frac{-i\gamma Bt}{2}}|-\rangle \\ &= e^{\frac{i\gamma Bt}{2}}\left(\cos\frac{\theta_0}{2}|+\rangle + \sin\frac{\theta_0}{2}e^{i(\phi_0-\gamma Bt)}|-\rangle\right). \end{aligned} \tag{3.6}$$

Ignoring the global phase we recognise that this is the same spin state as at $t = 0$, but now orientated along the angles $(\theta = \theta_0, \phi = \phi_0 - \gamma Bt)$. The spin has rotated around the z axis at a rate determined by the strength of the applied magnetic field. This precession is known as Lamor precession and a general spin precesses around an arbitrary field at the Lamor frequency

$$\boldsymbol{\omega}_L = -\gamma \boldsymbol{B}. \tag{3.7}$$

Lamor precession occurs for every single spin in our system. The electron and the nuclei all have their own spin vectors and evolve in multiple magnetic fields: the applied field, the field generated by the nuclei and the field generated by the electron. In a system of at least 10^5 constantly changing spins and magnetic fields, we have no hope of modelling all of their behaviour individually with either analytic or simulation methods. We must therefore treat the nuclear spins as a collective.

3.1 Nuclear Spins in Quantum Dots

A huge range of approximations and simulation methods have been put forward, including various numerical methods, master equation techniques and perturbation theory approaches. [102–107]. These techniques aim to capture the behaviours first introduced in Section 2.2.2.2: spin relaxation and spin dephasing.

3.1.1 Electron Spin Relaxation

Spin relaxation is the process of a spin[1] losing energy by flipping from the state $|\uparrow\rangle \rightarrow |\downarrow\rangle$, this is characterised as the T_1 time of the spin. In the general case of a free spin in a lattice this is largely

[1] In our case, an electron spin in a QD.

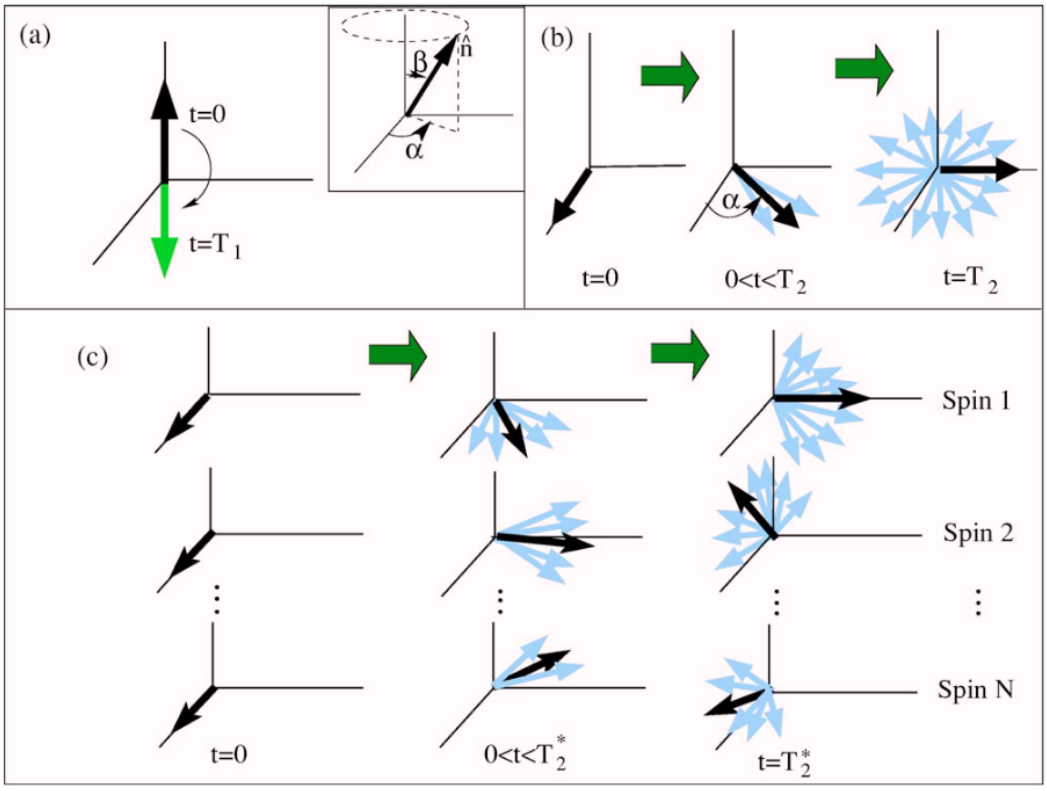

Figure 3.1: Illustration of T_1, T_2 and T_2^*. (a) T_1 is the average time for a spin to lose energy and flip from $|\uparrow\rangle \rightarrow |\downarrow\rangle$. Inset shows how 2 angles can be used to represent the direction of a spin. (b) T_2 is the time required for an observer to lose all knowledge of the possible phase of the spin, possible directions are show in blue. (c) T_2^* is the time required for an ensemble of N spins to become dephased with each other, possible directions are shown in blue. Reused with permission from [108].

the result of the spin-orbit interaction, which couples the spin and orbital angular momenta of an electron and further splits the valence and conduction bands [109–111]. However, in a quantum dot, the spin-orbit interaction is suppressed by the confinement of the electron [112–114], and hence the chief form of energy loss is via phonon interactions [115–117]. Experimental results indicate that T_1 is typically of the order of μs, but can be extended to the ms or s regime. As such, while spin relaxation places a ceiling on the timescales over which to implement an entanglement generation scheme, it is of less importance than the often far shorter dephasing times found in QDs.

3.1.2 Electron Spin Dephasing

Spin dephasing (or decoherence) is the loss of information contained in the phase of a superposition state. In a quantum dot, these processes are split into 2 types: homogeneous dephasing is irreversible and characterised by the T_2 time, while inhomogenous dephasing can be undone

via spin echos and is characterised by T_2^*. Theoretically, it is always the case that $T_2^* \leq T_2$, but equality is not achievable in practice due to the impossibility of knowing the initial state of every nuclear spin individually. Both homogeneous and inhomogeneous dephasing come about as a result of the hyperfine interaction between the electron and the nuclear spin bath.

3.1.2.1 The Hyperfine Interaction

We first consider the Hamiltonian of an electron in a magnetic field[2]

$$\hat{H}_e = \frac{1}{2m_e}(\hat{\boldsymbol{p}} + \frac{e}{c}\boldsymbol{A})^2 + 2\mu_B \hat{\boldsymbol{S}} \cdot \boldsymbol{B}, \tag{3.8}$$

where $\hat{\boldsymbol{p}}$ is the electron momentum, $\hat{\boldsymbol{S}}$ the electron spin and $\boldsymbol{B} = \nabla \times \boldsymbol{A}$ is the magnetic field. The vector potential $\boldsymbol{A}$ is chosen in such a way to satisfy the Coulomb gauge $\nabla \cdot \boldsymbol{A} = 0$, and for a stationary nucleus with magnetic moment $\boldsymbol{\mu}_N$ takes the form

$$\boldsymbol{A} = \frac{\boldsymbol{\mu}_N \times \boldsymbol{r}}{r^3} = \nabla \times \frac{\boldsymbol{\mu}_N}{r} \tag{3.9}$$

at a point defined by the displacement vector $\boldsymbol{r}$. By substituting this into Eq. 3.8 and expanding the first set of brackets we arrive at

$$\hat{H}_e = \frac{1}{2m_e}(\hat{\boldsymbol{p}}^2 + \frac{e}{c}(\hat{\boldsymbol{p}} \cdot \boldsymbol{A} + \boldsymbol{A} \cdot \hat{\boldsymbol{p}}) + \frac{e^2}{c^2}\boldsymbol{A}^2) + 2\mu_B \hat{\boldsymbol{S}} \cdot (\nabla \times \frac{\boldsymbol{\mu_N}}{r}). \tag{3.10}$$

We note that this Hamiltonian is structured as $\hat{H}_e = \hat{H}_0 + \hat{H}_i$, where $\hat{H}_0 = \frac{\hat{\boldsymbol{p}}^2}{2m_e}$ is the free electron Hamiltonian and $\hat{H}_i$ can be treated as a perturbation. By substituting Eq. 3.9 into Eq. 3.10, and taking only terms to first order in $\hat{\boldsymbol{A}}$, we find the interaction Hamiltonian

$$\hat{H}_i = \frac{e}{2m_e c}(\hat{\boldsymbol{p}} \cdot \hat{\boldsymbol{A}} + \hat{\boldsymbol{A}} \cdot \hat{\boldsymbol{p}}) + 2\mu_B \hat{\boldsymbol{S}} \cdot (\nabla \times (\nabla \times \frac{\boldsymbol{\mu_N}}{r})). \tag{3.11}$$

We can further separate this Hamiltonian into two parts $\hat{H}_i^L$ and $\hat{H}_i^S$. The second term

$$\hat{H}_i^S = 2\mu_B \hat{\boldsymbol{S}} \cdot (\nabla \times (\nabla \times \frac{\boldsymbol{\mu_N}}{r})), \tag{3.12}$$

describes the action of the spin component of electron angular momentum. It can be rewritten as

$$\hat{H}_i^S = 2\mu_B \left((\hat{\boldsymbol{S}} \cdot \nabla)(\boldsymbol{\mu}_N \cdot \nabla) - \frac{1}{3}(\hat{\boldsymbol{S}} \cdot \boldsymbol{\mu}_N)\nabla^2 \right) \left(\frac{1}{r} \right) - \frac{4\mu_B}{3}(\hat{\boldsymbol{S}} \cdot \boldsymbol{\mu}_N)\nabla^2 \left(\frac{1}{r} \right). \tag{3.13}$$

In the limit $r > 0$, the first term in Eq. 3.13 is equal to

$$2\mu_B \left(\frac{3(\hat{\boldsymbol{S}} \cdot \boldsymbol{r})(\boldsymbol{\mu}_N \cdot \boldsymbol{r})}{r^5} - \frac{(\hat{\boldsymbol{S}} \cdot \boldsymbol{\mu}_N)}{r^3} \right), \tag{3.14}$$

[2]This derivation can be found in [118], however this work is not for the faint of heart and does not go into the details of the required vector analysis. Any steps or identities we have found useful are noted in Appendix A.1.

and the second term is a δ function of $\boldsymbol{r}$ ($-\nabla^2 \frac{1}{r} = \delta(\boldsymbol{r})$). Hence we find that the spin part of the interaction takes the form

$$\hat{H}_i^S = 2\mu_B \left(-\frac{(\hat{\boldsymbol{S}} \cdot \boldsymbol{\mu}_N)}{r^3} + \frac{3(\hat{\boldsymbol{S}} \cdot \boldsymbol{r})(\boldsymbol{\mu}_N \cdot \boldsymbol{r})}{r^5} + \frac{8\pi\mu_B}{3}(\hat{\boldsymbol{S}} \cdot \boldsymbol{\mu}_N) \right). \tag{3.15}$$

It is useful to note that Eq. 3.14 is the standard dipole-dipole interaction between 2 spinning charges.

We now turn our attention to the first term in Eq. 3.11, which corresponds to the electron orbital angular momentum. Using the definition of orbital angular momentum $\hbar\hat{\boldsymbol{l}} = \hat{\boldsymbol{L}} = \boldsymbol{r} \times \hat{\boldsymbol{p}}$, we can rewrite the $\hat{H}_i^L = \frac{e}{2m_e c}(\hat{\boldsymbol{p}} \cdot \hat{\boldsymbol{A}} + \hat{\boldsymbol{A}} \cdot \hat{\boldsymbol{p}})$ term to be of the form

$$\hat{H}_L = 2\mu_B \frac{\hat{\boldsymbol{l}} \cdot \boldsymbol{\mu}_N}{r^3}. \tag{3.16}$$

From here we find the complete description of the interaction Hamiltonian by substituting Eqs. 3.15 and 3.16 into Eq. 3.11 to arrive at

$$\hat{H}_I = 2\mu_B \boldsymbol{\mu}_N \cdot \left(\frac{\hat{\boldsymbol{l}}}{r^3} - \frac{\hat{\boldsymbol{S}}}{r^3} + 3\frac{\boldsymbol{r}(\hat{\boldsymbol{S}} \cdot \boldsymbol{r})}{r^5} + \frac{8}{3}\pi\hat{\boldsymbol{S}}\delta(\boldsymbol{r}) \right). \tag{3.17}$$

The conduction band of a QD is made up of s orbitals with no orbital angular momentum. When evaluated for such an electron, all of the terms in Eq. 3.17 vanish, because of the lack of orbital angular momentum, and the symmetry of the s orbital, except the one proportional to $\delta(\boldsymbol{r})$. This surviving term is the Fermi contact interaction, and it forms the basis for spin flips in quantum dots. It is necessary to extend this Hamiltonian to account for the many nuclei present in a QD system, this is done by summing the contact term over all the nuclei to find

$$\begin{aligned} \hat{H}_{\mathrm{HF}} &= \sum_k A_k \hat{\boldsymbol{I}} \cdot \hat{\boldsymbol{S}} \\ &= \sum_k A_k I_k^z S^z + \sum_k \frac{A_k}{2}(S^+ I_k^- + S^- I_k^+), \end{aligned} \tag{3.18}$$

where we sum over the nuclei k and

$$A_k = \frac{16}{3}\pi\mu_B |\psi(0)|^2. \tag{3.19}$$

This Hamiltonian results in correlations between the electron and nuclear spins in a QD. In an experiment where we measure only the state of the electron (and hence trace out the nuclear spins) these correlations manifest as dephasing of the electron spin, a key phenomenon in the study of QD systems [98, 108, 119–122].

3.1.2.2 The Frozen Fluctuations Model

In many cases, this dephasing is well described by the frozen fluctuations model, first introduced in QDs by Merkulov *et al* in [123]. This model treats the nuclear spin bath as a randomly directed,

static magnetic field, termed the Overhauser field ($\boldsymbol{B}_N$), with which the electron then interacts alongside any externally applied field. We can treat $\boldsymbol{B}_N$ as static because the effect of the electron on any individual nucleus is much smaller than the effect of all the nuclei on the electron. The evolution of the electron spin under these assumptions can be found by first calculating $\boldsymbol{B}_N$ by taking the expectation value of $\hat{H}_I$ over all nuclear spin states

$$\boldsymbol{B}_N = \frac{1}{\mu_B g_e} \left\langle \sum_j A_j \hat{\boldsymbol{I}}_j \right\rangle, \tag{3.20}$$

and then evaluating this expectation value for a maximally mixed nuclear spin state to find a distribution of polarisation probabilities for the nuclear spin bath

$$p(\boldsymbol{B}_N) = \frac{1}{\pi^{\frac{3}{2}} \Delta^3} \exp\left(-\left(\frac{B_N}{\Delta}\right)^2\right), \tag{3.21}$$

which is a Gaussian distribution with variance

$$\Delta = \frac{2}{3} \sum_j I_j (I_j + 1) \left(\frac{A_j}{\mu_B g_e}\right)^2 \tag{3.22}$$

and mean $B_N = |\boldsymbol{B}_N|$. We now take the electron spin vector

$$\boldsymbol{S}(t) = \begin{pmatrix} \langle \hat{S}_x \rangle(t) \\ \langle \hat{S}_y \rangle(t) \\ \langle \hat{S}_z \rangle(t) \end{pmatrix} \tag{3.23}$$

and average it over all possible values of the total magnetic field experienced by the electron ($\boldsymbol{B}_T = \boldsymbol{B} + \boldsymbol{B}_N$) to find

$$\begin{aligned} \langle \boldsymbol{S}(t) \rangle = &(R_\parallel^\infty + R_\parallel(t))(\boldsymbol{S}_0 \cdot \boldsymbol{b})\boldsymbol{b} \\ &+ (R_\perp^\infty + R_\perp^0(t))(\boldsymbol{S}_0 - (\boldsymbol{S}_0 \cdot \boldsymbol{b})\boldsymbol{b}) \\ &+ R_\perp^1(t)((\boldsymbol{S}_0 - (\boldsymbol{S}_0 \cdot \boldsymbol{b})\boldsymbol{b}) \times \boldsymbol{b}). \end{aligned} \tag{3.24}$$

The coefficients $R(t)$ have analytic forms defined in [123], and describe the orientation of the various components of the electron spin relative to the externally applied field. The time-dependant coefficients all tend to 0 in the long time limit, therefore the electron spin polarisation will always eventually lie in the plane spanned by the initial spin $\boldsymbol{S}_0$ and the external field direction $\boldsymbol{b}$. If $|\boldsymbol{B}| \gg |\boldsymbol{B}_N|$ (the large field limit), then we also have $R_\parallel^\infty \gg R_\perp^\infty$ and the electron spin comes to align with the external magnetic field.

The decoherence here has been calculated by averaging over all possible orientations of the effective magnetic field, and as such is an ensemble effect. If the initial orientation and strength of the Overhauser field were known, and then the system allowed to evolve, we would not see this effect. It is only in the ensemble average of many dots, or a single dot measured many times, that we see this behaviour - see Fig. 3.1. For any single QD, the evolution of the electron spin

over short times is coherent. This can be seen by performing a spin echo[3] experiment, where the spin evolution is reversed by flipping the spin using optical pulses [124–126]. Such experiments have shown coherence times up to 3μs [65, 127]. Of course, Eq. 3.24 is only valid for timescales over which the nuclear spins are static[4]. At timescales longer than this, the evolution of the nuclear spins under interaction with each other and the central electron become significant, and the Overhauser field vector will have substantially changed from the initial randomly selected value as a result of nuclear spin flips. This evolution of the effective field leads to electron spin decoherence which cannot be undone by a spin echo as it is not coherent over even a single experimental run.

3.2 Controlling Nuclear Spins

Dephasing processes present a substantial barrier to the use of QDs as single or entangled photon sources. What then can be done to reduce these effects? The ideal case is of course that we engineer a single electron inside the QD, isolated perfectly from the nuclei[5] but this is obviously not practical. If we accept that there will be some interaction with the spin bath, what can we do to minimise its impact? There are 2 obvious routes to take: we can try to weaken the interaction between the electron and the nuclei, or we can try and prepare and maintain the nuclei in a known state and then undo or account for their impact on the electron spin. Weakening the interaction would require reducing the value of the coupling constants A_k, as we can see from Eq 3.19 this would require changing either the value of the fundamental magnetic moments of either the electron or nucleus, or moving them away from each other - neither of which are possible inside a specific quantum dot. We are thus left only with the option to prepare and maintain the nuclear spin bath in a specific, useful state. There also exist experimental protocols such as dynamic decoupling which have been used to extend heavy hole coherence times into the μs regime [128].

The ideal nuclear spin state will of course depend on what we are trying to do with the QD. In the case of generating entangled photons, we want long electron coherence times and low magnetic fields. Long coherence times will allow us to produce larger cluster states, both by allowing more cycles of the generating procedure and maintaining a high degree of indistinguishability between the first and last photons in the cluster. Low magnetic fields are needed specifically in the case of the CSMG as high fields cause spin rotations that are faster than trion decay and ruin the protocol. How can we achieve these twin goals? What state do we want the spin bath to be in? Equation 3.20 demonstrates that the Overhauser field $\boldsymbol{B}_N$ comes about as a result of the distribution of nuclear spins. In the extreme case that all of the nuclear spins were exactly

[3] Often also called a Hahn echo, which technically refers to the exact polarisation of the pulses used to generate the spin echo.

[4] Hence the term *frozen* fluctuations.

[5] And indeed any other environment save that created by our readout and manipulation pulses.

aligned, the resulting Overhauser field would be strong and well defined in a single direction. However, as nuclear spin flips occur and the distribution of nuclear spins changes, so too will the direction and strength of the resulting Overhauser field. In order to achieve long electron coherence times, we need to engineer an Overhauser field which is well defined and does not change quickly - we must polarise the nuclear spins in a specific direction and then keep them there for as long as possible. Knowing the direction of the Overhauser field allows us to apply an external field of the correct size and direction such that the overall magnetic field felt by the electron is exactly what we need for the particular experiment we are doing.

3.2.1 Preparation and Maintenance of the Bath

The most obvious method to polarise a nuclear spin bath is by applying a large magnetic field, which will align the spins in the same way as it would align an array of bar magnets. However, in the case of nuclear spins we must think about the relative size of thermal fluctuations to the splitting. For illustrative purposes, consider the case of a single spin in a field aligned along the z axis, the relevant Zeeman splitting has a magnitude of the order $|E_s| = \mu_N B$. Thermal fluctuations will be of the order $k_B T$, leading us to require

$$\begin{aligned} &\mu_N B > k_B T \\ \implies &\frac{B}{T} > \frac{k_B}{\mu_N} \approx 2700\text{T K}^{-1}. \end{aligned} \tag{3.25}$$

We might expect a typical QD experiment to occur with $T = 4$ K and $B = 1$ T, leading to a ratio of $\frac{B}{T} = 0.25$ TK^{-1}. Achieving the required ratio would require either temperatures of the order 10^{-4} K or magnetic fields of the order 10^4 T. Neither of these are currently practically achievable, and if they were would substantially alter the behaviour of the system in other ways. For example, a magnetic field of this strength would cause electron spin rotations to happen with a frequency of $f \approx 2.8 \times 10^{14}$ Hz - far faster than is useful for any practical purpose. Therefore we must find alternative methods to polarise the spin bath.

Several protocols have been put forward to solve this problem [129–131], most of which rely on dynamic nuclear polarisation (DNP). As an example we will discuss nuclear frequency focussing (NFF), a protocol first implemented by Greilich *et al* [132], in which the nuclear spin bath is used to synchronise the precession of an electron spin with an optical pulse to reduce dephasing.

3.2.1.1 Dynamic Nuclear Polarisation

Since it's theoretical prediction in the 1950s [133], dynamic nuclear polarisation (DNP) has been studied extensively. First confirmed soon after being predicted [134], it has since been studied in a huge array of contexts [123, 135–147]. Here we will present an outline of the mechanisms of DNP, further discussion can be found in works such as Economou & Barnes [148] and Wu *et al* [149].

The basic mechanism of DNP is very simple: the central electron spin is polarised via some external source of angular momentum, then this polarisation is passed to the nuclear spin bath via the contact interaction and finally the electron spin is re-polarised and the process repeats. Over time, this leads to a build up of nuclear spin polarisation, though complete polarisation cannot practically be obtained due to the precession of nuclear spins. In a quantum dot system, the polarisation of the electron spin is typically done optically [150, 151], though electrical pumping methods have also found success in double quantum dot systems [152, 153]. The end goal of much of this research is to use DNP to extend the coherence time of central electron spin. A protocol which has seen some success in this area is nuclear frequency focussing, which relies on DNP to synchronise the precession periods of the electron and the nuclei in a QD.

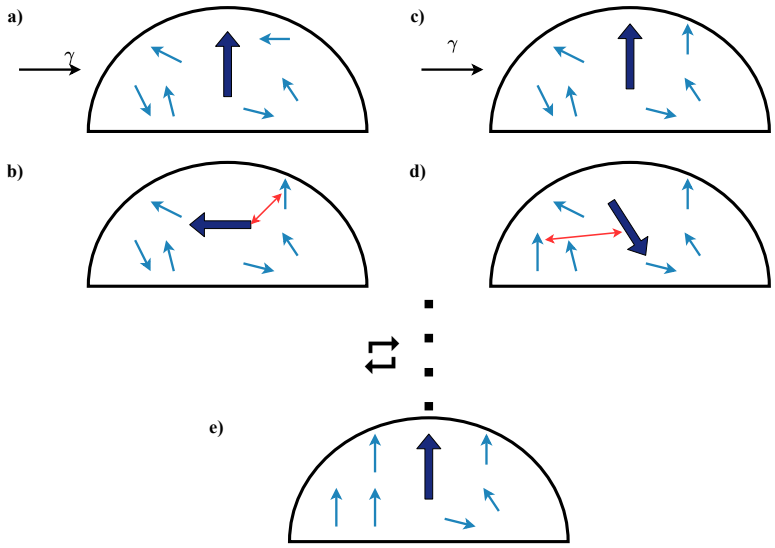

Figure 3.2: Schematic illustrating the principles of optical dynamic nuclear polarisation in a quantum dot. a) The central electron (large dark blue arrow) is polarised by an incoming photon. b) Exchange of angular momentum via the contact interaction (red double headed arrow) between the electron and a nearby nucleus (smaller, light blue arrows). c) The central electron is re-polarised by another incoming photon. d) Another exchange of angular momentum between the electron and a different nucleus in the bath. e) After many cycles of this process, a substantial fraction of the bath nuclei have been polarised.

3.2.1.2 Nuclear Frequency Focussing

First described by 2 papers by Greilich *et al* [99, 132], nuclear frequency focussing (NFF) is the result of applying a sequence of time-resolved Faraday rotations to a QD system. A mode locked laser is used to apply a periodic train of circularly polarised pulses, resulting in the synchronisation of the electron spin frequency across an ensemble of quantum dots. This synchronisation allows for constructive interference between the electron spins in the ensemble, and hence an increase in their overall coherence time. This procedure is therefore of great interest to anyone

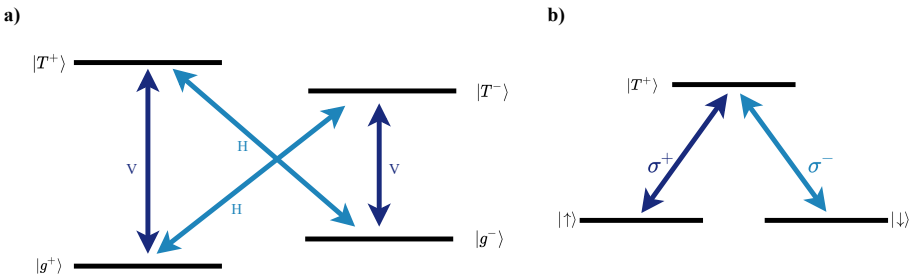

Figure 3.3: The energy level and transition structure of a negatively charged dot in a Voigt field. a) The energy level structure with respect to the eigenstates of the Hamiltonian, as described in Section 2.1.3, vertically (dark blue) and horizontally (light blue) polarised photons couple the ground states to individual trion states. b) The energy level structure as seen by circularly polarised light, interacting with spin states aligned along the optical axis of the QD. The state $|T\rangle$ is a trion state, composed of a mixture of the $|T^+\rangle$ and $|T^-\rangle$ states. Right (σ^+, dark blue) or left (σ^-, light blue) circularly polarised light both couple to the same mixed trion state, which can then decay to either spin state.

wanting to generate entangled cluster states, and running into the problems caused by short electron coherence times (as previously discussed in Section 2.2).

In the following section, we use a model put forward by Economou & Barnes [148], which has been used to understand multiple DNP processes including NFF. We note the labelling convention put forward by Economou & Barnes, in which the QD growth axis is labelled x and the perpendicular axis is labelled z. This is a rotation of the coordinate system used in the rest of this thesis, initially described in Fig. 1.2. We note that alternative models have recently been put forward, which use the central spin approach to model the behaviour of a QD undergoing NFF [131].

Consider a negatively charged QD, placed in a Voigt field (in the plane of the dot, labelled the z axis in this case). Such a dot will have an energy level structure as described in Section 2.1.3, and shown in Fig. 3.3. If we excite this dot using only light of a particular circular polarisation (σ^- for example), then only electrons in a specific spin state ($|\downarrow\rangle$) will be excited to the trion state. From there the spin can decay to either ground state, which are themselves rotating due to the applied magnetic field. As we are pumping only one of these ground states, over many repeated excitations there will be a shift in spin population to a steady state which is polarised towards the non pumped spin state ($|\uparrow\rangle$. This electron spin polarisation can last for as long as the pumping continues, and over time will begin to polarise the nuclear spin bath via the contact interaction. Eventually, the nuclear spin bath can become polarised enough that it acts to maintain the electron spin polarisation even in the absence of the pump excitation, this increases the coherence time of that electron which can then be used for other experiments - like single or entangled photon generation.

As shown in [148], and expanded on in [61][6], the Hamiltonian of this system has the form[7]

$$\hat{H} = \omega_e \hat{S}_z + \epsilon_T |T\rangle\langle T| + \sum_j q(t - jT_R)|\downarrow\rangle_z \langle T| + \text{H.C.} \tag{3.26}$$

where $\omega_e = g\mu_B B$ is the Lamor frequency of the electron and H.C. denotes the Hermitian conjugate of all prior terms. The term in $|T\rangle\langle T|$ gives the population of the trion state with energy ϵ_T, and the third term represents the pulse train. Each pulse is given a label j and described by a parameter $q = q_0 e^{i\phi}$, where $0 \leq q_0 \leq 1$ is the pulse area and $0 \leq \phi \leq 2\pi$ is the pulse detuning (which is also the angle of rotation about the x axis induced by the pulse). A resonant π pulse has $q = 0$, and no pulse has $q = 1$. Using this Hamiltonian as our starting point, we derive the following Kraus operators in the case where the trion decays equally to both spin states[8]

$$\begin{aligned} E_1 &= \begin{pmatrix} 1 & 0 \\ 0 & q \end{pmatrix} \\ E_2 &= \begin{pmatrix} 0 & \sqrt{\frac{1-q_0^2}{2}} \\ 0 & 0 \end{pmatrix} \\ E_3 &= \begin{pmatrix} 0 & 0 \\ 0 & \sqrt{\frac{1-q_0^2}{2}} \end{pmatrix}. \end{aligned} \tag{3.27}$$

These Kraus operators act on the generic initial density matrix

$$\rho_0 = \begin{pmatrix} \rho_{xx} & \rho_{x\bar{x}} \\ \rho_{\bar{x}x} & \rho_{\bar{x}\bar{x}} \end{pmatrix} \tag{3.28}$$

where we define $|x\rangle = |\uparrow\rangle, |\bar{x}\rangle = |\downarrow\rangle$ and $\rho_{ij} = |i\rangle\langle j|$. We note that ρ_0 does not represent the trion state, this is because it is defined only at those points in time after the trion state has decayed - ie before the initial excitation pulse, and shortly before each successive pulse thereafter. We are therefore assuming that the repetition rate of the pump laser is much slower than the lifetime of the trion state. To see the action of an optical pulse on the electron state we calculate

$$\begin{aligned} \rho_p &= \sum_k E_k \rho_0 E_k^\dagger \\ &= \begin{pmatrix} \rho_{xx} + \frac{1-q_0^2}{2}\rho_{\bar{x}\bar{x}} & q_0 e^{-i\phi}\rho_{x\bar{x}} \\ q_0 e^{i\phi}\rho_{\bar{x}x} & \frac{1+q_0^2}{2}\rho_{\bar{x}\bar{x}} \end{pmatrix}. \end{aligned} \tag{3.29}$$

Using this, we can see that in the case where no pulse is applied ($q_0 = 1, \phi = 0$), Eq 3.29 is equal to Eq 3.28 as expected. For a π pulse ($q_0 = 0$), we find that

$$\rho_\pi = \begin{pmatrix} \rho_{xx} + \frac{1}{2}\rho_{\bar{x}\bar{x}} & 0 \\ 0 & \rho_{\bar{x}\bar{x}} \end{pmatrix}. \tag{3.30}$$

[6]The appendices are of particular use, as they give a complete derivation of each term found in this model.

[7]We stress for the final time that the axis labels in this section are rotated from the convention used in the rest of this work.

[8]For a good introduction to the Kraus operator (also called operator-sum) formalism, we (as always) recommend [33].

Again, this is as expected - we have moved half the initial population of the state $|\bar{x}\rangle$ to the state $|x\rangle$.

Our goal with NFF is of course to generate electron polarisation along the z axis, which can then be passed onto the spin bath. We can measure the amount of such polarisation in the initial state by calculating $Z_0 = \langle z \rangle_{\rho_0} = \mathrm{tr}(\rho z) = \rho_{x\bar{x}} + \rho_{\bar{x}x} = 2\mathrm{Re}[\rho_{x\bar{x}}]$. It turns out to be useful to know the polarisation along the y axis as well, which is calculated similarly as $Y_0 = \langle y \rangle_{\rho_0} = \mathrm{tr}(\rho y) = i(\rho_{\bar{x}x} - \rho_{x\bar{x}}) = 2\mathrm{Im}[\rho_{x\bar{x}}]$. Combining these results, we can calculate the z polarisation generated by any pulse by calculating these quantities for the density matrix presented in Eq 3.29. Doing so we find

$$\begin{aligned} Z_{\mathrm{pol}} &= \mathrm{Re}[q_0 e^{-i\phi}\rho_{x\bar{x}} + q_0 e^{i\phi}\rho_{\bar{x}x}] \\ &= 2q_0(\cos(\phi)\mathrm{Re}[\rho_{x\bar{x}} + \sin(\phi)\mathrm{Im}[\rho_{x\bar{x}}] \\ &= q_0(\cos(\phi)Z_0 + \sin(\phi)Y_0). \end{aligned} \tag{3.31}$$

We can see from this that any increase in z polarisation requires $\phi \neq 0$ in order for the second term to exist and hence provide additional polarisation. We also require $q_0 \neq 0$ as otherwise any initial z polarisation will be destroyed. As such, we cannot use perfect π pulses, and all pulses must also rotate the spin around the x axis - a conclusion that agrees with our physical intuition.

So far our model only includes the effects of the optical pulses, we must now include the applied magnetic field that rotates the system between pulses. At the start of this chapter we showed that the action of this Lamor precession is described by a time evolution operator of the form

$$U_B = e^{-i\omega_e T_R |z\rangle\langle z|} = \begin{pmatrix} \cos(T_R\omega_e) & -i\sin(T_R\omega_e) \\ -i\sin(T_R\omega_e) & \cos(T_R\omega_e). \end{pmatrix} \tag{3.32}$$

We calculate the effect of this on an arbitrary initial density matrix as

$$\begin{aligned} \rho_B &= U_B \rho_0 U_B^\dagger \\ &= \begin{pmatrix} \cos(T_R\omega_e) & -i\sin(T_R\omega_e) \\ -i\sin(T_R\omega_e) & \cos(T_R\omega_e) \end{pmatrix} \begin{pmatrix} \rho_{xx} & \rho_{x\bar{x}} \\ \rho_{\bar{x}x} & \rho_{\bar{x}\bar{x}} \end{pmatrix} \begin{pmatrix} \cos(T_R\omega_e) & i\sin(T_R\omega_e) \\ i\sin(T_R\omega_e) & \cos(T_R\omega_e) \end{pmatrix} \\ &= \begin{pmatrix} \rho_{B,xx} & \rho_{B,x\bar{x}} \\ \rho_{B,\bar{x}x} & \rho_{B,\bar{x}\bar{x}} \end{pmatrix}, \end{aligned} \tag{3.33}$$

where

$$\begin{aligned} \rho_{B,xx} &= \rho_{xx}\cos^2(T_R\omega_e) + i(\rho_{x\bar{x}} - \rho_{\bar{x}x} + \rho_{\bar{x}\bar{x}}\sin^2(T_R\omega_e) \\ \rho_{B,x\bar{x}} &= \rho_{x\bar{x}}\cos^2(T_R\omega_e) + i(\rho_{xx} - \rho_{\bar{x}\bar{x}}\cos(T_R\omega_e)\sin(T_R\omega_e) + \rho_{\bar{x}x}\sin^2(T_R\omega_e) \\ \rho_{B,\bar{x}x} &= \rho_{x\bar{x}}\cos^2(T_R\omega_e) - i(\rho_{xx} - \rho_{\bar{x}\bar{x}}\cos(T_R\omega_e)\sin(T_R\omega_e) + \rho_{\bar{x}x}\sin^2(T_R\omega_e) \\ \rho_{B,\bar{x}\bar{x}} &= \rho_{xx}\sin^2(T_R\omega_e) - i(\rho_{x\bar{x}} - \rho_{\bar{x}x} + \rho_{\bar{x}\bar{x}}\cos^2(T_R\omega_e). \end{aligned} \tag{3.34}$$

We again calculate the effect this has on the z polarisation by calculating

$$\begin{aligned} Z_B &= 2\mathrm{Re}[\rho_{x\bar{x}}\cos^2(T_R\omega_e) + i(\rho_{xx} - \rho_{\bar{x}\bar{x}}\cos(T_R\omega_e)\sin(T_R\omega_e) + \rho_{\bar{x}x}\sin^2(T_R\omega_e)] \\ &= 2\cos^2(T_R\omega_e)\mathrm{Re}[\rho_{x\bar{x}}] + 2\sin^2(T_R\omega_e)\mathrm{Re}[\rho_{\bar{x}x}] \\ &= 2\mathrm{Re}[\rho_{x\bar{x}}](\cos^2(T_R\omega_e) + \sin^2(T_R\omega_e)) \\ &= 2\mathrm{Re}[\rho_{x\bar{x}}] \\ &= Z_0. \end{aligned} \tag{3.35}$$

Therefore, the Lamor rotation of the spin state leaves the z polarisation unchanged and the optical pulses are necessary to the procedure. We can combine the effects on the optical pulse and the applied field by defining new Kraus operators of the form

$$\mathscr{E}_i = E_i U_B, \tag{3.36}$$

meaning the state after n cycles of NFF (composed of a magnetic rotation followed by optical excitation) is given by[9]

$$\rho_{n+1} = \sum_i \mathscr{E}_i \rho_n \mathscr{E}_i^\dagger. \tag{3.37}$$

Using Eq 3.37 we can calculate the steady state of the electron, which will determine the amount of nuclear polarisation that can be generated using NFF. By writing the spin vector of the electron in matrix form, finding a recursive formula for the evolution of the state and then solving the resulting eigenvalue equation, it can be shown[10] that the steady state polarisation in the z direction is

$$S_z = \frac{q_0 \sin(\phi)\sin(\omega_e T_R)}{2 + q_0^2 - 2q_0\cos(\phi)\cos^2(\frac{\omega_e T_R}{2}) - cos(\omega_e T_R)}. \tag{3.38}$$

3.2.1.3 Dephasing in Nuclear Frequency Focussing

We now consider the result of applying a basic model of dephasing to the nuclear frequency focussing model described above. We introduce a toy model which we use to demonstrate the impact even a small amount of dephasing can have on a protocol, and hence why understanding and accounting for it is so important. This brief analysis is not intended to fully capture the behaviour of a system undergoing NFF, it is merely a demonstration that dephasing effects can very quickly become significant.

[9] We define a cycle as a rotation then an excitation as it allows us to incorporate the first cycle of NFF using the same formalism as all subsequent rounds.

[10] See the aforementioned appendices of Hinchliff 2018 [61] for the explicit calculations.

We take the standard Kraus operators for a generic dephasing channel [33] (rotated to account for the different basis definitions)[11], with a dephasing characterised by γ

$$\begin{aligned} D_1 &= \sqrt{\gamma}\mathbb{1} = \begin{pmatrix} \sqrt{\gamma} & 0 \\ 0 & \sqrt{\gamma} \end{pmatrix} \\ D_2 &= \sqrt{1-\gamma}\sigma_z = \begin{pmatrix} 0 & \sqrt{1-\gamma} \\ \sqrt{1-\gamma}, 0 & \end{pmatrix}, \end{aligned} \tag{3.39}$$

and apply them to the density matrix found in Eq. 3.37 to find

$$\begin{aligned} \rho_{d,n+1} &= \sum_m D_m \rho_{n+1} D_m^\dagger \\ &= \sum_m D_m \sum_i \mathscr{E}_i \rho_n \mathscr{E}_i^\dagger D_m^\dagger. \end{aligned} \tag{3.40}$$

We can then calculate the effect of this dephasing on the amount of polarisation generated in a single cycle of this dephased NFF protocol, acting on a simplified initial density matrix $\rho_0 = \left(\begin{smallmatrix} 0 & 0 \\ 0 & 1 \end{smallmatrix}\right)$, and we find the resulting polarisation to be

$$Z_D = (1-2\gamma) q_0^3 \sin(\omega_E T_R) \sin(\phi). \tag{3.41}$$

Applying the non-dephased protocol to the same initial state ρ_0 gives $Z = -q_0^3 \sin(\omega_E T_R)\sin(\phi)$. We can see therefore that even a small amount of dephasing will reduce the magnitude of generated polarisation substantially. The evolution of this model over time is much more complicated than that of the non-dephased model, and the resulting eigenvalue equation proved beyond the power of Mathematica to solve exactly. We can therefore draw only the intuitive conclusion that dephasing of the electron spin massively harms the usefulness of nuclear frequency focussing as a technique for producing electron spin coherence - which may go some way to explaining the apparent experimental limits to the technique.

3.2.1.4 Implementing Nuclear Frequency Focussing

The first examples of NFF being implemented are from Greilich *et al* in 2006 [99] and 2007 [132]. These experiments were done in the high field regime, using a magnetic field of 6T [155]. Later experiments have lowered the required field to 1T [156], with other demonstrations of the effect using fields of 3T [157] and 1.28T [158]. These fields are all much larger than the maximum fields tolerable when implementing a protocol like the CSMG which we have shown would benefit from the increased coherence times offered by NFF. It is of course not practical to simply implement NFF using a 1T field, and then rapidly switch to the 100mT field needed for the CSMG - commonly used superconducting magnets would likely quench during the switch, and a classical electromagnet would have significant heat problems and interfere with the cooling

[11] An exact understanding of the Kraus operator formalism is not necessary for any section besides this one, further details can be found in Nielsen and Chuang's excellent textbook [154].

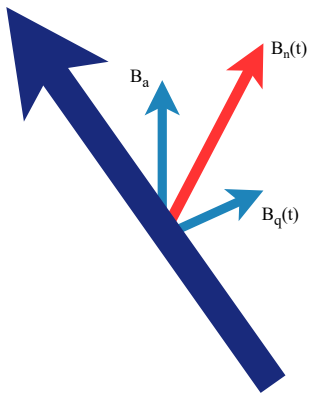

Figure 3.4: The interactions seen by a nuclear spin inside a quantum dot, ignoring hyperfine coupling. The nuclear spin (dark blue) is acted on by both an applied field B_a and an effective field B_q (both light blue) produced by the quadrupolar interaction and specific to that nuclear site. The total effective field B_n (red) is the vector sum of these 2 fields, and is therefore also different between each nuclear site.

required for the rest of the experiment. This all therefore begs the question: why has NFF not been performed at lower magnetic fields? What source of additional electron (or nuclear) decoherence becomes relevant at lower applied fields?

3.2.2 The Quadrupolar Interaction

The nuclear quadrupolar interaction (QI) is a second order interaction[12] between the spin of a nucleus, and the gradient of a nearby electric field. In a quantum dot the gradient of the electric field is determined by the local strain environment, via the 4^{th} rank gradient-elastic tensor S_{ijkl}, according to the relationship

$$V_{ij} = \sum_{k,l} S_{ijkl}\epsilon_{kl}. \tag{3.42}$$

As such each nucleus in a quantum dot will experience a different quadrupolar interaction and hence evolve differently over time. This has the effect of reducing the lifetime of the frozen fluctuations assumption, and hence the T_2 time of the central electron spin.

In order to understand the effects of the QI, we follow [159] and take as our starting point the classical expression for the interaction energy of 2 charge distributions, $\rho_n(\boldsymbol{r}_n)$ and $\rho_e(\boldsymbol{r}_e)$, representing the nucleus and an orbiting electron respectively

$$E = k \iint d\boldsymbol{r}_n d\boldsymbol{r}_e \frac{\rho_n(\boldsymbol{r}_n)\rho_e(\boldsymbol{r}_e)}{|\boldsymbol{r}_n - \boldsymbol{r}_e|}, \tag{3.43}$$

[12]The first order interaction is the dipole-dipole interaction.

with $k = \frac{1}{4\pi\epsilon_0}$. Assuming that $r_n < r_e$[13] we can use the following expansion of the denominator into spherical harmonics $Y_l^m(\theta,\phi)$[14] [160]

$$\frac{1}{|\boldsymbol{r}_n - \boldsymbol{r}_e|} = 4\pi \sum_{l=0}^{\infty} \sum_{m=-l}^{l} \frac{1}{2l+1} \frac{r_n^l}{r_e^{l+1}} Y_l^m(\theta_n,\phi_n) Y_l^{m*}(\theta_e,\phi_e). \tag{3.44}$$

to write this energy as a sum over operators A_l^m and B_l^m

$$E = \sum_{l=0}^{\infty} \sum_{m=-l}^{l} A_l^m B_l^{m*}, \tag{3.45}$$

where

$$A_l^m = \sqrt{\frac{4\pi}{2l+1}} \int d\boldsymbol{r}_n \rho_n(\boldsymbol{r}_n) r_n^l Y_l^m(\theta_n,\phi_n) \tag{3.46}$$

represents the nucleus and

$$B_l^m = \frac{1}{4\pi\epsilon_0} \sqrt{\frac{4\pi}{2l+1}} \int d\boldsymbol{r}_e \rho_e(\boldsymbol{r}_e) r_e^{-(l+1)} Y_l^m(\theta_e,\phi_e) \tag{3.47}$$

the electron. In order to introduce quantum mechanical behaviour to this model, we first write the nuclear ground state wavefunction $|\Psi_n(\boldsymbol{r}_1,\boldsymbol{r}_2,...,\boldsymbol{r}_{N_n})\rangle$, and define the nuclear charge density operator $\hat{\rho}_n(\hat{\boldsymbol{r}}_n)$ as

$$\hat{\rho}_n(\hat{\boldsymbol{r}}_n) = \left\langle \Psi_n \left| \sum_{i=1}^{N_n} e_i \delta(\hat{\boldsymbol{r}}_n - \hat{\boldsymbol{R}}_i) \right| \Psi_n \right\rangle. \tag{3.48}$$

This operator represents a nucleus as being made up of N nucleons, each with charge e_i[15]. We then plug this into Eq. 3.46 to find the expectation value of this charge distribution over the nucleus

$$\mathscr{A}_l^m = \left\langle \Psi_n \left| \int d\boldsymbol{r}_n \sqrt{\frac{4\pi}{2l+1}} \sum_{i=1}^{N_n} e_i \delta(\hat{\boldsymbol{r}}_n - \hat{\boldsymbol{R}}_i) r_n^l \hat{Y}_l^m(\theta_n,\phi_n) \right| \Psi_n \right\rangle. \tag{3.49}$$

Using the δ-function to evaluate the central integral, we find that the quantum mechanical nuclear operator is

$$\hat{A}_l^m = \sqrt{\frac{4\pi}{2l+1}} \sum_{i=1}^{N_n} e_i R_i^l \hat{Y}_l^m(\Theta_i,\Phi_i), \tag{3.50}$$

where R_i^l, Θ_i, Φ_i are the spherical coordinates of the i^{th} nucleon.

Following a similar procedure for the classical electron operator, we find its quantum equivalent

$$\hat{B}_l^m = -e \sqrt{\frac{4\pi}{2l+1}} \sum_{i=1}^{N_e} R_i^{-(l+1)} \hat{Y}_l^m(\Theta_i,\Phi_i), \tag{3.51}$$

[13] Valid, as the radius of a nucleus is much smaller than the orbital radius of any of it's electrons.

[14] An important note here is that the Y_l^m are spherical tensor operators. See Section A.2 for details on these and other tensors.

[15] e for protons, 0 for neutrons.

where the sum now runs over all electrons in the system rather than nucleons as before. We now use Eqs. 3.50 & 3.51 to find a fully quantum mechanical description for the interaction energy

$$\begin{aligned}\hat{H} &= \sum_{l=0}^{\infty}\sum_{m=-l}^{l} \hat{A}_l^m \hat{B}_l^{m\dagger} \\ &= \sum_{l=0}^{\infty}\sum_{m=-l}^{l} (-1)^m \hat{A}_l^m \hat{B}_l^{-m}.\end{aligned} \tag{3.52}$$

This provides a complete description of the electrostatic interactions between the electrons and the nucleus. The indices l and m are the total angular momentum and spin projection of the relevant particle. Though at first sight this sum is rather daunting, we note that it quickly converges as a result of all terms carrying a factor of $\frac{r_n^l}{r_e^{l+1}}$, which rapidly tends to 0 because $r_n << r_e$. We also note that all terms in A_l^m where l is odd vanish due to parity considerations [161]. Therefore the first term of interest is that of the order A_2^m, which describes the quadrupolar interaction. This term itself will only exist for nuclei with total spin $I \geq 1$, as a consequence of the Wigner-Eckart theorem[16].

Taking only the terms with $l = 2$, and defining the spherical harmonics in Cartesian coordinates [163] we find the components of $\hat{A}_2^m$

$$\begin{aligned}\hat{A}_2^0 &= \frac{1}{2}\sum_i e_i(3\hat{z}_i^2 - \hat{r}_i^2) \\ \hat{A}_2^{\pm 1} &= \mp\sqrt{\frac{3}{2}}\sum_i e_i \hat{z}_i(\hat{x}_i \pm \mathrm{i}\hat{y}_i^2) \\ \hat{A}_2^{\pm 2} &= \sqrt{\frac{3}{2}}\sum_i e_i(\hat{x}_i \pm \mathrm{i}\hat{y}_i^2)^2.\end{aligned} \tag{3.53}$$

The quadrupolar moment of a nucleus is defined to be

$$\begin{aligned}eQ &= 2\left\langle II \left| A_2^0 \right\| II \right\rangle \\ &= \left\langle II \left| \sum_i e_i(e\hat{Z}_i^2 - \hat{r}_i^2) \right| II \right\rangle,\end{aligned} \tag{3.54}$$

where the state $|II\rangle$ is one in which the spin projection m is equal to the total nuclear spin I. This quadrupolar moment is typically found experimentally. The Wigner-Eckart theorem (WET) is going to be useful again here, as it means we only need to know this single constant from Eq 3.54 and we can then calculate the other components of A_2^m. We can also exploit the WET and some generic properties of spherical-tensor operators [162] to rewrite the operators as sums of nuclear spin operators like so

$$\begin{aligned}\hat{Q}_2^0 &= \frac{2\alpha}{3}\hat{I}_z^2 - \hat{I}(\hat{I}+1)) \\ \hat{Q}_2^{\pm 1} &= \frac{\alpha}{\sqrt{2}}\left(\hat{I}_z\hat{I}_\pm + \hat{I}_\pm\hat{I}_z\right) \\ \hat{Q}_2^{\pm 2} &= \alpha\hat{I}_\pm^2\end{aligned} \tag{3.55}$$

[16]See Appendix A.2 for an introduction to this, or for a more detailed description we recommend Edmonds' book on spin and angular momentum [162].

We find the constant α by noting that these operators must produce the same physics as the original $\hat{A}_2^m$, leading us to

$$\begin{aligned}\langle II \left| A_2^0 \right\| II \rangle &= \frac{eQ}{2} = \alpha \langle II \left| Q_2^0 \right| II \rangle \\ &= \frac{\alpha}{2} I(2I-1) \\ \therefore \alpha &= \frac{eQ}{I(2I-1)}.\end{aligned} \tag{3.56}$$

Again we apply the same procedure to the electronic nuclear operators $\hat{B}_2^m$, plugging in the spherical harmonics as before, we find

$$\begin{aligned}\hat{B}_2^0 &= \frac{1}{2}\sum_{i=1}^{N_e}(-e)\frac{3\hat{z}_i^2 - \hat{r}_i^2}{\hat{r}_i^5}) \\ \hat{B}_2^{\pm 1} &= \frac{\sqrt{6}}{2}\sum_{i=1}^{N_e}(-e)\frac{(\hat{x}_i \pm \mathrm{i}\hat{y}_i)\hat{z}_i}{\hat{r}_i^5} \\ \hat{B}_2^{\pm 2} &= \frac{\sqrt{6}}{4}\sum_{i=1}^{N_e}(-e)\frac{(\hat{x}_i \pm \mathrm{i}\hat{y}_i)^2}{\hat{r}_i^5}.\end{aligned} \tag{3.57}$$

To make these more intuitive, we take advantage of classical electromagnetism. Electrons see a potential of the form $V = \frac{1}{r}$ from the nucleus of an atom, and therefore we calculate the following quantities:[17]

$$\begin{aligned}V_{zz} &= \frac{3\hat{z}^2 - \hat{r}^2}{\hat{r}^5} \\ V_{xz} \pm V_{yz} &= \frac{(\hat{x} \pm \mathrm{i}\hat{y})\hat{z}}{\hat{r}^5} \\ V_{xx} - V_{yy} \pm 2\mathrm{i}V_{xy} &= 3\frac{(\hat{x} \pm \mathrm{i}\hat{y})\hat{z}_i}{\hat{r}^5}\end{aligned} \tag{3.58}$$

By comparing equations 3.58 to equations 3.57, we can see that

$$\begin{aligned}\hat{B}_2^0 &= \frac{1}{2}V_{zz} \\ \hat{B}_2^{\pm 1} &= \frac{1}{\sqrt{6}}(V_{xz} \pm \mathrm{i}V_{yz}) \\ \hat{B}_2^{\pm 2} &= \frac{1}{2\sqrt{6}}(V_{xx} - V_{yy} \pm 2\mathrm{i}V_{xy}).\end{aligned} \tag{3.59}$$

We can now think about our choice of axes. The 9 possible second order derivatives V_{ij} form a symmetric second rank tensor, and this can be rotated to find the most useful form. We can therefore choose our axes such that the cross terms $V_{xy} = V_{xz} = V_{yz} = 0$, and then label the leftover components to ensure that

$$|V_{zz}| \geq |V_{yy}| \geq |V_{xx}|. \tag{3.60}$$

[17] We write $\frac{\partial V}{\partial x}$ as V_x and $\frac{\partial^2 V}{\partial x^2}$ as V_{xx}, and similarly for other mixtures of derivatives.

These axes define the principle axis frame, which differs between each nuclear site in a lattice. By convention, we define $V_{zz} = eq$ and $\eta = \frac{V_{xx}-V_{yy}}{V_{zz}}$ to arrive at the final form of the electronic operator components in the principal axis frame

$$\begin{aligned} \hat{B}_2^0 &= \frac{eq}{2} \\ \hat{B}_2^{\pm 1} &= 0 \\ \hat{B}_2^{\pm 2} &= \frac{eq\eta}{2\sqrt{6}}. \end{aligned} \tag{3.61}$$

We are now at last in a position to write the quadrupolar Hamiltonian by combining Eqs 3.52, 3.53, 3.55 and 3.57 we find

$$\hat{H}_Q = \frac{e^2qQ}{4I(2I-1)}\left(3\hat{I}_z - \hat{I}(\hat{I}+1) + \frac{\eta}{2}(\hat{I}_+^2 + \hat{I}_-^2)\right). \tag{3.62}$$

As presented here, $\hat{H}_Q$ is in units of Joules. Some works present it instead in frequency units, using the constant $\frac{\omega_Q}{2} = \frac{e^2qQ}{8\hbar I(2I-1)\hbar}$, while others instead use the line splitting found in a 0 field experiment $f_Q = \frac{3\omega_Q}{4\pi} = \frac{3e^2qQ}{2\hbar I(2I-1)}$. It is also possible to define the spin tensors inside the brackets differently, though this is not a common convention in more modern work. This Hamiltonian forms part of the total Hamiltonian of each nucleus in a quantum dot, but each nuclear site sees different values of η and eQ, according to the electric field gradient (EFG) at that point in the lattice. It is vital to understand that this Hamiltonian is given in the principle axis frame of a single nucleus, and comparisons between nuclei therefore require rotation back into a standard reference frame in order to be meaningful.

When using a quantum dot as a source of entangled photons, we have seen that it is vital to consider the impact of effects at each scale of the structure and how they interact. At the most fundamental level, we must consider the shape and composition of the structure itself (though we concentrate on InGaAs QDs in this work), these feed through by creating the strain profile of the dot. The strain profile then creates the electric field gradient felt by the nuclei, which each in turn evolve over time in an environment which may be unique to them. The sum total of nuclear effects is then felt by an electron spin trapped in the dot, which is then in turn used to produce entangled photons. A change to any part of this underlying chain of effects can have a substantial impact on the final quality and quantity of any photons produced from the dot. In the next chapter, we shall set out how the electric field gradient is created by the strain profile of a quantum dot, and investigate how updated measurements of the gradient elastic tensor result in dramatic changes to the strength and distribution of the quadrupolar interaction over a particular quantum dot. This allows us to draw informed conclusions about which measures of quality are useful for assessing the value of a dot for entangled photon production.

CHAPTER 4

CHANGING THE GRADIENT-ELASTIC TENSOR

4.1 Introduction and Methods

In this chapter we investigate the impact of recent improvements to measurements of the gradient elastic tensor (GET). We will calculate the strength and direction of the quadrupolar interaction in a quantum dot from a 2D slice through the structure, making reasonable assumptions about the strain distribution in order to do so. We will compare the results of these calculations with previous work, and show there is a substantial difference in the calculated nuclear spin environment. We extend previous analysis by investigating the distribution of quadrupolar strengths within the structure, and discussing the effect of increased biaxiality within each nucleus on the coherence time of a central electron spin. We also introduce a toy model of a 2D strained lattice in order to intuitively explain the behaviour of strained materials and the calculation of the relevant mathematical objects. The codebase underlying this analysis is used in later chapters to investigate hypothetical highly symmetric quantum dots according to the measures of quality set out in this chapter, and therefore here we shall also briefly outline how it functions.

Intuitively, the gradient elastic tensor is responsible for translating the mechanical strain in a material into an electric field gradient (EFG). As such, we can expect that changing any of the components of the tensor will result in a different EFG than would be measured using a different tensor. Therefore if we were to compare 2 structures with the same strain distribution, but with somehow different GET components[1] we would find them to have different resulting EFGs. As we have seen in Section 3.2.2, the EFG determines the size and direction of the quadrupolar interaction felt by each nucleus. Section 3.1.2 demonstrated the importance of a central electron

[1]This would imply the structures being made of different materials, but pretend that it doesn't for the purposes of this paragraph.

interacting with homogeneous nuclear spins. Therefore in the ideal case, the EFG should be as similar as possible throughout the dot and we therefore require the strain to be as similar as possible as well. However, the precise impact of the strain is mediated by the GET, and hence accurate knowledge of the components of this tensor is vital to any attempt to assessing the usefulness of a particular QD. Hence, we investigate just how large an impact the GET has on the overall quadrupolar field across all nuclei in a QD, and show that slight changes to the component values make a significant difference to the resulting quadrupolar field.

4.1.1 Strain

As we saw in Section 1.2, a QD grown by the Stranski-Krastanov method must be a strained structure. By this we mean that the position of the atoms within the InGaAs portion of the lattice are different from where they would be in a pure GaAs structure. A simple way of understanding this is to think of a 2-dimensional grid of alternately coloured blocks connected by springs. A red block represents a gallium atom and a blue block represent an arsenic atom. The tension in a spring connecting 2 blocks represents the strength of the bond between the 2 atoms, and the length of the spring represents their distance apart. In a toy model consisting of such a grid covering an infinite plane, we would expect each spring to have exactly equal length and tension, and we can think of these values as the 'natural' values. If we now introduce a green block in place of a red (representing indium replacing gallium in the lattice), with its own springs of different natural length and tension we will see a distortion of the lattice surrounding that point. If the springs attached to the green block are weaker than the red then the surrounding blue blocks will be pulled away from the green, and vice versa if the springs are stronger.

We can examine this behaviour using a simulation in which we create a lattice of interlinked springs, each with their own spring constant k and natural length x_0. Hooke's law tells us that the energy of a spring of length x is therefore $E = k(x - x_0)^2$. The total energy H of this system of springs is found by simply summing over the energies of the springs individually

$$H = \sum_n E_n = \sum_n k_n (x_n - x_{0,n})^2. \tag{4.1}$$

We minimise this function under varying ${x_n}$[2] to find the configuration with the lowest total energy. From there, we take the lengths of each spring and calculate the new positions of the blocks. An example of the results of this procedure is shown in Fig. 4.1

The parameters of the toy model can then be varied to match the relative bond strengths and lengths of In-As and Ga-As bonds, in order to get a quick understanding for the effect on the lattice that an indium atom (or a collection therefore) may have. These parameters are well known - see Vurgaftman *et al* [164] and we only need their relative values as summarised in Table 4.1

[2]Subject to constraints on the total length of the springs in the x and y directions.

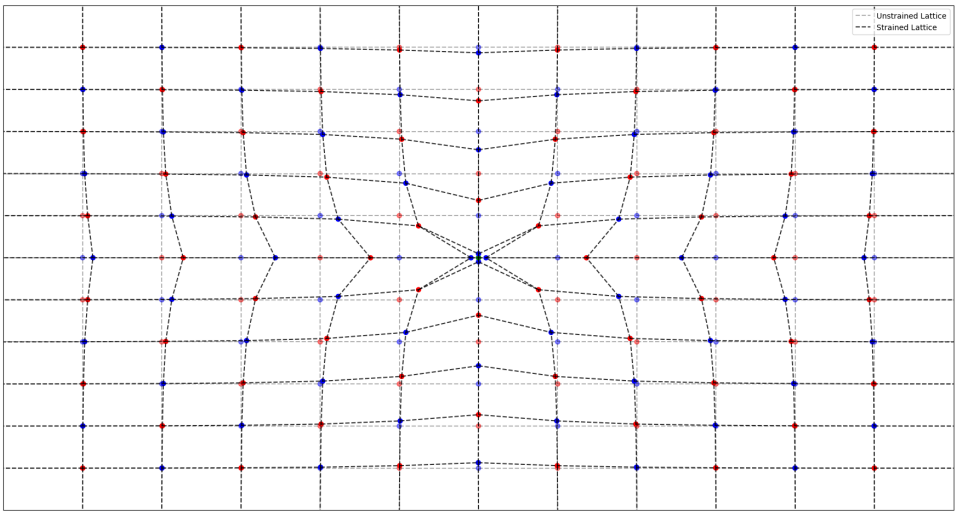

Figure 4.1: The effect of adding a green block with far stronger springs can be clearly seen. The strained lattice is massively distorted by the impact of a single green block, which pulls the surrounding blocks towards itself. In this extreme example, the green block both pulls on blue blocks 20 times harder and is connected to them via springs which are 10 times shorter than those connecting red and blue blocks. These are significantly larger effects than would ever be seen in a real crystal.

	Length	Strength
Ga-Ga	1	1
Ga-As	1	2.56
Ga-In	1	1.22
As-As	1	2.99
As-In	1.06	2.30
In-In	1	1.58

Table 4.1: The lengths and strengths of various bonds that could be found in an InGaAs lattice, each normalised with respect to the Ga-Ga bond. Data taken from [164]. Only the data in the highlighted rows is used in the calculation of most lattice structures, we include the rest for completeness.

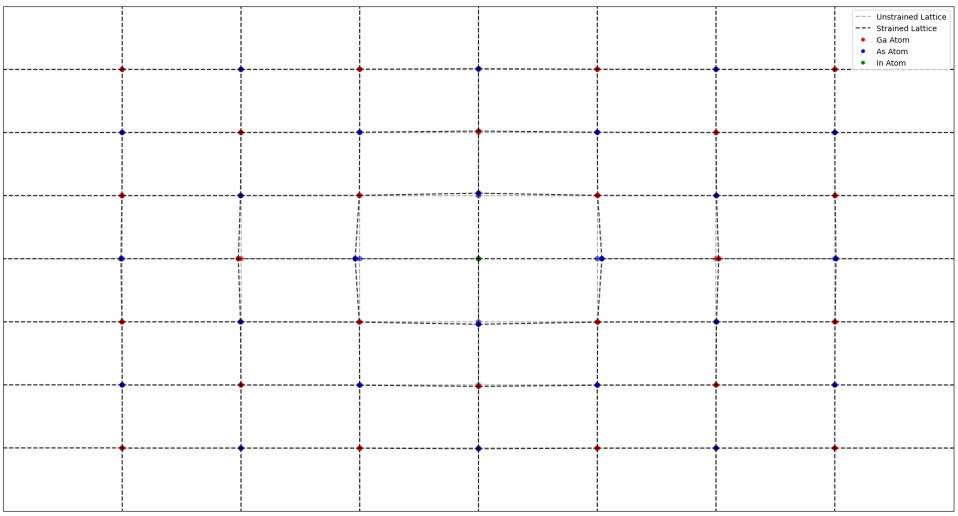

Figure 4.2: The effect of introducing a single indium atom to a 2D lattice of GaAs. We show only a small region, to highlight that the effect of a single indium atom is small.

Having obtained the positions of the atoms in the new lattice, we can then calculate the strain tensor for this simple model, according to the definition

$$\epsilon_{kl} = \frac{1}{2}\left(\frac{\delta u_k}{\delta x_l} + \frac{\delta u_l}{\delta x_k}\right) \tag{4.2}$$

where $u_k = x_k - x_{k,0}$ is the displacement of a point from it's original position and the corresponding derivative captures the change in displacement with respect to each axis [165]. To do this, we first define 2 sets of vectors to define the displacements between each point k and every other lattice point, respectively before and after the strain is applied: $\{R_{k1}, R_{k2}, ..., R_{kl}\}$ and $\{r_{k1}, r_{k2}, ..., r_{kl}\}$. We can then define the deformation gradient F according to[3] $r_{kl} - FR_{kl} = 0$ where $F = WV^{-1}$ [167] and

$$\begin{aligned} W &= \sum_l r_{kl} \otimes R_{kl} \\ V &= \sum_l R_{kl} \otimes R_{kl}. \end{aligned} \tag{4.3}$$

The displacement gradient $\nabla u = F - \mathbb{1}$ can then be calculated and from that we calculate the strain tensor at the site k as

$$\epsilon = \frac{1}{2}\left(\nabla u + (\nabla u)^T\right). \tag{4.4}$$

Unfortunately, we have now reached the limit of what this toy model can tell us about the system, the computational time required to calculate the positions and consequent strains on a large

[3]This is the Cauchy-Born approximation [166], and in practice it is often computationally faster to minimise this expression to be as close to 0 as possible than it is to minimise the total energy. We have described minimising the energy as we find this description of the model to be more intuitive.

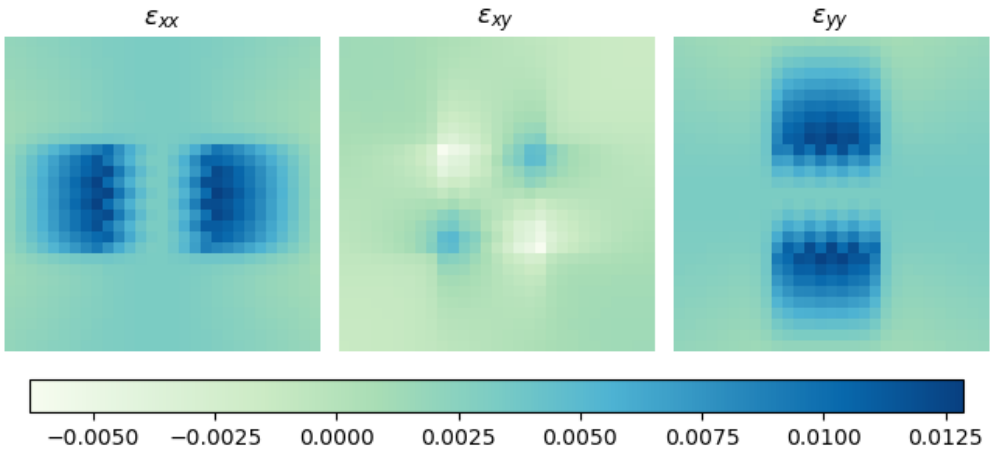

Figure 4.3: Map of the strain tensor components for a system consisting of a rectangular block of indium inside a GaAs lattice. We omit the ϵ_{yx} component as the tensor is symmetric.

system of atoms is much larger - notwithstanding the need to extend the model to 3D for it to be a complete simulation. Such extended calculations are typically conducted using software like LAMMPS [168], though other methods have also been proposed [167]. Examples of such calculations for InGaAs quantum dots can be found in work by Bulutay [169], among others.

4.1.2 The Gradient Elastic Tensor

The gradient-elastic tensor (GET), denoted S_{ijkl}, is a 4^{th} rank symmetric tensor which relates the strain in a material ϵ_{kl} to the electric field gradient (EFG) V_{ij} according to

$$V_{ij} = \sum_{k,l} S_{ijkl}\epsilon_{kl}. \tag{4.5}$$

Though it is a purely phenomenological parameter, accurate knowledge of its components is necessary for simulating the effect of strain in a variety of nanostructures. As a 4^{th} rank tensor in 3D space, the tensor has $3^4 = 81$ components - fortunately many of these are inter-dependant due to the symmetries present in any particular lattice structure. For a cubic crystal lattice as found in an InGaAs QD, the tensor can be described using only 3 components [170]: $S_{xxxx} = S_{yyyy} = S_{zzzz} \equiv S_{11}$, $S_{xxyy} = S_{yyzz} = S_{xxzz} \equiv S_{12}$ and $S_{xyxy} = S_{yzyz} = S_{xzxz} \equiv S_{44}$. These terms are commonly described in the literature using Voigt notation of the form S_{mn} [171]. In addition, we can define $S_{12} = -\frac{S_{11}}{2}$ by assuming that the gradient of the electric field vanishes at the centre of each nucleus[4], further simplifying the information needed to calculate the EFG. All other components of the tensor are 0 in a cubic lattice, and thus we need only to know the values of S_{11}, S_{12} and S_{44} in order to calculate the EFG from the strain.

[4]Mathematically, this is done by requiring that $\mathrm{Tr}[S] = 0$.

	NAR Measurements				NMR/PL Measurements			
	^{69}Ga	^{71}Ga	^{75}As	^{115}In	^{69}Ga	^{71}Ga	^{75}As	^{115}In
S_{11}	2.73	2.73	3.96	5.01	-2.2	-	2.42	-
S_{12}	-1.365	-1.365	-3.97	-2.505	1.1	-	-1.21	-
S_{44}	-2.76	-2.73	7.94	-2.998	0.88	-	4.792	-

Table 4.2: The relevant components of S_{mn} as found by NAR [172, 173] and PL/NMR spectroscopy [176, 177]. All values are given in SI units of 10^{22} Vm^{-2}, measurements originally given in cgs units of statcoulomb cm^{-3} have been converted by multiplying them by 2997924.580^5. So far, PL/NMR spectroscopy has not been used to measure either ^{71}Ga or ^{115}In - we believe this would be a very valuable experiment given the drastic changes in both magnitude and sign of the components for other species - ^{69}Ga especially.

The values of S_{ijkl} vary with atomic species and lattice structure, and must be measured experimentally. The most extensive of these experiments were performed using nuclear acoustic resonance (NAR) by Sundfors in 1974 and 1976 [172, 173]. In these experiments, a material sample is attached to a quartz transducer and the resulting change in the resonance frequency of the transducer is used to measure the elastic response of the crystal. Using these measurements and knowledge of the quadrupole moment of the nuclei the values of S_{ijkl} can be found. Sundfors performed these measurements for a vast array of nuclei and crystal structures, and they have been in regular use since then. However, work performed since then has found that NAR experiments tend to systematically overestimate the values of S_{ijkl} [174, 175], potentially as a result of the lower absorption of acoustic waves for materials with a smaller quadrupolar moment [172]. In 2018/19, Chekovich, Griffiths *et al* performed photoluminescence (PL) and nuclear magnetic resonance (NMR) spectroscopy to measure the values of S_{mn} in a GaAs/AlGaAs quantum dot [176, 177]. In these experiments, they measure the change in bandgap across the structure when it is mechanically stressed between 2 plates. Different combinations of magnetic field orientation and incoming photon polarisation are used to measure bandgaps across different nuclear spin polarisation regimes so that all the relevant terms of S_{mn} can be found. These experiments showed a significant deviation from the values found using NAR for both ^{69}Ga and ^{75}As nuclei, and are all summarised in Table 4.2. As these results are based on a direct measurement of quadrupolar effects, they are likely to be more accurate than those found using NAR. In addition, modern crystallography techniques have lead to the production of much higher quality samples than were feasible in the 1970s. Therefore, we believe that the NMR/PL results are closer to the true value and that there is a need to investigate how much of a difference this change might make.

4.1.3 Calculating the EFG

By assuming that the QD is cylindrically symmetric[6], we can let $\epsilon_{xy} = \epsilon_{yz} = \epsilon_{zx}$ and $\epsilon_{xx} = \epsilon_{yy}$ and hence the calculation of the EFG is reduced to

$$V = \begin{pmatrix} S_{12}(\epsilon_{zz} - \epsilon_{xx}) & 0 & S_{44}\epsilon_{xz} \\ 0 & (S_{12} + S_{11})\epsilon_{xx} + S_{12}\epsilon_{zz} & S_{44}\epsilon_{xz} \\ S_{44}\epsilon_{xz} & S_{44}\epsilon_{xz} & 2S_{12}\epsilon_{xx} + S_{11}\epsilon_{zz} \end{pmatrix}, \tag{4.6}$$

where we have also exploited the inherent symmetry of the strain tensor to set $\epsilon_{ij} = \epsilon_{ji}$ for the off-diagonal terms. From this we see that the data present in Fig. 4.6 is sufficient to calculate the EFG. The EFG varies across the structure, and is therefore calculated separately for each lattice point, the resulting matrix can be used to find the principal axis frame of a particular nucleus via eigenvalue decomposition. We then have $V'_{ij} = RV_{ij}$, where $V'_{ij} = 0 \forall i \neq j$ and $|V'_{zz}| \geq |V'_{yy}| \geq |V'_{xx}|$ are the components of the EFG in the principal axis frame as described in Section 3.2.2 and R is the matrix formed by the eigenvectors of V arranged in descending order of eigenvalue. From R we can also calculate the angle of the principal axis frame with respect to the laboratory frame, defined by the external field and QD growth axis [179][7]. It is this angle that determines the orientation of the quadrupolar interaction for a nucleus at a particular lattice site, and which would therefore be identical between nuclei in the ideal case.

4.2 Analysing a Quantum Dot

4.2.1 Calculation Methods

The calculations presented throughout this thesis are done primarily in Python 3, with some assistance from Mathematica when necessary. We make heavy use of the following packages: Numpy [180] for large scale array manipulations and general mathematics, Scipy [181] for fitting distributions, Qutip [182, 183] for the calculation of Hamiltonians, matrix elements and the implementation of a wide variety of quantum operators and Matplotlib [184] for figure plotting. The code itself closely follows the mathematics presented in previous sections, with some differences for the purposes of minimising computational time when dealing with large arrays - these changes make no difference to the results of the calculations, but allow us to do them in parallel and hence significantly reduce the time required[8]. The results of these methods can be compared to similar work like that of Bulutay [185], which instead of using real strain and

[6] This is a strong assumption, and marks a significant difference between this work and a full 3D simulation as done by Bulutay for example [169]. The advantages of our method are the speed of calculation and the relative ease with which real data can be used as an input to the model.

[7] We define the Euler angles as rotating around the axes of the laboratory frame in the order $X \rightarrow Y \rightarrow Z$. Other conventions would give the same final angles, but we find this order to be the most intuitive.

[8] The full codebase is reasonably accessible to anyone familiar with Python 3, and it and the data used are available on Gitlab here.

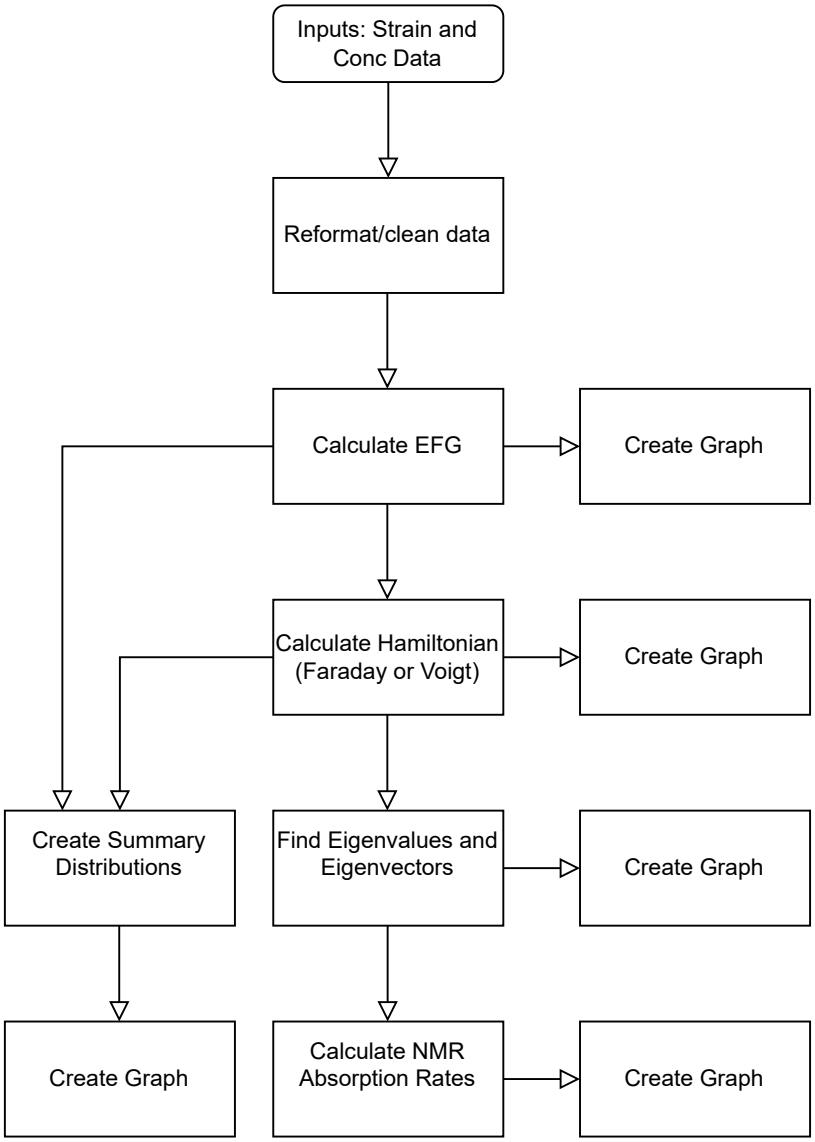

Figure 4.4: A schematic outline of the logic employed in our code. This entire process is reasonably similar between both single and many nuclei. In the many nuclei case we are able to run the calculations on individual nuclei in parallel using the mapping functions available in numpy and scipy. The full codebase is available on Gitlab here.

concentration data uses atomistic simulation as a base point. We include Fig 4.19 for comparison with our similar plot Fig 4.20.

4.2.2 Taking Real Strain Data

Instead of our toy model, here we shall consider the strain fields present in a real quantum dot, as measured using high angle annular dark-field (HAADF) imaging and reconstructed from geometric phase analysis (GPA). The data we use is that originally found in Sokolov *et al* [3], and

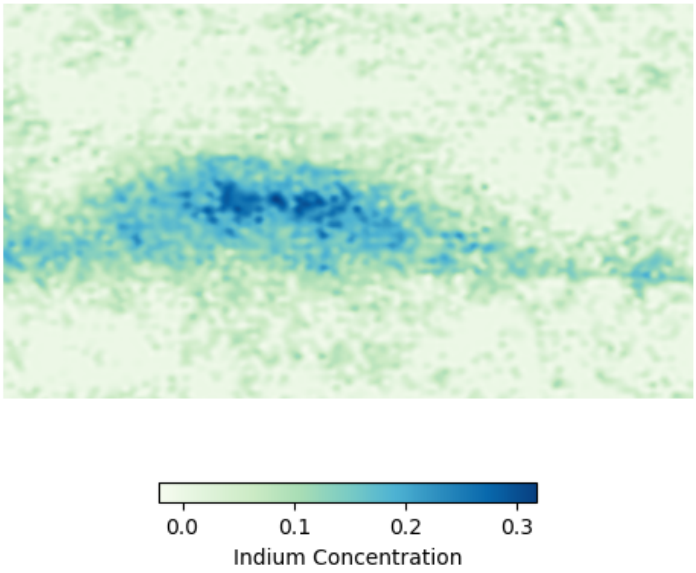

Figure 4.5: The In concentration across part of a lattice, as measured by Sokolov *et al* using HAADF imaging [3]. The central region with a higher concentration defines the quantum dot, and the shape of it appears in many other measures throughout this work.

our analysis begins in a similar place to theirs - though we later extend it to show distributions of quadrupolar effects and the impact of more recent knowledge to the values of the gradient-elastic tensor. This data consists of arrays of xx, xz and zz strain tensor components and indium concentrations - for the latter array we use a cubic spline interpolation algorithm to populate it to the same resolution as the strain tensor components. The quantum dot structure takes up an area of approximately 1100x450 data points in the centre of an image, at a resolution of approximately 1 atom per 25 square pixels of the image. As such, we cannot be sure exactly where any particular atom or nucleus is, and there is little value in assessing the particular qualities of any individual lattice point. We can however assess the overall distribution of parameters across the structure - and it is on this idea that we base our analysis. The dot can be clearly seen by mapping out the indium concentration through the lattice, as found by HAADF imaging and shown in Fig 4.5. In this image we see the typical lens like shape of a dot grown by Stranski-Krastanov growth, with a slight bump apparent on the left hand side. This bump is of particular interest, as we expect asymmetry in the dot structure to lead to asymmetry in the strain profile and hence in the resulting quadrupolar interaction.

The strain environment present in the structure (as found using GPA) is shown in Fig 4.6 - in this and all subsequent figures showing a quantum dot we align the growth axis along the z axis of the image, and refer to the horizontal axis as x[9]. Though we only have data for a 2D slice through the centre of the QD, by assuming the dot to be cylindrically symmetric we can

[9]Of course, this could be the y axis as we have assumed a level of cylindrical symmetry.

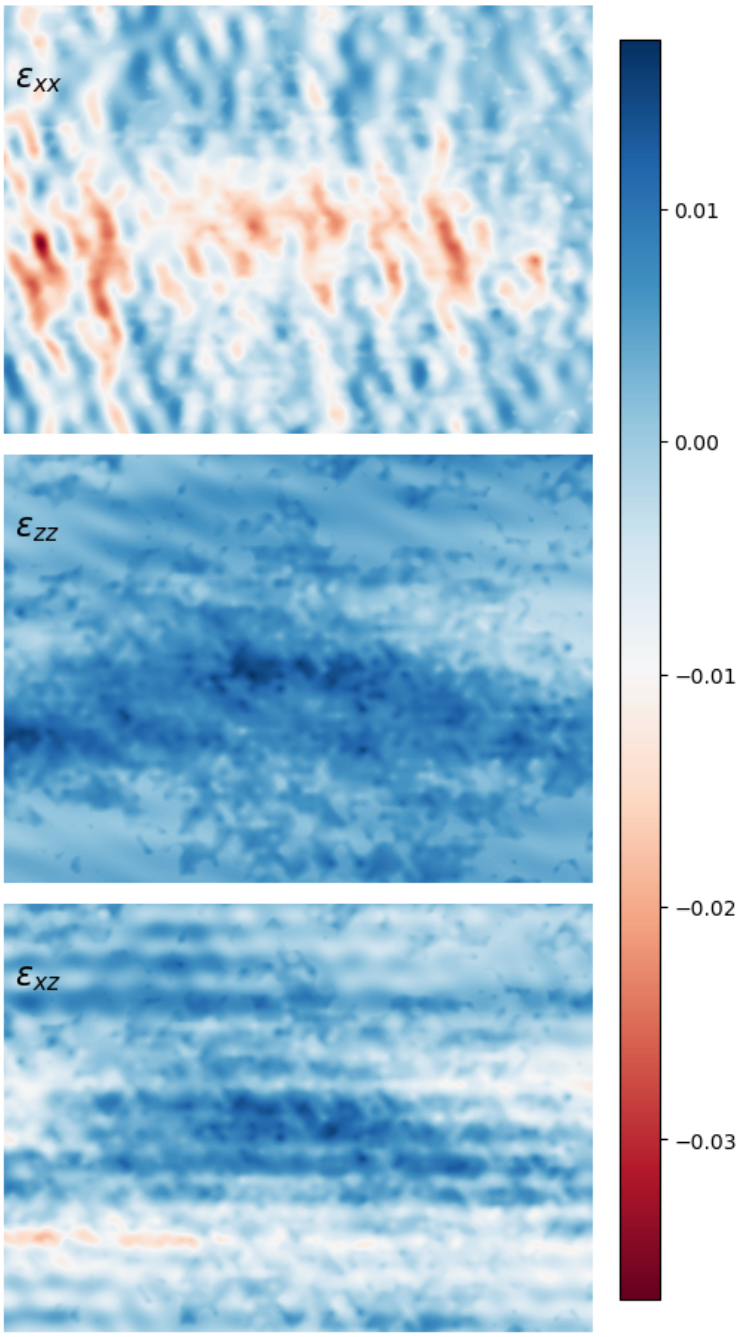

Figure 4.6: The measured strain environment of the quantum dot, as first described in Sokolov *et al* [3]. Here we use the original data from that paper (kindly provided by Paul Sokolov) to recreate their results using a cubic spline interpolation.

calculate the electric field gradient according to Eq 4.6. Of course, the results of this calculation depend on the values of the GET components that we decide to use. Once we have found the EFG, we can calculate and plot the direction and magnitude of the quadrupolar interaction across the quantum dot, according to the equations derived in Section 3.2.2. We do this first using the components of the GET as found using NAR, as was originally done by Sokolov *et al* - the results of this calculation are shown in Fig 4.7. We also plot the local xy asymmetry (the biaxiality) of the quadrupolar field at each point in Fig 4.8. All of these results agree with those found by Sokolov *et al*, which also used the values of the GET as found by NAR.

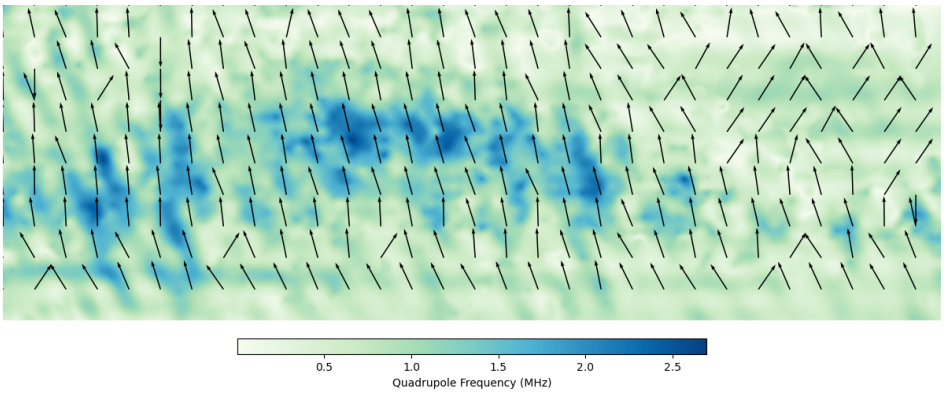

Figure 4.7: The direction and strength of the quadrupolar interaction felt by a ^{69}Ga nucleus is shown by the size and direction of the black arrows, while the background colour represents the strength of the quadrupolar interaction felt by the nucleus. As we do not know exactly which species is present at which lattice site, we show the field as a ^{69}Ga nucleus would see it were one to be present.

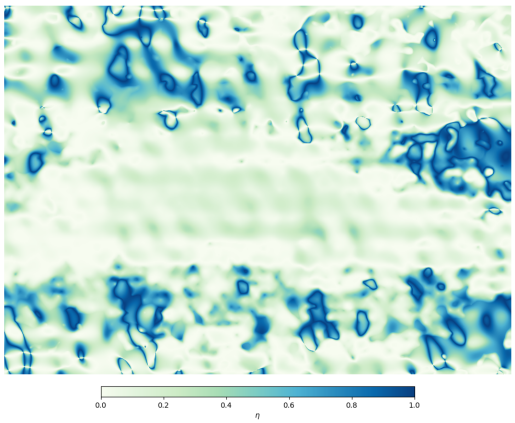

Figure 4.8: The biaxiality (η) of ^{69}Ga nuclei, as calculated originally in Sokolov *et al*. The central hemispherical region is the quantum dot, which is found to have a low value of η throughout. The outer substrate has some regions of higher biaxiality. 4.7

We now introduce the results of the NMR/PL experiments into our calculations. Using the

same strain and concentration data, we again calculate the EFG across the dot and the resulting quadrupolar field strength, direction and biaxiality at each point. We expect these calculations to give different results by virtue of having updated the parameters, though exactly how they will change is difficult to intuit due to the inherent complexity of tensor multiplication. The results of this parameter update are shown for ^{69}Ga in Figures 4.9 and 4.10.

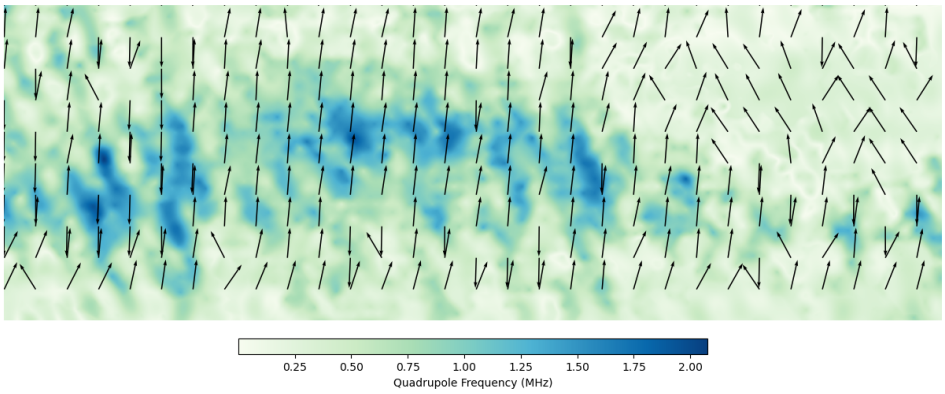

Figure 4.9: An updated version of Fig 4.7, in which we have performed the same calculation using the updated values of the GET as found by Chekhovich and Griffiths. We note that inside the quantum dot, there is a much stronger tendency towards the vertical direction than is present in the original figure, and many of the interactions are weaker as well.

As expected, in Fig 4.9 we see a substantial change in both the average direction and overall strength of the quadrupolar field throughout the QD as compared to Fig 4.7. At least for ^{69}Ga, the newly recalculated field is (at least qualitatively) much more aligned to the growth axis of the QD, and the maximum strength of the interaction has decreased by almost 20% from being equivalent to an applied field of almost 2.5T to one of just over 2T. These results are in agreement with other values found in the literature, where the quadrupolar interaction has been found to be equivalently to a field of approximately 1.3T [186]. Bearing the ideas of Section 3.1.2 in mind, we might therefore expect this recalculation to result in a smaller contribution of the Overhauser field of the ^{69}Ga nuclei to the overall dephasing rate than would have been predicted using the NAR measurements of the GET.

We also see in Fig 4.10 that the biaxiality has a much higher average value when found using the NMR/PL values of the GET components, though the overall distribution appears to be the same. This increase in magnitude of the biaxiality is of key importance, as it further increases the differences between any pair of nuclei in the structure. If we again consider the quadrupolar Hamiltonian as first introduced in Section 3.2.2:

$$\hat{H}_Q = \frac{e^2qQ}{4I(2I-1)}\left(3\hat{I}_z - \hat{I}(\hat{I}+1) + \frac{\eta}{2}(\hat{I}_+^2 + \hat{I}_-^2)\right), \tag{4.7}$$

we see that an increase in biaxiality (η) will result in any particular nucleus being significantly different from its neighbours when rotated back to the common laboratory frame, as the ladder

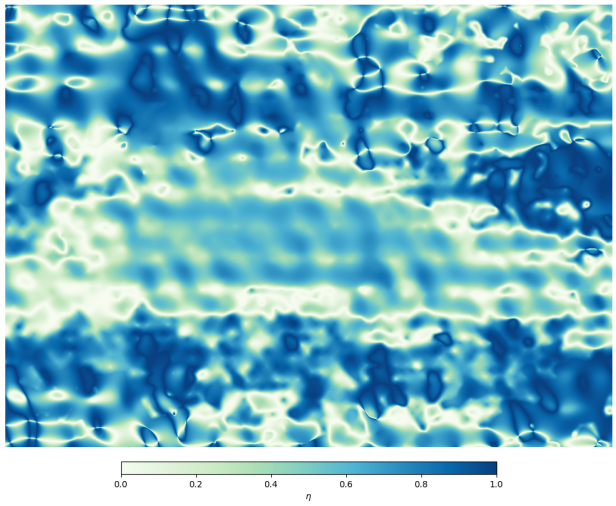

Figure 4.10: The biaxiality (η) of ^{69}Ga nuclei, as calculated using the gradient elastic tensor as measured by Chekhovich and Griffiths using NMR and PL spectroscopy [176, 177]. The central region in which the dot lies is again fairly uniform, but the entire structure is now shown to exhibit a much higher biaxiality than was found when using the older measurement values.

operator terms $\hat{I}_{\pm}$ take on a more significant role. Following the arguments of Chapter 3, we see that this will lead to a lowering of the lifetime of the Overhauser field, and hence a decrease in overall electron coherence time. While for most nuclear characteristics it is the spread that is important, for biaxiality an increase in magnitude has much the same effect as an increase in, for example, the variance of the strength of the quadrupolar field.

Thus far, our analysis has been qualitative - though the effects are clear to see from the graph. In order to pin down exactly what is going on, we now extend our analysis to the distributions of quadrupolar frequency.

4.2.3 Distribution of Quadrupolar Frequencies

In order to more clearly see the effect of changing these values, we plot the distributions of the first quadrupolar frequencies for each species present in the dot, using both the NAR measured values (shown in Fig 4.11) and the NMR/PL values (shown in Fig 4.12). A direct comparison of the changes is shown in Fig 4.13 - showing only the distributions for ^{69}Ga and ^{75}As as we do not have NMR/PL data for the components of the GET for ^{71}Ga or ^{115}In[10]. We see that the distribution of values for ^{69}Ga has broadened significantly, while that for ^{75}As has narrowed slightly. There is also a change in the modal direction of the interaction as seen by ^{69}Ga. All of these plots drop to 0 at a frequency of 0Hz. We believe this to be the result of our data sample containing no nuclei with 0 strain. This is an artefact of the interpolation we have applied to the

[10]Though the values for ^{71}Ga can be calculated using the ratio of quadrupolar moments between ^{69}Ga and ^{71}Ga. We do not calculate it here as there is so little ^{71}Ga in our sample (< 1% of the Gallium present that it makes no difference to any of our calculations.

original data to align the strain and concentration data. Without a perfectly aligned set of strain and concentration data, performing this interpolation is unavoidable and hence these graphs will all suffer from this flaw. We do not believe it detracts from the overall message of the graph, which is the drastic change in shape of the distributions[11].

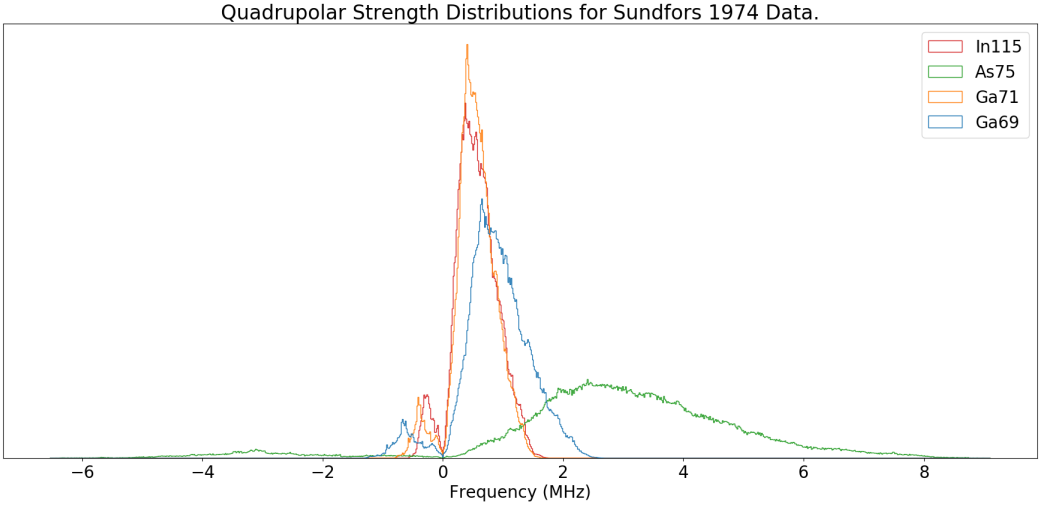

Figure 4.11: The distribution of quadrupolar frequencies over all nuclei in the quantum dot, calculated using the Sundfors acoustic resonance values of the GET. The frequency here refers to the energy level splitting between the lowest energy states of the nucleus, with the sign of the frequency corresponding to alignment (or anti-alignment) with the external field.

To directly compare the change, we fit a gamma distribution

$$f(x) = \frac{1}{\Gamma(k)\theta^k} x^{k-1} e^{-\frac{x}{\theta}} \tag{4.8}$$

to the absolute values of the transition frequencies. Our fitting parameters are the shape k and scaled θ of the distribution, and we fit to the absolute value as our distributions are weighted heavily to a single sign (positive for ^{71}Ga, ^{75}As and ^{115}In, negative for ^{75}As) and this allows us to directly compare them. An example of this fit is shown in Fig. 4.14, and a complete summary in Table 4.3. A gamma distribution is appropriate as it captures the probability of a member of an ensemble having a particular energy, typically this is applied to an ideal gas by setting $k = \frac{3}{2}$ and $\theta = k_B T$. In our case, the ensemble is the nuclear spin bath rather than the molecules of an ideal gas, hence we allow k to vary as we are not modelling a particle with 3 velocity degrees of freedom, though we can estimate the effective temperature of the bath as $T = \frac{\theta}{k_B}$ as would be done classically. The fitting is done using a maximum likelihood estimation algorithm, as implemented in Scipy.

We find that the distribution for ^{69}Ga widens by a factor of 3, though this result is distorted slightly by taking the absolute value and hence absorbing the fraction of oppositely aligned

[11] Experimental results showing the effect of near 0 strain nuclei on a central electron can be found in the work of Ragunathan [187].

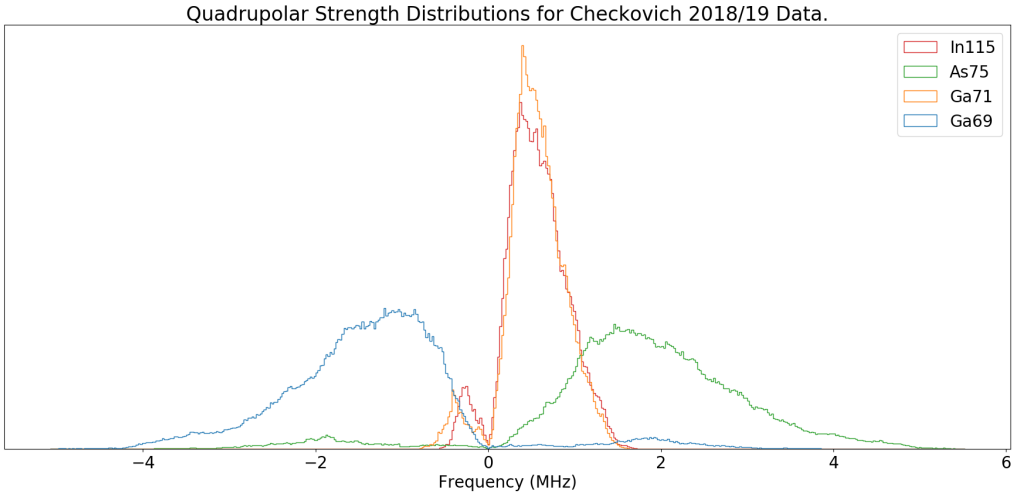

Figure 4.12: The distribution of quadrupolar frequencies across the dot as calculated using the Chekhovich measurements. Note that ^{115}In and ^{71}Ga remain unchanged as the values of the GET for those species has not been found via NMR/PL.

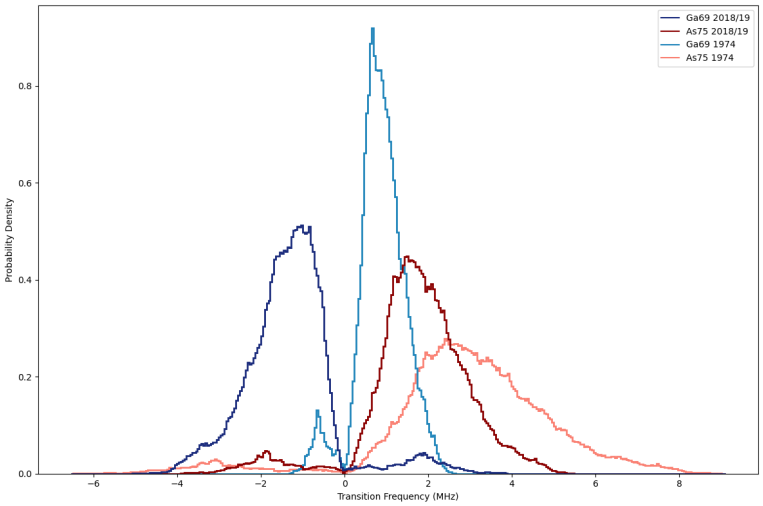

Figure 4.13: A direct comparison of the distributions shows the size of the shift and the change in width when using updated (in dark colours) and older (in light colours) of the GET. ^{69}Ga is shown in blue, and ^{75}As in green. Other species are omitted as the GET for them has not been measured using NMR/PL.

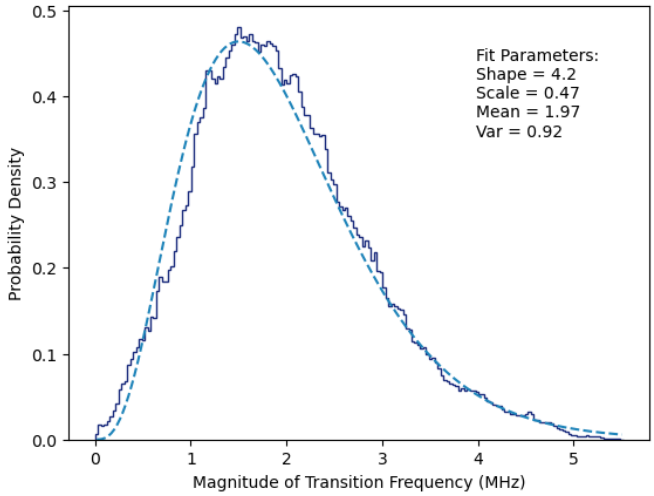

Figure 4.14: The distribution of transition frequencies for ^{75}As nuclei (as calculated using NMR/PL GET measurements), is show in dark blue, with a fitted gamma distribution overlaid as a light blue dashed line. The fitted distribution has a mean value of 1.97 MHz and a variance of 0.92 MHz, both significantly reduced from the NAR measurement based calculations, suggesting that the effects of the quadrupolar interaction would be lower in this dot than could be assumed by using the NAR values of the GET.

frequencies into the overall distribution - it is likely that this distortion results in a narrower distribution than is actually present and hence the increase may be of a larger size than we report here. The distribution for ^{75}As is found to narrow by a factor of ≈ 2.7, when combined with the significant reduction in the mean value (from 3.25 to 1.97MHz) this demonstrates a large reduction in the number of outlying nuclei and hence an increase in uniformity over what would have been found using the NAR GET values.

	NAR Measurements				NMR/PL Measurements			
	^{69}Ga	^{71}Ga	^{75}As	^{115}In	^{69}Ga	^{71}Ga	^{75}As	^{115}In
Shape (k)	3.85	3.83	4.20	3.14	3.35	-	4.20	-
Scale (θ)	0.25	0.15	0.77	0.19	0.45	-	0.47	-
Mean (MHz)	0.94	0.59	3.24	0.58	1.52	-	1.97	-
Variance (MHz)	0.23	0.09	2.50	0.11	0.69	-	0.92	-

Table 4.3: The parameters (shape and scale) for and results of fitting a gamma distribution to the calculated distributions of quadrupolar frequencies, as found using both NAR and NMR/PL GET values. Dashes (-) indicate data which cannot be found as there are no new parameters for calculation. The distribution for ^{69}Ga is wider by a factor of 3 when using updated values, whereas for ^{75}As it is approximately 2.7 times narrower with a significantly reduced mean value. This highlights the need to update the values for both ^{71}Ga and ^{115}In, as it is not so simple as to say that the distributions will definitely narrow or widen.

4.3 NMR and Quadrupolar Spectra

An excellent way of assessing the properties of a quantum is by nuclear magnetic resonance (NMR) spectroscopy, in which an oscillating magnetic field is used to probe the natural transition frequencies of the nuclei being examined. This is the same technique by which the components of the gradient elastic tensor were re-measured by Chekhovich and Griffiths. We examine the NMR & quadrupolar spectra of both individual nuclei and the quantum dot as a whole to assess how suitable this quantum dot might be to various protocols that have been suggested in the literature. The methods described are applicable to any set of strain and concentration data in the same format as this data.

4.3.1 Quadrupolar Spectra

We begin by finding the quadrupolar spectra for single atoms within the quantum dot. We select a nuclear site within the structure, and construct the quadrupolar Hamiltonian in the principal axis frame (denoted by primed coordinates), according to

$$\hat{H}_Q = \frac{3e^2qQ}{2I(2I-1)}\left(2\hat{I'}_z^2 + (\eta-1)\hat{I'}_x^2 - (\eta+1)\hat{I'}_y^2\right). \tag{4.9}$$

This Hamiltonian is equivalent to Eq 3.62, but we use this form to highlight the requirement to rotate the spins appropriately.The energy level structure of this nucleus can then be found by calculating the total Hamiltonian, including the Zeeman splitting experienced by a nucleus in an external magnetic field, as

$$\hat{H} = \hat{H}_Z + \hat{H}_Q. \tag{4.10}$$

At this point it becomes necessary to specify the orientation of the external magnetic field (Faraday or Voigt), and apply the appropriate rotations to the spin terms to transform the Hamiltonian into the principle axis frame. We calculate the spin operators in the principal axis frame as

$$\hat{I'} = R\hat{I}R^\dagger. \tag{4.11}$$

where R is a rotation operator defined by the Euler angles $(\alpha, \beta\&\gamma)$ of the principle axis frame with respect to the laboratory frame:

$$R = e^{(-i\alpha\hat{I}_x)} \times e^{(-i\beta\hat{I}_y)} \times e^{(-i\gamma\hat{I}_z)}. \tag{4.12}$$

The size of the Euler angles depends on which field orientation we are investigating, as we always keep the component rotations in the order $X \rightarrow Y \rightarrow Z$, as defined in the laboratory frame by the growth axis of the quantum dot. The final nuclear spin Hamiltonian then has the form

$$\hat{H} = \omega_B B\hat{I}_{z,x} + \frac{3e^2qQ}{2hI(2I-1}\left(2R\hat{I}_z^2R^\dagger + (\eta-1)R\hat{I}_x^2R^\dagger - (\eta+1)R\hat{I}_y^2R^\dagger\right), \tag{4.13}$$

where $R, R^\dagger$ and $\hat{I}_{z,x}$ all depend on the choice of external field orientation. The constants ω_B (a conversion factor between applied field and Zeeman frequency) and Q depend on the choice of nuclei, and the values we use for them are shown in Table 4.4.

	^{69}Ga	^{71}Ga	^{75}As	^{115}In
Q ($10^{-}31m^2$)	172	107	314	770
ω_B (MHz T^{-1})	10.22	12.98	7.22	9.33

Table 4.4: Values of the quadrupolar moment Q and the Zeeman frequency per Tesla ω_B used in this work. Values for quadrupolar moments are as found in [188], and for Zeeman frequency per Tesla as found in [189].

4.3.1.1 Single Nucleus Energy Spectra

We can now find the eigenvalues and eigenstates of this Hamiltonian, and hence it's energy structure. This structure will of course change depending on the exact parameters of the Hamiltonian, including external field orientation and strength, and hence in section **a** of Figure 4.15 we plot an example of the results of this calculation for an indium atom with parameter values taken from a single lattice point within our data set, and an external field in the Faraday orientation. It must be noted that these images do not represent experiments that could be easily performed - scanning over multiple values of the external field would be incredibly difficult over large ranges, and the procedure to measure the energy states would then destroy the quantum character of the system before the external field was adjusted. As indium has a spin of $I = \frac{9}{2}$, we expect it to split into $2I + 1 = 10$ energy levels when an external field is applied - which we see in this plot. However, the quadrupolar interaction also splits the spin states without an external field being present, supporting the notion of thinking about the quadrupolar field as acting like another applied field for the purposes of intuition. We can also see the differences between the Faraday and Voigt geometries by plotting the same features with a different orientation, as seen in Fig 4.15 section **b**. In this graph we see the same energy level structures as the Faraday case at both low and high external fields, but in the mid-field range there is a significantly different mixing of the energy levels.

Previously, we discussed the impact of the biaxiality (η) of the quadrupolar field on the behaviour of the nuclei. By analysing the splitting of the Hamiltonian with respect to changing η, we can more properly see why it is so important for η to be low when producing single photons. Fig 4.16 shows the significant impact that biaxiality has on the energy structure of an indium nucleus. As η increases, the topmost energy levels remain approximately static, but the lower levels are split significantly more, with the gap between the lowest levels increasing from approximately 2 MHz at $\eta = 0$ to over 6MHz at $\eta = 1$. Most of this variation occurs as η varies from 0.5 to 1 - the range in which we found it to be inside the quantum dot in Section 4.2.2. This further highlights the conclusions drawn there - in the high biaxiality regime there is significantly more variation between otherwise comparable nuclear spins which can lead to a decrease in electron coherence times as discussed in Section 3.1.2.

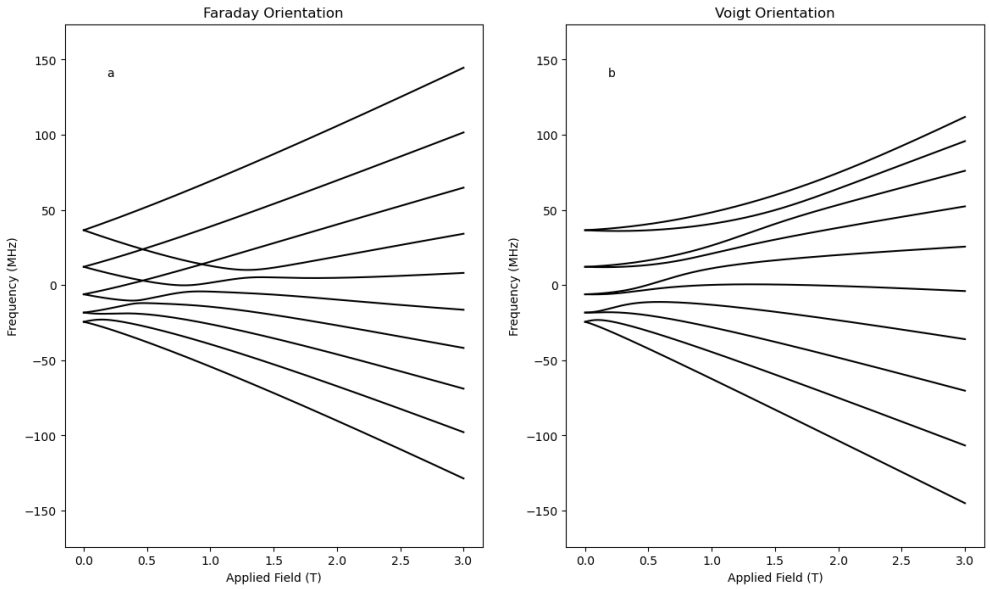

Figure 4.15: a) The energy structure of ^{115}In in a Faraday geometry, constructed using data from a point within the dot structure introduced in Chapter 4. We can see that at high external fields ($B > 1$T), the Zeeman splitting dominates, but at sub 1T fields there is significant mixing between spin states. At 0 field, as expected, we see only the quadrupolar splitting. b) The energy structure of ^{115}In in a Voigt geometry. While the features are the same as the Faraday case at 0 field and in the high field limit, there is a significant difference in the intermediate field.

4.3.2 Multiple Nuclei Energy Spectra

We now use the same procedure to investigate this structure specifically, by looking at the spectra for multiple nuclei randomly sampled from across the quantum dot. In doing so, we hope to gain further insight into the spread of quadrupolar effects within the dot. A large spread of course leading to a lower electron coherence time and therefore a QD that is less useful for production of entangled photons. We see from Fig 4.17 that a random sample of indium nuclei preserves the basic structure that we see for a single nucleus in Fig 4.15, but there is a substantial overlap between the energy levels before the Zeeman splitting takes over at higher fields. The threshold for defining a 'high field' also increases, with distinct bands only emerging above approximately 2.3T in the Voigt orientation, in comparison to a clear separation being seen at approximately 1.5T in the single nucleus case. This increase in mixing demonstrates that even among a relatively small number of nuclei (a random sample of 25 was used to generate Fig 4.17) there can be a large variation in quadrupolar characteristics. This obviously conflicts with the ideal case of maximally similar quadrupolar effects.

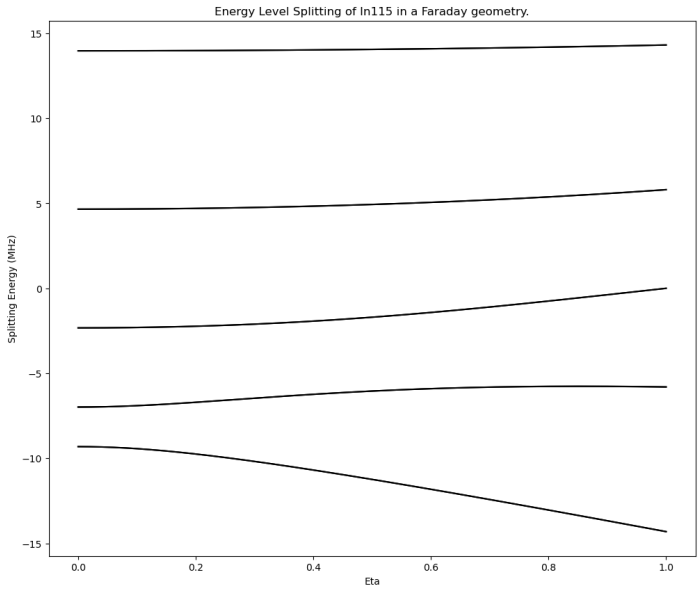

Figure 4.16: The change in energy level splitting of an ^{115}In nucleus with respect to a changing biaxiality, as calculated at 0 external field. In the absence of Zeeman splitting, we can see how the same nucleus experiences significant splitting just as a result of different values of η.

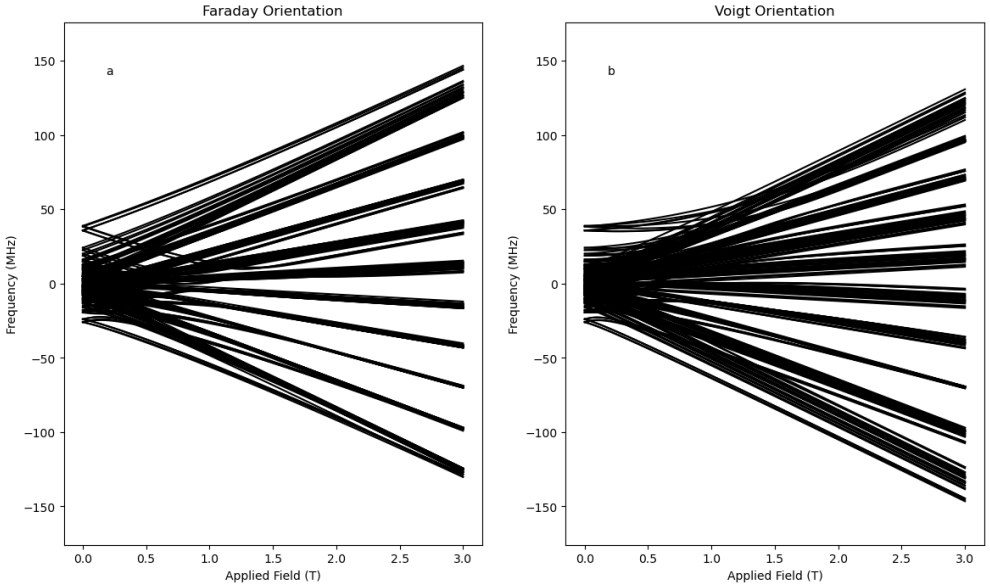

Figure 4.17: By taking a random sample of ^{115}In nuclei and combining their spectra, we can understand the mixing of quadrupolar energy levels within the structure. We plot the Faraday orientation in a), and the Voigt in b). The stark differences present in Fig 4.15 are still observable at the extreme ends of the energy scale, but at smaller energies the orientations are almost indistinguishable. We see that at larger fields the Zeeman splitting dominates - as we would expect.

4.3.3 NMR Spectra

Nuclear magnetic reference (NMR) is an excellent way of characterising the properties of material or structure. When exposed to a radio frequency field, while in a magnetic field, nuclei within a structure transition between the spin energy levels that have been split by the magnetic field. The exact frequency of this varies between different nuclear species (according primarily to their spin) and between nuclei of the same species (according to whatever changes the eigenstructure of the Hamiltonian as seen in Section 4.3.2). Therefore, we can gain insight into a material or structure by measuring the NMR effect at a variety of radio frequency (RF) field and external field strengths/orientations. An example of experimental work of this type can be found in [190].

We can simulate the results of an NMR experiment by considering the effect of an applied field and incident RF field on a nuclear spin system. The eigenstates of the Hamiltonian of a nucleus (see Eq. 4.9) exposed to an RF field with angular frequency ω_{rf} along an axis defined by $B_x^{rf}, B_y^{rf}, B_z^{rf}$ are mixed by the action of the RF Hamiltonian according to

$$\hat{H}_{\text{rf}} = -\hbar\gamma\left(B_x^{rf}\hat{I}_x + B_y^{rf}\hat{I}_y + B_z^{rf}\hat{I}_z\right)\cos(\omega_{rf}t). \tag{4.14}$$

Here the $\hat{I}_k$ are the nuclear spin operators in the principle axis frame and γ defines the amplitude of the field. We use Fermi's golden rule to calculate the absorption rate W_{ij} between an initial state $|i\rangle$ and final state $|j\rangle$ as

$$W_{ij}(\omega_rf) = |\langle j|\hat{H}'_{rf}|i\rangle|^2 \frac{\frac{2\Delta}{\hbar}}{(E_j - E_i - \hbar\omega_{rf})^2 + \Delta^2}, \tag{4.15}$$

where $\hat{H}'_{rf} = -\hbar\gamma\left(B_x^{rf}\hat{I}_x + B_y^{rf}\hat{I}_y + B_z^{rf}\hat{I}_z\right)$ and Δ is the fundamental linewidth of the transition in question (which we take to be 10 kHz for all species in this work [191]). By calculating this rate for a range of incident RF fields and applied fields, we can examine the behaviour of individual nuclei, or a structure as a whole.

In Fig 4.18 we plot the simulated outcome of an NMR experiment on a single indium nucleus within the quantum dot structure. We can clearly see specific spin transitions shown in the absorption spectra - as ^{115}In is a spin $\frac{9}{2}$ particle we expect there to be $^{10}C_2 = 45$ possible transitions[12], which are present in the spectra. Though this simulation is inherently nonphysical (we cannot investigate a single nucleus within a quantum dot), it demonstrates the possibility of calculating spectra from the data we have.

Similar plots can be found in the work of Bulutay [169], and the results seen in 4.18 can be compared directly with that work. A plot from Bulutay is included in Fig We observe the same structure in the transition lines as Bulutay, without requiring the use of complex and computationally expensive modelling using software such as LAAMPS. Though the run time of a calculation is of course dependant on the computer used, our python code can generate an NMR

[12] A spin $\frac{9}{2}$ particle has $2 * \frac{9}{2} + 1 = 10$ spin energy levels, and a transition can in principle occur between any 2 such levels. Hence there $^{10}C_2$ possible transitions.

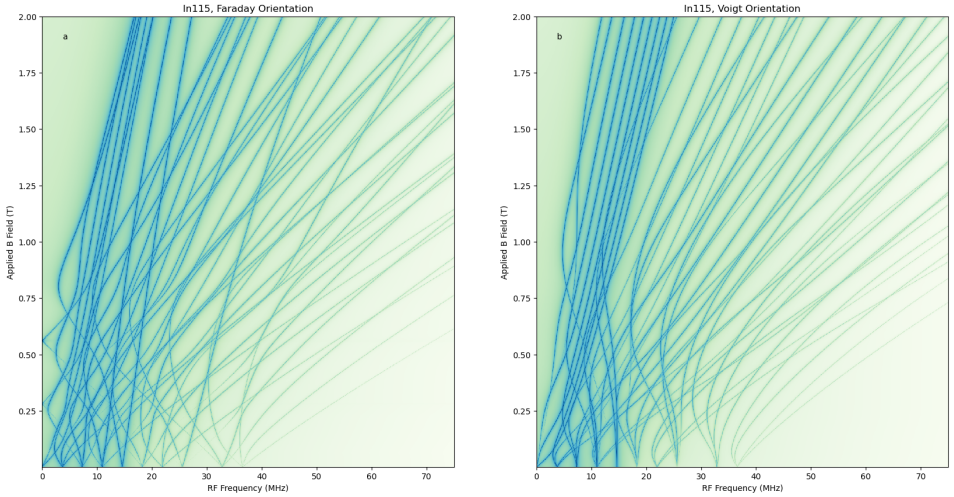

Figure 4.18: The simulated NMR spectra of a single ^{115}In nucleus in the centre of the quantum dot. In (a) we show the results for a Faraday orientated field, and in (b) we show the results for a Voigt field. Darker colours indicate a stronger absorption. We can see significant differences in the structure over the entire range of applied field and RF frequency.

plot from initial strain and concentration data in under an hour on a modern laptop - significantly faster than is possible when performing a complete molecular-statics simulation. Much of this advantage comes from the use of real strain and concentration data rather than performing the relaxation required for a full simulation. Our code is well suited for rapidly understanding the potential of a real structure, without resorting to a full simulation.

We can also sample from the set of available indium nuclei to get a better understanding of the overall distribution of parameters for that atomic species[13]. In Fig. 4.20 we show the result of sampling from multiple indium atoms across the entire dot structure. The resulting spectra is significantly noisier (as might be expected), but still displays the same essential structure as the single nucleus spectra shown in Fig. 4.18.

In order to investigate the impact of updating the gradient elastic tensor (GET) on the NMR spectrum of the sample, we must look at the spectra for either ^{69}Ga or ^{75}As, as the measured values for ^{115}In have not changed significantly since the original NAR experiments in 1974. We plot these comparisons for ^{69}Ga in Fig. 4.21 and for ^{75}As in Fig. 4.22. The results shown in these graphs agree with those shown in Section 4.2. We see that the spectra for ^{69}Ga is significantly wider when using the NMR/PL values of the GET than when found using the NAR values, in agreement with the increase in width of the frequency distribution as summarised in Table 4.3. This again suggests that these nuclei would have a larger than previously anticipated effect on the coherence time of a central electron spin in this dot. We also see the same result as we found previously for ^{75}As nuclei - a significant narrowing of the NMR spectra can clearly be seen. This

[13]Of course, this analysis can also be done for other atomic species - such graphs are included in Appendix A.3.

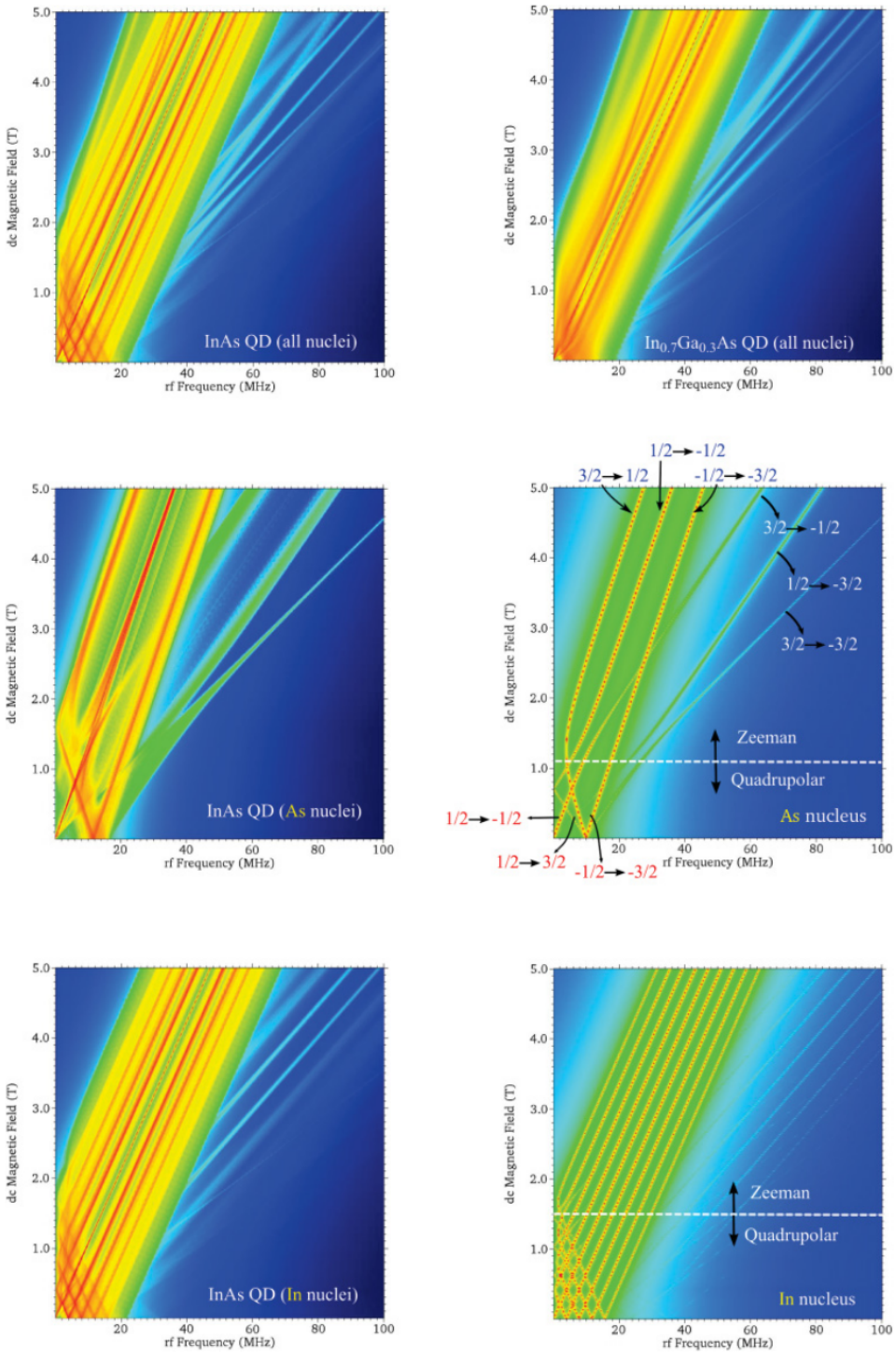

Figure 4.19: A comparison figure from Bulutay [169] showing Faraday geometry NMR spectra for InAs and In 0.7 Ga 0.3 As QD nuclei (top row), together with their element-resolved contributions, As (centre row) and In (bottom row) for the InAs QD, contrasted with respective single-nucleus spectra (right panel, centre and bottom rows). It can be clearly seen that these figures are in agreement with the relevant plots from our work. This demonstrates the usefulness of our calculation methods.

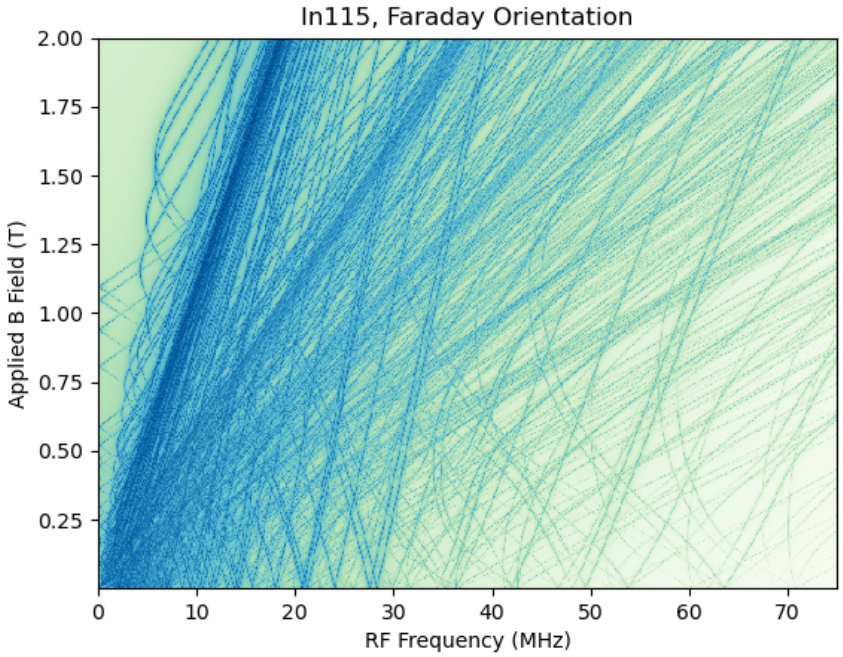

Figure 4.20: The outcome of an NMR probe on a random sample of 16 indium 115 nuclei from within the quantum dot. The wide variation in the spectra suggests it would be very difficult to isolate an individual nucleus (for use in a quantum memory for example), and that the indium atoms present in this dot would cause a large reduction in the coherence time of a central electron exposed to them. Sampling a larger number of atoms is possible with our methods, but does not significantly change the result.

is in good agreement with the effect found previously, where the distribution of quadrupolar frequencies narrowed substantially, and supports the conclusion that these nuclei would have a lesser effect on electron coherence times than would previously have been found. All further simulations have been done using only the NMR/PL values of the GET, though the same analysis is of course possible using the older values.

These simulations are of course nonphysical - if an NMR experiment is performed, there is no reason to believe that only a single nuclear species would resonate at any one time. As we can see from Figures 4.20, 4.21 and 4.22, there is substantial overlap between the resonant frequencies of all the component nuclei in this quantum dot. Whether or not this is a problem depends on what we wish to gain by conducting an NMR experiment. Our simulations up to this point have investigated primarily the effect of re-measuring the gradient elastic tensor and the implied impact of that on electron coherence times. However, quantum dots are a leading candidate for the demonstration of other quantum effects and the creation of other devices beside photon sources. Chief amongst these at the moment is the quantum memory. In essence, a quantum memory is some device or system in which a quantum state can be stored for an extended period

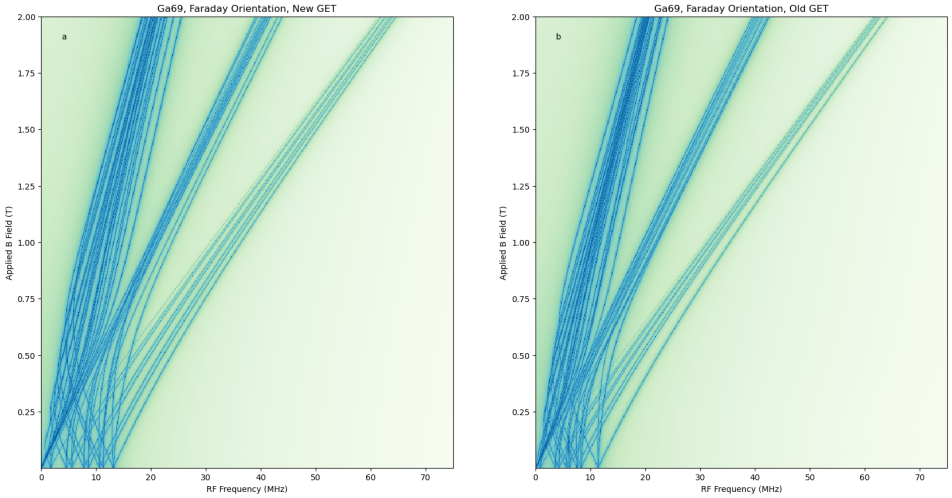

Figure 4.21: The NMR spectra of a sample of 8 ^{69}Ga nuclei within the quantum dot structure, under a Faraday geometry. In (a) we plot the spectra as found using the NMR/PL values of the GET, while in (b) we plot the spectra as found using the NAR values. We find for ^{69}Ga there is a qualitative broadening of the NMR spectra, implying that the nuclei are more different to each other than previously thought. Therefore we would expect them to cause a larger decrease in the coherence time of an electron in the quantum dot than we would have previously thought.

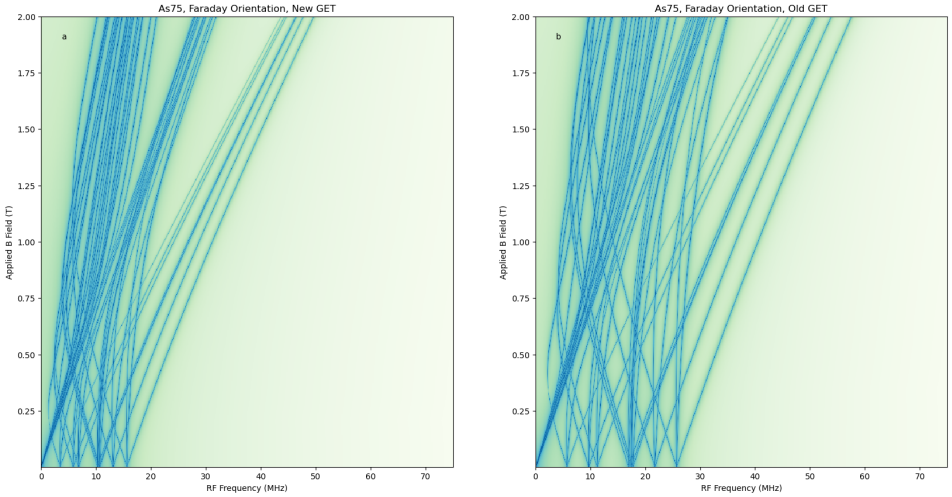

Figure 4.22: The NMR spectra of a sample of 8 ^{75}As nuclei within the quantum dot structure, under a Faraday geometry. In (a) we plot the spectra as found using the NMR/PL values of the GET, while in (b) we plot the spectra as found using the NAR values. We find for ^{75}As there is a significant narrowing of the NMR spectra, which results in a lowering of the required frequency for transitions to occur. This suggests that the nuclei are behaving more alike to each other, and hence would cause a smaller reduction in the coherence time of a central electron.

of time, and then recovered unchanged. Such devices have been suggested as almost essential for a realistic implementation of fault tolerant quantum communication and computation [192, 193], and quantum dots are a front runner in terms of their applicability to this problem [194, 195], with some systems achieving lifetimes in the milliseconds [196]. In a quantum dot, the basic principle is to imprint the desired quantum state onto the nuclear spin bath, via the hyperfine interaction between a central electron and the bath [197–199]. Once the state is written onto the bath, it should last for the lifetime of the Overhauser field (as this lifetime is defined as the time taken for the spin bath configuration to substantially change). It may also be possible to write the state onto a small subset of the spin bath which is sufficiently separate energetically - such a subset essentially forming a smaller spin bath. These methods both require the nuclear spins to be very similar to each other: in the first case the similarity must extend over the entire bath, and in the second there must be at least 2 subsets which are internally similar but differ significantly from each other. A more realistic simulation of an NMR experiment should show us whether this dot is suitable for such a task. For the first case, we would ideally see only a narrow band of transitions, indicating that the total nuclear spin bath is very self-similar - judging from Figures 4.20, 4.21 and 4.22 this seems unlikely given the inherent variation seen in those graphs. The second case may be more plausible - we require some subset of transitions to be energetically separate from the rest, which may be seen at the higher frequency range.

In Figures 4.23 and 4.24 we plot the result of simulating an actual NMR experiment on this quantum dot in the Faraday and Voigt geometries respectively. These results are calculated using the same method as previous figures, but with a higher number of sites sampled - 40 in this case[14], out of an estimated 55 nuclear sites within our image. We weight the proportion of indium nuclei examined according to the experimentally measured indium concentration (see Fig. 4.5) at the sample site and assume that 50% of nuclei within the lattice are ^{75}As with the remainder being ^{69}Ga. Unfortunately, the results of this simulation do not suggest this quantum dot would be a good candidate for the first type of quantum memory in either orientation - the transition lines are too broadly spread to be useful, even in the Voigt field where they are much closer than in Faraday. This agrees with the work of Gangloff and Denning *et al*, which places an upper limit on quadrupolar induced inhomogeneity of approximately 100 kHz [194, 195], and goes on to suggest such low bounds are only achievable in quantum dots grown via droplet epitaxy - which are inherently low strain, especially in comparison to strain based dots such as this one. The second type may however be a possibility. The indium nuclei are the only ones to respond to fields in the regime of $F_{RF} > 40$ MHz at lower fields, and the relevant transitions are strong and well defined for a Faraday orientated magnetic field.

[14]The number of sites used is always a multiple of 8, to best take advantage of the 8 cores of our machine.

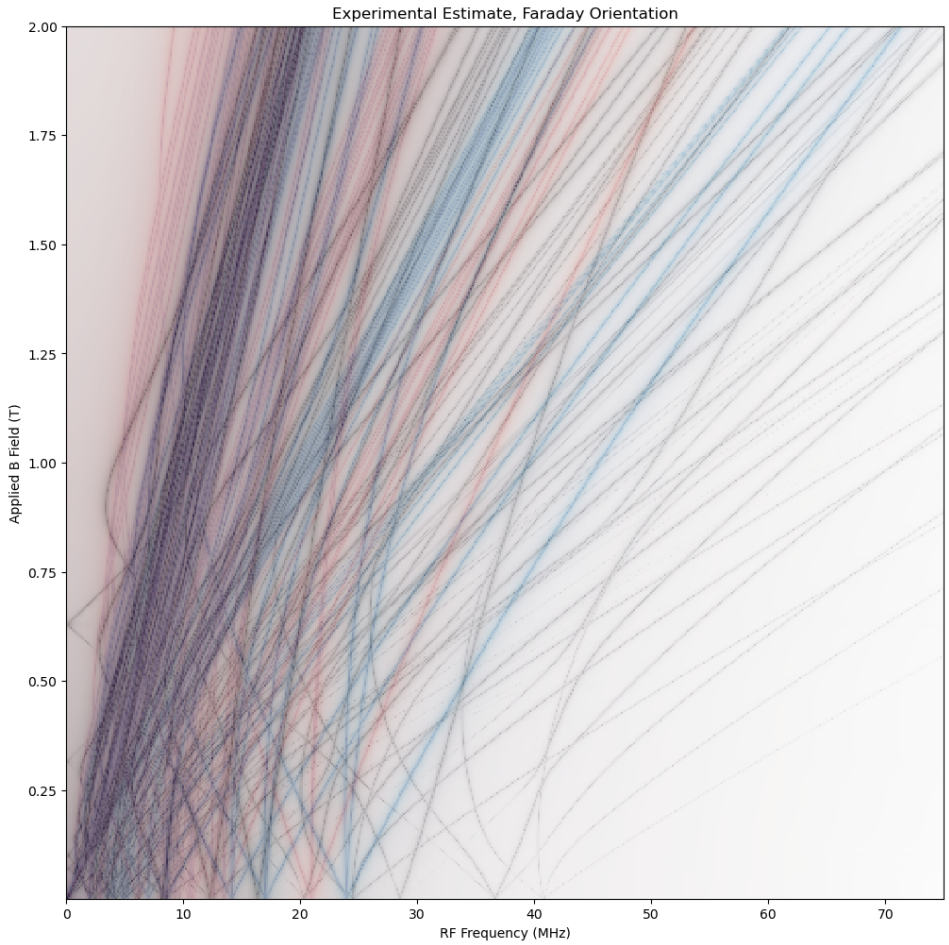

Figure 4.23: Simulation outcome of an NMR experiment on our quantum dot, with a Faraday orientated field. Lines are coloured according to the atomic species that produced them, in order to identify if any subsets of interest belong to a particular species. Grey features correspond to ^{115}In nuclei, blue to ^{69}Ga and red to ^{75}As. We ignore the tiny fraction of ^{71}Ga present in the sample. We see that at lower applied fields, there is significant mixing between the different species over a broad range of frequencies, though only ^{115}In nuclei resonate at high frequency at low field. This may allow us to isolate a subset of these nuclei from the others to use as a quantum memory. Transitions which are resonant with an RF frequency greater than 40 MHz, with applied fields of less than 0.75 T are distinct in comparison to other regions and may be well suited to such an approach.

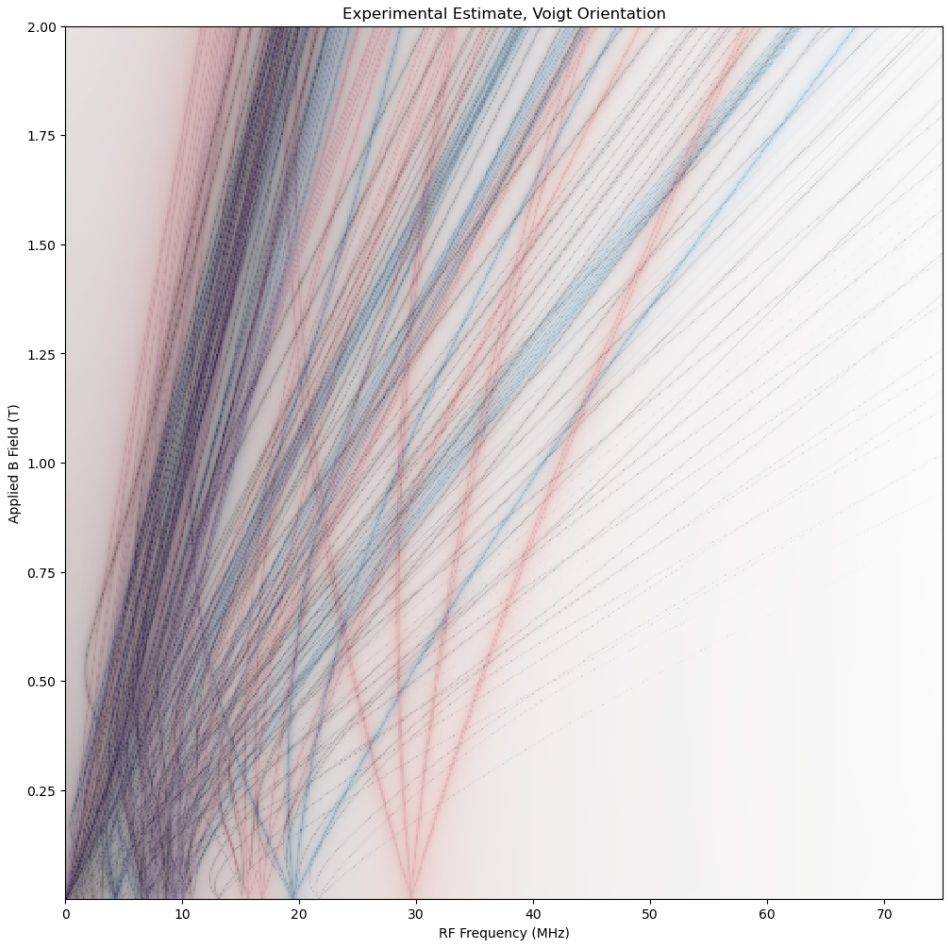

Figure 4.24: Simulation outcome of an NMR experiment on our quantum dot, with a Voigt orientated field. Lines are coloured according to the atomic species that produced them, in order to identify if any subsets of interest belong to a particular species. Grey features correspond to ^{115}In nuclei, blue to ^{69}Ga and red to ^{75}As. We ignore the tiny fraction of ^{71}Ga present in the sample. We see significant clustering at low applied fields, though still broader than would be needed to implement a quantum memory. At higher fields the transitions begin to separate by species, though to a lesser extent than occurred in the Faraday orientation. There are almost no absorption lines present at low fields for RF frequencies greater than 35 MHz, and at higher fields such lines are much weaker than in the Faraday case. The Voigt orientation is therefore much less desirable for use as an isolated spin quantum memory than the Faraday case, where such absorption lines are both stronger and more isolated.

4.4 Conclusions

We find that the update of the measured values of the gradient elastic tensor as found in [176, 177] can result in a significant change in the calculated properties of an InGaAs quantum dot. When characterising such a system, one may well be led to wrongly throw out acceptable dots as a result of calculating distributions using old/incorrect values of the relevant parameters - which can lead to 3-fold changes in the width of the nuclear quadrupole distributions. However, the required experimental work has not yet been conducted to investigate whether or not the standard values of the GET in ^{115}In need to be updated - we suggest this would be a very valuable experiment to perform. We also show that these parameter changes have a significant impact on the simulated NMR spectra of this quantum dot, and use such simulated spectra to qualitatively assess the suitability of this dot for use as a either a magnon or spin-subset based quantum memory, finding that it is likely not suitable for the former (in agreement with previous research into strain based quantum dots) but may hold promise for the latter - especially if the electron coherence time might be improved. By incorporating real data, we are able to calculate these results substantially faster than performing an otherwise necessary molecular-statics simulation. The resulting code will be of use to anyone who wishes to rapidly estimate the results of an NMR experiment on a specific quantum dot or assess whether that dot is well suited to a particular task.

In the next chapter we will consider how we might improve the suitability of a strain based InGaAs quantum dot by making it more symmetric. As can be seen in Fig. 4.5, the dot we are studying has a large bulge on the upper left hand side, and a long tail to the right of the image. This has the effect of creating an asymmetric strain distribution throughout the dot (as can be seen in Fig. 4.6) and hence a wide distribution of quadrupolar frequencies across the dot (see Table 4.3). We propose therefore that a more symmetric dot might have narrower distributions of quadrupolar frequency, and a more ordered overall spectrum. Unfortunately, we were unable to obtain more experimental data to test this hypothesis due to the COVID-19 pandemic. Therefore we instead create ‘fake’ dots by mirroring the underlying strain and concentration data along the central axis of the dot we have data for. We will investigate the properties of these mirrored dots in the next chapter, using the tools introduced here.

CHAPTER 5

MIRRORED QUANTUM DOTS

5.1 Introduction

In the previous chapter, we saw how more accurate measurements of the Gradient Elastic Tensor (GET) can lead to substantial changes in the predicted behaviour of an InGaAs quantum dot, both in terms of the coherence time of any central electron and in the potential for the QD to serve as a quantum memory. Here we investigate how we might improve the performance of a strained quantum dot in these key functions.

First, let us set out the interactions at work, the scale at which they are present and how they interact with each other. At the largest relevant scale we have the quantum dot structure itself - in our case this is a region within a GaAs lattice which has a non-negligible concentration of indium, as a result of Stranski–Krastanov growth processes. The formation of this structure is reliant on strain, and the presence of indium causes the structure to be strained in comparison to the surrounding GaAs lattice (as seen in Section 4.1.1). If we zoom in slightly, we see the electron trapped within the confining potential of the dot. This electron is the one used in the production of single photons, and its wavefunction is distributed throughout the structure - as such it 'sees' the following interactions: Zeeman effects due to any external magnetic field and hyperfine interactions between the electron and the nuclear spin bath. The Zeeman effect is unchanging in direction and strength, while the relative size and direction of the hyperfine interaction changes as the nuclear spin bath evolves (see Section 3.1) - the timescale over which the bath remains the same is therefore a limit to the coherence time of the electron, defining the frozen fluctuations time (see Section 3.1.2.2). If we zoom in more, we see the atoms which make up the lattice, and their nuclei which make up the nuclear spin bath seen by the electron. This spin bath (if thought of as a single large spin) interacts with any external field, and with the central electron via the

hyperfine interaction and will thus precess over time - setting an upper limit to the lifetime of the frozen fluctuations model. This limit is lowered further by the interactions between nuclei that make up the bath. Each of these nuclei sees the following effects: the external magnetic field, a component of the hyperfine interaction with the electron, nuclear-nuclear interactions and the quadrupolar interaction with the local electric field gradient (which is determined by the strain and the values of the GET, though for this chapter we will solely be using the updated values of the GET found using NMR/PL spectroscopy). Of these, we are primarily interested in the quadrupolar interaction. Each nucleus sees a different electric field gradient, and has a quadrupolar interaction strength which depends on its spin and quadrupolar moment (both dependant on the nuclear species). The different electric field gradients seen by each nucleus cause each to precess subtly differently from all the others (even within a particular species while assuming that the effect of the external field and the hyperfine interaction are the same between nuclei - assumptions which are not necessarily valid). As a result, the nuclear spin bath will change at a higher rate if its component nuclei are experiencing significantly different electric field gradients - as would be caused by substantially varying strain.

5.2 Mirrored Dots

The obvious way to improve the performance is to minimise the variation in the strain across the quantum dot - which is equivalent to making the overall structure more symmetric. Experimentally this might be achieved via processes such as thermal annealing. Annealing results in a diffusion of impurities in the lattice (indium in the case of an InGaAs quantum dot) from areas of high to low concentration, leading to a more uniform distribution and hence a more even strain and quadrupolar distribution [200, 201]. This process has also been experimentally shown to decrease fine structure splitting [202] and modelling predicts that the resulting changes in electron localisation volume and central indium concentration will reduce the variance in hyperfine interaction between different quantum dots after annealing [203]. A simple way to investigate this hypothesis is to take the strain and concentration data we already have and mirror it along the vertical axis to create an artificially symmetric structure. We can create 2 structures in this way by mirroring the dot left -> right to create one, and then right -> left to create the other. This mirroring is not at the scale of the individual strain components, but rather a replication of the data such that the strain tensor of a nucleus located immediately to the left of the mirror line is exactly equal to that of one immediately to the right of the line. Mirroring the structure at the exact strain level essentially amounts to performing a full-scale atomic simulation of a different structure, a process we are explicitly trying to avoid in this analysis[1].

We can then investigate these structures using the techniques described in Chapter 4, and determine if the artificially symmetric structures would perform better than the original from

[1] An extension of this method could be to create a 'superposition' of strain data such that Mirrored Dot = $\frac{\text{Dot LR}}{2} + \frac{DotRL}{2}$, which may provide a better approximation of an artificially highly symmetric dot.

which they are derived. This method has some clear limitations - it introduces a significant discontinuity along the mirror line which would not be present in a physically grown structure, the choice of line along which to mirror is completely arbitrary and the resulting structure has not been adjusted to take into account higher or lower strain than was previously present and is therefore inherently nonphysical in that respect. Improving the model in this respect would be highly complicated, and would be less worthwhile than completely simulating a highly symmetric structure using a library such as LAMMPS. Our approach is designed to highlight the effect of structural symmetry while still being based in real data. We have chosen to mirror along a line which falls approximately halfway down the structure, which in this case allows us to investigate the effect of the inherent asymmetry of the original structure. The non-mirrored dot (see Fig. 4.5) has a large bulge on the upper left of the image, which results in greatly different shapes of the 2 structures created by mirroring along a central line.

5.2.1 Indium Concentrations

The two mirrored dots are shown in Figures 5.1 & 5.2. The first was created by mirroring the left hand side of the structure along the central axis, and the second by mirroring the right hand side. The resulting structures are of course highly symmetric, but maintain some differences between each other. The left-right flipped dot (referred to as Dot LR) is larger than the right-left flipped dot (Dot RL), and has a slightly higher peak indium concentration (0.32 vs 0.30). It also has a long thin tail out to each side, which widens its footprint without substantially increasing the total volume of the structure.

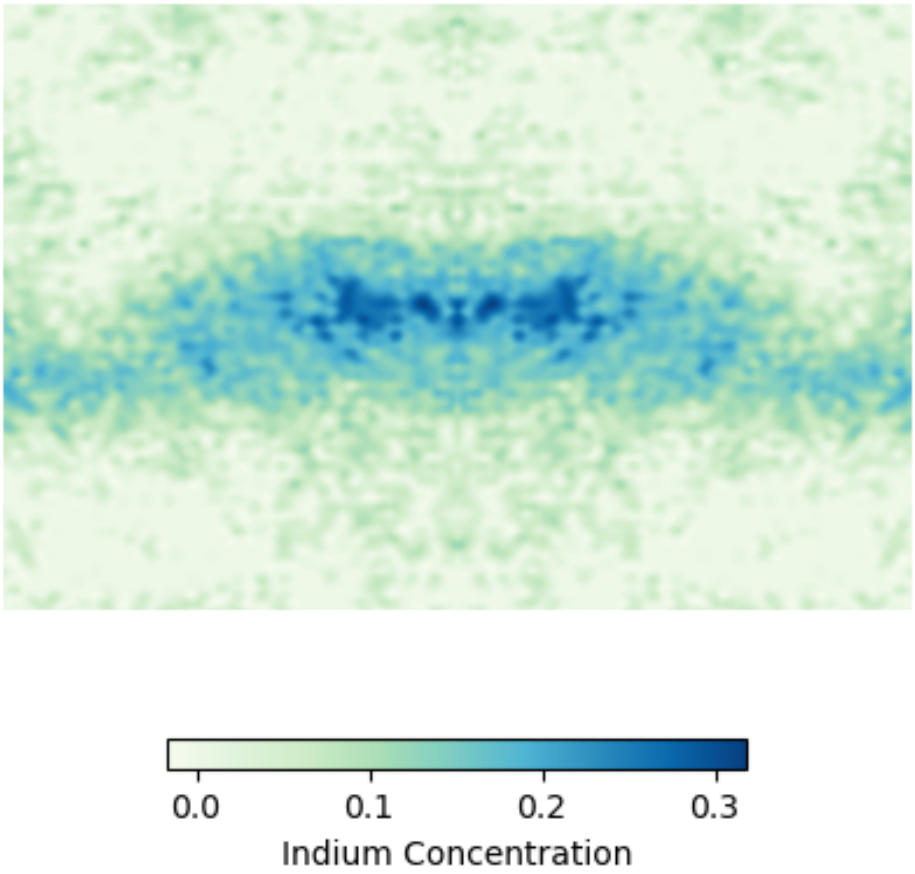

Figure 5.1: The indium concentration of the structure created by mirroring the left hand side of the original quantum dot. This structure is wider than the original due to the tail present in the original and the bulge on the left hand side of the original structure results in a doubly humped shape in the new structure. The peak indium concentration is 0.32, as a result of the original structure having its highest concentration on the left hand side. The large size and irregular shape of this structure leads us to believe that it will have a wider distribution of nuclear spin environments than the dot created by reflecting the right hand side.

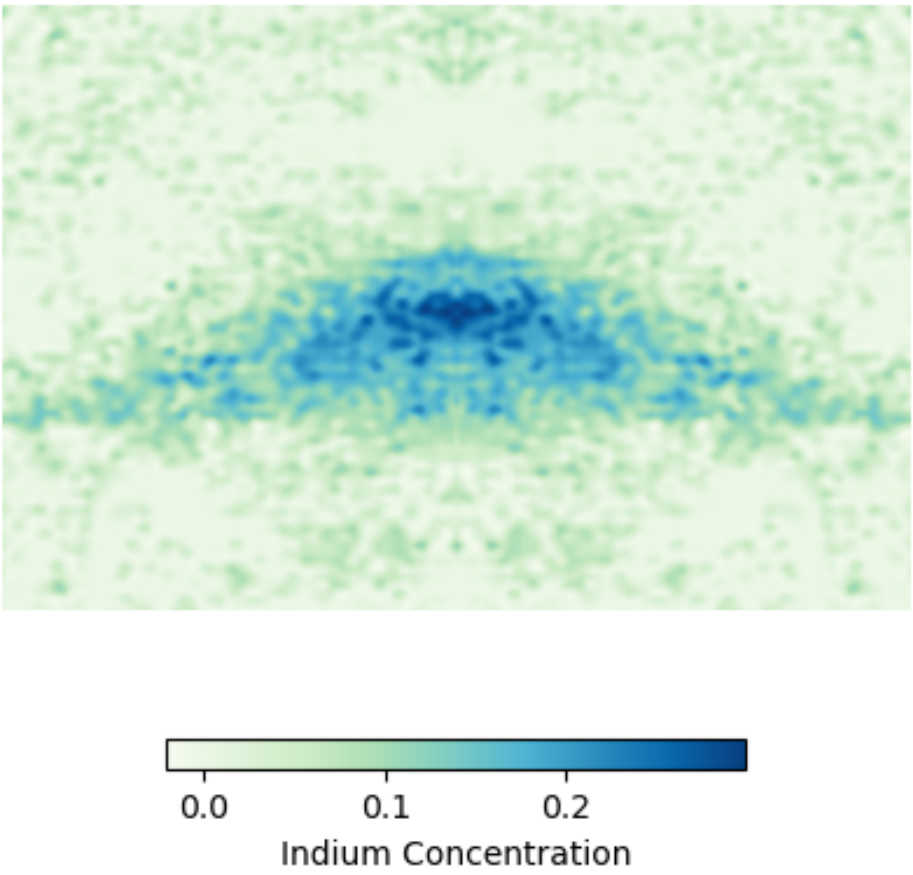

Figure 5.2: The indium concentration of the structure created by mirroring the right hand side of the original quantum dot. This structure is smaller than the original, and has a more uniform shape. The maximum indium concentration is 0.30, as a result of the original structure having its highest concentration on the left hand side. As a result of the highly uniform shape of this dot, we expect it to have a narrower distribution of nuclear spin environments than both the original and left-right mirrored dot.

5.2.2 Strain Profiles

As before, the first step in our analysis is to map out the strain profiles of these 2 structures along the $xx, xz \& zz$ directions. These mappings are shown in Figures 5.3 & 5.4 respectively and show that Dot LR shows a smaller difference between the strain inside the structure as compared to the lattice surrounding it, even though the Dot LR has a larger maximum strain than Dot RL. This suggests that Dot LR may be less isolated from the surrounding lattice, further reinforcing the idea that it will have a wider distribution of nuclear environments (though it should still be narrower than found in the original data). The strain in Dot RL is highly centralised to the dot itself, showing a clear differentiation between the dot and the surrounding lattice.

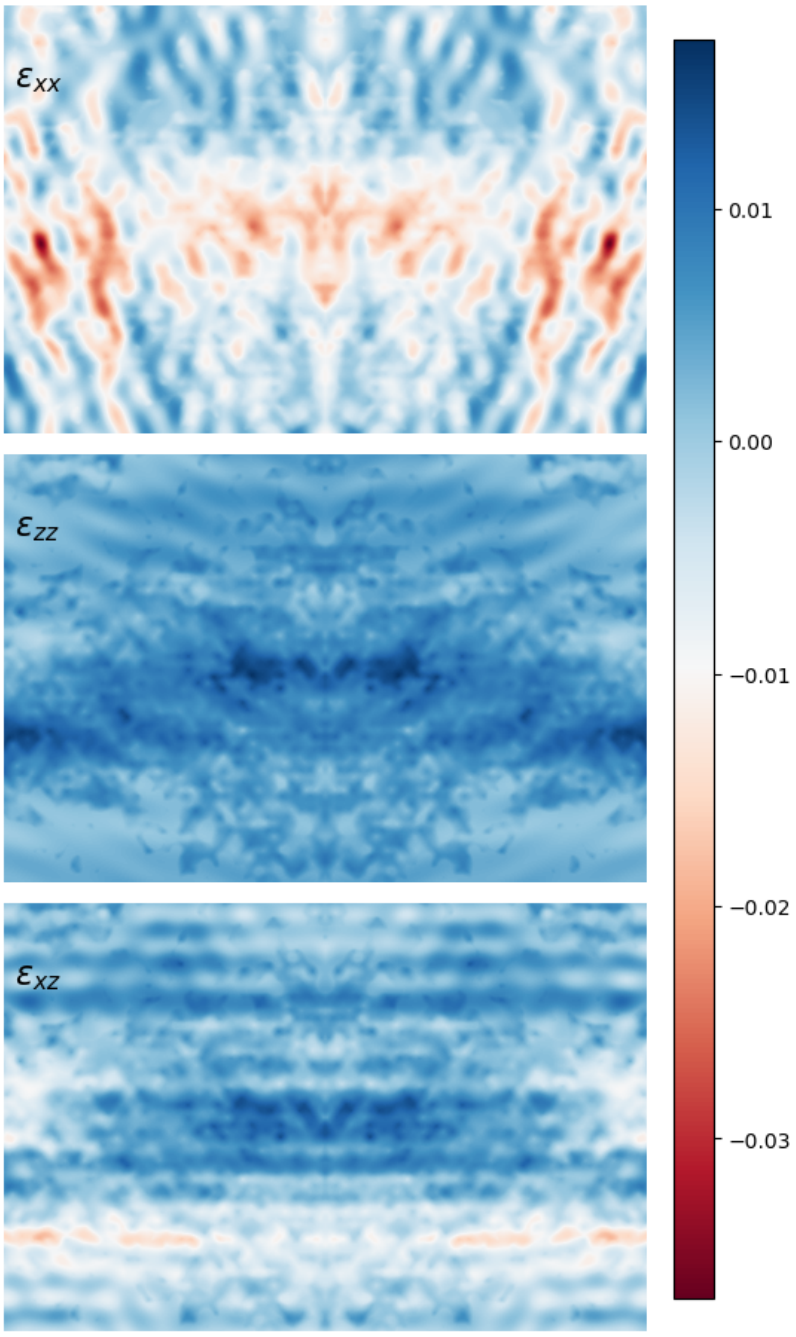

Figure 5.3: The strain environment of Dot LR, as expected we see a much more uniform distribution of strain in a mirrored dot than we do in the original, though this example has more high-strain regions due to most of these being present on the left hand side of the original structure. The second image (showing ϵ_{zz}) clearly outlines the shape of the new structure, which has a significantly higher strain than the background lattice (as expected for a quantum dot grown using Stranski–Krastanov methods).

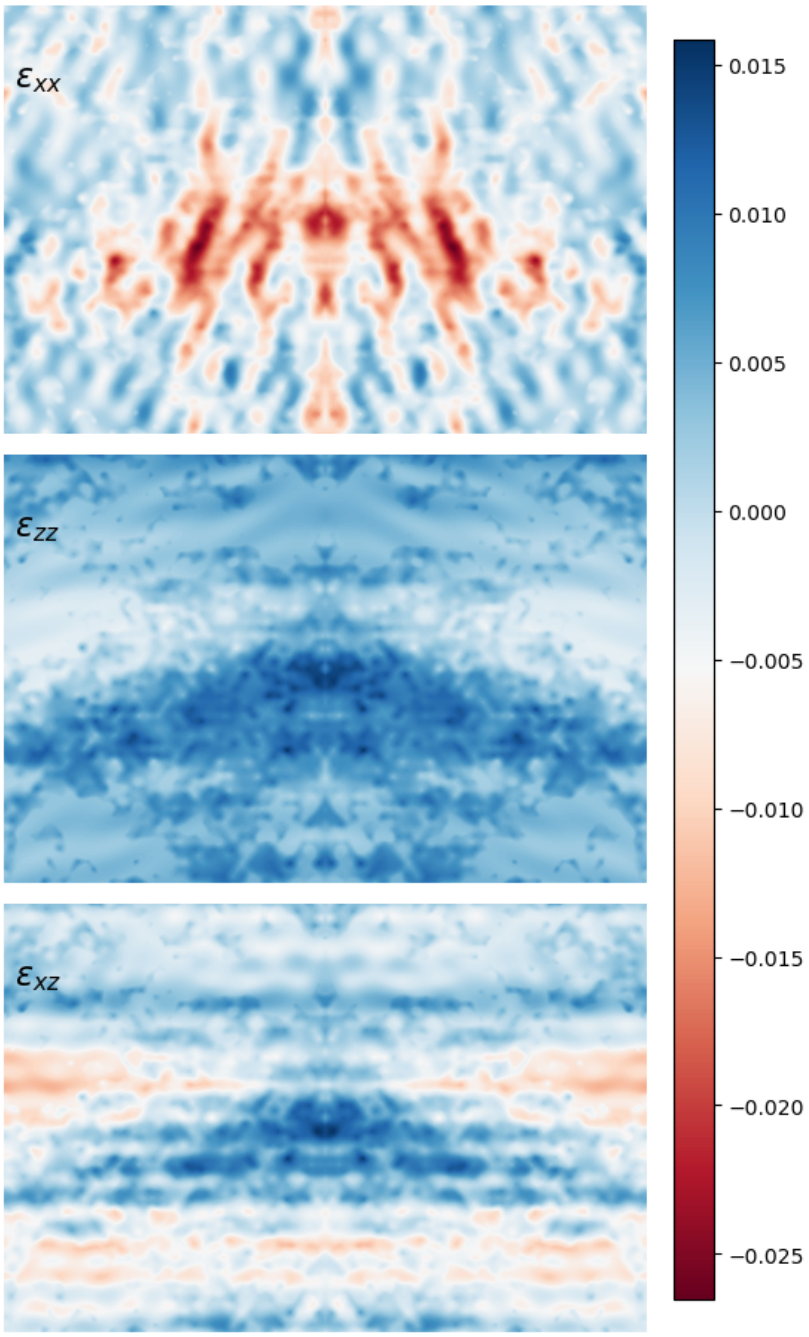

Figure 5.4: The strain environment of Dot RL. The ϵ_{xx} strain in this structure is far more centralised than in DOT LR, though it has a slightly lower maximum value - as would be expected for a structure with a slightly lower maximum indium concentration. There is a very clear contrast between the quantum dot and the surrounding GaAs lattice along all 3 strain axes.

5.2.3 Electric Field Gradients

We use Eq 4.6 to calculate the electric field gradient (EFG) across the structure as we did in Section 4.2.2. After calculating this at each lattice site, we again find the principal axis frame and hence the size and direction of the quadrupolar interaction that each nuclear species would feel at each lattice point. The results of these calculations for indium are shown in Figures 5.5 & 5.6. In both of these graphs we see a much more homogeneous direction to the quadrupolar field, especially in the case of Dot LR, which has an almost uniform field across the entire structure. Dot RL has a similar uniformity across the dot structure, but has a large region of inhomogeneous field *outside* of the dot in the top left and right corners of the image. This is important to note, as these data will need to be accounted for when calculating distributions across the quantum dot, as they are a part of the lattice and not the quantum dot itself.

In Figures 5.5 & 5.6 we show the fields as felt by an ^{115}In nucleus, however the same calculation can be performed for each nuclear species[2], leading to similar conclusions regarding the direction and strength of the field in all cases. It is important to note that the direction of the effective field is reversed for ^{69}Ga nuclei, as was the case for the original structure when using the NMR/PL gradient elastic tensor values. This again highlights the importance of updating the values of the gradient elastic tensor - we cannot predict whether a similar reversing of the field direction will occur for either ^{115}In or (less importantly) ^{71}Ga without performing the requisite experiments, and the results of these experiments may have a drastic impact on the results we present here.

[2]See Appendix A.4 for these graphs.

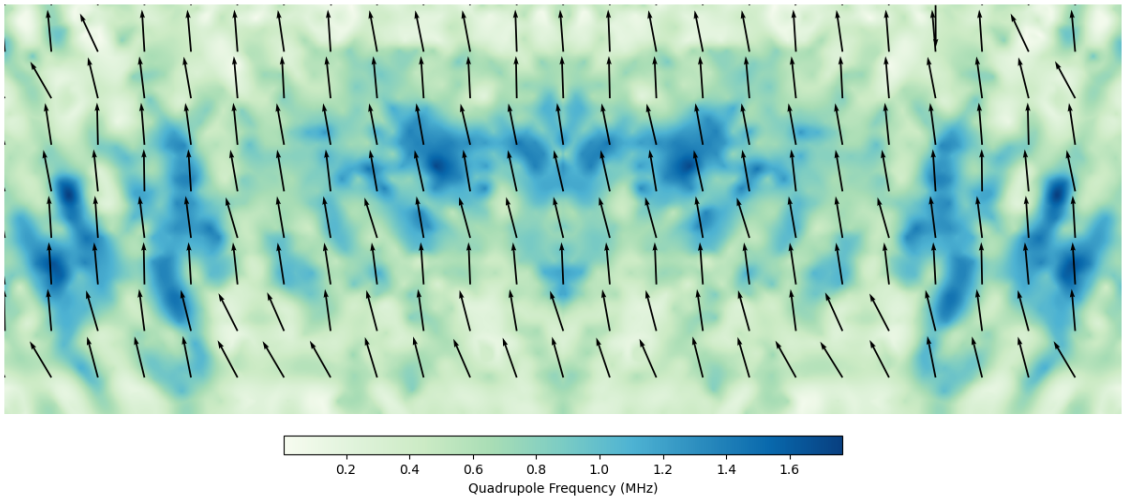

Figure 5.5: The direction (arrows) and strength (background colour) of the quadrupolar field as felt by an indium 115 nucleus at each point in the structure of Dot LR. The field is approximately uniform in direction, though varies in magnitude according to indium concentration - as would be expected. This dot almost entirely fills the rectangular area defining the image, and thus there is little need to exclude external regions from subsequent analysis.

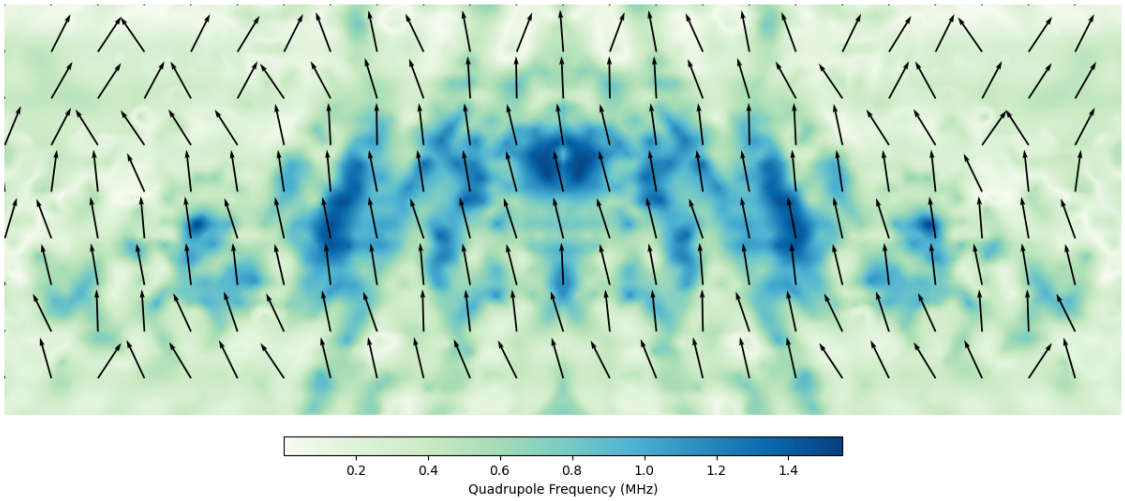

Figure 5.6: The direction (arrows) and strength (background colour) of the quadrupolar field as felt by an indium 115 nucleus at each point in the structure of Dot RL. Inside the dot, the field is almost uniform in direction, and very similar in strength as well. The regions outside show significant deviation, but this is misleading as these are regions of the GaAs lattice, not the quantum dot itself and thus there is no indium present. As such, we must be careful to exclude these regions from subsequent analysis.

5.2.4 Frequency Distributions and Fits

Plotting the distribution of quadrupolar frequencies (see Figures 5.7 & 5.7) highlights both the narrowing of possible nuclear environments across Dots LR and RL, and the problems caused by mirroring a region outside the quantum dot itself. In Fig 5.7, the distributions of quadrupolar frequencies are very similar in shape to those seen in the original structure, though they have been narrowed by the mirroring effect as expected. However, in Fig 5.8 the shape of the distributions has changed significantly. For each nuclear species, we see 2 distinct peaks in the distribution - one over positive frequencies and the other over negative frequencies.

The absolute sign of the distribution is an artefact of the method used to calculate the principal axis frame (a spin pointed left on a diagram such as Fig 5.5 has a positive sign and vice versa) and hence tells us little about the preferred alignment of the spin in reality, a substantial splitting of the values around 0 means there is a significant spin population orientated differently to the others. In the case of Dot RL, we can see from Fig 5.6 that this discrepancy likely results from regions outside the quantum dot that have nonetheless been caught by our calculation programme. The ideal solution to this issue is of course to only include that region of the image which is the quantum dot, however this presents some implementation challenges[3]. Instead, we will choose to throw out the data with a negative value for transition frequency[4], we justify

[3]It is substantially more difficult than one might expect to select a triangular region of an array in Python, and any region selected like this is fundamentally an arbitrary choice of what is or isn't part of the quantum dot.

[4]Or a positive value of Ga69, as the predominant spin direction inside Dot RL is reversed for this species.

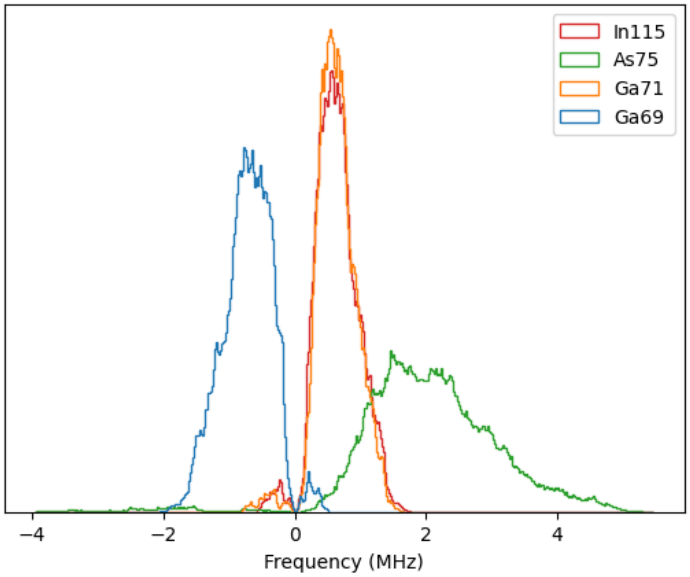

Figure 5.7: The distribution of quadrupolar frequencies in Dot LR. In comparison to the original data (shown in Fig 4.12) there is a substantial narrowing in the distribution of Ga69 transition frequencies, and a lesser narrowing in the distribution of ^{75}As transition frequencies.

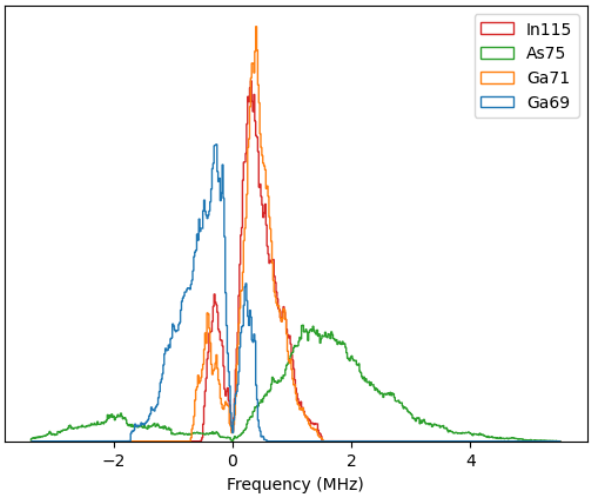

Figure 5.8: The distribution of quadrupolar frequencies in Dot RL. The same narrowing is seen here as is seen for Dot LR in Fig 5.7, but in this case there is a substantial secondary peak (of opposite sign to the primary peak) for each of the nuclear species present. We believe this to be a result of the mirroring of a distorted region of the GaAs lattice, which when duplicated has an oversized effect on the resulting distribution.

this by noting that inside the Dot RL structure all spins are pointing the same direction - spins pointing the other way exist only in regions outside of the dot.

In order to analyse these distributions, we fit gamma distributions to the data, and from these calculate the mean and variance of the nuclear quadrupole transition frequency. These data are summarised in Table 5.1 and the fits for all nuclear species for both dots are shown in Figures 5.9 & 5.10 respectively. We would expect these new structures to have a narrower distribution of nuclear spin transition frequencies than the original structure, both as a result of their increased symmetry and because we have simply removed some data from the calculation.

We find that for both Dot LR and RL there is a decrease in the variance of the quadrupolar frequency distributions as compared to the original structure, for all 4 nuclear species. This narrowing is most pronounced for Ga69 for which the fitted distributions have a variance of 0.14 MHz^2 and 0.13 MHz^2 for Dots LR and RL respectively, as compared to the variance of the distribution over the original structure 0.69 MHz^2. The decrease in variance for ^{75}As is less pronounced, dropping from 0.92 MHz^2 in the original quantum dot to 0.86 MHz^2 in Dot LR and 0.84 in Dot RL. The variance for the distributions of both ^{71}Ga and ^{115}In is not substantial, though for these species we are forced to use the outdated NAR values in our calculations and therefore we have less confidence that these results reflect the reality of the original structure and we can draw fewer conclusions about the effect of mirroring these species than we can for Ga69 or ^{75}As. We also note that these distributions were very narrow to begin with, and therefore a reduction in their variance is much harder to achieve by any means. In all cases we find a slightly lower variance in transition frequency in Dot RL than Dot LR - as expected given Dot

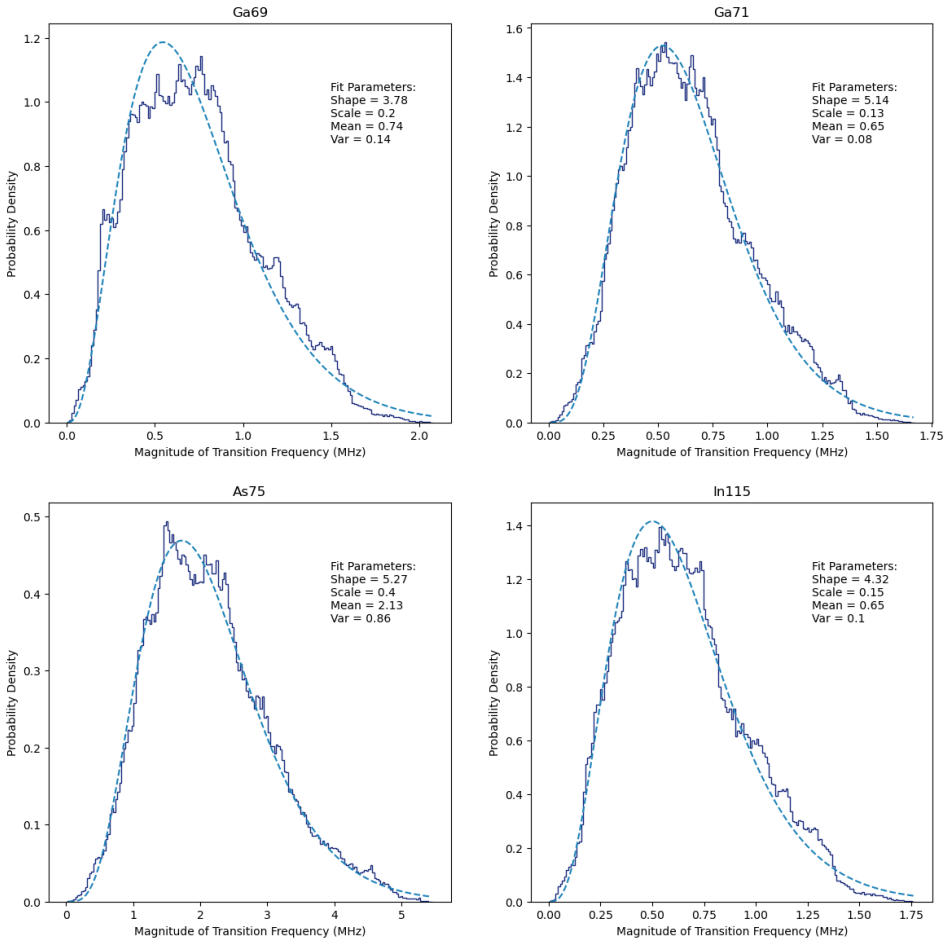

Figure 5.9: Fitted gamma distributions for Dot LR. Absolute values of the quadrupolar frequencies are shown in dark blue, while the fitted distributions are overlaid in light blue. Each fit was calculated using a maximum likelihood estimation, as implemented in Scipy. Each of these fitted distributions (except that for Ga69) has a slightly higher mean frequency than was found for the original dot, but a substantially lower variance.

RL is a result of mirroring the side of the original QD without a bulge and that we discounted some of the data representing the outer edge of the lattice when performing our calculations. All of these results support the hypothesis that a more symmetrical dot will experience a lower variation in nuclear spin environment and will therefore be better suited to acting as a source of single or entangled photons.

The effect on the mean values of the transition frequency is slightly more complex. For all 4 nuclear species, Dot LR has a higher mean frequency than Dot RL - a result of the higher indium concentration in this structure causing a higher average strain across the dot and hence a larger electric field gradient. In the case of Ga69, the mean frequency is lower in both mirrored structures than it was in the original. This comes about because of the large variance of the distribution over the original QD results in a higher mean value compared to the far narrower

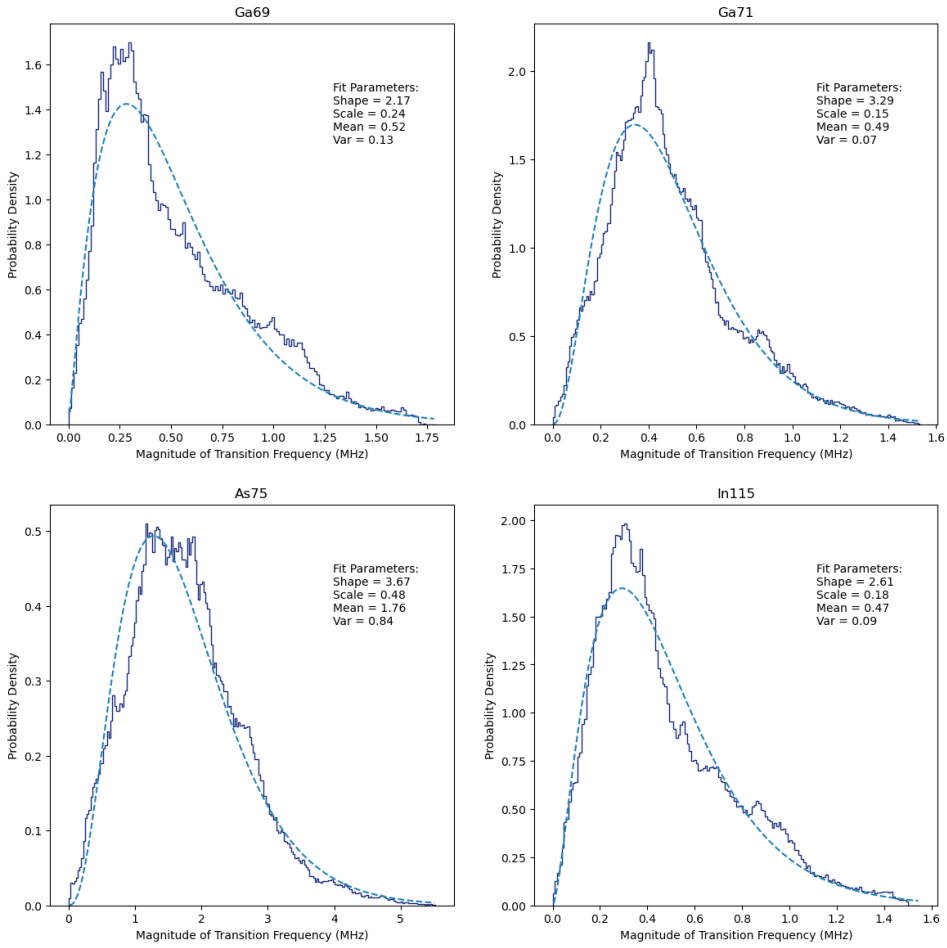

Figure 5.10: Fitted gamma distributions for Dot RL. Absolute values of the quadrupolar frequencies are shown in dark blue, while the fitted distributions are overlaid in light blue. Each fitted distribution has a lower mean and substantially lower variance than was found for the original structure.

distributions over Dots LR and RL. The mean frequencies for all of ^{71}Ga, ^{75}As and ^{115}In are higher in Dot LR than they are in the original dot, and lower in Dot RL. This effect can be understood by considering that the original structure has an asymmetric strain profile, with a higher strain on the left hand side due to the bulge present on that side (see Fig 4.5), and hence will have an average strain somewhere between that of the structures formed by mirroring either side. As the magnitude of the strain directly contributes to the value of V_{zz}, this leads to the pattern of mean values of quadrupolar frequency seen here.

	Left-Right Mirror				Right-Left Mirror			
	Ga69	^{71}Ga	^{75}As	^{115}In	Ga69	^{71}Ga	^{75}As	^{115}In
Shape (k)	3.78	5.14	5.27	4.32	2.17	3.29	3.67	2.61
Scale (θ)	0.20	0.13	0.40	0.15	0.24	0.15	0.48	0.18
Mean (MHz)	0.74	0.65	2.13	0.65	0.52	0.49	1.76	0.47
Variance (MHz)	0.14	0.08	0.86	0.10	0.13	0.07	0.84	0.09

Table 5.1: Fitting parameters (shape and scale), and mean and variance values for gamma distributions fit to quadrupolar frequency data calculated for Dots LR and RL. All fitted distributions are defined to begin at 0 MHz.

5.2.5 NMR Simulation

As before, we wish to understand the behaviour of our mirrored dots under NMR spectroscopy, so that we might gain insight into how useful they would be for use as quantum memories or sources of entangled photons. Therefore we again simulate the results of an NMR experiment performed on Dots LR and RL in both the Faraday and Voigt geometries, with the contributions of each species weighted by the indium concentration of the new structures (as shown in Figures 5.1 & 5.2).

The two types of spin memory will be represented in very different ways in such an NMR spectra, and thus we have 2 measures of quality to look for. A magnon spin memory requires a very narrow frequency response, where all of the spins in the bath behave as a single much larger spin onto which we can project the quantum state we wish to store. This will manifest in the simulated NMR spectra as a significant clumping together of possible transitions, with very low absorption present outside this narrow band. The results of Section 5.2.4 suggest we are unlikely to see such a result for either Dot LR or RL. While the quadrupolar distributions have narrowed significantly, they are still spread over a range of MHz - far too large for the nuclei across the dots to show up as almost identical under in an NMR experiment. Our other measure of quality is the identification of a set of transitions which could be used to isolate a subset of the spin bath that might be suitable for use as a memory of a different kind. Our previous results (see Section 4.3.3) suggest that the Faraday orientation may give better results for this than a Voigt orientated field, though we examine both orientations here to determine if this differences carries over to our mirrored dots.

There is a significant change in the simulated spectra of Dot LR in comparison to that of the original structure. In the Faraday orientation, shown in Figures 5.11 & 4.23 for Dot LR and the original structure respectively, we see a dramatic clustering of the absorption lines in Dot LR, especially at lower applied fields. At 0 field the original dot has an indium absorption line at ≈ 41 MHz, while the reflected structure's highest absorbed frequency is one for ^{75}As which occurs at ≈ 25 MHz. Investigating the different species in turn, we see that Ga69 forms a much tighter cluster at much lower frequencies in the reflected dot, as does ^{115}In (though ^{115}In still extends to higher frequencies at lower fields than the other 2 species). The absorption of ^{75}As however

is spread over a wider range of frequencies at low fields, but broadens slower such that it ends up with a very similar structure between the 2 structures at higher fields. This clustering is potentially good news for using Dot LR as a magnon type quantum memory, however the spread of absorption lines is still very wide relative to the 100 kHz width suggested to be necessary by Denning *et al* [195]. The Faraday orientation appeared to be the better of the 2 choices for the construction of a subset type memory, however this advantage disappears for Dot LR at low fields where there are no well isolated subsets. Several bands of absorption lines can be seen at fields between 0.75 and 1 T for RF frequencies above 40 MHz, however they are faint relative to those seen at lower frequencies - suggesting there are fewer nuclei than would be necessary to form a well isolated subset. The story could not be more different in the Voigt orientation, shown in Figures 5.12 & 4.24, in which we see a significant spreading of absorption lines at all applied fields - especially at lower applied fields, though the trend continues all the way to 2 T. There are not large differences between the spectra of Ga69 and ^{75}As, though there is a slight narrowing in the overall structure of the spectra for both species. It is in the spectra of ^{115}In that the difference appears. At 0 field we see absorption lines present for ^{115}In all the way up to 55 MHz, with strong lines present up to 45 MHz. The indium absorption lines remain strong and well isolated over the entire region spanning 45-75 MHz and 0-1.5 T, presenting a substantial regime where it may be possible to create a subset style quantum memory using indium nuclei. The prospects of a magnon type memory are again lacklustre, especially given the wide spread of absorption lines exhibited by indium. Turning our attention to Dot RL, we again find significant differences in the expected NMR spectra as compared to the original structure. Beginning with the Faraday orientation, shown in Fig 5.13, we see a sharp increase in the density of absorption lines in low field at frequencies above 30 MHz. This trend continues as the field increases, with indium nuclei dominating the spectrum at higher frequencies until the field reaches approximately 1.25 T. The absorption bands corresponding to arsenic nuclei are much narrower for any range of frequency and applied field, while those for gallium are almost unchanged. Overall, this structure is likely unsuitable for use as a magnon based quantum memory due to the broad nature of the absorption spectra. The original structure in a Faraday orientation may have been suited for use as a subset-type memory if an experiment were addressing the low field/high frequency transitions, however Dot RL does not exhibit the same set of well isolated transitions in this orientation and so would most likely not work for this type of memory either. The most significant difference in the spectra of Dot RL in a Voigt orientated field (see Fig 5.14 is a substantial clustering of absorption lines in the low field regime. At 0 field, the mirrored structure has no absorption of frequencies higher than 20 MHz, as compared to a clear absorption line at 30 MHz as seen in the spectra of the original structure. Both Ga69 and ^{75}As nuclei retain the same spectral structure as the applied field increases, differing only in that their absorption lines begin at lower frequencies in Dot RL than they would otherwise. This translation of absorption lines is not as apparent for ^{115}In nuclei, though there is a small reduction in their frequency at 0 field. As a

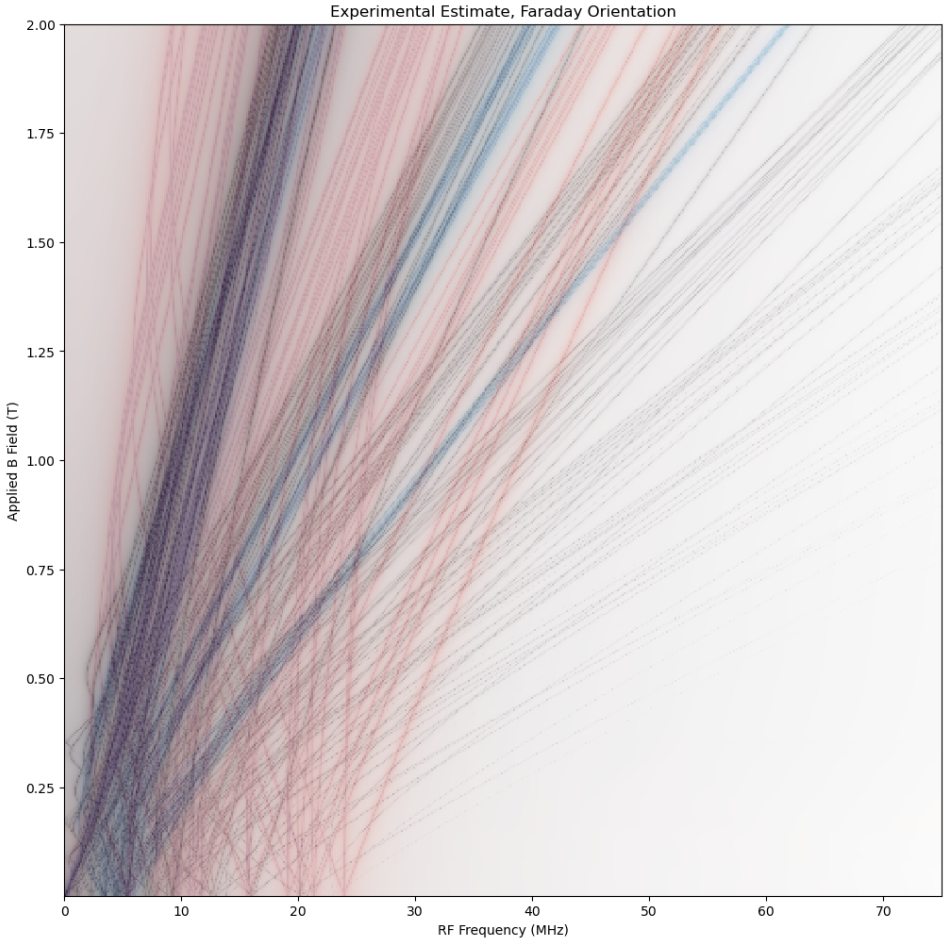

Figure 5.11: Simulation of the results of an NMR experiment conducted on Dot LR in a Faraday orientated field. Ga69 transitions are in blue, ^{75}As in red and ^{115}In in grey. We ignore the tiny fraction of ^{71}Ga present in the sample. We can see there is a tighter clustering of absorption lines at lower applied fields than is present in the original quantum dot, though the overall structure of the spectrum is similar. We no longer see the isolation of ^{115}In transitions in the high frequency/low field regime, though as the field strength increases the nuclear species begin to separate as before.

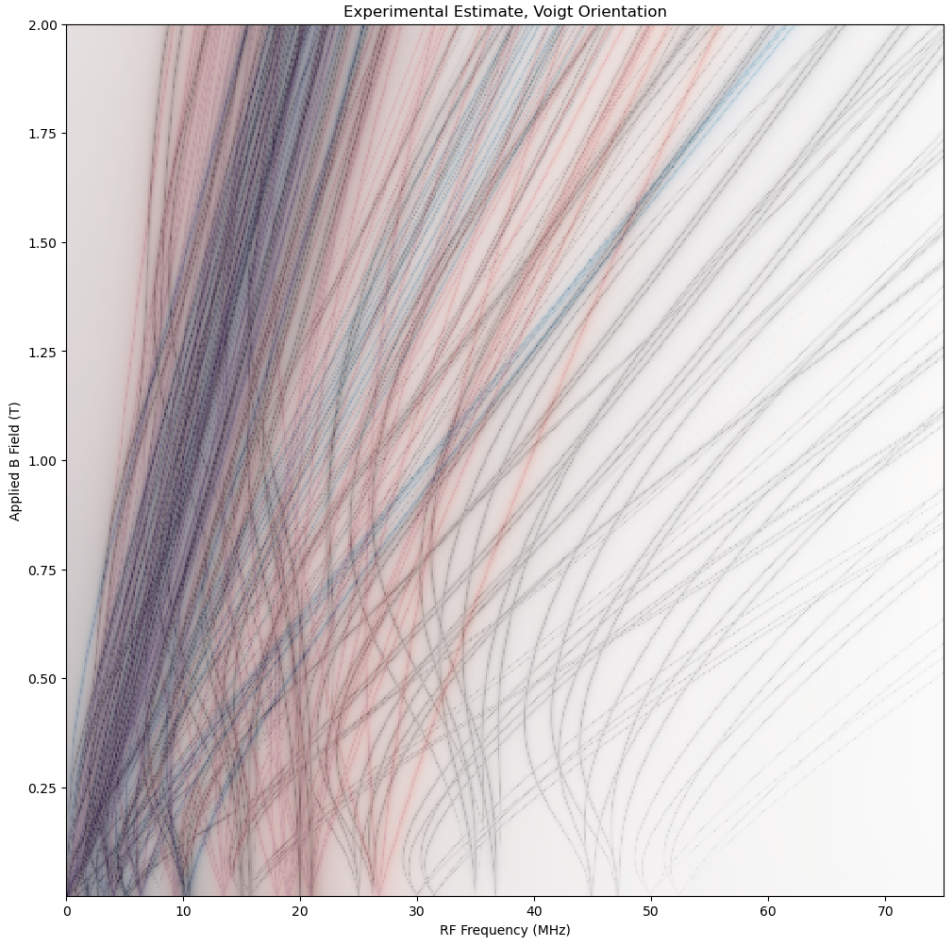

Figure 5.12: Simulation of the results of an NMR experiment conducted on Dot LR in a Voigt orientated field. Ga69 transitions are in blue, ^{75}As in red and ^{115}In in grey. We ignore the tiny fraction of ^{71}Ga present in the sample. This plot is substantially different from the equivalent plot as found from the original structure. The separation of multiple indium nuclei can be seen very clearly in the high frequency/low field regime to the bottom-left of the image. These transitions are both strong and separated from the others, suggesting the presence of a set of indium nuclei that are energetically well isolated from the bath and hence might be suitable for use as a quantum memory.

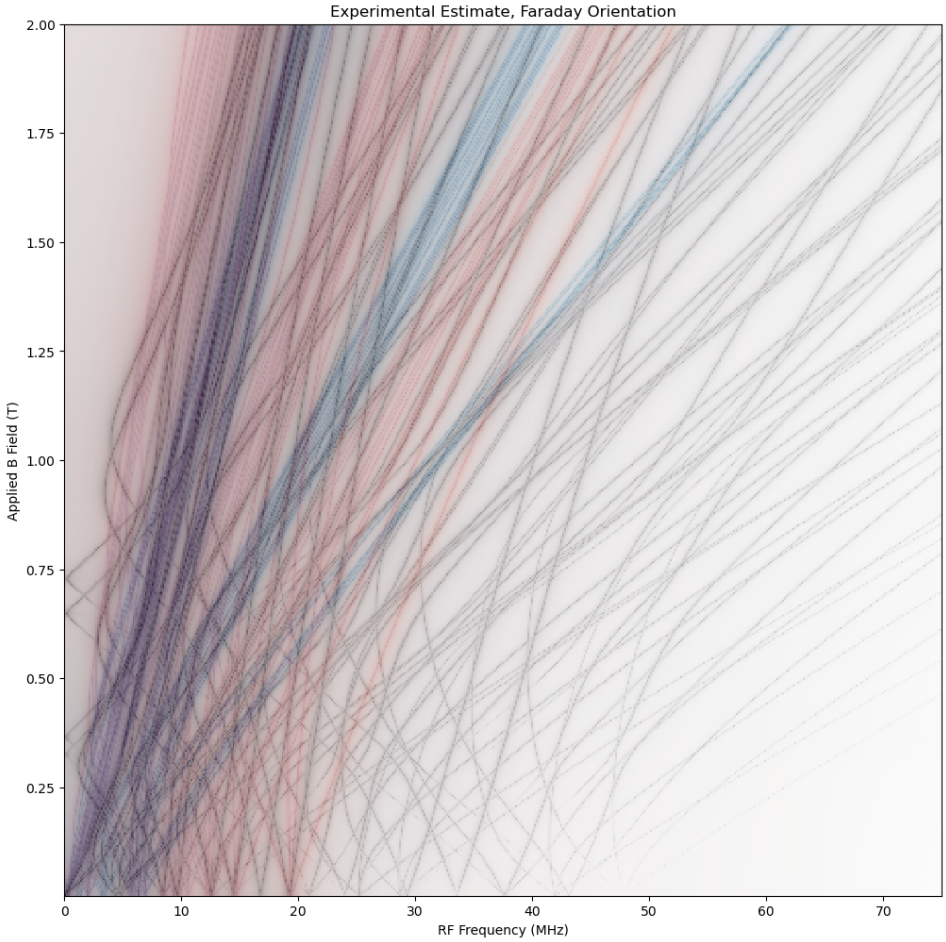

Figure 5.13: Simulation of the results of an NMR experiment conducted on Dot RL in a Faraday orientated field. Ga69 transitions are in blue, ^{75}As in red and ^{115}In in grey. We ignore the tiny fraction of ^{71}Ga present in the sample. At lower fields, this plot is almost identical to that of the original dot, though it shows a slightly more complex distribution of indium spins at low frequencies and fields of ≈ 0.75 T. Both the Ga69 and ^{75}As absorption lines are more tightly clustered in this dot, while the ^{115}In lines are much more spread out - with absorption present at frequencies in the range of 50 MHz at fields lower than 0.25 T.

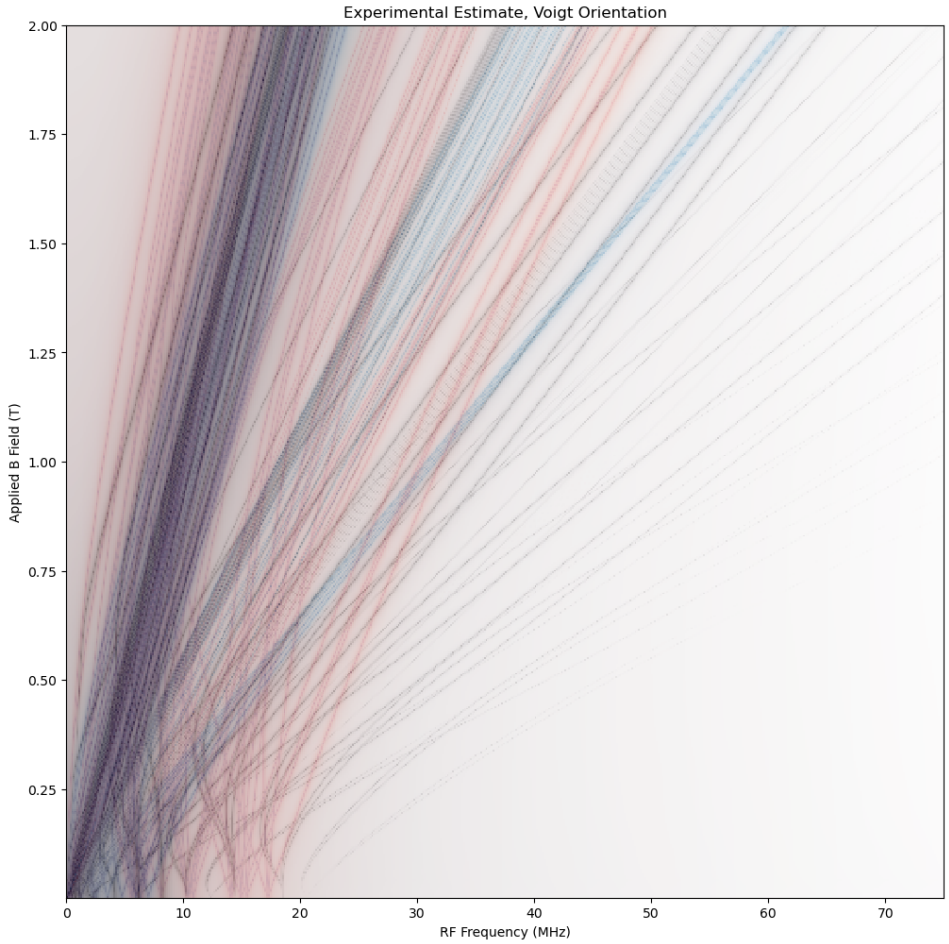

Figure 5.14: Simulation of the results of an NMR experiment conducted on Dot RL in a Voigt orientated field. Ga69 transitions are in blue, ^{75}As in red and ^{115}In in grey. We ignore the tiny fraction of ^{71}Ga present in the sample. The overall structure of this plot remains unchanged, however there is a significant narrowing of the spectra as a whole. At low field there is no absorption of frequencies higher than 20 MHz, in comparison to the ^{75}As absorption at 30 MHz seen in the original dot. At higher applied fields, this clustering continues but to a lesser extent, with ^{115}In absorption lines branching out to almost the same degree once the field passes 0.75 T.

result, we see an almost entirely unchanged structure between the original structure and Dot RL - especially as the applied field increases. Overall, we would not expect Dot RL to function well as either type of quantum memory. Though the overall NMR spectra has narrowed slightly, it is not narrow enough to function as a magnon type memory. There are also no suitably isolated yet strongly absorbing sets of transitions that would be suitable for a subset type memory. In summary, we observe changes in the NMR spectra of both Dot LR and RL in comparison to the original structure from which they are derived. In the case of Dot LR, we find that the Voigt orientation offers the best outlook for creating a subset style quantum memory - and could well be a better fit for this than the original dot. However, Dot LR performs no better as either type

of memory in the Faraday orientation, and may in fact be a worse structure for a subset type memory due to the vanishing of any isolated indium absorption lines. Dot RL fares worse than Dot LR as a prospect for a quantum memory - in neither orientation does it exhibit the required features to act well as either type of memory, though its prospects have improved somewhat for both kinds from the original.

5.3 Toy Model of Decoherence

In order to understand how the electron coherence time of these structures may have changed from the original, we construct a simple toy model to illustrate the effect of narrowing the width of the quadrupolar distribution - as has been the case for all species in both Dot LR and RL, but most clearly for Ga69. This toy model approximates an electron spin as a cosine wave of some frequency (the exact magnitude of the frequency merely sets the timescale for the decay, and as we are only interested in relative decay rates we do not need to pick any particular frequency), and then observes how this wave decays when mixed with other waves whose frequencies are drawn from a gamma distribution matching those found in our previous analysis. A collection of waves mixed like this decays in much the same way as a damped oscillator, and hence we can fit a function $g(f,\lambda,t) = \exp(-\lambda t)\cos(2\pi f t)$ of frequency f and time t to the overall waveform to find the decay rate λ of the envelope. A model this simple cannot be expected to capture the real behaviour of a spin in a quantum dot, but it should provide a quick estimate of the effect of reducing the variance of the quadrupolar distribution. According to Section 3.1.2.2, we would expect a reduction in the variance σ^2 of the nuclear spin distribution to be met with a proportional increase in the lifetime of the electron spin coherence τ_c.

We perform this analysis for all 4 nuclear species, across the three structures we have been investigating (the original quantum dot, Dot LR and Dot RL). The results for Ga69 shown in Figure 5.15[5]. As can be seen from Table 5.2, there is not a 1:1 ratio between a reduction in the width of the quadrupolar frequency distribution and the corresponding increase in estimated electron coherence time. For example, the width of the Ga69 quadrupolar frequency distribution in Dot LR is 5 times smaller than that of the original dot, but we find that the lifetime increases only by a factor of 2. In every case except that of ^{71}Ga in Dot LR we find that a reduction in the variance of the quadrupolar frequency distribution corresponds to an increase in the estimated electron coherence time. In the case of ^{71}Ga for Dot LR we see a small reduction in variance resulting in a slight decrease in coherence time. We believe this anomaly to be the result of the much smaller variance of the quadrupolar frequency distribution for ^{71}Ga in the original structure combined with the margin for error of the fitting - the decay rate λ varies by ± 0.03 between modelling runs.

[5]Similar graphs for other species can be found in Appendix A.5.

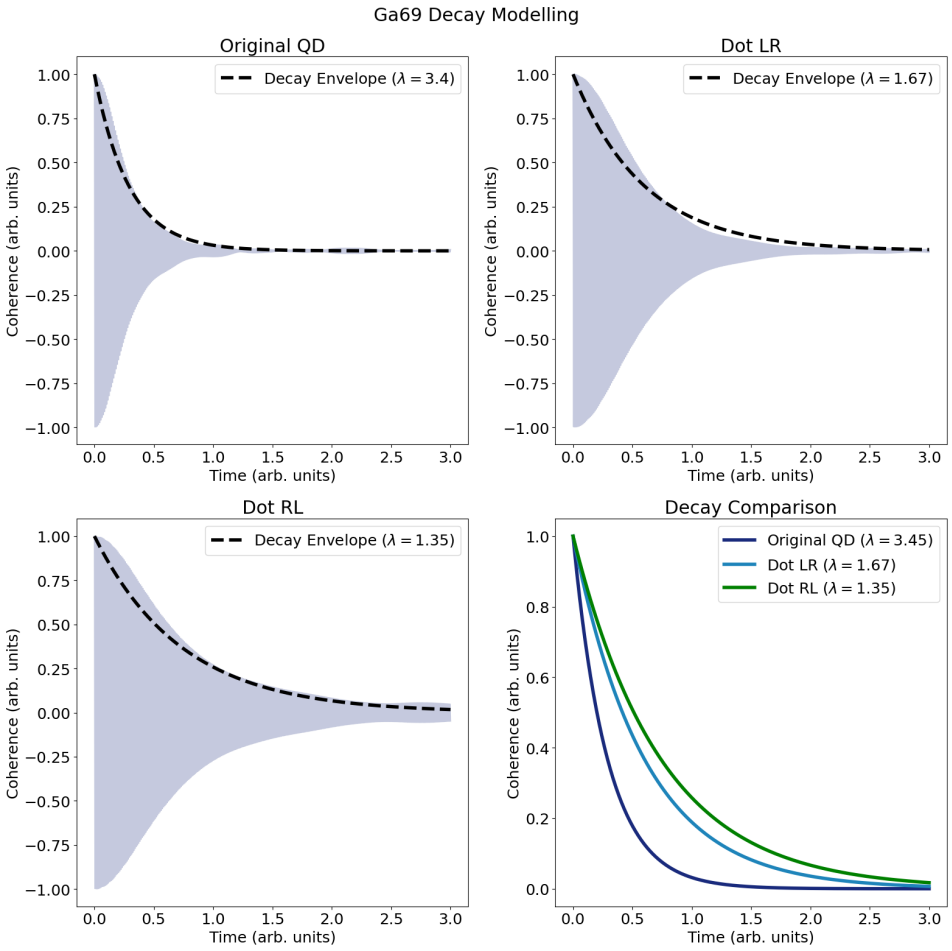

Figure 5.15: Modelling the decay of an electron exposed to the distribution of Ga69 nuclei within each of the quantum dot structures we have introduced. Coherence and time are both measured in arbitrary units, as we are only interested in the comparison between decay rates - not in calculating expected coherence times. The decay envelopes are found using a least squares estimation. We see that both mirrored dots have slower decay envelopes (and hence longer coherence times) than the original dot structure, as would be expected from the dramatic reduction in the variance of the quadrupolar field for Ga69 nuclei in those structures.

	σ^2	λ	τ_c	$\frac{\sigma^2}{\sigma_0^2}$	$\frac{\tau_c}{\tau_{c,0}}$
Ga69 (QD)	0.69	3.46	0.29	-	-
Ga69 (LR)	0.14	1.70	0.59	0.20	2.03
Ga69 (RL)	0.13	1.40	0.71	0.19	2.47
^{71}Ga (QD)	0.09	1.27	0.79	-	-
^{71}Ga (LR)	0.08	1.29	0.78	0.89	0.98
^{71}Ga (RL)	0.07	1.14	0.88	0.78	1.11
^{75}As (QD)	0.92	4.19	0.24	-	-
^{75}As (LR)	0.86	4.07	0.25	0.93	1.03
^{75}As (RL)	0.84	3.87	0.26	0.91	1.08
^{115}In (QD)	0.11	1.37	0.73	-	-
^{115}In (LR)	0.10	1.33	0.75	0.91	1.03
^{115}In (RL)	0.09	1.13	0.88	0.82	1.21

Table 5.2: Data found via the fitting to the results of our toy model of electron spin coherence. The data generally follow our expectation that a decrease in variance of the quadrupolar frequency (as seen in Column 4 of this table) results in an increase in expected electron coherence time (in Column 5). However, this correspondence is not 1:1.

This model supports our expectation that reducing the variance of the quadrupolar frequency distribution across an InGaAs quantum dot increases the coherence time of an electron within the dot. In almost all cases we demonstrate that reducing the variance of the distribution by making the underlying structure more symmetrical has a noticeable impact on the coherence time. Dot LR consistently underperforms Dot RL according to the relative increase in coherence time, in agreement with the results of Section 5.2.4 in which we showed that Dot RL has a narrower distribution of quadrupolar frequencies. The indium concentration maps shown in Figures 5.1 & 5.2 show us that Dot RL is visually more symmetric as well - lacking the outward bulge seen in the original structure and hence replicated in Dot LR. Unfortunately we do not have enough data, nor is our model suitably physical, to properly calculate the relationship between the change in variance and the change in coherence time. However, we do not expect it to be 1:1 based on these results and suggest this as a possible extension to this section of the work.

5.4 Conclusions

In this chapter we have investigated the effect of an artificial increase in symmetry on the characteristics of an InGaAs quantum dot. We have done this by taking the data defining the structure first seen in Chapter 4 and mirroring it along the central axis of the quantum dot. This ‘creates’ 2 more structures with an artificially high degree of lateral symmetry - Dots LR and RL. By applying the same techniques as introduced in Chapter 4 we investigate the strain profiles, electric field gradients, quadrupolar frequency distributions and the expected results of NMR spectroscopy of these fabricated structures.

We show that this increase in symmetry results in a decrease in the variance of the quadrupolar frequency distribution across all nuclear species present in the quantum dots, though the effect is most pronounced for Ga69, which exhibits a 5-fold decrease in this variance. Both ^{71}Ga and ^{115}In exhibit a very small change, which we attribute to their already incredibly narrow distributions of quadrupolar frequency. We treat the results for these 2 species with a grain of salt, as the calculations rely on data from 1974, for which more modern values are not yet available but sorely needed (as seen in Chapter 4). The simulated NMR results are examined in the context of assessing suitability for using the dot in question as a quantum memory - based on either magnons or a spin subset. Our results in this section are less heartening. We find that while artificially increasing the symmetry of a dot does substantially change the NMR spectrum, it does not do so in a particularly consistent way and not to the degree necessary to enable such a dot to function as a memory of a type it was not already suited for. In particular, we agree with previous results that suggest that InGaAs quantum dots may never be appropriate for use as a magnon based quantum memory, due in large part to the wide variance of the quadrupolar frequency distribution within them. Spin subset based quantum dots may fare better, though we note that our results suggest that careful choice of which magnetic field direction is best will be necessary to best isolate a particular set of transitions within the ensemble.

We finally introduce a simple toy model to begin to capture the effect of decreasing variance on electron coherence time. By modelling a central electron as a collection of cosine waves whose frequencies are drawn form a gamma distribution representing the quadrupolar spin bath, we show that decreasing the variance of this distribution can increase the coherence time by up to 147%. However, in most cases an increase in symmetry does not have this substantial an impact, and it may well be the case that growing a strain free dot results in larger benefits. This model does not capture the complex dynamics and behaviour of an electron in a quantum dot, but serves as a useful benchmark against which to check our intuition. Though we have kept our analysis tied to the data we have, the introduction of arbitrary frequency distributions may be useful to further investigate the relationship between nuclear quadrupole frequency variance and electron spin coherence time.

CHAPTER 6

NUCLEAR SPIN MEMORIES

In Chapters 4 & 5 we briefly investigated how useful the Sokolov and mirrored dots would be as quantum memories. In this chapter we will deepen this investigation by simulating the impact of RF pulses on absorption spectra. Following on from the results discussed in these previous chapters, we will focus on single spin quantum memories as it is plain to see from the experimental NMR spectra previously presented that a magnon type memory is unlikely to succeed with a strain based quantum dot - a result born out by recent experimental work into these memories [194, 195, 204, 205].

6.1 Quantum Memories

A quantum memory is a device into which we can write a quantum state, and later retrieve that state with a high degree of fidelity. Quantum dots have been put forward as a leading candidate for such memories due to their long coherence times - ranging into the milliseconds in some experiments [197, 198]. As we have previously seen, there are 2 candidate methods for the implementation of this in quantum dots: magnon based memories and single spin memories. Below we give a brief introduction to each, along with the requirements they impose on the host quantum dot. We will then extend the qualitative analysis of previous chapters by simulating the effect of an RF pulse on our quantum dot system. This analysis is not intended to be a full-scale simulation of a possible experiment, but more to investigate the feasibility of such control in an ideal case. While we discuss the experimental practicality, it was not the focus of this work to design or simulate a working nuclear spin memory experiment.

6.1.1 Magnon Memories

Though magnons are a phenomenon more commonly associated with the study of crystal lattices, it has become common to borrow the terminology to describe the collective behaviour of nuclear spin waves in a quantum dot. Therefore, when we use the term magnon we are discussing an excitation of the entire spin bath (or at least a very large subset of it). Work by Denning *et al* [195] has shown that it is in principle possible to use the electron spin as an intermediary to write the quantum state of a photon onto the nuclear spin bath. This process requires that the nuclear spin bath be as homogeneous as possible. Intuitively, we can understand this by considering a perfectly homogeneous spin bath to be a single very large spin which can then interact with the central electron via the hyperfine interaction as would any other individual nuclear spin. As the bath becomes less homogeneous this approximation breaks down and each nucleus in the bath interacts with the electron slightly differently. This results in both the reading and writing processes of the memory having a significantly reduced fidelity and eventually the memory is no longer able to read or write a quantum state at all.

The requirements on a quantum dot to be useful as a magnon based memory are then chiefly that the nuclear spins be as homogeneous as possible. We therefore presume (and our presumption is supported by the NMR spectra seen in Chapter 4) that a strain based dot such as those studied in this thesis is unlikely to be suitable for this type of memory. This is because the variation in strain across such a dot results in a large variation of nuclear energy levels. We have seen this manifest in both the original structure (see Section 4.3 and the 2 artificially mirrored structures (see Section 5.2.5). In neither case could we see that the NMR spectra was narrow enough to reasonably expect the nuclear spin bath to be homogeneous. This is further supported by the work of Denning *et al* in which they show that their protocol can tolerate quadrupolar frequency distribution widths of approximately 50 kHz - far lower than the MHz width distributions we have found in Sections 4.2.3 & 5.2.4. Therefore, we will instead focus our quantitative analysis on single spin memories.

6.1.2 Single Spin Memories

A single spin memory works along much the same lines as a magnon based memory, but replaces the collective spin excitation with that of a single, well isolated, spin. A protocol for such an experiment was put forward by Hinchliff [61] in which a photon state is mapped onto a central electron and then a $\sqrt{\text{SWAP}}$ gate is used to write the electron spin onto a single nucleus. The electron-nuclear system can then be disentangled and the photon's initial state is then stored on the nucleus until readout. Readout itself is performed via a quantum non-demolition measurement[1] using an ancillary polarised photon. The different polarisation components of this photon experience a different phase shift depending on the electron spin state (which is itself

[1] For more detail on these, please see [206, 207].

entangled with the nuclear spin state) - from this we can then use a single photon detector to read the photon spin state and hence the nuclear spin state[2].

This protocol is designed for a system in which the electron spin only interacts with a single nuclear spin, and also assumes a symmetric strain environment (to ensure there is no mixing between ground states of the nuclear spin state [208]). Obviously this is not well suited to our quantum dots with their variable strain distribution. However, we can see from the full NMR spectra presented in Figures 4.24, 5.12 & 5.14 there are distinct sets of transitions which may be the result of a small isolated set of nuclei that are very self-similar. If such a subset exists, we can think of it as working essentially like a small magnon style memory within the greater nuclear spin bath. Here we assess whether or not we can find such a small subset by investigating the available transitions more closely. We therefore will refer to this type of memory as a spin-subset type.

6.2 Dot Analysis

In previous chapters we have presented results such as Figures 4.24, 5.12 & 5.14. These give a good initial picture of the transitions within a quantum dot, but are time consuming to create at high enough resolution to use as the basis for identifying specific sets of transitions which may be useful for a spin-subset type memory. The first step is to identify which field orientation is best for our use case. From there we need to identify the best experimental parameters for a memory. These include the strength of the applied magnetic field, the number of nuclei we wish to include in our simulation and the relative amplitude of the RF pulse.

6.2.1 Simulation Parameters

First, we try to identify the better of the magnetic field orientations for the observation of an isolated set of nuclear transitions. Ideally, we would find that the Voigt orientation sees such a set of transitions as it is the required orientation to perform fast electron spin rotations. In Figures 6.1 & 6.2 we plot the absorption spectra of a single ^{115}In nucleus in a 3T magnetic field applied in the Faraday and Voigt orientations respectively. In both cases we see isolated peaks corresponding to the transitions present in an indium nucleus. We scan over a frequency range of 0-150 MHz with a resolution of 100 kHz. These spectra are calculated using Eq. 4.15, which we state again below for ease of reading. The Hamiltonian $\hat{H}_{rf}$ contains a parameter γ which defines the amplitude of the pulse. For these simulations we set $\gamma = 0.005$, the same value as used in previous chapters.

$$W_{ij}(\omega_r f) = |\langle j|\hat{H}'_{rf}|i\rangle|^2 \frac{\frac{2\Delta}{\hbar}}{(E_j - E_i - \hbar\omega_{rf})^2 + \Delta^2}. \tag{6.1}$$

[2]A full description of this protocol, with accompanying mathematics can be found in Chapter 4 of [61].

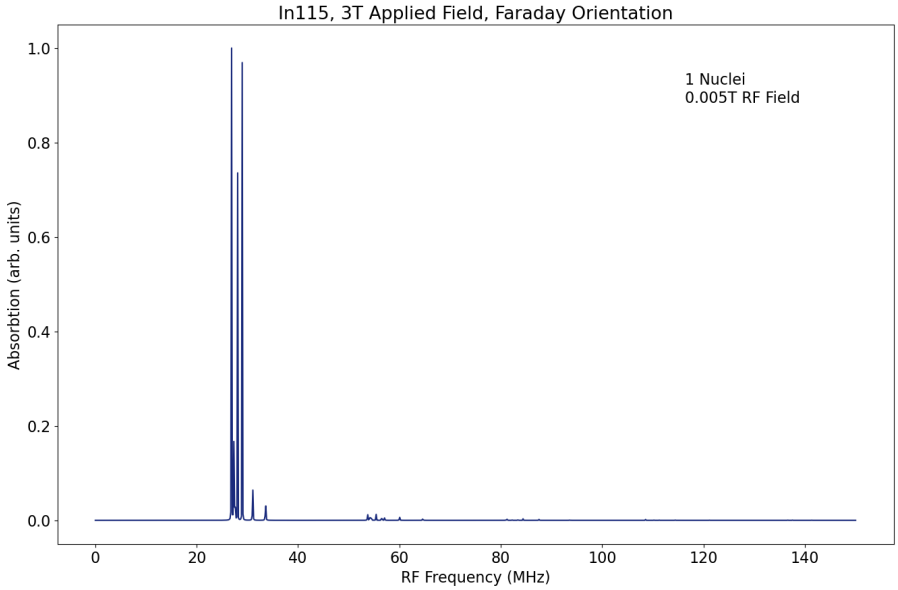

Figure 6.1: The NMR absorption spectrum of a single ^{115}In nucleus in Faraday geometry. The y-axis is presented in arbitrary units, scaled to the highest absorption peak. The simulation uses an applied field of 3T, and an RF-field strength of 0.005T - though we shall later show that this value does not affect the overall behaviour. We see a large cluster of peaks between 20-40 MHz, a smaller cluster at 50-60 MHz and a small isolated peak at approximately 80 MHz.

The absorption described by Eq. 6.1 is the simplest way of modelling the absorption rate. A more complete method is via the Optical Bloch Equations, which describe the coupling between a 2-level quantum system and an electromagnetic field. The simulation we describe here is meant only as a first-look approximation, and thus we do not believe bringing the full force of these equations to bear is necessary for our discussion. Implementation of these interactions would be an excellent extension of this work. In particular, the behaviour of a π pulse under the action of these equations may well be different than that discussed using the method presented here.

In both orientations we see a large collection of peaks between RF values of 20-40 MHz, with other peaks appearing at approximately 60 and 80 MHz. Other simulation runs extended to higher RF frequencies, but we did not find significant absorption peaks above 100 MHz and thus we present these simulations which run up to 150 MHz. The Faraday geometry has a larger peak at 60 MHz, which for our purposes presents a problem - we want whichever peak we use as a memory to be as isolated as possible and thus if we wish to use the peak at 80 MHz, the presence of a large peak at 60 MHz limits the bandwidth of our the excitation pulse as we do not want to excite that peak. For that reason, and bearing in mind the inherent advantages of the Voigt geometry we will ignore the Faraday orientation in the subsequent parameter search, concentrating only on the Voigt geometry.

Figures 6.1 & 6.2 show the absorption spectra of a single nucleus, chosen at random from all those points for which we have data within the quantum dot. In a real dot however, an incident

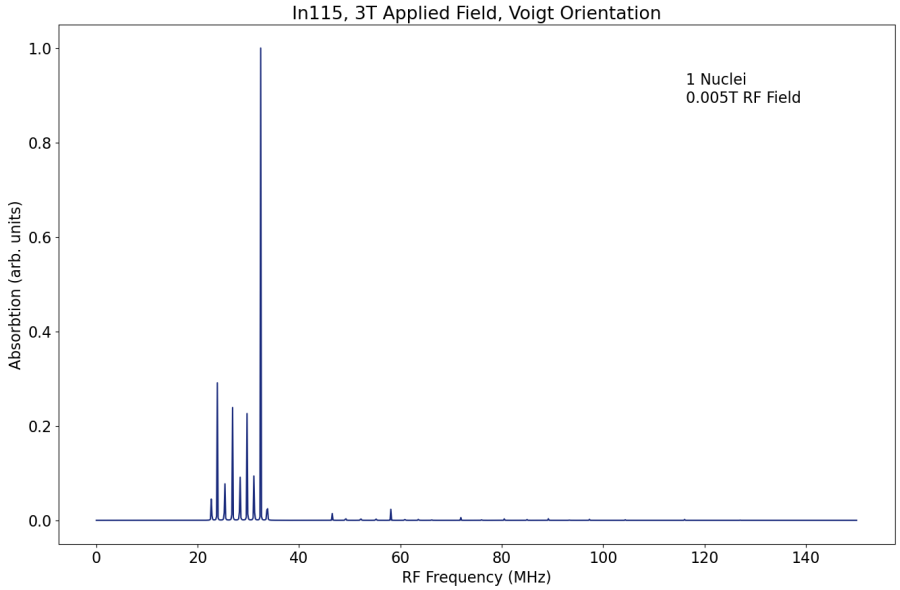

Figure 6.2: The NMR absorption spectrum of a single ^{115}In nucleus in Voigt geometry. The y-axis is presented in arbitrary units, scaled to the highest absorption peak. The simulation uses an applied field of 3T, and an RF-field strength of 0.005T - though we shall later show that this value does not affect the overall behaviour. We see a large cluster of peaks between 20-40 MHz, and small isolated peaks at approximately 60 and 80 MHz.

RF pulse would see the entire spin bath, consisting of the order 10^5 nuclei. Figure 6.3 shows the result of calculating the NMR spectrum for varying numbers of nuclei within the quantum dot. When multiple nuclei are included we select them randomly from the central region of the quantum dot, and for the larger numbers of nuclei (10,000 or more) we are likely to select the same data point multiple times. The computation time required for larger numbers of nuclei scales approximately linearly with the number required, though due to the parallel nature of the simulation code there is some small overhead which makes up a larger percentage of overall run time for smaller numbers of nuclei. The data presented here for 10,000 nuclei required upwards of 5 hours of computational time on a modern desktop. The most significant change that occurs as we add additional nuclei is a broadening of the absorption peaks that we first identified in the previous section. We also see an increase in the overall strength of the absorption, though the units of this remain arbitrary. The difference between simulations of 1000 and 10,000 nuclei is not substantial - we observe peaks of approximately the same width centred on the same location in both cases. However, the computational cost is significantly lower and we avoid the problem of sampling the same data point multiple times. Therefore we use simulations of approximately 1000 nuclei for the remainder of this chapter[3]

We now investigate the effect of varying magnetic field on the absorption spectrum. We

[3]We actually use 1200 nuclei in most of these simulations, as it is a round number that is cleanly divisible by both 6 and 8 - the number of cores in the 2 computers used to perform all our simulations.

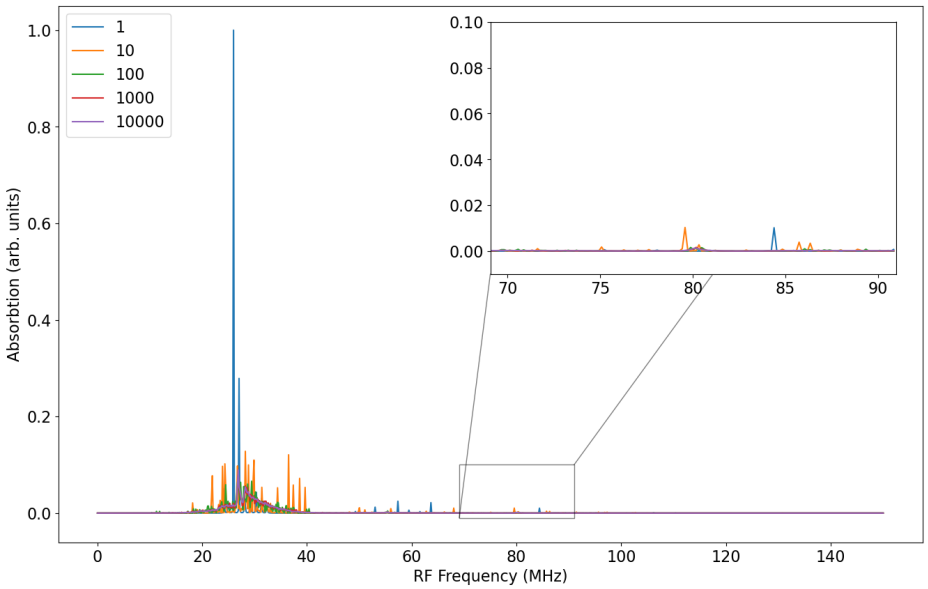

Figure 6.3: The effect of varying the number of nuclei present in the simulation on the resulting absorption spectrum for ^{115}In nuclei in a Voigt orientated magnetic field. We see the same peaks as are present in Figure. 6.2, though each has widened from a single line to a distribution, and hence lowered in height as all distributions are normalised to the same area. Larger numbers of nuclei dramatically increase the computational time required to run these simulations.

have seen in previous chapters that higher magnetic fields are associated with the absorption spectra becoming dominated by magnetic field splitting rather than quadrupolar effects. In these parameter finding simulations we are only considering indium nuclei, which are the only nuclei with transitions at higher RF frequencies until impractically large applied magnetic fields. In Figure. 6.4 we plot the absorption spectra of 1200 indium nuclei for an increasing set of applied magnetic fields in Voigt geometry. We see that there is a general trend for significant peaks to move towards higher RF frequencies as the applied field increases. This trend continues as fields increase, with no significant variation until we apply fields that are substantially too large to be practical for an experiment.

The governing Hamiltonian for the RF interaction is

$$\hat{H}_{\mathrm{rf}} = -\hbar\gamma\left(B_x^{rf}\hat{I}_x + B_y^{rf}\hat{I}_y + B_z^{rf}\hat{I}_z\right)\cos(\omega_{rf}t), \tag{6.2}$$

where the parameter γ represents the interaction strength between the RF pulse and the nuclear spin. Our model does not model pulses in any detail beyond this, concentrating as we are on nuclear spin physics. However, in Figure 6.5 we plot the change in absorption spectra with changing γ. As might be expected from the Hamiltonian and the rate equation (Eq. 4.15), increasing γ has the effect of increasing the absorption - as a direct result of increasing the interaction probability. Because we do not model pulse physics accurately, this is the only direct effect. The spectrum appears to widen in Figure 6.5 but this in an artefact of all of the peaks

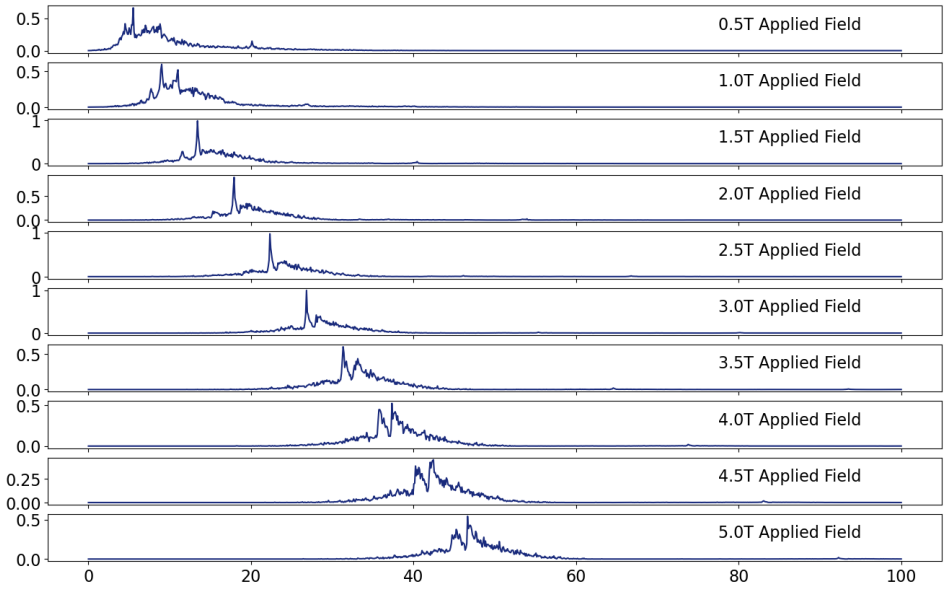

Figure 6.4: The effect of increasing the strength of the applied magnetic field on the absorption spectra of 1200 ^{115}In nuclei in a Voigt field. The general structure matches that seen in Figure 4.24 - at higher field strengths the absorption shifts to higher RF frequencies. We limit ourselves to fields of up to 5T as larger fields become experimentally more difficult and do not substantially change the behaviour of the system.

being normalised to the same height and not a real physical effect. As such, we keep the value $\gamma = 0.005$ throughout our simulations, primarily because it is the same value used in our previous chapters and in other works [169].

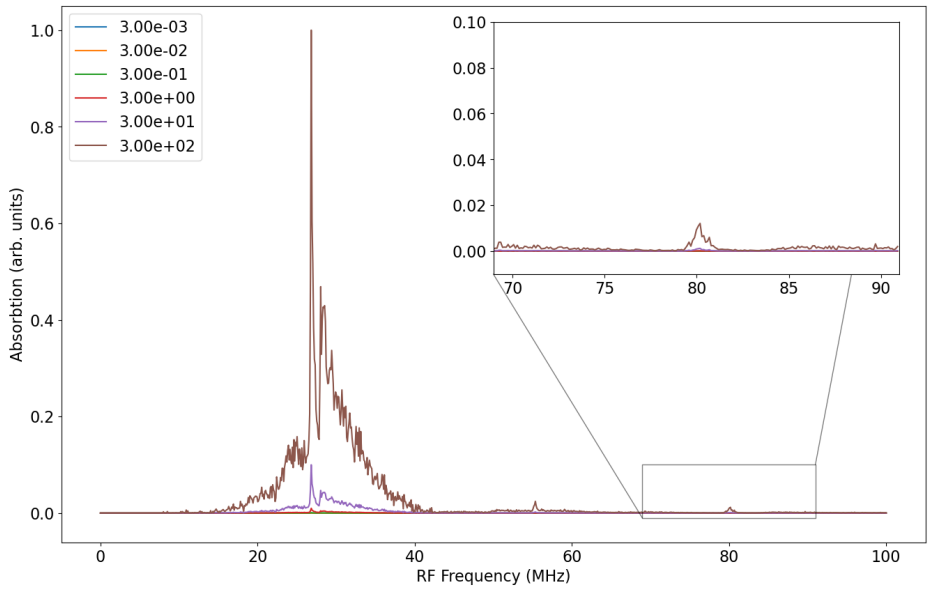

Figure 6.5: The effect of increasing the value of the RF field strength γ (as defined in Eq. 4.14). While there is an increase in the overall height of the peaks as γ increases, there is no substantial change to the shape of the spectrum, and thus we choose to keep $\gamma = 0.005$ T constant throughout all other simulations.

6.2.2 Applying a Pulse

Now that we have found a set of simulation parameters that are both experimentally reasonable and somewhat optimal for observing the absorption lines that we require to use the dot as a quantum memory. We now move to simulate the effect of an RF pulse on these spectra. Fast and highly specific pulses are a necessary component of the quantum memories described earlier. A simple way to think about the initialisation of a spin-subset quantum memory is that we are attempting to apply a π pulse to a small subset of transitions while leaving the others alone. This highlights the need for isolation we have discussed in the previous section - if the target transitions are not well isolated from the rest of the bath then an applied pulse will rotate other nuclei in addition to the target set. These other nuclei will be rotated by some amount proportional to how much of a full π pulse they have received, which is itself related to the energy absorbed by that region of the spectra.

In Figure 6.6 we show the total line spectra for a RF pulses between 0-150 MHz, for a field of 3T, for 1200 nuclei allocated proportionally according to the nuclear concentrations we first presented in Figure 4.5. The addition of ^{69}Ga, ^{71}Ga and ^{75}As has resulted in a widening of the largest peak to RF values between 20-40 MHz. There is also an additional spike in this range at almost exactly 40 MHz, this is due to the presence of ^{75}As specifically. The smaller peaks at larger RF values are the best candidates - the further they are from the large peak the better. We use a simple peak finding algorithm to identify the exact locations of these peaks, and find

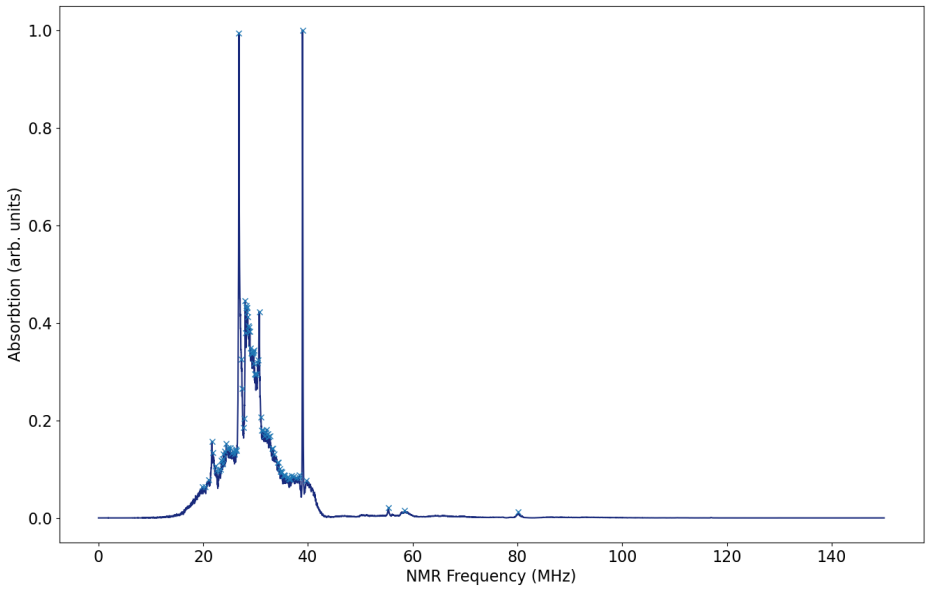

Figure 6.6: Simulation of an NMR experiment on the original Sokolov quantum dot discussed in Chapter 4. We use a simple peak finding algorithm (as implemented in Scipy) to find the exact location of each absorption peak. The likely best candidate for use as a memory is found to be at an RF frequency of 80.2 MHz.

that the best candidate is found at $f_{\mathrm{RF}} = 80.2$ MHz. We therefore centre our applied pulse on this frequency.

Electromagnetic pulses are most often modelled by Lorentzian distributions of the form

$$P(f) = \frac{1}{\pi} \frac{\frac{1}{2}\Gamma}{(f - f_0)^2 + (\frac{1}{2}\Gamma)^2}, \tag{6.3}$$

where f_0 is the location of the pulse and Γ specifies the width of the distribution [209]. We know that our pulses need to be centred on $f_0 = 80.2$ MHz, but the width still needs to be found. In general, the optimal pulse will be as wide as possible such that the operations it performs on the quantum dot happen as quickly as possible. However, a wider pulse will be absorbed by more transitions than we want it to be. If we make the pulse too wide, we will start to see the transitions that make up the large peak at 20-40 MHz. In addition, there is a minimum width required to capture the entirety of the absorption peak. Figure 6.8 shows that this peak extends over the range $77.5 - 82.5$ MHz, and therefore we require a sufficiently wide pulse to capture this peak entirely.

In principle it is possible to craft a pulse or series of pulses to exactly perform a desired operation. This field of research is known as optimal control theory, an introduction to which can be found in the works of Khaneja and Palao [210–212]. Were we aiming to design an experiment completely it would absolutely be necessary to incorporate that work into this simulation. However, the complexity of that field does not well suit the simplicity of a model

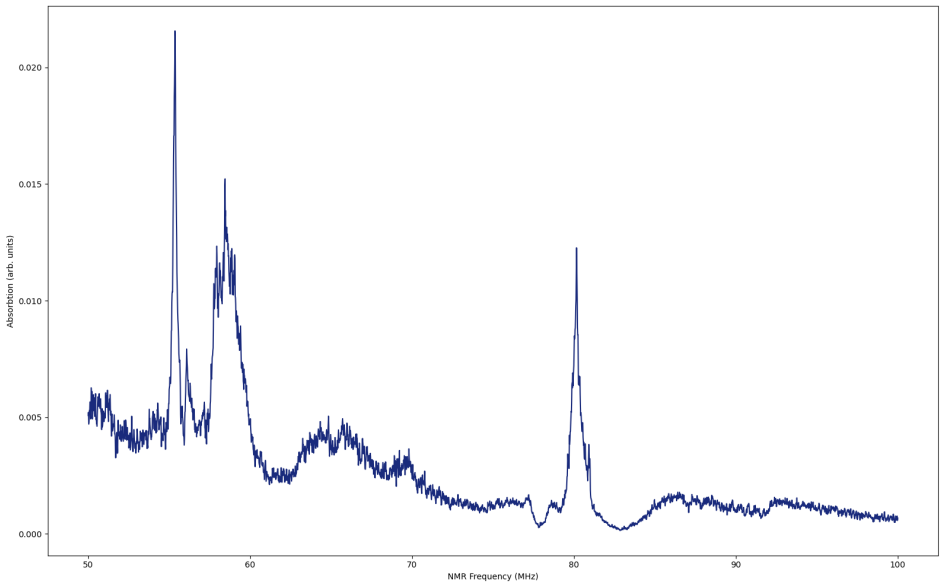

Figure 6.7: The smaller peaks found in the combined NMR spectrum at 3 T. We can see that what appeared in 6.6 to be a single peak at approximately 60 MHz is in fact 2 smaller peaks. These are not suitable for use as a memory even though they are of a larger area because of both this split and the proximity to the substantially larger peaks found between 20-40 MHz. We therefore centre our applied pulse at the frequency of 80.2 MHz.

such as the one presented here, and hence we neglect it in favour of the simpler application of a Lorentzian pulse. It is also worth noting that while a Lorentzian is the standard assumed shape of an incident electromagnetic pulse, other distributions can well be applied. A Gaussian pulse for example has smaller tails than an equivalently defined Lorentzian and may well be more suitable for the purposes discussed here.

In Figure 6.9 we plot the effect of pulses of increasing width on the absorption spectra shown in Figure 6.6. These effect of a pulse on the spectrum is found by applying a Lorentzian filter to the spectrum, which was generated by uniformly exciting each transition. In the leftmost plot we apply an incredibly narrow pulse that picks up only the absorption at exactly 80.2 MHz. We then expand the width of the pulse in 1 MHz steps and very quickly observe the presence of the 20-40 MHz peak due to it's large height relative to the 80.2 MHz peak. Applying a peak of width 9 MHz (80.2 ± 4.5 MHz) is sufficient that the absorption from this large peak is of equal height to that of the target peak. However, the height of a peak in this graph is not the best measure of the number of nuclear transitions, instead we must calculate the area under each peak. This is proportional to the energy absorbed by the nuclei and hence functions as an approximate measure of the fidelity of our access to the memory.

The speed at which we can apply operations is critical for any application of quantum dots. Given an optimistic lifetime measured in milliseconds, we must be able to perform operations on a timescale of at most 100s of nanoseconds. We therefore require a distribution of width at

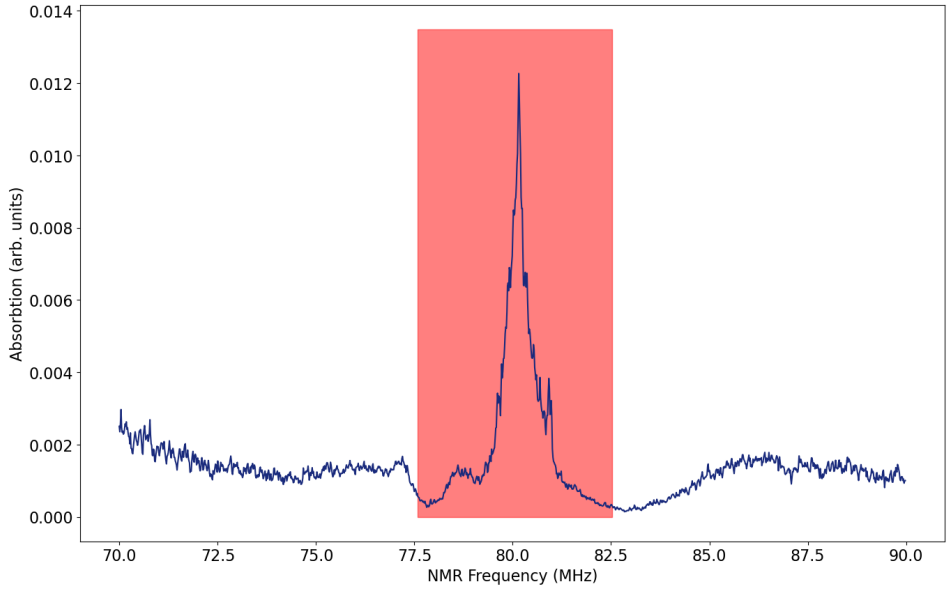

Figure 6.8: The peak we are targeting with our pulse is highlighted in red. We can see that in order to fully capture the peak our pulse must be approximately uniform over the region 77.5 – 82.5 MHz.

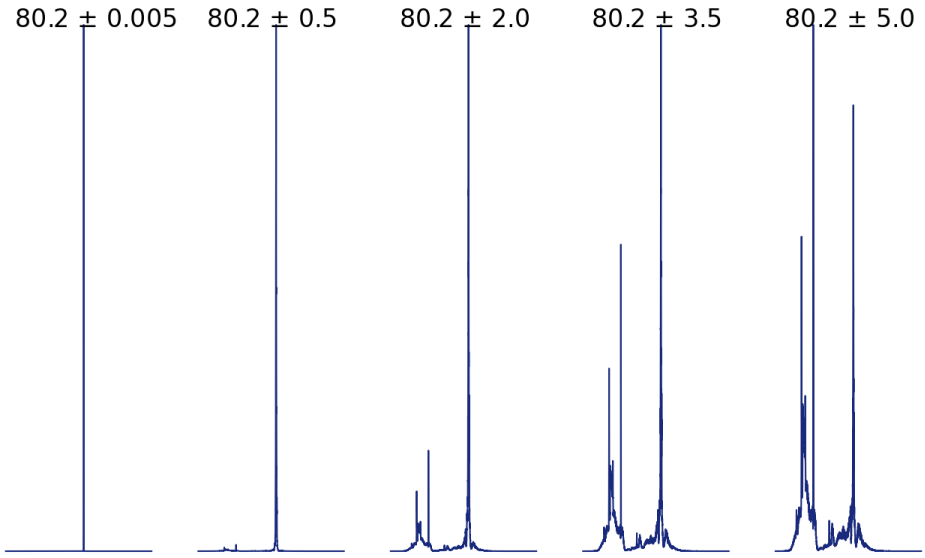

Figure 6.9: A comparison of the effect of applying pulses of different widths on the spectrum shown in Figure. 6.6. Each peak is a Lorentzian centred on 80.2 MHz, with widths increasing from left to right. At arbitrarily small widths we see only the peak the distribution is centred on, and as the width increases we begin to observe the far larger peaks seen between 20-40 MHz. At widths of approximately ±4.5 MHz these peaks are equivalent in height, and the 80.2 MHz peak is lower in height than the 20-40 MHz peak when the applied pulse is wider than this.

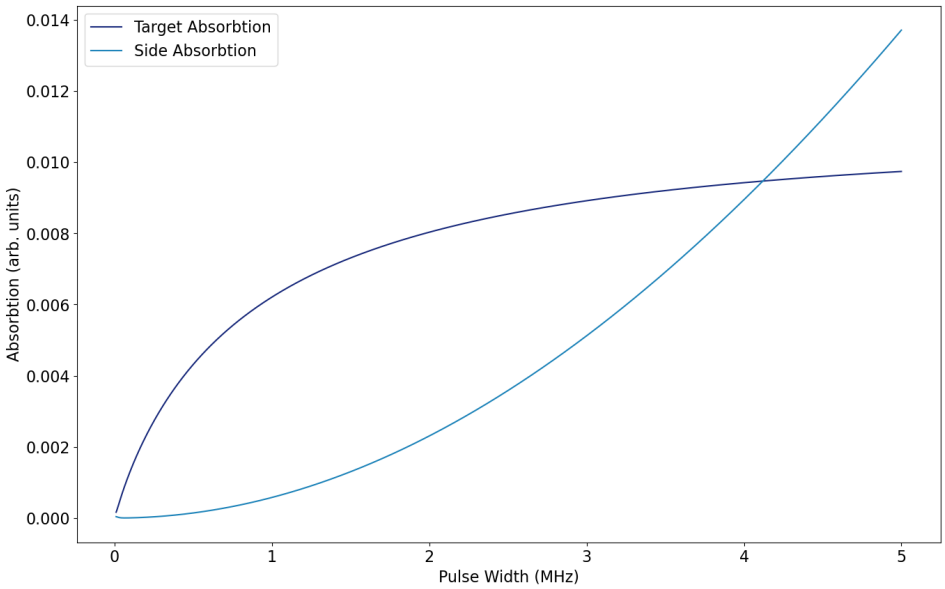

Figure 6.10: The absorption (in arbitrary units) in the target region (78.5-82.5 MHz) is show in dark blue, and the absorption into the rest of the transitions is show in light blue. We can see that at low pulse widths ($\Gamma < 1.5$ MHz) the absorption is dominated by the target transitions. However, as Γ increases absorption into the rest of the spectrum begins to dominate.

least $\frac{1}{100\text{ns}} = 10$MHz. Our other conditions on the pulse are that it must be wide enough such that transitions in the target frequency range (approximately 78.5-82.5 MHz) are excited with as close to uniform intensity as possible - these are the spins we wish to apply a full π pulse to. Both of these conditions essentially impose a lower bound on pulse width (Γ) that we must meet. An upper bound is imposed by the requirement that we not substantially excite other transitions, so as to minimise the spin flips generated in other regions of the spin bath. Figure 6.10 shows the absorption into the target region of the spectrum compared with those transitions we do not wish to excite. This graph suggests that we cannot apply a pulse with $\Gamma = 10$ MHz as we can see that pulses with $\Gamma > 4$ MHz are already absorbed predominantly by transitions outside of the target region. However, we note that absorption into the target region begins to level off when $\Gamma > 3$ MHz, suggesting this as a plausible lower bound to satisfy the second of our minimum width criteria.

The flattening off of the absorption into the target region (and hence the saturation of these transitions) is in stark contrast to the behaviour of the absorption into the rest of the spectrum. This is because the rest of the spectrum contains far more transitions than the small region we are trying to excite, and thus can absorb significantly more energy. In fact, the peak at the target region comprises less than 1% of the total area of the spectrum. This plays to our advantage - it takes a lot more energy to perform a π pulse on the rest of the spectrum than it does on the target region. To highlight the impact of this, we plot in Figure 6.11 the same data as presented

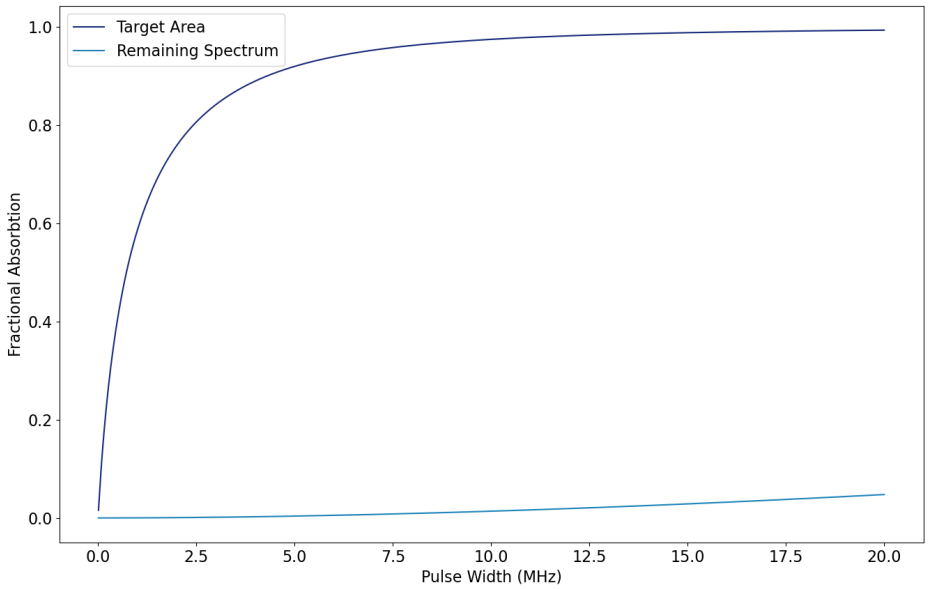

Figure 6.11: The energy absorbed by the target region of the spectrum is shown in dark blue, and that of the remainder of the spectrum is shown in light blue. Each are scaled to the areas of the respective spectral regions before any pulse is applied. A fractional absorption value of 1 indicates that a particular set of transitions has absorbed as much energy as possible, and hence felt the full effect of whatever pulse is applied to it.

in Figure 6.10, now scaled to the respective areas of each region of the spectrum before a pulse is applied. In this plot we can clearly see that the target region is saturated quickly in comparison to the rest of the spectrum. When the transitions in the target region are saturated, we are guaranteed to have performed the operation we are attempting - for example a π pulse. The rest of the transitions meanwhile will have experienced some fraction of the effects of the pulse dependent on the energy absorbed. Figure 6.11 therefore suggests we can increase the pulse width substantially beyond 10 MHz before running the risk of significantly altering the state of the rest of the spin bath. However, this analysis fails to capture a vitally important feature of the spectrum as a whole, one we have been relying on implicitly throughout this section. Different transitions are not located uniformly throughout the spectrum, and therefore the pulse is not split evenly amongst them. We are taking advantage of this to apply a pulse only to the target region, but we cannot ignore the variations in absorption that will be present in the rest of the spectrum.

The full spectrum (as seen in Figure 6.6) shows us there are 2 significant sets of transitions we do not wish to excite - a very broad set of peaks between 20-40 MHz, and a much smaller set spanning 50-70 MHz. In Figure 6.12 we plot the fractional absorption for each of these peaks as compared to the target region. As expected, we see that the target region is saturated first, but even as we increase the width of the applied pulse to 20 MHz, the set of transitions between 50-70 MHz are only absorbing up to 20% of the energy required for a perfect operation, while

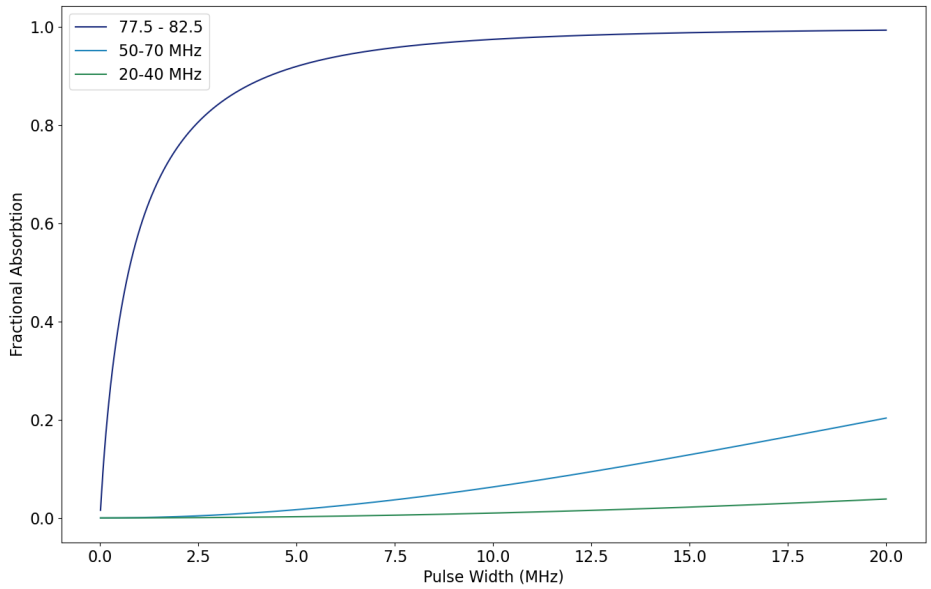

Figure 6.12: The fractional absorption into distinct regions of the spectrum. The target region of 77.5-82.5 MHz is shown in dark blue, the 50-70 MHz transition set is shown in light blue, and the 20-40 MHz set in green.

the set between 20-40 MHz remain substantially lower than this throughout. These results are sufficient to say that a pulse with $\Gamma = 10$ MHz is plausibly wide enough to saturate the target transitions, while remaining narrow enough to not have a substantial action on other transitions to cause them to have a high chance of ruining a subset-style quantum memory protocol.

Setting $\Gamma = 10$ MHz should allow an experiment to perform a π pulse with a timescale of ≈ 100 ns. This is the minimum necessary time to allow us to perform the multiple operations needed for a quantum memory protocol. In the ideal case, wider pulses would be used on quantum dots possessing longer coherence times. We have not attempted to simulate the effect of the exact pulse sequence needed to run the protocols discussed in Section 6.1.1, as this goes beyond the scope of the programme we have written. We also do not discuss or simulate the effect of pulse sequences designed to narrow the range of excited transitions for a given pulse width, or those (like the Hahn echo) designed to undo the effects of decoherence in a particular part of the spin bath. We intend this work to be a study of the plausibility of spin-subset type memories in strain based dots, rather than a complete description of a protocol[4].

6.2.2.1 Experimental Feasibility

The simulation discussed above pays very little attention to the experimental feasibility of the required pulses. While we believe that is appropriate for a theoretically lead discussion, it would be remiss to avoid the implications of what we have discussed entirely. Our simulations have

[4]Such a protocol is left as an exercise to the reader.

suggested that a pulse of width 10MHz would be required. Such a pulse obviously has a lifetime of approximately 10ns. A back of the envelope calculation of the power required to generate such a pulse uses the relationship $E_f = \mu_N B$, where E_f is the pulse energy in frequency units, and μ_N is the nuclear magneton, which has a value of 7.6 MHz T^{-1} [101]. Plugging in a pulse frequency of approximately 80 MHz results in a required magnetic field of approximately 11T. This is a large, but not yet ridiculous, magnetic field. However, this field must be reached in less than 10ns, resulting in a required magnetic flux of approximately 10^9 T s^{-1}. This is an extremely large rate of change of magnetic field, and would present a significant experimental challenge to implement. So much so that it may well be impossible[5].

6.3 Conclusions

We have shown in this chapter that the quantum dot we have studied may plausibly be used to construct a spin-subset type quantum memory. Through simulation of the NMR spectra under a variety of possible experimental configurations - as first presented in previous chapters, we have identified a set of nuclear spin transitions that are suitably well isolated. We have then simulated the action of an incident π pulse on this structure, having identified the peak location exactly. The effect of varying pulse width on the resulting excitation was examined, and we determined that a lower bound of 10 MHz is the minimum required width to allow for the successful action of a π pulse on our target set of transitions. We investigated the impact of such a pulse on the entire set of transitions present in the spectrum, and determined that such a pulse would not have too large an impact on the rest of the bath to render the spin-subset style memory implausible. The practical requirements of the experiment are likely to need closer examination. The next steps in this work might be to examine the impact of a specific set of pulses on the nuclear spin bath. The simulation code developed for this project could prove invaluable, as it is capable of quickly simulating both the NMR spectrum of large numbers of nuclei based on experimental data, and the action of RF pulses on the spin bath. It can be quickly updated to include new measurements of GET values, and is easily extendable to other quantum dots beside InGaAs. Given only strain and concentration data, we may be able to design RF pulses or pulse sequences that are specific to a particular structure.

[5]By now we hope it is clear that the author are not an experimental physicist.

CHAPTER 7

CONCLUSIONS AND FURTHER WORK

In this thesis we have first introduced quantum dots as a field of study, and provided a brief motivation for their use in various quantum technologies - specifically measurement based quantum computation and the creation of quantum memories. We outline the mechanisms of both of these technologies, and show where and how quantum dots may be of use. We also provide an introduction to the methods of fabrication for InGaAs quantum dots via Stranski–Krastanov growth, and show how this strain based fabrication method goes on to influence the properties and behaviour of the dot across multiple use cases. In Chapter 2 we discuss the physics of electrons in quantum dots. We examine the band structure, the emission of photons via the creation of excitons and the differences in energy level structure between Faraday and Voigt geometries. We move on to highlight various protocols that have been proposed to produce strings of entangled photons from a quantum dot, focussing on the cluster state machine gun. We discuss the theoretical operation of the machine gun, and highlight potential issues regarding the magnetic fields necessary to allow the required spin rotations to occur while still remaining measureable. Other entanglement schemes are also discussed, with a focus on how they mitigate the downsides of the machine gun or address the decoherence issues that are apparent in InGaAs quantum dot. In Chapter 3 we zoom in past the electron trapped in a quantum dot to examine the nuclei that make up the lattice. We see how the hyperfine interaction between an electron and a nucleus causes both relaxation and dephasing of the electron spin as it precesses around any relevant magnetic fields. The hyperfine interaction is derived from the Hamiltonian of an electron in a magnetic field, and we include all relevant mathematical steps to ensure ease of comprehension. The dephasing that arises as a result of the hyperfine interaction is modelled according to the frozen fluctuations approximation, in which the spin bath is assumed to evolve far slower than the precession frequency of the electron. It is in this section that we first discuss the

ideas that form the heart of this thesis. An electron will 'see' any field applied by an experiment, and an effective field resulting from its collective interaction with the nuclear spin bath. The longer this spin bath remains unchanged, and the smaller any changes in it are, the higher the ceiling on the coherence time of the electron. It is therefore vitally important to understand the mechanisms that cause changes in the collective state of the nuclear spin bath, so that the behaviour on an electron interacting with that bath might be better understood as a result. To this end we discuss dynamic nuclear polarisation and nuclear frequency focussing - mechanisms for preparing and maintaining a well behaved nuclear spin bath. Dynamic nuclear polarisation is an observed effect allowing for the transfer of spin polarisation from a trapped electron to the spin bath, while nuclear frequency focussing is an experimental protocol which has been to designed to consistently inject electron angular momentum in such a way that we achieve a desired polarisation state of the nuclear spin bath via dynamic nuclear polarisation. We present a mathematical treatment of NFF which places requirements on the pulse used, and then introduce a simple form of dephasing to that formalism in order to understand how the protocol itself acts when exposed to a non-ideal environment. We find that even a small amount of such dephasing has a significant impact on the effectiveness of the protocol, which may go some way to explaining the limited experimental success it has found. In the second half of Chapter 3 we describe the nuclear quadrupolar interaction by deriving the interaction Hamiltonian from the interaction energy between 2 classical charges. We again present the derivation in its entirety so that the effect of the interaction can best be understood. Our attempts to understand the effect of this interaction on the behaviour of an InGaAs quantum dot form the basis of the results presented in Chapters 4 & 5.

Chapter 4 presents our work on understanding the gradient elastic tensor, and how recent experimental work to update the measured values of the tensor components necessitate a recalculation of the properties of an InGaAs quantum dot. We first present a toy model of strain across a 2-dimensional lattice, to ensure we have an intuitive understanding of how varying electric field gradients arise within a quantum dot. This toy model also provides an ideal testing ground for methods to calculate more complex properties of a quantum dot without requiring a more computationally intensive molecular simulation. We then detail the gradient elastic tensor, a phenomenological object which relates the lattice strain to the electric field gradient felt by nuclei within said lattice. We explain the simplifying assumptions we make regarding the symmetry of the lattice, and of the strain field for which we have data. The data we use was kindly provided by Paul Sokolov, and consists of indium concentration and strain field measurements across an InGaAs quantum dot. Using this data, we first replicate previously described plots showing the electric field gradient across the structure, before extending the analysis to include updated values of some components of the gradient elastic tensor. We compare the differences between the calculated values of a variety of observable quantities within the quantum dot: the electric field gradient, the resulting quadrupolar field (both its strength and its direction), the

distribution of possible quadrupolar transition frequencies and the nuclear magnetic resonance spectra. For all such quantities we find significant differences between them when calculated using the older (as found using nuclear acoustic resonance (NAR) spectroscopy) and newer (as found using nuclear magnetic resonance/photo-luminescence (NMR/PL) spectroscopy) values of the gradient elastic tensor. Most importantly, when separated by nuclear species we find that the changes in each property are inconsistent - for example the transition frequency distribution of ^{69}Ga nuclei becomes 3 times wider when found using the NMR/PL values, while that of ^{75}As narrows by a factor of 2.7. This highlights the need for further measurements to be conducted using the newer technique to ensure confidence in the values of these parameters for ^{71}Ga and, more importantly, ^{115}In . When examining the simulated NMR spectra, we also consider how this dot may be used as a quantum memory. We define 2 types of quantum memory - magnon and spin-subset, and discuss the necessary properties for each in order to determine the possible uses of this quantum dot. We find that in neither a Faraday nor a Voigt orientated field would it be plausible to use this dot as a magnon type memory, owing to the wide range and strong mixing of absorption lines seen in the spectra. However, the dot may be suitable for use as a spin-subset memory when in a Voigt orientated field where we see strongly absorbing yet isolated transitions between ^{115}In energy levels. We compare our calculated NMR results with those found using full molecular lattice simulations and find they produce very similar results while taking a fraction of the calculation time due to the inclusion of real strain data.

Chapter 5 investigates the effect of increasing the symmetry of the quantum dot studied in Chapter 4. We do this to test the following intuition: a more symmetric dot should contain a more self-similar set of nuclei, and hence these nuclei will produce an Overhauser field that is longer lasting and more stable - increasing the ceiling on the electron spin coherence time. Unfortunately, the COVID-19 pandemic put a stop to our efforts to gather more data from real quantum dots, and so we create 2 new structures from the data used in the previous chapter. By taking both our strain and indium concentration data, and reflecting the data arrays along the central axis we are able to generate 2 new structures which are physically plausible but by construction much more symmetric than the original from which they are derived. We refer to these structures as Dot LR (left-right reflected) and Dot RL (right-left reflected). We then use those tools introduced in Chapter 4 to analyse the impact of this increase in symmetry. As expected we find that for all species in both new dots there is a decrease in the width of the quadrupolar frequency distribution, though the magnitude of that decrease varies considerably. The already narrow distributions of ^{71}Ga and ^{115}In are barely affected (though of course these results rely on old values of the gradient elastic tensor and should therefore be treated with caution), while those of ^{75}As and ^{69}Ga are changed by a much larger amount. We introduce another toy model to investigate the impact that decreasing the width of these distributions has on the electron coherence time. Modelling the electron spin as a cosine wave, we mix in additional waves with frequencies drawn from the distributions we calculate in previous sections. The

resulting waveforms are well modelled by a cosine wave decaying within an exponential envelope. We calculate the decay constant of this envelope and hence the relative coherence time of the electron. By comparing the change in coherence time between different our 3 structures to the change in quadrupolar frequency variance we find that a decrease in variance corresponds to an increase in coherence time. Unfortunately we do not have enough data to meaningfully calculate this relationship, however we can say with some certainty that it is not a simple 1:1 ratio where reducing the variance by a certain factor increases the coherent time by the same amount. Large decreases in variance are needed to produce relatively small increases in coherence time. Finally, we refer to the calculated NMR spectra of Dots LR and RL to assess their suitability for use as either type of quantum memory. The results of this analysis are sadly similar to those of the base structure. Increasing the symmetry of the quantum dot does result in changes to the NMR spectra - in particular it narrows the spectra in almost all circumstances. However these changes are never significant enough to create the conditions necessary to use the dot as a magnon type memory - this agrees with previous work which suggests that a strain based quantum dot is unlikely to ever be suitable for use as this type of memory. There is more hope in the world of spin-subset memories, where we find that both new structures may be suitable, though in different orientations. We suggest that this type of memory is the better way to go when using an InGaAs (or any other strain based) quantum dot.

Chapter 6 addresses the possible uses of strain based dots as quantum memories in more detail. We further discuss the differences between magnon and spin-subset type quantum memories, with a particular focus on the requirements each places on the structure of a quantum dot. We first discount the possibility of a magnon type memory in a strain based quantum dot, based both on our own results showing that the spin bath is too varied across such dots (even if they are made arbitrarily more symmetric) and external experimental results on droplet epitaxy dots that have been published recently. We then quantitatively investigate the possibility of a spin-subset type memory (itself an extension of a single nuclear spin memory) by first searching for the ideal set of simulation parameters. Having found these, we apply Lorentzian pulses to our absorption spectra in an attempt to minimise the timescale of the operations needed to initialise or control a quantum memory. The width of these pulses have 2 separate constraints - the first is that a wider pulse results in faster optical operations and the second is that a narrower pulse results in absorption only into those nuclear transitions we have identified as suitable for a quantum memory. Analysis of these conditions allows us to suggest that a 10 MHz pulse is of sufficient width to ensure both saturation of the target transitions as well as providing an operational time of 100 ns - fast enough to allow for the multiple pulses necessary in the creation of a spin-subset memory within the coherence time of an InGaAs quantum dot. The effect of such a pulse on the rest of the nuclei is found to be small enough that they are likely to have little impact on the overall workings of such a memory.

This most obvious expansion of this work is to perform the calculations we have presented

using data found from other structures. This would serve the dual purpose of validating the methods demonstrated here, and showing how the inclusion of data into models of this type serves to dramatically speed up the calculation process. We would also like to use the results of future experiments into the values of the gradient elastic tensor in both ^{71}Ga and ^{115}In to further investigate the behaviour of these species - which under our current understanding behave very similarly in a lattice despite being quite different species. The electron coherence time model presented here could be improved upon with the addition of more physically grounded calculations of spin projection, perhaps incorporating the ideas we mention in Chapter 2. The tools developed for the simulation of the action of RF pulses on an NMR spectrum may well prove useful in the design of pulse sequences - potentially allowing for the fine tuning of pulse sequences to a specific quantum dot should the strain profile and indium concentration be known.

The understanding and characterisation of quantum dots is vital if they are to serve a role in the emerging world of quantum technologies, the ideas and methods presented here go some way towards those goals and can be built upon to even further develop our knowledge.

APPENDIX A

APPENDICES

A.1 The Hyperfine Hamiltonian

The derivation of the hyperfine interaction Hamiltonian presented in Section 3.1.2.1 is complete, but several steps are not immediately obvious. Here we have written out these steps in detail, including where necessary the vector calculus/analysis identities required. Hopefully this will make the derivation a little easier to follow than how it is presented in Abragam [118]. A good introduction to the mathematical framework and identities used here can be found in Chapter 10 of Riley [163].

A.1.1 Spin Component

The exact steps required to go from Eq. 3.12 to Eq 3.13 are reasonably involved. We begin with the stated form of the spin component of the interaction Hamiltonian

$$\hat{H}_i^S = 2\mu_B \hat{\mathbf{S}} \cdot \left(\nabla \times \left(\nabla \times \frac{\boldsymbol{\mu_N}}{r} \right) \right), \tag{A.1}$$

and then expand the curl of the curl operator according to the standard formula $\nabla \times (\nabla \times \boldsymbol{a}) = \nabla(\nabla \cdot \boldsymbol{a}) - \nabla^2 \boldsymbol{a}$ to arrive at

$$\hat{H}_i^S = 2\mu_B \hat{\mathbf{S}} \cdot \left(\nabla \left(\nabla \cdot \frac{\boldsymbol{\mu}_N}{r} \right) - \nabla^2 \frac{\boldsymbol{\mu}_N}{r} \right). \tag{A.2}$$

In order to evaluate the divergence of $\frac{\boldsymbol{\mu}_N}{r}$ we employ the product rule, and use the fact that $\boldsymbol{\mu}_N$ is independent of position and thus $\nabla \cdot \boldsymbol{\mu}_N = 0$ to find that

$$\begin{aligned} \nabla \cdot \frac{\boldsymbol{\mu}_N}{r} &= \boldsymbol{\mu}_N \cdot \nabla \frac{1}{r} + \frac{1}{r} (\nabla \cdot \boldsymbol{\mu}_N) \\ &= \boldsymbol{\mu}_N \cdot \nabla \frac{1}{r}. \end{aligned} \tag{A.3}$$

We then plug this into Eq. A.2 to find

$$\hat{H}_i^S = 2\mu_B \hat{\boldsymbol{S}} \cdot \left(\nabla \left(\boldsymbol{\mu}_N \cdot \nabla \frac{1}{r} \right) - \nabla^2 \frac{\boldsymbol{\mu}_N}{r} \right). \tag{A.4}$$

Our next step is to evaluate the first term inside the brackets. We can again use a standard identity, this time for $\nabla(\boldsymbol{a}\cdot\boldsymbol{b}) = \boldsymbol{a}\times(\nabla\times\boldsymbol{b}) + \boldsymbol{b}\times(\nabla\times\boldsymbol{a}) + (\boldsymbol{a}\cdot\nabla)\boldsymbol{b} + (\boldsymbol{b}\cdot\nabla)\boldsymbol{a}$ to show that

$$\begin{aligned} \nabla \left(\boldsymbol{\mu}_N \cdot \nabla \frac{1}{r} \right) &= \boldsymbol{\mu}_N \times (\nabla \times \nabla \frac{1}{r}) + \nabla \frac{1}{r} \times (\nabla \times \boldsymbol{\mu}_N) + (\boldsymbol{\mu}_N \cdot \nabla) \nabla \frac{1}{r} + (\nabla \frac{1}{r} \cdot \nabla) \boldsymbol{\mu}_N \\ &= (\boldsymbol{\mu}_N \cdot \nabla) \nabla \frac{1}{r}. \end{aligned} \tag{A.5}$$

Here we have used the fact that $\nabla \times \nabla\phi = 0$ for any scalar field ϕ to eliminate the first term, the fact that $\nabla \times \boldsymbol{\mu}_N = 0$ (because $\boldsymbol{\mu}_N$ is independent of position) to eliminate the second term, and the fact that $\boldsymbol{\mu}_N$ is a constant and therefore any directional derivative of it will be 0 to eliminate the fourth term. We can also exploit the independence of $\boldsymbol{\mu}_N$ from position to see that $\nabla^2 \frac{\boldsymbol{\mu}_N}{r} = \boldsymbol{\mu}_N \nabla^2 \frac{1}{r}$. By plugging these results into Eq. A.4 we find

$$\hat{H}_i^S = 2\mu_B \hat{\boldsymbol{S}} \cdot \left((\boldsymbol{\mu}_N \cdot \nabla) \nabla \frac{1}{r} - \boldsymbol{\mu}_N \nabla^2 \frac{1}{r} \right). \tag{A.6}$$

From here we apply the dot product with the spin vector $\hat{\boldsymbol{S}}$, move the $\frac{1}{r}$ outside the brackets to the right, and rearrange the scalar products of the form $(\boldsymbol{a}\cdot\nabla)$ to arrive at

$$\hat{H}_i^S = 2\mu_B \left((\hat{\boldsymbol{S}} \cdot \nabla)(\boldsymbol{\mu}_N \cdot \nabla) - (\hat{\boldsymbol{S}} \cdot \boldsymbol{\mu}_N \nabla^2) \right) \frac{1}{r}. \tag{A.7}$$

At this point, we split the term in $(\hat{\boldsymbol{S}} \cdot \boldsymbol{\mu}_N)$ into 2 pieces with relative magnitudes $\frac{2}{3}$ and $\frac{4}{3}$ respectively. The term of magnitude $\frac{2}{3}$ is grouped with the other terms, while that with magnitude $\frac{4}{3}$ is separated and will form the basis of the contact interaction[1]. We thus arrive at Eq. 3.13

$$\hat{H}_i^S = 2\mu_B \left((\hat{\boldsymbol{S}} \cdot \nabla)(\boldsymbol{\mu}_N \cdot \nabla) - \frac{1}{3} (\hat{\boldsymbol{S}} \cdot \boldsymbol{\mu}_N) \nabla^2 \right) \left(\frac{1}{r} \right) - \frac{4\mu_B}{3} (\hat{\boldsymbol{S}} \cdot \boldsymbol{\mu}_N) \nabla^2 \left(\frac{1}{r} \right). \tag{A.8}$$

The result in Eq. 3.14 is found by first noting the following definitions: $r = \sqrt{x^2 + y^2 + z^2}$,

$$\boldsymbol{\mu}_N = \begin{pmatrix} \mu_N^x \\ \mu_N^y \\ \mu_N^z \end{pmatrix}, \hat{\boldsymbol{S}} = \begin{pmatrix} \hat{S}^x \\ \hat{S}^y \\ \hat{S}^z \end{pmatrix}, \text{ and } \nabla = \begin{pmatrix} \frac{d}{dx} \\ \frac{d}{dy} \\ \frac{d}{dz} \end{pmatrix}.$$

[1] The justification for this is unclear. We believe it is necessary so that the theory agrees with experimental results. In principle, both of these new terms should result in δ functions, and hence contribute to the contact interaction magnitude.

Using these, we evaluate the first term in Eq. A.7

$$\begin{aligned}(\hat{\boldsymbol{S}}\cdot\nabla)(\boldsymbol{\mu}_N\cdot\nabla)\frac{1}{r} &= (\hat{\boldsymbol{S}}\cdot\nabla)\left(\mu_N^x\frac{d}{dx}\left(\frac{1}{r}\right)+\mu_N^y\frac{d}{dy}\left(\frac{1}{r}\right)+\mu_N^x\frac{d}{dx}\left(\frac{1}{r}\right)\right)\\ &= (\hat{\boldsymbol{S}}\cdot\nabla)\left(-\frac{\mu_N^x x+\mu_N^y y+\mu_N^z z}{r^3}\right) = (\hat{\boldsymbol{S}}\cdot\nabla)M\\ &= \hat{S}^x\frac{d(M)}{dx}+\hat{S}^y\frac{d(M)}{dy}+\hat{S}^z\frac{d(M)}{dz}\\ &= \frac{3}{r^5}\left(\hat{S}^x\mu_N^x x^2+\hat{S}^y\mu_N^y y^2+\hat{S}^z\mu_N^z z^2\right)-\frac{\hat{S}^x\mu_N^x+\hat{S}^y\mu_N^y+\hat{S}^z\mu_N^z}{r^3},\end{aligned} \tag{A.9}$$

and find the form of Eq. 3.14

$$\frac{3\left((\hat{\boldsymbol{S}}\cdot\boldsymbol{r})(\boldsymbol{\mu}_N\cdot\boldsymbol{r})\right)}{r^5}-\frac{\hat{\boldsymbol{S}}\cdot\boldsymbol{\mu}_N}{r^3}. \tag{A.10}$$

A.1.2 Orbital Angular Momentum Component

The orbital angular momentum component of the interaction as presented in Eq. 3.16 is easier to find, but does involve some complications. We begin with the first term in the overall Hamiltonian

$$\hat{H}_i^L = \frac{e}{2m_e c}(\hat{\boldsymbol{p}}\cdot\hat{\boldsymbol{A}}+\hat{\boldsymbol{A}}\cdot\hat{\boldsymbol{p}}). \tag{A.11}$$

We then act with this Hamiltonian on some electronic wavefunction $\psi(\boldsymbol{r})$, and use the definitions of the momentum operator $\hat{\boldsymbol{p}} = -i\hbar\nabla$ and the Bohr magneton $\mu_B = \frac{e\hbar}{2m_e c}$ to write[2]

$$\begin{aligned}\hat{H}_i^L\psi(\boldsymbol{r}) &= -i\mu_B\left(\nabla\cdot\hat{\boldsymbol{A}}+\hat{\boldsymbol{A}}\cdot\nabla\right)\psi(\boldsymbol{r})\\ &= -i\mu_B\left(\nabla\cdot\hat{\boldsymbol{A}}\psi(\boldsymbol{r})+\hat{\boldsymbol{A}}\cdot\nabla\psi(\boldsymbol{r})\right).\end{aligned} \tag{A.12}$$

Applying the product rule to the first term, and remembering that we are using the Coulomb gauge with $\nabla\cdot\hat{\boldsymbol{A}} = 0$, we find

$$\begin{aligned}\hat{H}_i^L\psi(\boldsymbol{r}) &= -i\mu_B\left(\hat{\boldsymbol{A}}\cdot\nabla\psi(\boldsymbol{r})+\psi(\boldsymbol{r})(\nabla\cdot\hat{\boldsymbol{A}})+\hat{\boldsymbol{A}}\cdot\nabla\psi(\boldsymbol{r})\right)\\ &= -2i\mu_B\left(\hat{\boldsymbol{A}}\cdot\nabla\psi(\boldsymbol{r})\right).\end{aligned} \tag{A.13}$$

We now use the definition[3] $\hat{\boldsymbol{A}} = \nabla\times\frac{\boldsymbol{\mu}_N}{r} = \boldsymbol{\mu}_N\times\frac{\boldsymbol{r}}{r^3}$ to write

$$\begin{aligned}\hat{H}_i^L\psi(\boldsymbol{r}) &= -2i\mu_B\left(\left(\frac{\boldsymbol{\mu}_N\times\boldsymbol{r}}{r^3}\right)\cdot\nabla\right)\psi(\boldsymbol{r})\\ &= \frac{2\mu_B}{\hbar}\left(\left(\frac{\boldsymbol{\mu}_N\times\boldsymbol{r}}{r^3}\right)\cdot\hat{\boldsymbol{p}}\right)\psi(\boldsymbol{r}),\end{aligned} \tag{A.14}$$

and then use the cyclic property of the scalar triple product to write

$$\hat{H}_i^L\psi(\boldsymbol{r}) = \frac{2\mu_B}{\hbar}\left(\left(\frac{\boldsymbol{r}\times\hat{\boldsymbol{p}}}{r^3}\right)\cdot\boldsymbol{\mu}_N\right)\psi(\boldsymbol{r}). \tag{A.15}$$

[2]This definition of μ_B, and the entire hyperfine interaction as presented here, are written in the Gaussian CGS units system. Converting to SI units doesn't change the structure, but does change the value of some constants.

[3]The second equality in this definition can be shown by direct calculation, and is not as bad as it first appears. Not fun, but not awful either.

Recognising that the LHS of this dot product is equal to the orbital angular momentum $\hat{\boldsymbol{L}} = \boldsymbol{r} \times \hat{\boldsymbol{p}}$ we can now write this as

$$\begin{aligned} \hat{H}_i^L \psi(\boldsymbol{r}) &= \frac{2\mu_B}{\hbar} \left(\frac{\hat{\boldsymbol{L}} \cdot \boldsymbol{\mu}_N}{r^3} \right) \psi(\boldsymbol{r}) \\ &= 2\mu_B \left(\frac{\hat{\boldsymbol{l}} \cdot \boldsymbol{\mu}_N}{r^3} \right) \psi(\boldsymbol{r}) \end{aligned} \tag{A.16}$$

where the last line is found by substituting $\hat{\boldsymbol{l}} = \frac{\hat{\boldsymbol{L}}}{\hbar}$. We therefore recognise that the Hamiltonian for the orbital angular momentum interaction has the form given in Eq. 3.16

$$\hat{H}_i^L = 2\mu_B \left(\frac{\hat{\boldsymbol{l}} \cdot \boldsymbol{\mu}_N}{r^3} \right). \tag{A.17}$$

A.2 Notes on Tensors Relevant to the Quadrupolar Interaction

Much of the following draws on books by Rowe [213], Zare [214] and Jones [215]. It is not intended to provide much more than a passing introduction to the ideas needed to understand the derivation present in Section 3.2.2.

A.2.1 Tensors

Tensors are the general class of objects that represent transformations between vectors, matrices, scalars and other tensors. The *order* of a tensor is essentially the dimension of the array required to write it out[4]. So a scalar is a 0^{th} order tensor, a vector is a 1^{st} order tensor, a matrix a 2^{nd} order tensor and so on[5]. All of the spin tensors found in this thesis are of 2^{nd} order, and are therefore written with 2 indices, eg A_l^m. The number of possible values of each index does not affect the order of the tensor, what matters is there are 2 of them. The positioning of the labels denotes whether the respective index is co-variant (denoted as a subscript) or contra-variant (a superscript). The differences between these are not so important for this surface level discussion, but we will attempt to be consistent nonetheless.

A.2.1.1 Rotations of Tensors

The most significant difference between tensors of different orders is how they behave under rotations. Indeed, it is this property that determines which order tensor is needed to model a physical quantity. Something that is invariant under rotation is represented using a 0^{th} order tensor and behaves as

$$\begin{aligned} \hat{R}(\Omega) : a &\mapsto a' \\ &= a \end{aligned} \tag{A.18}$$

[4]This quality is also called the *rank* of a tensor.

[5]Strictly speaking, one can make an argument that these objects merely *represent* the underlying tensors. For our purposes this distinction makes little difference, and so we shall ignore it.

With $\hat{R}(\Omega)$ denoting a generic rotation (in the abstract sense). As a has been unchanged by the action of $\hat{R}(\Omega)$, we know that a is an 0^{th} order tensor[6]. Moving on to a vector $\boldsymbol{V}_i$, whose rotation behaves as

$$\begin{aligned}\hat{R}(\Omega):\boldsymbol{V}_i &\mapsto \boldsymbol{V}'_i \\ &= \sum_{i'} R(\Omega)_{ii'}\boldsymbol{V}_{j'} \\ &= R(\Omega)\boldsymbol{V}.\end{aligned} \tag{A.19}$$

Here $R_{ii'}(\Omega)$ is the *matrix representation* of the operator $\hat{R}(\Omega)$, and the third line expresses this sum as standard matrix multiplication. For example, if $\hat{R}(\Omega)$ is a rotation of an angle θ around the z axis in 3D, then

$$\hat{R}(\Omega) = R_z(\theta) = \begin{pmatrix} cos(\theta) & -sin(\theta) & 0 \\ sin(\theta) & cos(\theta) & 0 \\ 0 & 0 & 1 \end{pmatrix}. \tag{A.20}$$

From now on I omit the Ω when writing the rotation operator. Note that the rotation operator itself is unchanged regardless of the object it acts on, but the representation of it changes according to the order of the target. Now, let us look at the rotation of 2^{nd} order tensors T_{ij}. Rotations act on these objects as

$$\begin{aligned}\hat{R}: T_{ij} &\mapsto T'_{ij} \\ &= \sum_{primed} R_{ii'}R_{jj'}T_{i'j'}.\end{aligned} \tag{A.21}$$

Again we have that $R_{\alpha\beta}$ is the matrix representation of $\hat{R}$. It is important to note that there is only one matrix in equation A.21, but it is being used to rotate both elements of T_{ij}. It is of course possible to define the rotations of tensors of any order, but as we only need those of 2^{nd} order, we shall go no further in this particular quest.

A.2.1.2 Spherical Tensor Operators

A tensor operator is a tensor where each element is itself an operator. As tensors, they also are defined in large part by how they behave under rotation, but sometimes additional care must be taken to account for the components being operators rather than numbers. Unfortunately, there is not a standard notation for writing tensors of this form, and in various literature you may find the following notations in use: $T^{(k)}_q, T^k_q, T^q_k$. All of those refer to the q^{th} element of an operator of *order* k. This is a **fundamentally different notation** to the one used above for 2^{nd} order tensors (T_{ij}). The number $q = i \times j$, and uniquely labels each element of the tensor. We will adopt this notation in the following sections, as it aligns with our intuition when specifically discussing angular momentum and the Wigner-Eckart theorem.

[6]Note that a requires 0 indices to define, so both definitions work.

The tensor operators found in Section 3.2.2 are specifically *spherical tensor operators*. These are a sub-class of tensor operators which possess some form of spherical symmetry. Angular momentum states possess such symmetries, and can therefore be represented by spherical tensor operators. The most common example of such operators are the spherical harmonics Y_l^m, which can be used to represent objects with total spin l and spin projection m - an written Y_2^0 is therefore the 0^{th} element of a 2^{nd} order tensor. A powerful result about this type of tensor is that a relationship that holds for one of them will also hold for others, up to changes of some scale factor [162].

A.2.1.3 The Wigner-Eckart Theorem

The Wigner-Eckart theorem (WET) states that for any spherical tensor, T_k^q, we can calculate matrix elements with respect to any 2 angular momentum states ($|j'm'\rangle, |jm\rangle$) by splitting it into angular and radial components:

$$\langle j'm' \left| T_k^q \right| jm \rangle = \langle j'm'; kq \left| jm \right\rangle \langle j \left\| T_k \right\| j' \rangle . \tag{A.22}$$

On the LHS of this equation we have the matrix element we want to calculate. The first term on the RHS is the Clebsch-Gordon coefficient (CGC) for the coupling of angular momentum states. The second is what's called the *reduced matrix element*, which depends only on the total angular momenta j, j', not on the projections m, m' of the states in question. The advantage comes in that this second term is unchanging with respect to q, m, m', and so if we calculate an easy matrix element we can then look up the required CGC and find the reduced matrix element using

$$\langle j \left\| T_k \right\| j' \rangle = \frac{\langle j'm' \left| T_k^q \right| jm \rangle}{\langle j'm'; kq \left| jm \right\rangle}. \tag{A.23}$$

From there, we can then use this to calculate other, more difficult, matrix elements as long as we do not change q. An example may make this more apparent. Let's take the STO $\hat{L}_1^m$, with specific elements

$$\begin{aligned} \hat{L}_1^1 &= -\frac{\hat{L}_+}{\sqrt{2}} \\ \hat{L}_1^0 &= \hat{L}_z \\ \hat{L}_1^{-1} &= \frac{\hat{L}_-}{\sqrt{2}}. \end{aligned} \tag{A.24}$$

We now calculate the reduced matrix element $\langle J'M' \left| L_0 \right| JM \rangle$

$$\langle J'M' \left| \hat{L}_1^0 \right| JM \rangle = \langle J'M' \left| \hat{L}_z \right| JM \rangle = \delta_{JJ'} \delta_{MM'} M \tag{A.25}$$

And so we know use the Wigner-Eckart theorem to calculate

$$\begin{aligned}\left\langle J \left\| \hat{L}_z \right\| J \right\rangle &= \frac{\left\langle JM \left| \hat{L}_z \right| JM \right\rangle}{\langle JM;10|JM\rangle} \\ &= \frac{M}{\frac{M}{((2J+1)J(J+1))^{\frac{1}{2}}}} \\ &= ((2J+1)J(J+1))^{\frac{1}{2}} \\ &\therefore \\ \left\langle J' \left\| \hat{L}_z \right\| J \right\rangle &= ((2J+1)J(J+1))^{\frac{1}{2}} \delta_{JJ'}.\end{aligned} \tag{A.26}$$

Armed with this knowledge we can then calculate more exotic matrix elements of L_0^q, for example:

$$\begin{aligned}\left\langle 42 \left| \hat{L}_1^{-1} \right| 41 \right\rangle &= \left\langle 42 \left| \hat{L}_- \right| 41 \right\rangle \\ &= \langle 42;1-1|41\rangle \left\langle 4 \left\| \hat{L}_1 \right\| 4 \right\rangle \\ &= \frac{3}{2\sqrt{5}} * ((2*4+1)*4*(4+1))^{\frac{1}{2}} \\ &= \frac{3}{2\sqrt{5}} * \sqrt{5*4*5} \\ &= 3\sqrt{5}.\end{aligned} \tag{A.27}$$

The point of all this is that we did one calculation to find $\left\langle J' \left\| \hat{L}_1 \right\| J \right\rangle$, which we can then use to trivialise the calculation of any other matrix elements of $\hat{L_1^q}$.

A.2.1.4 Angular Momentum Coupling

The other important use of the Clebsch-Gordon coefficients is in the coupling of angular momentum states. The idea is to construct states with a specific total angular momentum, by combining systems of lower angular momenta. Mathematically, this is analogous to constructing a spherical tensor of higher order out of multiple lower ordered tensors. In general, this is done as follows

$$\hat{T}_{KQ} = \sum_{jj'mm'} (jm,j'm'|KQ)\hat{T}_{jm}\hat{T}_{j'm'}. \tag{A.28}$$

We must always have: $K = j+j'$, while ensuring that $j, j' < K$, and that $-K \leq Q \leq K$ and $Q = m+m'$. Physically, these restrictions amount to conservation of angular momentum.

A physically motivated example may make this clearer. Let us try and construct the spin operator $\hat{S}_{21}$ out of 2 lower order spin operators. We take $K = 2$ and $Q = 1$, and therefore must restrict our values of j, j', m and m' accordingly. The first restriction is that $j = j' = 1$, as this is the only combination such that $j + j' = 2$ while still keeping $j, j' < 2$. These constraints then create constraints on m, m', as we also require that $-j \leq m \leq j$ and $-j' \leq m' \leq j'$. The possible combinations of m and m' are therefore

m	m'
0	1
1	0

After staring at this for a while, we notice that if we set $j = j' = 1$ and $m' = 1 - m$, we can replace the sum over all j, j', m, m' in equation A.28 with a single sum over m running from 0 to 1. Thus, the equation becomes

$$\begin{aligned}\hat{S}_{21} &= \sum_{m=0}^{1} (1m, 1(1-m)|21)\hat{S}_{1m}\hat{S}_{1(1-m)} \\ &= (10, 11|21)\hat{S}_{10}\hat{S}_{11} + (11, 10|21)\hat{S}_{11}\hat{S}_{10} \\ &= \frac{1}{\sqrt{2}}\hat{S}_{10}\hat{S}_{11} + \frac{1}{\sqrt{2}}\hat{S}_{11}\hat{S}_{10} \\ &= \frac{1}{\sqrt{2}}(\hat{S}_z\hat{S}_+ + \hat{S}_+\hat{S}_z).\end{aligned} \tag{A.29}$$

Here we have calculated the CGCs using Mathematica, but tables of them are also available. Now that we have this operator, we could use equation A.28 again to calculate higher rank operators if we so desired.

A.3 Additional NMR Spectra

Here we present additional figures showing the calculated NMR spectra as found for ^{115}In nuclei in Section 4.3. First we present comparisons between the spectra of single nuclei in the Faraday and Voigt geometries (similar to Fig 4.18), followed by comparisons of the Voigt orientated spectra for both ^{69}Ga and ^{75}As - similar to the Faraday orientated spectra of Figures 4.21 & 4.22. These graphs all demonstrate the same effects as seen in Section 4.3, and thus we include them here for completeness rather than to gain new insight.

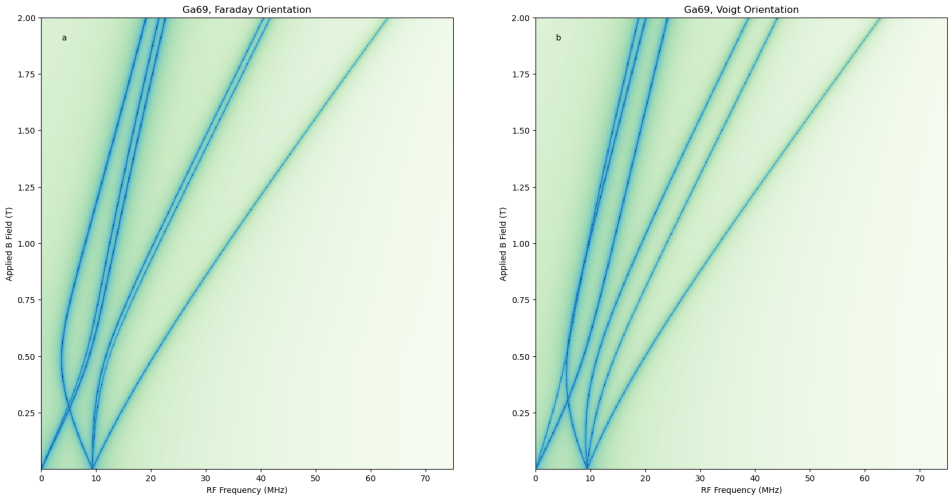

Figure A.1: The simulated NMR spectra of a single ^{69}Ga nucleus in the centre of the quantum dot. In (a) we show the results for a Faraday orientated field, and in (b) we show the results for a Voigt field. Darker colours indicate a stronger absorption.

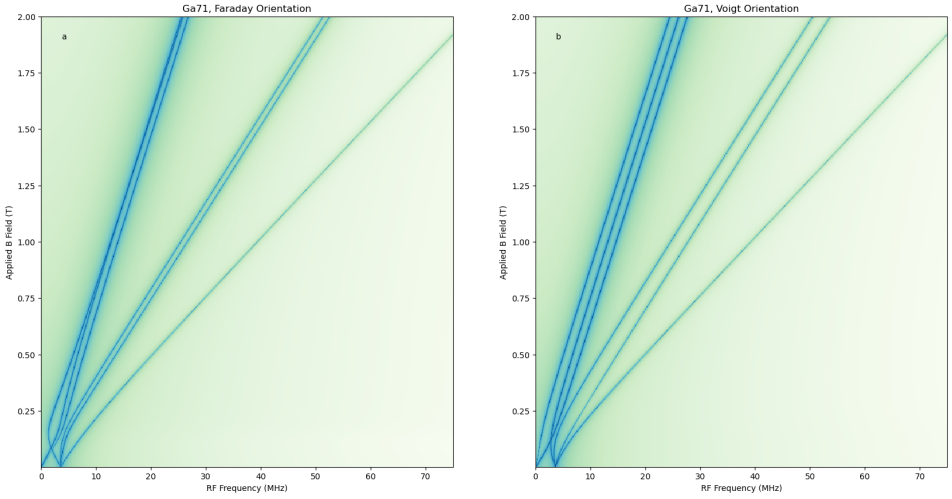

Figure A.2: The simulated NMR spectra of a single ^{71}Ga nucleus in the centre of the quantum dot. In (a) we show the results for a Faraday orientated field, and in (b) we show the results for a Voigt field. Darker colours indicate a stronger absorption. The change in structure is least obvious for ^{71}Ga out of all the nuclear species in the quantum dot, however it accounts for a negligible fraction of the overall number of gallium nuclei in the lattice and therefore we do not investigate it in any more detail than we do the other species.

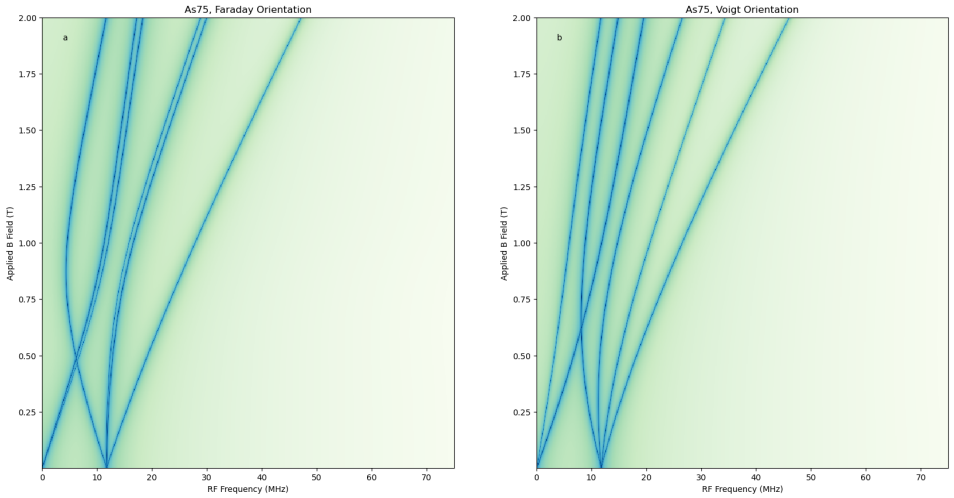

Figure A.3: The simulated NMR spectra of a single ^{75}As nucleus in the centre of the quantum dot. In (a) we show the results for a Faraday orientated field, and in (b) we show the results for a Voigt field. Darker colours indicate a stronger absorption. There is a significant difference in the structure of the spectra between the 2 field orientations, demonstrating the effects discussed in Section 2.1.

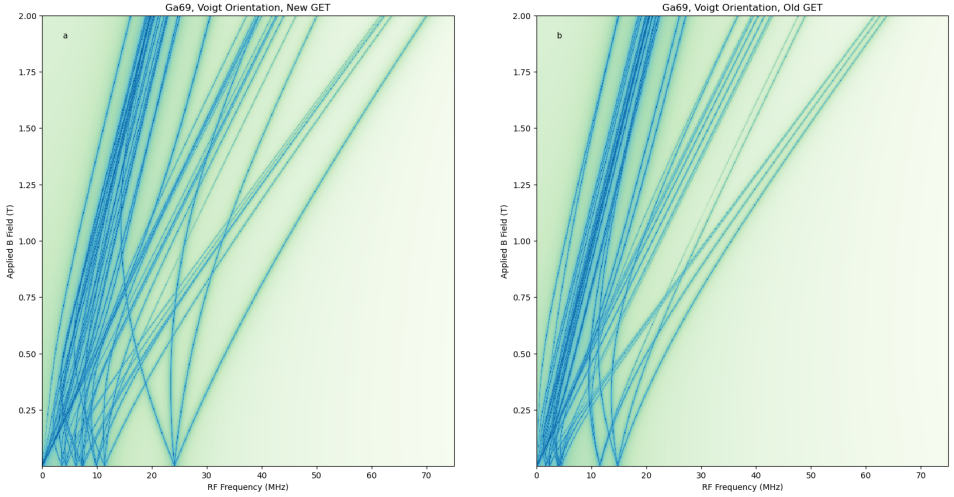

Figure A.4: The NMR spectra of a sample of 8 ^{69}Ga nuclei within the quantum dot structure, under a Voigt orientated magnetic field. In (a) we plot the spectra as found using the NMR/PL values of the GET, while in (b) we plot the spectra as found using the NAR values. We see a clustering of absorption lines as the underlying quadrupolar frequency distribution narrows.

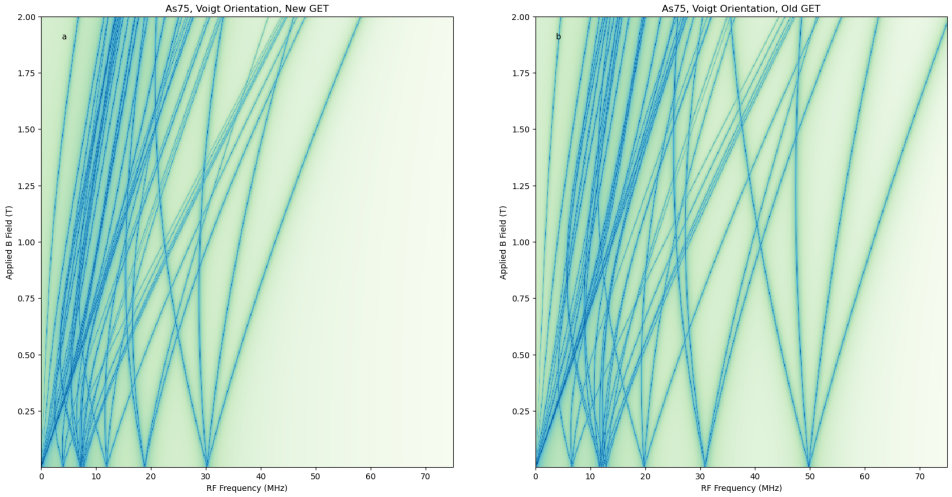

Figure A.5: The NMR spectra of a sample of 8 ^{75}As nuclei within the quantum dot structure, under a Voigt orientated magnetic field. In (a) we plot the spectra as found using the NMR/PL values of the GET, while in (b) we plot the spectra as found using the NAR values. We see a clustering of absorption lines as the underlying quadrupolar frequency distribution narrows, in addition there are fewer outlying ^{75}As nuclei in our sample set - an unfortunate artefact of the random sampling method we employ to create these plots.

A.4 Additional EFG Calculations

Here we present additional figures showing the electric field gradients for ^{69}Ga, ^{71}Ga and ^{75}As in both mirrored dots - as is done for ^{115}In in Figures 5.5 & 5.6.

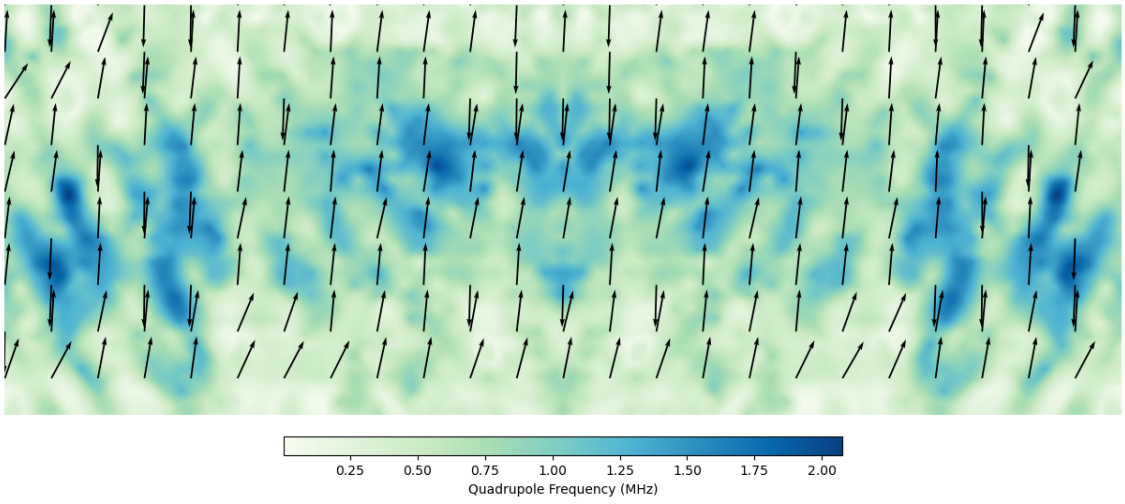

Figure A.6: The direction (arrows) and strength (background colour) of the quadrupolar field as felt by a ^{69}Ga nucleus at each point in the structure of Dot LR. We see here the wide nature of Dot LR, resulting from the long tail present on the left hand side of the original structure.

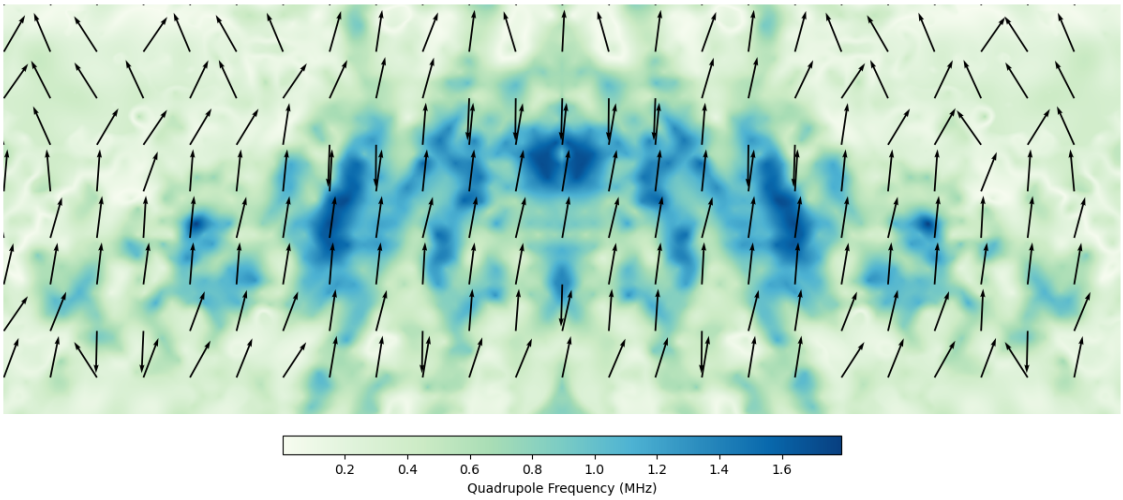

Figure A.7: The direction (arrows) and strength (background colour) of the quadrupolar field as felt by a ^{69}Ga nucleus at each point in the structure of Dot RL. Dot RL is much more compact than Dot LR, which is reflected here in the centralised nature of the EFG.

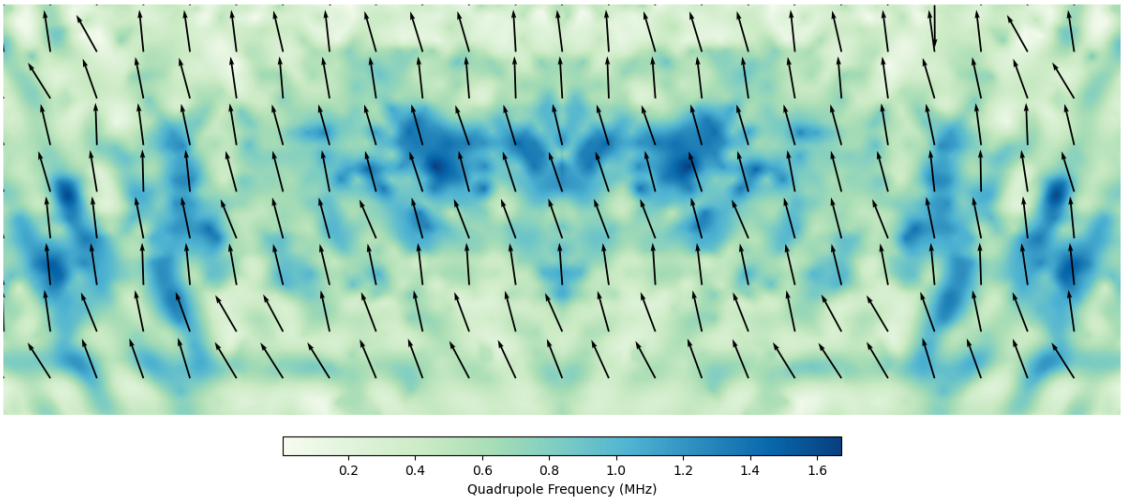

Figure A.8: The direction (arrows) and strength (background colour) of the quadrupolar field as felt by a ^{71}Ga nucleus at each point in the structure of Dot LR. Though these results appear similar to those of ^{69}Ga, it is important to note that the field points the opposite direction for ^{71}Ga, and the maximum value of the EFG is much lower in this species than in ^{69}Ga.

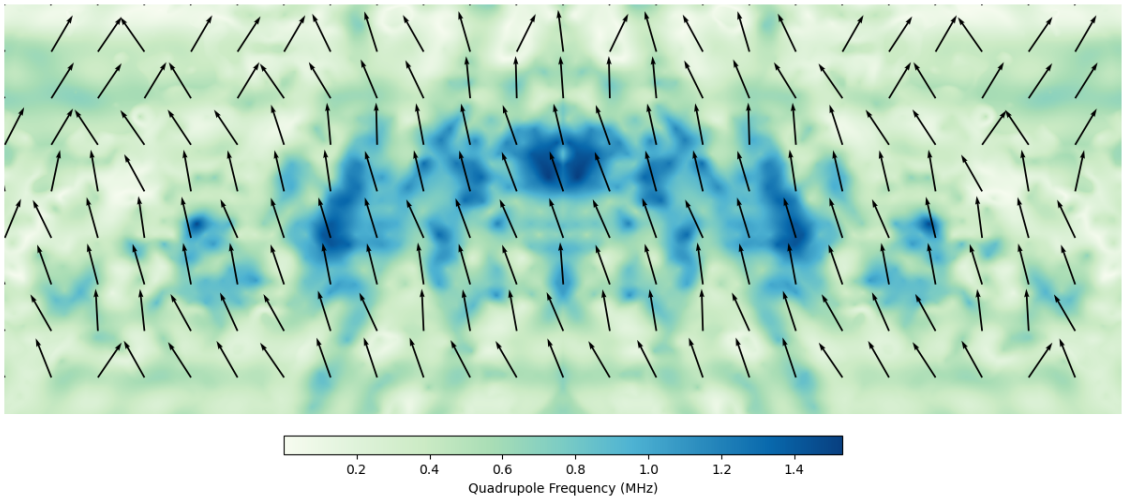

Figure A.9: The direction (arrows) and strength (background colour) of the quadrupolar field as felt by a ^{71}Ga nucleus at each point in the structure of Dot RL. Though these results appear similar to those of ^{69}Ga, it is important to note that the field points the opposite direction for ^{71}Ga, and the maximum value of the EFG is much lower in this species than in ^{69}Ga.

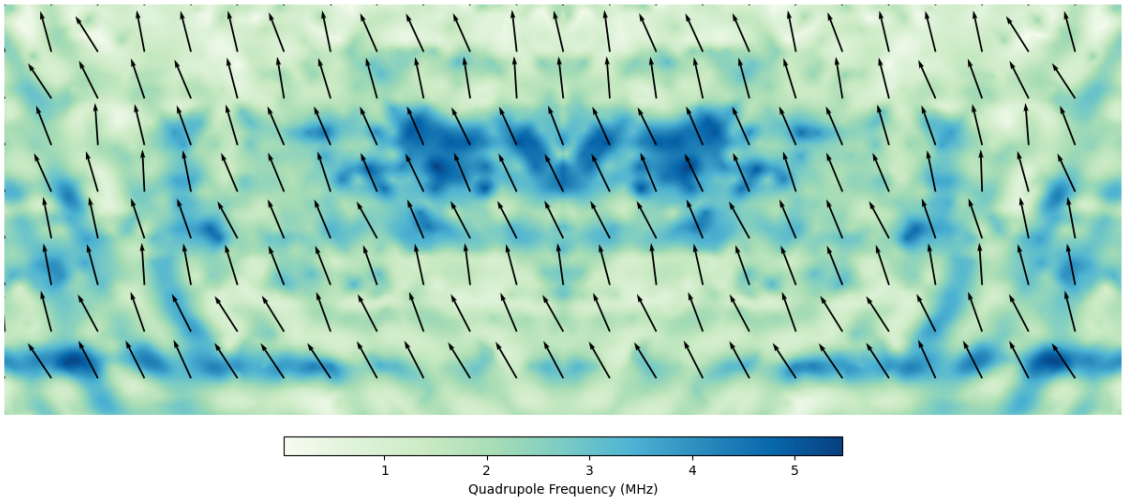

Figure A.10: The direction (arrows) and strength (background colour) of the quadrupolar field as felt by an ^{75}As nucleus at each point in the structure of Dot LR. The strength map plots out a distinct picture for Dot LR, with the region of high EFG being much more centrally concentrated. This central region also has a much higher peak value, necessitating careful comparison between this and similar plots for other species.

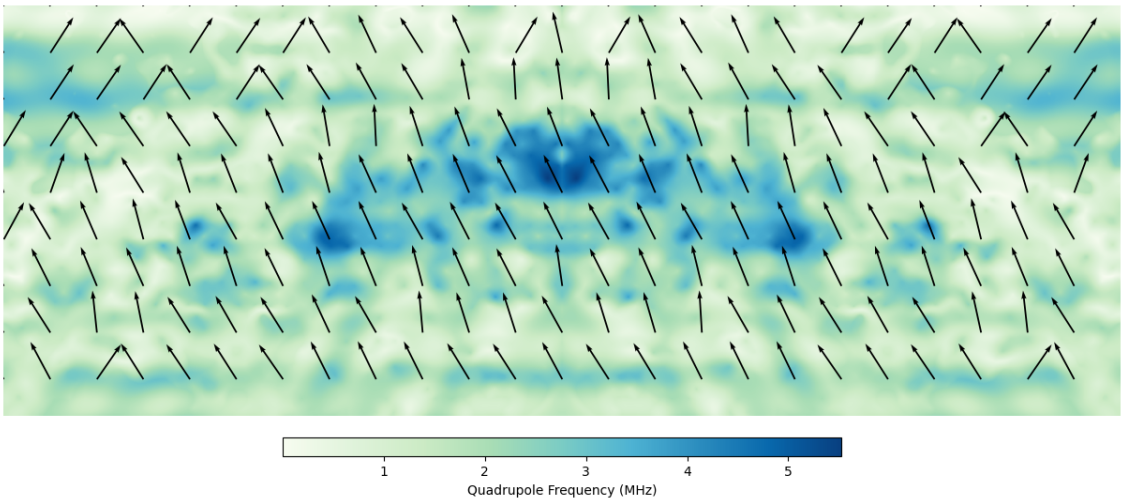

Figure A.11: The direction (arrows) and strength (background colour) of the quadrupolar field as felt by an ^{75}As nucleus at each point in the structure of Dot RL. This plot is much the same as those for other species in Dot RL, though as for all ^{75}As EFG plots, we must notice that the maximum value of the EFG is much higher in this species than any other.

A.5 Additional Decay Modelling

Here we present additional figures showing the modelled decays of ^{71}Ga, ^{75}As and ^{115}In as found using the toy model introduced in Section 5.3. These do not show as significant a difference between the original and mirrored structures, as a result of the smaller decreases in variance between the original structures and those found in the mirrored dots. Nevertheless, in all cases except ^{71}Ga in Dot LR, we find that a decrease in variance results in an increase in coherence time.

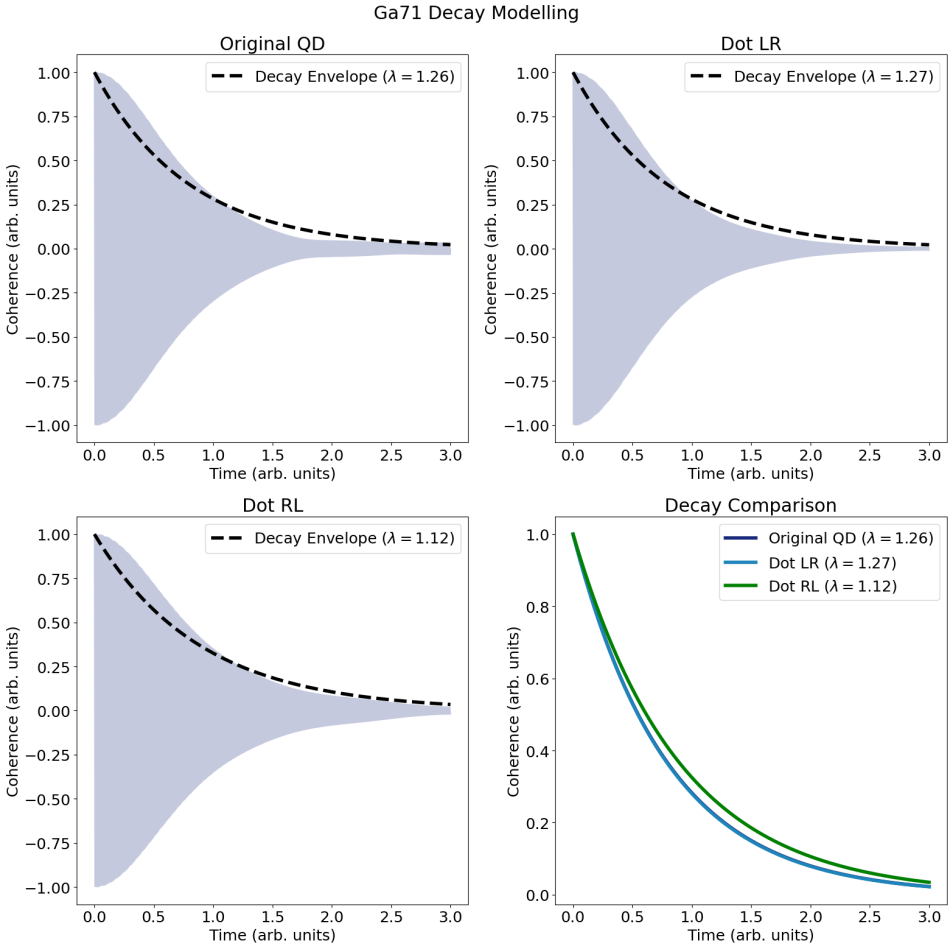

Figure A.12: Modelling the decay of an electron exposed to a set of ^{71}Ga nuclei, as described in Section 5.3. Here Dot LR has a shorter coherence time, despite the underlying distribution having a smaller variance. However, the differences are incredibly small, and well within the margin of error for the fitting process. In addition, the distributions are calculated using older NAR-derived values of the gradient elastic tensor, and therefore care should be taken when analysing them.

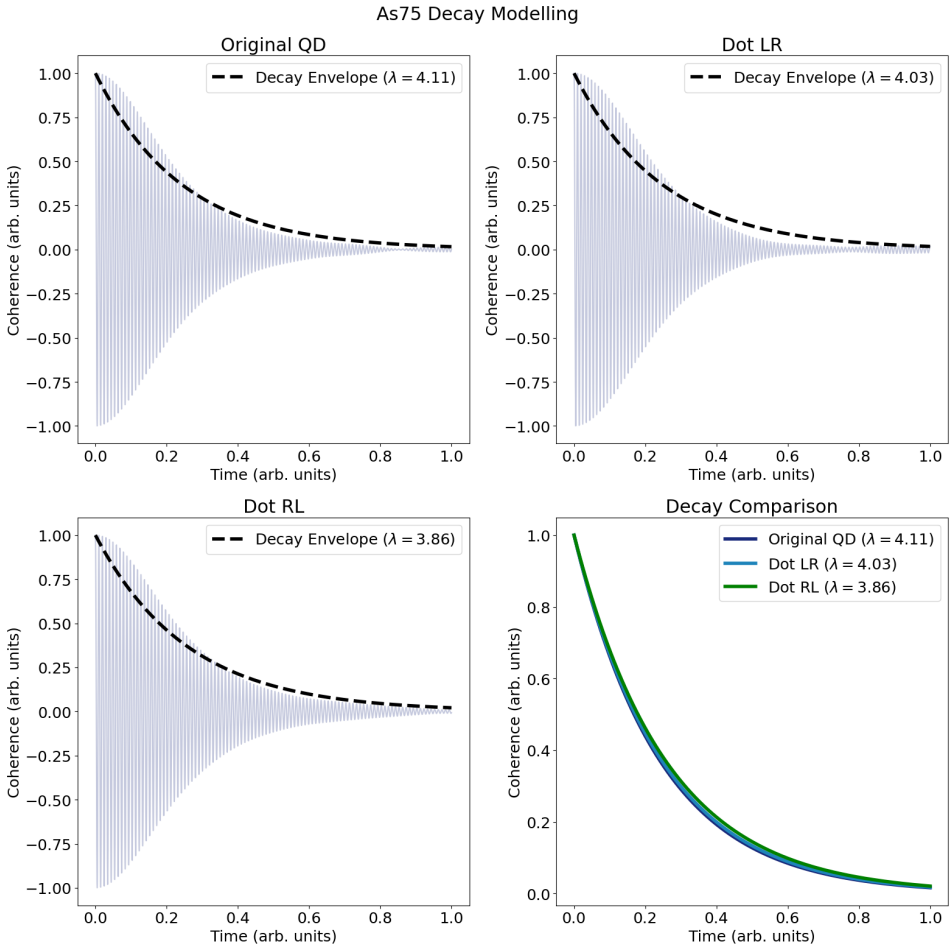

Figure A.13: Modelling the decay of an electron exposed to a set of ^{75}As nuclei, as described in Section 5.3. Again we find that Dot RL has the longest coherence time, in addition to the narrowest distribution of quadrupolar frequencies - though the times are very similar in this case.

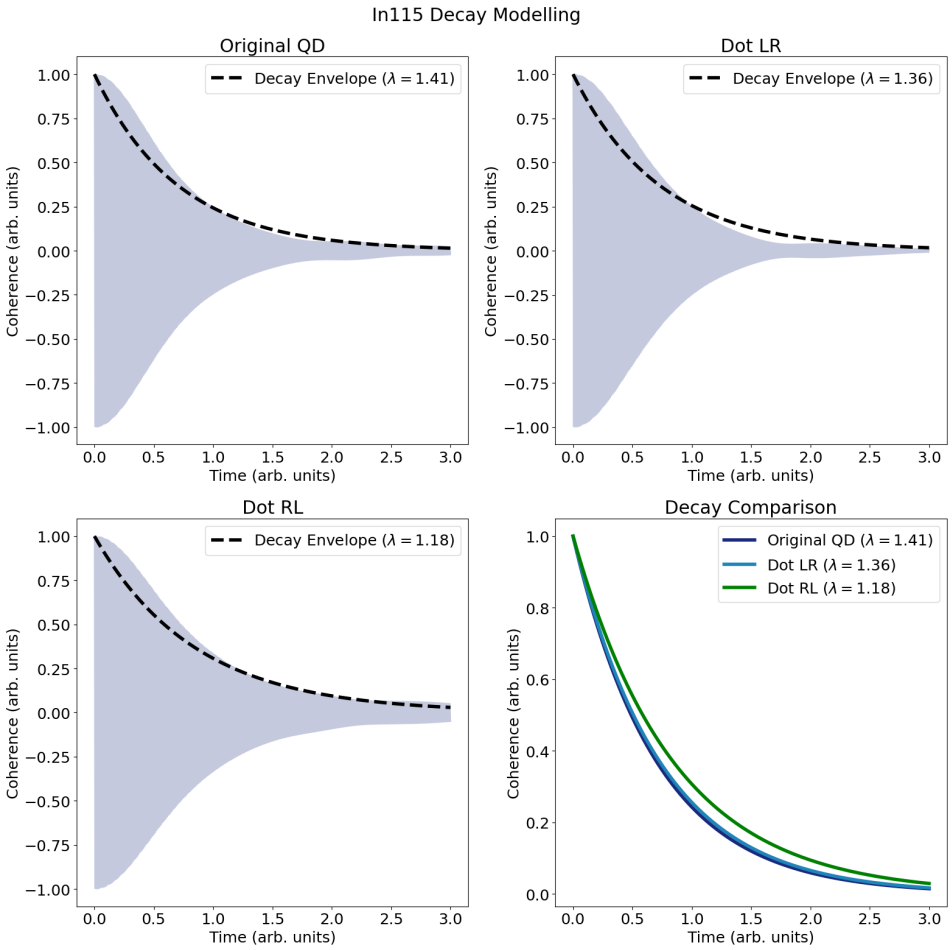

Figure A.14: Modelling the decay of an electron exposed to a set of ^{115}In nuclei, as described in Section 5.3.Dot RL exhibits a much longer coherence time than either the original structure or Dot LR, a consequence of it's much narrower quadrupolar frequency distribution.

BIBLIOGRAPHY

[1] R. Dettmer, "The quest for the quantum dot," *IEE Review*, vol. 34, pp. 395–397, Nov. 1988. Conference Name: IEE Review.

[2] D. Bimberg, M. Grundmann, and N. N. Ledentsov, *Quantum Dot Heterostructures*. John Wiley & Sons, Mar. 1999. Google-Books-ID: 2dcNOpIRfJkC.

[3] P. S. Sokolov, M. Y. Petrov, T. Mehrtens, K. Müller-Caspary, A. Rosenauer, D. Reuter, and A. D. Wieck, "Reconstruction of nuclear quadrupole interaction in (In,Ga)As/GaAs quantum dots observed by transmission electron microscopy," *Physical Review B*, vol. 93, p. 045301, Jan. 2016. Publisher: American Physical Society.

[4] I. N. Stranski and L. Krastanow, "Abhandlungen der mathematisch-naturwissenschaftlichen klasse iib.," *Akademie der Wissenschaften Wien*, vol. 146, pp. 797–810, 1938.

[5] B. A. Joyce, "Molecular beam epitaxy," *Reports on Progress in Physics*, vol. 48, pp. 1637–1697, Dec. 1985. Publisher: IOP Publishing.

[6] J. R. Arthur, "Molecular beam epitaxy," *Surface Science*, vol. 500, pp. 189–217, Mar. 2002.

[7] M. A. Herman and H. Sitter, *Molecular Beam Epitaxy: Fundamentals and Current Status*. Springer Science & Business Media, Dec. 2012. Google-Books-ID: FHPtCAAAQBAJ.

[8] M. Gurioli, Z. Wang, A. Rastelli, T. Kuroda, and S. Sanguinetti, "Droplet epitaxy of semiconductor nanostructures for quantum photonic devices," *Nature Materials*, vol. 18, pp. 799–810, Aug. 2019. Number: 8 Publisher: Nature Publishing Group.

[9] I. Aharonovich, D. Englund, and M. Toth, "Solid-state single-photon emitters," *Nature Photonics*, vol. 10, pp. 631–641, Oct. 2016.

[10] P. Senellart, G. Solomon, and A. White, "High-performance semiconductor quantum-dot single-photon sources," *Nature Nanotechnology*, vol. 12, pp. 1026–1039, Nov. 2017.

[11] J. G. Keizer, J. Bocquel, P. M. Koenraad, T. Mano, T. Noda, and K. Sakoda, "Atomic scale analysis of self assembled GaAs/AlGaAs quantum dots grown by droplet epitaxy," *Applied Physics Letters*, vol. 96, p. 062101, Feb. 2010.

[12] T. Mano and N. Koguchi, "Nanometer-scale GaAs ring structure grown by droplet epitaxy," *Journal of Crystal Growth*, vol. 278, pp. 108–112, May 2005.

[13] T. Mano, K. Watanabe, S. Tsukamoto, H. Fujioka, M. Oshima, and N. Koguchi, "Fabrication of InGaAs quantum dots on GaAs(001) by droplet epitaxy," *Journal of Crystal Growth*, vol. 209, pp. 504–508, Feb. 2000.

[14] K. Kawasaki, D. Yamazaki, A. Kinoshita, H. Hirayama, K. Tsutsui, and Y. Aoyagi, "GaN quantum-dot formation by self-assembling droplet epitaxy and application to single-electron transistors," *Applied Physics Letters*, vol. 79, pp. 2243–2245, Sept. 2001.
Publisher: American Institute of Physics.

[15] C. Somaschini, S. Bietti, N. Koguchi, F. Montalenti, C. Frigeri, and S. Sanguinetti, "Self-assembled GaAs islands on Si by droplet epitaxy," *Applied Physics Letters*, vol. 97, p. 053101, Aug. 2010.
Publisher: American Institute of Physics.

[16] V. M. Kaganer, B. Jenichen, R. Shayduk, W. Braun, and H. Riechert, "Kinetic Optimum of Volmer-Weber Growth," *Physical Review Letters*, vol. 102, p. 016103, Jan. 2009.

[17] I. V. Markov, *Crystal Growth For Beginners: Fundamentals Of Nucleation, Crystal Growth And Epitaxy (Third Edition)*.
World Scientific, Dec. 2016.
Google-Books-ID: VhGyDgAAQBAJ.

[18] T. Mano, M. Abbarchi, T. Kuroda, C. A. Mastrandrea, A. Vinattieri, S. Sanguinetti, K. Sakoda, and M. Gurioli, "Ultra-narrow emission from single GaAs self-assembled quantum dots grown by droplet epitaxy," *Nanotechnology*, vol. 20, p. 395601, Sept. 2009.

[19] W. Langbein, P. Borri, U. Woggon, V. Stavarache, D. Reuter, and A. D. Wieck, "Control of fine-structure splitting and biexciton binding in In x G 1-x As quantum dots by annealing," *Physical Review B*, vol. 69, p. 161301, Apr. 2004.
Publisher: American Physical Society.

[20] C. Heyn, A. Stemmann, and W. Hansen, "Nanohole formation on algaas surfaces by local droplet etching with gallium," *Journal of crystal growth*, vol. 311, no. 7, pp. 1839–1842, 2009.

[21] R. P. Feynman, "Simulating physics with computers," *International Journal of Theoretical Physics*, vol. 21, pp. 467–488, June 1982.

[22] J. Preskill, "Quantum computing and the entanglement frontier," *arXiv:1203.5813 [cond-mat, physics:quant-ph]*, Nov. 2012.
arXiv: 1203.5813.

[23] C. Palacios-Berraquero, L. Mueck, and D. M. Persaud, "Instead of 'supremacy' use 'quantum advantage'," *Nature*, vol. 576, pp. 213–213, Dec. 2019.
Number: 7786 Publisher: Nature Publishing Group.

[24] P. W. Shor, "Polynomial-Time Algorithms for Prime Factorization and Discrete Logarithms on a Quantum Computer," *SIAM Review*, vol. 41, pp. 303–332, Jan. 1999.

[25] L. K. Grover, "A fast quantum mechanical algorithm for database search," in *Proceedings of the twenty-eighth annual ACM symposium on Theory of Computing*, STOC '96, (New York, NY, USA), pp. 212–219, Association for Computing Machinery, July 1996.

[26] S. Lloyd, "Universal Quantum Simulators," *Science, New Series*, vol. 273, no. 5278, pp. 1073–1078, 1996.

[27] D. S. Abrams and S. Lloyd, "Simulation of Many-Body Fermi Systems on a Universal Quantum Computer," *Physical Review Letters*, vol. 79, pp. 2586–2589, Sept. 1997.
Publisher: American Physical Society.

[28] R. Babbush, P. J. Love, and A. Aspuru-Guzik, "Adiabatic Quantum Simulation of Quantum Chemistry," *Scientific Reports*, vol. 4, p. 6603, Oct. 2014.

[29] A. Aspuru-Guzik, A. D. Dutoi, P. J. Love, and M. Head-Gordon, "Simulated Quantum Computation of Molecular Energies," *Science*, vol. 309, pp. 1704–1707, Sept. 2005.
Publisher: American Association for the Advancement of Science Section: Report.

[30] S. Wei, H. Li, and G. Long, "A Full Quantum Eigensolver for Quantum Chemistry Simulations," *Research*, vol. 2020, pp. 1–11, Mar. 2020.

[31] F. Arute, K. Arya, R. Babbush, D. Bacon, J. C. Bardin, R. Barends, R. Biswas, S. Boixo, F. G. S. L. Brandao, D. A. Buell, B. Burkett, Y. Chen, Z. Chen, B. Chiaro, R. Collins, W. Courtney, A. Dunsworth, E. Farhi, B. Foxen, A. Fowler, C. Gidney, M. Giustina, R. Graff, K. Guerin, S. Habegger, M. P. Harrigan, M. J. Hartmann, A. Ho, M. Hoffmann, T. Huang, T. S. Humble, S. V. Isakov, E. Jeffrey, Z. Jiang, D. Kafri, K. Kechedzhi, J. Kelly, P. V. Klimov, S. Knysh, A. Korotkov, F. Kostritsa, D. Landhuis, M. Lindmark, E. Lucero, D. Lyakh, S. Mandrà, J. R. McClean, M. McEwen, A. Megrant, X. Mi, K. Michielsen, M. Mohseni, J. Mutus, O. Naaman, M. Neeley, C. Neill, M. Y. Niu, E. Ostby, A. Petukhov,

J. C. Platt, C. Quintana, E. G. Rieffel, P. Roushan, N. C. Rubin, D. Sank, K. J. Satzinger, V. Smelyanskiy, K. J. Sung, M. D. Trevithick, A. Vainsencher, B. Villalonga, T. White, Z. J. Yao, P. Yeh, A. Zalcman, H. Neven, and J. M. Martinis, "Quantum supremacy using a programmable superconducting processor," *Nature*, vol. 574, pp. 505–510, Oct. 2019.
Number: 7779 Publisher: Nature Publishing Group.

[32] E. Pednault, J. A. Gunnels, G. Nannicini, L. Horesh, and R. Wisnieff, "Leveraging Secondary Storage to Simulate Deep 54-qubit Sycamore Circuits," *arXiv:1910.09534 [quant-ph]*, Oct. 2019.
arXiv: 1910.09534.

[33] M. A. Nielsen and I. L. Chuang, *Quantum Computation and Quantum Information: 10th Anniversary Edition*.
Cambridge University Press, Dec. 2010.

[34] R. Raussendorf, D. E. Browne, and H. J. Briegel, "Measurement-based quantum computation on cluster states," *Physical Review A*, vol. 68, p. 022312, Aug. 2003.
Publisher: American Physical Society.

[35] R. Jozsa, "An introduction to measurement based quantum computation," *NATO Science Series, III: Computer and Systems Sciences*, Aug. 2005.
arXiv: quant-ph/0508124.

[36] D. Gottesman and I. L. Chuang, "Demonstrating the viability of universal quantum computation using teleportation and single-qubit operations," *Nature*, vol. 402, pp. 390–393, Nov. 1999.
Number: 6760 Publisher: Nature Publishing Group.

[37] R. Raussendorf and H. J. Briegel, "A One-Way Quantum Computer," *Physical Review Letters*, vol. 86, pp. 5188–5191, May 2001.
Publisher: American Physical Society.

[38] S. Morley-Short, S. Bartolucci, M. Gimeno-Segovia, P. Shadbolt, H. Cable, and T. Rudolph, "Physical-depth architectural requirements for generating universal photonic cluster states," *Quantum Science and Technology*, vol. 3, p. 015005, Jan. 2018.

[39] S. Morley-Short, *Towards realistic architectures for linear optical quantum computing*.
PhD thesis, Bristol University, Mar. 2019.

[40] O. Mandel, M. Greiner, A. Widera, T. Rom, T. W. Hänsch, and I. Bloch, "Controlled collisions for multi-particle entanglement of optically trapped atoms," *Nature*, vol. 425, pp. 937–940, Oct. 2003.
Number: 6961 Publisher: Nature Publishing Group.

[41] I. Bloch, "Ultracold quantum gases in optical lattices," *Nature Physics*, vol. 1, pp. 23–30, Oct. 2005.

[42] P. Walther, K. J. Resch, T. Rudolph, E. Schenck, H. Weinfurter, V. Vedral, M. Aspelmeyer, and A. Zeilinger, "Experimental one-way quantum computing," *Nature*, vol. 434, pp. 169–176, Mar. 2005.
Number: 7030 Publisher: Nature Publishing Group.

[43] K. Chen, C.-M. Li, Q. Zhang, Y.-A. Chen, A. Goebel, S. Chen, A. Mair, and J.-W. Pan, "Experimental Realization of One-Way Quantum Computing with Two-Photon Four-Qubit Cluster States," *Physical Review Letters*, vol. 99, p. 120503, Sept. 2007.
Publisher: American Physical Society.

[44] R. Prevedel, P. Walther, F. Tiefenbacher, P. Böhi, R. Kaltenbaek, T. Jennewein, and A. Zeilinger, "High-speed linear optics quantum computing using active feed-forward," *Nature*, vol. 445, pp. 65–69, Jan. 2007.
Number: 7123 Publisher: Nature Publishing Group.

[45] C.-Y. Lu, X.-Q. Zhou, O. Gühne, W.-B. Gao, J. Zhang, Z.-S. Yuan, A. Goebel, T. Yang, and J.-W. Pan, "Experimental entanglement of six photons in graph states," *Nature Physics*, vol. 3, pp. 91–95, Feb. 2007.
Number: 2 Publisher: Nature Publishing Group.

[46] Y. Tokunaga, S. Kuwashiro, T. Yamamoto, M. Koashi, and N. Imoto, "Generation of High-Fidelity Four-Photon Cluster State and Quantum-Domain Demonstration of One-Way Quantum Computing," *Physical Review Letters*, vol. 100, p. 210501, May 2008.
Publisher: American Physical Society.

[47] S. Yokoyama, R. Ukai, S. C. Armstrong, C. Sornphiphatphong, T. Kaji, S. Suzuki, J.-i. Yoshikawa, H. Yonezawa, N. C. Menicucci, and A. Furusawa, "Ultra-large-scale continuous-variable cluster states multiplexed in the time domain," *Nature Photonics*, vol. 7, pp. 982–986, Dec. 2013.
Number: 12 Publisher: Nature Publishing Group.

[48] I. Schwartz, D. Cogan, E. R. Schmidgall, Y. Don, L. Gantz, O. Kenneth, N. H. Lindner, and D. Gershoni, "Deterministic generation of a cluster state of entangled photons," *Science*, vol. 354, pp. 434–437, Oct. 2016.
arXiv: 1606.07492v1 Publisher: American Association for the Advancement of Science.

[49] D. Istrati, Y. Pilnyak, J. C. Loredo, C. Antón, N. Somaschi, P. Hilaire, H. Ollivier, M. Esmann, L. Cohen, L. Vidro, C. Millet, A. Lemaître, I. Sagnes, A. Harouri, L. Lanco, P. Senellart, and H. S. Eisenberg, "Sequential generation of linear cluster states from a single photon emitter," *Nature Communications*, vol. 11, p. 5501, Oct. 2020.

Number: 1 Publisher: Nature Publishing Group.

[50] B. P. Lanyon, P. Jurcevic, M. Zwerger, C. Hempel, E. A. Martinez, W. Dür, H. J. Briegel, R. Blatt, and C. F. Roos, "Measurement-Based Quantum Computation with Trapped Ions," *Physical Review Letters*, vol. 111, p. 210501, Nov. 2013.
Publisher: American Physical Society.

[51] D. P. DiVincenzo, "The Physical Implementation of Quantum Computation," *Fortschritte der Physik*, vol. 48, no. 9-11, pp. 771–783, 2000.
_eprint: https://onlinelibrary.wiley.com/doi/pdf/10.1002/1521-3978%28200009%2948%3A9/11%3C771%3A%3AAID-PROP771%3E3.0.CO%3B2-E.

[52] D. Gottesman, "An Introduction to Quantum Error Correction and Fault-Tolerant Quantum Computation," *arXiv:0904.2557 [quant-ph]*, Apr. 2009.
arXiv: 0904.2557.

[53] S. J. Devitt, W. J. Munro, and K. Nemoto, "Quantum error correction for beginners," *Reports on Progress in Physics*, vol. 76, p. 076001, July 2013.

[54] V. M. Schäfer, C. J. Ballance, K. Thirumalai, L. J. Stephenson, T. G. Ballance, A. M. Steane, and D. M. Lucas, "Fast quantum logic gates with trapped-ion qubits," *Nature*, vol. 555, pp. 75–78, Mar. 2018.
Number: 7694 Publisher: Nature Publishing Group.

[55] M. Saffman, "Quantum computing with atomic qubits and Rydberg interactions: progress and challenges," *Journal of Physics B: Atomic, Molecular and Optical Physics*, vol. 49, p. 202001, Oct. 2016.
Publisher: IOP Publishing.

[56] T. Rudolph, "Why I am optimistic about the silicon-photonic route to quantum computing," *APL Photonics*, vol. 2, p. 030901, Mar. 2017.
Publisher: American Institute of Physics.

[57] D. Su, I. Dhand, L. G. Helt, Z. Vernon, and K. Brádler, "Hybrid spatiotemporal architectures for universal linear optics," *Physical Review A*, vol. 99, p. 062301, June 2019.
Publisher: American Physical Society.

[58] V. Lahtinen and J. Pachos, "A Short Introduction to Topological Quantum Computation," *SciPost Physics*, vol. 3, p. 021, Sept. 2017.

[59] D. Loss and D. P. DiVincenzo, "Quantum computation with quantum dots," *Physical Review A*, vol. 57, pp. 120–126, Jan. 1998.
Publisher: American Physical Society.

[60] C. Kloeffel and D. Loss, "Prospects for Spin-Based Quantum Computing in Quantum Dots," *Annual Review of Condensed Matter Physics*, vol. 4, no. 1, pp. 51–81, 2013.
_eprint: https://doi.org/10.1146/annurev-conmatphys-030212-184248.

[61] J. Hinchliff, *Nuclear spin control and manipulation in self-assembled quantum dots General*.
PhD thesis, University of Bristol, 2018.

[62] M. V. Gurudev Dutt, J. Cheng, Y. Wu, X. Xu, D. G. Steel, A. S. Bracker, D. Gammon, S. E. Economou, R.-B. Liu, and L. J. Sham, "Ultrafast optical control of electron spin coherence in charged GaAs quantum dots," *Physical Review B*, vol. 74, p. 125306, Sept. 2006.
Publisher: American Physical Society.

[63] J. Berezovsky, M. H. Mikkelsen, N. G. Stoltz, L. A. Coldren, and D. D. Awschalom, "Picosecond Coherent Optical Manipulation of a Single Electron Spin in a Quantum Dot," *Science*, vol. 320, pp. 349–352, Apr. 2008.
Publisher: American Association for the Advancement of Science Section: Report.

[64] A. Greilich, S. E. Economou, S. Spatzek, D. R. Yakovlev, D. Reuter, A. D. Wieck, T. L. Reinecke, and M. Bayer, "Ultrafast optical rotations of electron spins in quantum dots," *Nature Physics*, vol. 5, pp. 262–266, Apr. 2009.
Number: 4 Publisher: Nature Publishing Group.

[65] D. Press, K. De Greve, P. L. McMahon, T. D. Ladd, B. Friess, C. Schneider, M. Kamp, S. Höfling, A. Forchel, and Y. Yamamoto, "Ultrafast optical spin echo in a single quantum dot," *Nature Photonics*, vol. 4, pp. 367–370, June 2010.
Publisher: Nature Publishing Group.

[66] J. Berezovsky, M. H. Mikkelsen, O. Gywat, N. G. Stoltz, L. A. Coldren, and D. D. Awschalom, "Nondestructive Optical Measurements of a Single Electron Spin in a Quantum Dot," *Science*, vol. 314, pp. 1916–1920, Dec. 2006.
Publisher: American Association for the Advancement of Science Section: Report.

[67] M. Atatüre, J. Dreiser, A. Badolato, and A. Imamoglu, "Observation of Faraday rotation from a single confined spin," *Nature Physics*, vol. 3, pp. 101–106, Feb. 2007.
Number: 2 Publisher: Nature Publishing Group.

[68] M. H. Mikkelsen, J. Berezovsky, N. G. Stoltz, L. A. Coldren, and D. D. Awschalom, "Optically detected coherent spin dynamics of a single electron in a quantum dot," *Nature Physics*, vol. 3, pp. 770–773, Nov. 2007.
Number: 11 Publisher: Nature Publishing Group.

[69] A. Nick Vamivakas, Y. Zhao, C.-Y. Lu, and M. Atatüre, "Spin-resolved quantum-dot resonance fluorescence," *Nature Physics*, vol. 5, pp. 198–202, Mar. 2009.
Number: 3 Publisher: Nature Publishing Group.

[70] A. N. Vamivakas, C.-Y. Lu, C. Matthiesen, Y. Zhao, S. Fält, A. Badolato, and M. Atatüre, "Observation of spin-dependent quantum jumps via quantum dot resonance fluorescence," *Nature*, vol. 467, pp. 297–300, Sept. 2010.
Number: 7313 Publisher: Nature Publishing Group.

[71] N. H. Lindner and T. Rudolph, "Proposal for pulsed On-demand sources of photonic cluster state strings," *Physical Review Letters*, vol. 103, p. 113602, Sept. 2009.
Publisher: American Physical Society.

[72] E. V. Denning, J. Iles-Smith, D. P. McCutcheon, and J. Mørk, "Protocol for generating multiphoton entangled states from quantum dots in the presence of nuclear spin fluctuations," *Physical Review A*, vol. 96, p. 062329, Dec. 2017.
Publisher: American Physical Society.

[73] D. E. Browne and T. Rudolph, "Resource-Efficient Linear Optical Quantum Computation," *Physical Review Letters*, vol. 95, p. 010501, June 2005.
Publisher: American Physical Society.

[74] Y. Sugiyama, Y. Sakuma, S. Muto, and N. Yokoyama, "Novel InGaAs/GaAs quantum dot structures formed in tetrahedral-shaped recesses on (111)B GaAs substrate using metalorganic vapor phase epitaxy," *Applied Physics Letters*, vol. 67, p. 4, May 1995.

[75] C. Kittel and P. McEuen, *Introduction to solid state physics*.
Wiley, 2018.
OCLC: 1097548279.

[76] P. YU and M. Cardona, *Fundamentals of Semiconductors: Physics and Materials Properties*.
Springer Science & Business Media, Apr. 2010.
Google-Books-ID: 5aBuKYBT_hsC.

[77] A. M. Smith and S. Nie, "Semiconductor Nanocrystals: Structure, Properties, and Band Gap Engineering," *Accounts of Chemical Research*, vol. 43, pp. 190–200, Feb. 2010.
Publisher: American Chemical Society.

[78] P. Harrison, *Quantum Wells, Wires and Dots: Theoretical and Computational Physics of Semiconductor Nanostructures*.
Wiley, 2nd ed., 2005.

[79] G. W. Bryant, "Excitons in quantum boxes: Correlation effects and quantum confinement," *Physical Review B*, vol. 37, pp. 8763–8772, May 1988.
Publisher: American Physical Society.

[80] M. Boero, J. M. Rorison, G. Duggan, and J. C. Inkson, "A detailed theory of excitons in quantum dots," *Surface Science*, vol. 377-379, pp. 371–375, Apr. 1997.

[81] M. Bayer, G. Ortner, O. Stern, A. Kuther, A. A. Gorbunov, A. Forchel, P. Hawrylak, S. Fafard, K. Hinzer, T. L. Reinecke, S. N. Walck, J. P. Reithmaier, F. Klopf, and F. Schäfer, "Fine structure of neutral and charged excitons in self-assembled In(Ga)As/(Al)GaAs quantum dots," *Physical Review B*, vol. 65, p. 195315, May 2002.
Publisher: American Physical Society.

[82] R. J. Warburton, C. S. Dürr, K. Karrai, J. P. Kotthaus, G. Medeiros-Ribeiro, and P. M. Petroff, "Charged Excitons in Self-Assembled Semiconductor Quantum Dots," *Physical Review Letters*, vol. 79, pp. 5282–5285, Dec. 1997.
Publisher: American Physical Society.

[83] V. V. Belykh, A. Greilich, D. R. Yakovlev, M. Yacob, J. P. Reithmaier, M. Benyoucef, and M. Bayer, "Electron and hole g factors in InAs/InAlGaAs self-assembled quantum dots emitting at telecom wavelengths," *Physical Review B*, vol. 92, p. 165307, Oct. 2015.
Publisher: American Physical Society.

[84] M. Gimeno-Segovia, P. Shadbolt, D. E. Browne, and T. Rudolph, "From Three-Photon Greenberger-Horne-Zeilinger States to Ballistic Universal Quantum Computation," *Physical Review Letters*, vol. 115, p. 020502, July 2015.
Publisher: American Physical Society.

[85] F. Ewert and P. van Loock, "$3/4$-Efficient Bell Measurement with Passive Linear Optics and Unentangled Ancillae," *Physical Review Letters*, vol. 113, p. 140403, Sept. 2014.
Publisher: American Physical Society.

[86] D. M. Greenberger, M. A. Horne, and A. Zeilinger, "Going Beyond Bell's Theorem," in *Bell's Theorem, Quantum Theory and Conceptions of the Universe* (M. Kafatos, ed.), Fundamental Theories of Physics, pp. 69–72, Dordrecht: Springer Netherlands, 1989.

[87] P. Borri, S. Schneider, W. Langbein, and D. Bimberg, "Ultrafast carrier dynamics in InGaAs quantum dot materials and devices," *Journal of Optics A: Pure and Applied Optics*, vol. 8, pp. S33–S46, Mar. 2006.
Publisher: IOP Publishing.

[88] W. Sheng, S. J. Xu, and P. Hawrylak, "Electron g-factor distribution in self-assembled quantum dots," *Physical Review B*, vol. 77, p. 241307, June 2008.

Publisher: American Physical Society.

[89] B. Odom, D. Hanneke, B. D'Urso, and G. Gabrielse, "New Measurement of the Electron Magnetic Moment Using a One-Electron Quantum Cyclotron," *Physical Review Letters*, vol. 97, p. 030801, July 2006.
Publisher: American Physical Society.

[90] Ş. K. Özdemir, E. Matsunaga, T. Tashima, T. Yamamoto, M. Koashi, and N. Imoto, "An optical fusion gate for w-states," *New Journal of Physics*, vol. 13, no. 10, p. 103003, 2011.

[91] S. E. Economou, N. Lindner, and T. Rudolph, "Optically Generated 2-Dimensional Photonic Cluster State from Coupled Quantum Dots," *Physical Review Letters*, vol. 105, p. 093601, Aug. 2010.
Publisher: American Physical Society.

[92] M. V. G. Dutt, J. Cheng, B. Li, X. Xu, X. Li, P. R. Berman, D. G. Steel, A. S. Bracker, D. Gammon, S. E. Economou, R.-B. Liu, and L. J. Sham, "Stimulated and Spontaneous Optical Generation of Electron Spin Coherence in Charged GaAs Quantum Dots," *Physical Review Letters*, vol. 94, p. 227403, June 2005.
Publisher: American Physical Society.

[93] S. E. Economou and T. L. Reinecke, "Optically induced spin gates in coupled quantum dots using the electron-hole exchange interaction," *Physical Review B*, vol. 78, p. 115306, Sept. 2008.
Publisher: American Physical Society.

[94] D. Kim, S. G. Carter, A. Greilich, A. S. Bracker, and D. Gammon, "Ultrafast optical control of entanglement between two quantum-dot spins," *Nature Physics*, vol. 7, pp. 223–229, Mar. 2011.
Number: 3 Publisher: Nature Publishing Group.

[95] K. M. Weiss, J. M. Elzerman, Y. L. Delley, J. Miguel-Sanchez, and A. Imamoğlu, "Coherent Two-Electron Spin Qubits in an Optically Active Pair of Coupled InGaAs Quantum Dots," *Physical Review Letters*, vol. 109, p. 107401, Sept. 2012.
Publisher: American Physical Society.

[96] S. G. Carter, A. S. Bracker, M. K. Yakes, K. X. Tran, J. Q. Grim, and D. Gammon, "Coherent Optical Control of Quantum Dot Hole Spins using Triplet Trion States," in *Frontiers in Optics / Laser Science (2020), paper FW1C.6*, p. FW1C.6, Optical Society of America, Sept. 2020.

[97] C.-Y. Lu, Y. Zhao, A. N. Vamivakas, C. Matthiesen, S. Fält, A. Badolato, and M. Atatüre, "Direct measurement of spin dynamics in InAs/GaAs quantum dots using time-resolved resonance fluorescence," *Physical Review B*, vol. 81, p. 035332, Jan. 2010.
Publisher: American Physical Society.

[98] B. Beschoten, E. Johnston-Halperin, D. K. Young, M. Poggio, J. E. Grimaldi, S. Keller, S. P. DenBaars, U. K. Mishra, E. L. Hu, and D. D. Awschalom, "Spin coherence and dephasing in GaN," *Physical Review B - Condensed Matter and Materials Physics*, vol. 63, p. 121202, Mar. 2001.
Publisher: American Physical Society.

[99] A. Greilich, D. R. Yakovlev, A. Shabaev, A. L. Efros, I. A. Yugova, R. Oulton, V. Stavarache, D. Reuter, A. Wieck, and M. Bayer, "Mode Locking of Electron Spin Coherences in Singly Charged Quantum Dots," *Science*, vol. 313, pp. 341–345, July 2006.
Publisher: American Association for the Advancement of Science Section: Report.

[100] X. Xu, B. Sun, P. R. Berman, D. G. Steel, A. S. Bracker, D. Gammon, and L. J. Sham, "Coherent population trapping of an electron spin in a single negatively charged quantum dot," *Nature Physics*, vol. 4, pp. 692–695, Sept. 2008.
Number: 9 Publisher: Nature Publishing Group.

[101] P. Mohr, D. Newel, B. Taylor, and E. Tiesinga, "Fundamental Physical Constants from NIST," May 2019.

[102] K. A. Al-Hassanieh, V. V. Dobrovitski, E. Dagotto, and B. N. Harmon, "Numerical Modeling of the Central Spin Problem Using the Spin-Coherent-State P Representation," *Physical Review Letters*, vol. 97, p. 037204, July 2006.
Publisher: American Physical Society.

[103] W. Zhang, N. Konstantinidis, K. A. Al-Hassanieh, and V. V. Dobrovitski, "Modelling decoherence in quantum spin systems," *Journal of Physics: Condensed Matter*, vol. 19, p. 083202, Feb. 2007.
Publisher: IOP Publishing.

[104] G. Chen, D. L. Bergman, and L. Balents, "Semiclassical dynamics and long-time asymptotics of the central-spin problem in a quantum dot," *Physical Review B*, vol. 76, p. 045312, July 2007.
Publisher: American Physical Society.

[105] M. Bortz and J. Stolze, "Exact dynamics in the inhomogeneous central-spin model," *Physical Review B*, vol. 76, p. 014304, July 2007.
Publisher: American Physical Society.

[106] E. Barnes, L. Cywinski, and S. Das Sarma, "Master equation approach to the central spin decoherence problem: Uniform coupling model and role of projection operators," *Physical Review B*, vol. 84, p. 155315, Oct. 2011.
Publisher: American Physical Society.

[107] E. Barnes, L. Cywinski, and S. Das Sarma, "Nonperturbative Master Equation Solution of Central Spin Dephasing Dynamics," *Physical Review Letters*, vol. 109, p. 140403, Oct. 2012.
Publisher: American Physical Society.

[108] X. R. Wang, Y. S. Zheng, and S. Yin, "Spin relaxation and decoherence of two-level systems," *Physical Review B*, vol. 72, p. 121303, Sept. 2005.
Publisher: American Physical Society.

[109] G. Dresselhaus, "Spin-Orbit Coupling Effects in Zinc Blende Structures," *Physical Review*, vol. 100, pp. 580–586, Oct. 1955.
Publisher: American Physical Society.

[110] E. I. Rashba and V. I. Sheka, "Symmetry of Energy Bands in Crystals of Wurtzite Type II. Symmetry of Bands with Spin-Orbit Interaction Included," *New Journal of Physics*, vol. 17, p. 16, 2015.

[111] G. Bihlmayer, O. Rader, and R. Winkler, "Focus on the Rashba effect," *New Journal of Physics*, vol. 17, p. 050202, May 2015.
Publisher: IOP Publishing.

[112] A. V. Khaetskii and Y. V. Nazarov, "Spin-flip transitions between Zeeman sublevels in semiconductor quantum dots," *Physical Review B*, vol. 64, p. 125316, Sept. 2001.
Publisher: American Physical Society.

[113] D. M. Zumbühl, J. B. Miller, C. M. Marcus, K. Campman, and A. C. Gossard, "Spin-Orbit Coupling, Antilocalization, and Parallel Magnetic Fields in Quantum Dots," *Physical Review Letters*, vol. 89, p. 276803, Dec. 2002.
Publisher: American Physical Society.

[114] D. V. Bulaev and D. Loss, "Spin relaxation and anticrossing in quantum dots: Rashba versus Dresselhaus spin-orbit coupling," *Physical Review B*, vol. 71, p. 205324, May 2005.
Publisher: American Physical Society.

[115] L. C. Camenzind, L. Yu, P. Stano, J. D. Zimmerman, A. C. Gossard, D. Loss, and D. M. Zumbühl, "Hyperfine-phonon spin relaxation in a single-electron GaAs quantum dot," *Nature Communications*, vol. 9, p. 3454, Aug. 2018.

Number: 1 Publisher: Nature Publishing Group.

[116] A. V. Mikhailov, V. V. Belykh, D. R. Yakovlev, P. S. Grigoryev, J. P. Reithmaier, M. Benyoucef, and M. Bayer, "Electron and hole spin relaxation in InP-based self-assembled quantum dots emitting at telecom wavelengths," *Physical Review B*, vol. 98, p. 205306, Nov. 2018.
Publisher: American Physical Society.

[117] A. L. Vartanian, A. A. Kirakosyan, and K. A. Vardanyan, "Spin relaxation mediated by spin-orbit and acoustic phonon interactions in a single-electron two-dimensional quantum dot," *Superlattices and Microstructures*, vol. 122, pp. 548–556, Oct. 2018.

[118] A. Abragam, *The Principles of Nuclear Magnetism*.
Clarendon Press, 1983.
Google-Books-ID: 9M8U_JK7K54C.

[119] A. V. Khaetskii and Y. V. Nazarov, "Spin relaxation in semiconductor quantum dots," *Physical Review B*, vol. 61, pp. 12639–12642, May 2000.
Publisher: American Physical Society.

[120] M. Paillard, X. Marie, P. Renucci, T. Amand, A. Jbeli, and J. M. Gérard, "Spin Relaxation Quenching in Semiconductor Quantum Dots," *Physical Review Letters*, vol. 86, pp. 1634–1637, Feb. 2001.
Publisher: American Physical Society.

[121] A. V. Khaetskii, D. Loss, and L. Glazman, "Electron Spin Decoherence in Quantum Dots due to Interaction with Nuclei," *Physical Review Letters*, vol. 88, p. 186802, Apr. 2002.
Publisher: American Physical Society.

[122] G. Gillard, I. M. Griffiths, G. Ragunathan, A. Ulhaq, C. McEwan, E. Clarke, and E. A. Chekhovich, "Fundamental limits of electron and nuclear spin qubit lifetimes in an isolated self-assembled quantum dot," *npj Quantum Information*, vol. 7, pp. 1–8, Feb. 2021.
Number: 1 Publisher: Nature Publishing Group.

[123] I. A. Merkulov, A. L. Efros, and M. Rosen, "Electron spin relaxation by nuclei in semiconductor quantum dots," *Physical Review B - Condensed Matter and Materials Physics*, vol. 65, pp. 2053091–2053098, Apr. 2002.
Publisher: American Physical Society.

[124] E. L. Hahn, "Spin Echoes," *Physical Review*, vol. 80, pp. 580–594, Nov. 1950.
Publisher: American Physical Society.

[125] S. Meiboom and D. Gill, "Modified spin-echo method for measuring nuclear relaxation times," *Review of Scientific Instruments*, vol. 29, no. 8, pp. 688–691, 1958.

[126] J. Hennig, "Echoes—how to generate, recognize, use or avoid them in MR-imaging sequences. Part I: Fundamental and not so fundamental properties of spin echoes," *Concepts in Magnetic Resonance*, vol. 3, pp. 125–143, July 1991.

[127] S. M. Clark, K.-M. C. Fu, Q. Zhang, T. D. Ladd, C. Stanley, and Y. Yamamoto, "Ultrafast Optical Spin Echo for Electron Spins in Semiconductors," *Physical Review Letters*, vol. 102, p. 247601, June 2009.
Publisher: American Physical Society.

[128] L. Huthmacher, R. Stockill, E. Clarke, M. Hugues, C. Le Gall, and M. Atatüre, "Coherence of a dynamically decoupled quantum-dot hole spin," *Physical Review B*, vol. 97, pp. 1–5, June 2018.
arXiv: 1711.09169 Publisher: American Physical Society.

[129] J. Scheuer, I. Schwartz, Q. Chen, D. Schulze-Sünninghausen, P. Carl, P. Höfer, A. Retzker, H. Sumiya, J. Isoya, B. Luy, M. B. Plenio, B. Naydenov, and F. Jelezko, "Optically induced dynamic nuclear spin polarisation in diamond," *New Journal of Physics*, vol. 18, p. 013040, Jan. 2016.
Publisher: IOP Publishing.

[130] G. Éthier Majcher, D. A. Gangloff, R. Stockill, E. Clarke, M. Hugues, C. Le Gall, and M. Atatüre, "Improving a Solid-State Qubit through an Engineered Mesoscopic Environment," *Physical Review Letters*, vol. 119, no. 13, pp. 1–6, 2017.
arXiv: 1706.07749.

[131] P. Schering, J. Hüdepohl, G. S. Uhrig, and B. Fauseweh, "Nuclear frequency focusing in periodically pulsed semiconductor quantum dots described by infinite classical central spin models," *Physical Review B*, vol. 98, p. 024305, July 2018.
Publisher: American Physical Society.

[132] A. Greilich, A. Shabaev, D. R. Yakovlev, A. L. Efros, I. A. Yugova, D. Reuter, A. D. Wieck, and M. Bayer, "Nuclei-Induced Frequency Focusing of Electron Spin Coherence," *Science*, vol. 317, pp. 1896–1899, Sept. 2007.

[133] A. W. Overhauser, "Polarization of Nuclei in Metals," *Physical Review*, vol. 92, pp. 411–415, Oct. 1953.
Publisher: American Physical Society.

[134] T. R. Carver and C. P. Slichter, "Polarization of Nuclear Spins in Metals," *Physical Review*, vol. 92, pp. 212–213, Oct. 1953.
Publisher: American Physical Society.

[135] A. Abragam and M. Goldman, "Principles of dynamic nuclear polarisation," *Reports on Progress in Physics*, vol. 41, pp. 395–467, Mar. 1978.

[136] S. W. Brown, T. A. Kennedy, D. Gammon, and E. S. Snow, "Spectrally resolved Overhauser shifts in single GaAs/Al_xga_(1-x)As As quantum dots," *Physical Review B*, vol. 54, pp. R17339–R17342, Dec. 1996.
Publisher: American Physical Society.

[137] K. Ono and S. Tarucha, "Nuclear-Spin-Induced Oscillatory Current in Spin-Blockaded Quantum Dots," *Physical Review Letters*, vol. 92, p. 256803, June 2004.
Publisher: American Physical Society.

[138] W. A. Coish and D. Loss, "Hyperfine interaction in a quantum dot: Non-Markovian electron spin dynamics," *Physical Review B*, vol. 70, p. 195340, Nov. 2004.
Publisher: American Physical Society.

[139] F. H. L. Koppens, C. Buizert, K. J. Tielrooij, I. T. Vink, K. C. Nowack, T. Meunier, L. P. Kouwenhoven, and L. M. K. Vandersypen, "Driven coherent oscillations of a single electron spin in a quantum dot," *Nature*, vol. 442, pp. 766–771, Aug. 2006.
Number: 7104 Publisher: Nature Publishing Group.

[140] C. Deng and X. Hu, "Analytical solution of electron spin decoherence through hyperfine interaction in a quantum dot," *Physical Review B*, vol. 73, p. 241303, June 2006.
Publisher: American Physical Society.

[141] W. Yao, R.-B. Liu, and L. J. Sham, "Theory of electron spin decoherence by interacting nuclear spins in a quantum dot," *Physical Review B*, vol. 74, p. 195301, Nov. 2006.
Publisher: American Physical Society.

[142] L. Cywinski, W. M. Witzel, and S. Das Sarma, "Pure quantum dephasing of a solid-state electron spin qubit in a large nuclear spin bath coupled by long-range hyperfine-mediated interactions," *Physical Review B*, vol. 79, p. 245314, June 2009.
Publisher: American Physical Society.

[143] I. T. Vink, K. C. Nowack, F. H. Koppens, J. Danon, Y. V. Nazarov, and L. M. Vandersypen, "Locking electron spins into magnetic resonance by electron-nuclear feedback," *Nature Physics*, vol. 5, no. 10, pp. 764–768, 2009.
arXiv: 0902.2659 Publisher: Nature Publishing Group.

[144] C. Latta, A. Högele, Y. Zhao, A. N. Vamivakas, P. Maletinsky, M. Kroner, J. Dreiser, I. Carusotto, A. Badolato, D. Schuh, W. Wegscheider, M. Atature, and A. Imamoglu, "Confluence of resonant laser excitation and bidirectional quantum-dot nuclear-spin polarization," *Nature Physics*, vol. 5, pp. 758–763, Oct. 2009.

Number: 10 Publisher: Nature Publishing Group.

[145] C. Kloeffel, P. A. Dalgarno, B. Urbaszek, B. D. Gerardot, D. Brunner, P. M. Petroff, D. Loss, and R. J. Warburton, "Controlling the Interaction of Electron and Nuclear Spins in a Tunnel-Coupled Quantum Dot," *Physical Review Letters*, vol. 106, p. 046802, Jan. 2011.
Publisher: American Physical Society.

[146] E. Barnes and S. E. Economou, "Electron-Nuclear Dynamics in a Quantum Dot under Nonunitary Electron Control," *Physical Review Letters*, vol. 107, p. 047601, July 2011.
Publisher: American Physical Society.

[147] T. Nutz, E. Barnes, and S. E. Economou, "Solvable quantum model of dynamic nuclear polarization in optically driven quantum dots," *Physical Review B*, vol. 99, p. 035439, Jan. 2019.
Publisher: American Physical Society.

[148] S. E. Economou and E. Barnes, "Theory of dynamic nuclear polarization and feedback in quantum dots," *Physical Review B - Condensed Matter and Materials Physics*, vol. 89, p. 165301, Apr. 2014.
arXiv: 1312.5741 Publisher: American Physical Society.

[149] N. Wu, W. Ding, A. Shi, and W. Zhang, "Inhomogeneous dynamic nuclear polarization and suppression of electron polarization decay in a quantum dot," *Physics Letters A*, vol. 380, pp. 2706–2712, Aug. 2016.

[150] A. S. Bracker, E. A. Stinaff, D. Gammon, M. E. Ware, J. G. Tischler, A. Shabaev, A. L. Efros, D. Park, D. Gershoni, V. L. Korenev, and I. A. Merkulov, "Optical Pumping of the Electronic and Nuclear Spin of Single Charge-Tunable Quantum Dots," *Physical Review Letters*, vol. 94, p. 047402, Feb. 2005.
Publisher: American Physical Society.

[151] X. Xu, W. Yao, B. Sun, D. G. Steel, A. S. Bracker, D. Gammon, and L. J. Sham, "Optically controlled locking of the nuclear field via coherent dark-state sopctroscopy," *Nature*, vol. 459, pp. 1105–1109, June 2009.
Publisher: Nature Publishing Group.

[152] J. R. Petta, J. M. Taylor, A. C. Johnson, A. Yacoby, M. D. Lukin, C. M. Marcus, M. P. Hanson, and A. C. Gossard, "Dynamic nuclear polarization with single electron spins," *Physical Review Letters*, vol. 100, p. 067601, Feb. 2008.
Publisher: American Physical Society.

[153] D. J. Reilly, J. M. Taylor, J. R. Petta, C. M. Marcus, M. P. Hanson, and A. C. Gossard, "Exchange Control of Nuclear Spin Diffusion in a Double Quantum Dot," *Physical Review Letters*, vol. 104, p. 236802, June 2010.

Publisher: American Physical Society.

[154] M. A. Nielsen and I. Chuang, "Quantum Computation and Quantum Information," *American Journal of Physics*, vol. 70, p. 558, Apr. 2002.
Publisher: American Association of Physics TeachersAAPT.

[155] A. Greilich, A. Shabaev, D. R. Yakovlev, A. L. Efros, I. A. Yugova, D. Reuter, A. D. Wieck, and M. Bayer, "Supporting Online Material: Nuclei-Induced Frequency Focusing of Electron Spin Coherence," *Science*, 2007.
Publisher: American Association for the Advancement of Science.

[156] A. Greilich, D. R. Yakovlev, and M. Bayer, "Optical tailoring of electron spin coherence in quantum dots," *Solid State Communications*, vol. 149, pp. 1466–1471, Sept. 2009.

[157] S. G. Carter, A. Shabaev, S. E. Economou, T. A. Kennedy, A. S. Bracker, and T. L. Reinecke, "Directing Nuclear Spin Flips in InAs Quantum Dots Using Detuned Optical Pulse Trains," *Physical Review Letters*, vol. 102, p. 167403, Apr. 2009.
Publisher: American Physical Society.

[158] E. Evers, N. E. Kopteva, I. A. Yugova, D. R. Yakovlev, D. Reuter, A. D. Wieck, M. Bayer, and A. Greilich, "Suppression of nuclear spin fluctuations in an InGaAs quantum dot ensemble by GHz-pulsed optical excitation," *npj Quantum Information*, vol. 7, pp. 1–7, Apr. 2021.
Bandiera_abtest: a Cc_license_type: cc_by Cg_type: Nature Research Journals Number: 1 Primary_atype: Research Publisher: Nature Publishing Group Subject_term: Quantum dots;Qubits;Spintronics Subject_term_id: quantum-dots;qubits;spintronics.

[159] A. Jerschow, "From nuclear structure to the quadrupolar NMR interaction and high-resolution spectroscopy," *Progress in Nuclear Magnetic Resonance Spectroscopy*, vol. 46, pp. 63–78, Mar. 2005.

[160] B. C. Carlson and G. S. Rushbrooke, "On the expansion of a Coulomb potential in spherical harmonics," *Mathematical Proceedings of the Cambridge Philosophical Society*, vol. 46, pp. 626–633, Oct. 1950.
Publisher: Cambridge University Press.

[161] S. S. M. Wong and S. S. Wong, *Introductory nuclear physics*.
Wiley Online Library, 1998.

[162] A. R. Edmonds, *Angular Momentum in Quantum Mechanics*.
Princeton University Press, Aug. 2016.
Publication Title: Angular Momentum in Quantum Mechanics.

[163] K. F. Riley, M. P. Hobson, and S. J. Bence, *Mathematical Methods for Physics and Engineering: A Comprehensive Guide*.
Cambridge University Press, Aug. 2002.
Google-Books-ID: ol6pZCDG5SYC.

[164] I. Vurgaftman, J. R. Meyer, and L. R. Ram-Mohan, "Band parameters for III–V compound semiconductors and their alloys," *Journal of Applied Physics*, vol. 89, pp. 5815–5875, June 2001.
Publisher: American Institute of Physics.

[165] L. D. Landau, E. M. Lifshitz, A. M. Kosevich, and L. P. Pitaevskii, *Theory of Elasticity: Volume 7*.
Elsevier, Jan. 1986.

[166] P. Steinmann, A. Elizondo, and R. Sunyk, "Studies of validity of the Cauchy–Born rule by direct comparison of continuum and atomistic modelling," *Modelling and Simulation in Materials Science and Engineering*, vol. 15, pp. S271–S281, Dec. 2006.
Publisher: IOP Publishing.

[167] J. J. Ramsey, E. Pan, and P. W. Chung, "Modelling of strain fields in quantum wires with continuum methods and molecular statics," *Journal of Physics Condensed Matter*, vol. 20, no. 48, 2008.

[168] S. Plimpton, "Fast Parallel Algorithms for Short-Range Molecular Dynamics," *Journal of Computational Physics*, vol. 117, pp. 1–19, Mar. 1995.
Available at: https://www.lammps.org/.

[169] C. Bulutay, "Quadrupolar spectra of nuclear spins in strained In xGa 1-xAs quantum dots," *Physical Review B - Condensed Matter and Materials Physics*, vol. 85, p. 115313, Mar. 2012.
arXiv: 1111.1499 Publisher: American Physical Society.

[170] R. J. Harrison and P. L. Sagalyn, "Trace Relations for Tensors Relating Electric Fields and Elastic Strains to Nuclear Quadrupole Effects," *Physical Review*, vol. 128, pp. 1630–1631, Nov. 1962.

[171] W. Voigt, *Lehrbuch der kristallphysik:(mit ausschluss der kristalloptik)*, vol. 34.
BG Teubner, 1910.

[172] R. K. Sundfors, "Experimental gradient-elastic tensors and chemical bonding in III-V semiconductors," *Physical Review B*, vol. 10, pp. 4244–4252, Nov. 1974.

[173] R. K. Sundfors, R. K. Tsui, and C. Schwab, "Experimental gradient elastic tensors: Measurement in I-VII semiconductors and the ionic contribution in III-V and I-VII compounds," *Physical Review B*, vol. 13, pp. 4504–4508, May 1976.

[174] V. Bogdanov and V. Lemanov, "Experimental determination of relationship between intracrystalline electric field gradient at nucleus and elastic deformation of lattice in cubic crystals naf nacl and kcl," *SOVIET PHYSICS SOLID STATE, USSR*, vol. 9, no. 2, pp. 357–+, 1967.

[175] V. Bogdanov and V. Lemanov, "Electric field gradients at atomic nuclei in elastically deformed a super iii b super v- type crystals(s tensor components by measuring nuclear magnetic resonance in semiconducting crystals under elastic strain)," *SOVIET PHYSICS-SOLID STATE*, vol. 10, pp. 159–163, 1968.

[176] E. A. Chekhovich, I. M. Griffiths, M. S. Skolnick, H. Huang, S. F. C. da Silva, X. Yuan, and A. Rastelli, "Cross calibration of deformation potentials and gradient-elastic tensors of GaAs using photoluminescence and nuclear magnetic resonance spectroscopy in GaAs/AlGaAs quantum dot structures," *Physical Review B*, vol. 97, no. 23, pp. 1–13, 2018.
arXiv: 1804.06879 Publisher: American Physical Society.

[177] I. M. Griffiths, H. Huang, A. Rastelli, M. S. Skolnick, and E. A. Chekhovich, "Complete characterization of GaAs gradient-elastic tensors and reconstruction of internal strain in GaAs/AlGaAs quantum dots using nuclear magnetic resonance," *Physical Review B*, vol. 99, no. 12, pp. 1–9, 2019.
Publisher: American Physical Society.

[178] R. T. Birge, "On Electric and Magnetic Units and Dimensions," *American Journal of Physics*, vol. 2, pp. 41–48, May 1934.

[179] G. G. Slabaugh, "Computing Euler angles from a rotation matrix," 1999.

[180] C. R. Harris, K. J. Millman, S. J. van der Walt, R. Gommers, P. Virtanen, D. Cournapeau, E. Wieser, J. Taylor, S. Berg, N. J. Smith, R. Kern, M. Picus, S. Hoyer, M. H. van Kerkwijk, M. Brett, A. Haldane, J. F. del Rio, M. Wiebe, P. Peterson, P. Gerard-Marchant, K. Sheppard, T. Reddy, W. Weckesser, H. Abbasi, C. Gohlke, and T. E. Oliphant, "Array programming with NumPy," *Nature*, vol. 585, pp. 357–362, Sept. 2020.

[181] P. Virtanen, R. Gommers, T. E. Oliphant, M. Haberland, T. Reddy, D. Cournapeau, E. Burovski, P. Peterson, W. Weckesser, J. Bright, S. J. van der Walt, M. Brett, J. Wilson, K. J. Millman, N. Mayorov, A. R. J. Nelson, E. Jones, R. Kern, E. Larson, C. J. Carey, i. Polat, Y. Feng, E. W. Moore, J. VanderPlas, D. Laxalde, J. Perktold, R. Cimrman,

I. Henriksen, E. A. Quintero, C. R. Harris, A. M. Archibald, A. H. Ribeiro, F. Pedregosa, and P. van Mulbregt, "SciPy 1.0: fundamental algorithms for scientific computing in Python," *Nature Methods*, vol. 17, pp. 261–272, Mar. 2020.

[182] J. R. Johansson, P. D. Nation, and F. Nori, "QuTiP: An open-source Python framework for the dynamics of open quantum systems," *Computer Physics Communications*, vol. 183, pp. 1760–1772, Aug. 2012.

[183] J. R. Johansson, P. D. Nation, and F. Nori, "QuTiP 2: A Python framework for the dynamics of open quantum systems," *Computer Physics Communications*, vol. 184, pp. 1234–1240, Apr. 2013.

[184] J. D. Hunter, "Matplotlib: A 2D Graphics Environment," *Computing in Science Engineering*, vol. 9, pp. 90–95, May 2007.
Conference Name: Computing in Science Engineering.

[185] C. Bulutay, E. A. Chekhovich, and A. I. Tartakovskii, "Nuclear magnetic resonance inverse spectra of InGaAs quantum dots: Atomistic level structural information," *Physical Review B - Condensed Matter and Materials Physics*, vol. 90, no. 20, pp. 1–16, 2014.

[186] R. Stockill, C. Le Gall, C. Matthiesen, L. Huthmacher, E. Clarke, M. Hugues, and M. Atatüre, "Quantum dot spin coherence governed by a strained nuclear environment Supplementary Material," *Nature Communications*, vol. 7, no. 1, 2016.

[187] G. Ragunathan, *Nuclear Spin Phenomena in III-V and II-VI Semiconductor Quantum Dots*. PhD thesis, University of Sheffield, 2019.

[188] P. Pyykkö, "Year-2017 nuclear quadrupole moments," *Molecular Physics*, vol. 116, pp. 1328–1338, May 2018.
Publisher: Taylor & Francis _eprint: https://doi.org/10.1080/00268976.2018.1426131.

[189] R. Stockill, C. Le Gall, C. Matthiesen, L. Huthmacher, E. Clarke, M. Hugues, and M. Atatüre, "Quantum dot spin coherence governed by a strained nuclear environment," *Nature Communications*, vol. 7, p. 12745, Nov. 2016.
Publisher: Nature Publishing Group.

[190] M. S. Kuznetsova, K. Flisinski, I. Y. Gerlovin, M. Y. Petrov, I. V. Ignatiev, S. Y. Verbin, D. R. Yakovlev, D. Reuter, A. D. Wieck, and M. Bayer, "Nuclear magnetic resonances in (In,Ga)As/GaAs quantum dots studied by resonant optical pumping," *Physical Review B - Condensed Matter and Materials Physics*, vol. 89, no. 12, pp. 1–11, 2014.

[191] D. Mao and P. C. Taylor, "Nuclear-spin echoes in GaAs:Zn and GaAs:In," *Physical Review B*, vol. 52, pp. 5665–5671, Aug. 1995.
Publisher: American Physical Society.

[192] H.-J. Briegel, W. Dür, J. I. Cirac, and P. Zoller, "Quantum Repeaters: The Role of Imperfect Local Operations in Quantum Communication," *Physical Review Letters*, vol. 81, pp. 5932–5935, Dec. 1998.
Publisher: American Physical Society.

[193] H. J. Kimble, "The quantum internet," *Nature*, vol. 453, pp. 1023–1030, June 2008.
Bandiera_abtest: a Cg_type: Nature Research Journals Number: 7198 Primary_atype: Reviews Publisher: Nature Publishing Group.

[194] D. A. Gangloff, G. Éthier Majcher, C. Lang, E. V. Denning, J. H. Bodey, D. M. Jackson, E. Clarke, M. Hugues, C. L. Gall, and M. Atatüre, "Quantum interface of an electron and a nuclear ensemble," *Science*, vol. 364, pp. 62–66, Apr. 2019.
Publisher: American Association for the Advancement of Science Section: Report.

[195] E. V. Denning, D. A. Gangloff, M. Atatüre, J. Mørk, and C. Le Gall, "Collective Quantum Memory Activated by a Driven Central Spin," *Physical Review Letters*, vol. 123, no. 14, p. 140502, 2019.
arXiv: 1904.11180 Publisher: American Physical Society.

[196] E. A. Chekhovich, M. Hopkinson, M. S. Skolnick, and A. I. Tartakovskii, "Suppression of nuclear spin bath fluctuations in self-assembled quantum dots induced by inhomogeneous strain," *Nature Communications*, vol. 6, p. 6348, May 2015.
arXiv: 1403.1510 Publisher: Nature Publishing Group.

[197] J. M. Taylor, C. M. Marcus, and M. D. Lukin, "Long-Lived Memory for Mesoscopic Quantum Bits," *Physical Review Letters*, vol. 90, p. 206803, May 2003.
Publisher: American Physical Society.

[198] J. M. Taylor, A. Imamoglu, and M. D. Lukin, "Controlling a Mesoscopic Spin Environment by Quantum Bit Manipulation," *Physical Review Letters*, vol. 91, p. 246802, Dec. 2003.
Publisher: American Physical Society.

[199] Z. Kurucz, M. W. Sørensen, J. M. Taylor, M. D. Lukin, and M. Fleischhauer, "Qubit Protection in Nuclear-Spin Quantum Dot Memories," *Physical Review Letters*, vol. 103, p. 010502, July 2009.
Publisher: American Physical Society.

[200] S. Malik, C. Roberts, R. Murray, and M. Pate, "Tuning self-assembled InAs quantum dots by rapid thermal annealing," *Applied Physics Letters*, vol. 71, pp. 1987–1989, Oct. 1997.
Publisher: American Institute of Physics.

[201] M. O. Lipinski, H. Schuler, O. G. Schmidt, K. Eberl, and N. Y. Jin-Phillipp, "Strain-induced material intermixing of InAs quantum dots in GaAs," *Applied Physics Letters*, vol. 77, pp. 1789–1791, Sept. 2000.

Publisher: American Institute of Physics.

[202] A. I. Tartakovskii, M. N. Makhonin, I. R. Sellers, J. Cahill, A. D. Andreev, D. M. Whittaker, J.-P. P. Wells, A. M. Fox, D. J. Mowbray, M. S. Skolnick, K. M. Groom, M. J. Steer, H. Y. Liu, and M. Hopkinson, "Effect of thermal annealing and strain engineering on the fine structure of quantum dot excitons," *Physical Review B - Condensed Matter and Materials Physics*, vol. 70, pp. 1–4, Nov. 2004.
Publisher: American Physical Society.

[203] M. Y. Petrov, I. V. Ignatiev, S. V. Poltavtsev, A. Greilich, A. Bauschulte, D. R. Yakovlev, and M. Bayer, "Effect of thermal annealing on the hyperfine interaction in InAs/GaAs quantum dots," *Physical Review B*, vol. 78, p. 045315, July 2008.
Publisher: American Physical Society.

[204] D. M. Jackson, D. A. Gangloff, J. H. Bodey, L. Zaporski, C. Bachorz, E. Clarke, M. Hugues, C. Le Gall, and M. Atatüre, "Quantum sensing of a coherent single spin excitation in a nuclear ensemble," *Nature Physics*, vol. 17, pp. 585–590, May 2021.
Bandiera_abtest: a Cg_type: Nature Research Journals Number: 5 Primary_atype: Research Publisher: Nature Publishing Group Subject_term: Condensed-matter physics;Quantum dots;Quantum physics;Semiconductors Subject_term_id: condensed-matter-physics;quantum-dots;quantum-physics;semiconductors.

[205] D. A. Gangloff, L. Zaporski, J. H. Bodey, C. Bachorz, D. M. Jackson, G. Éthier Majcher, C. Lang, E. Clarke, M. Hugues, C. Le Gall, and M. Atatüre, "Witnessing quantum correlations in a nuclear ensemble via an electron spin qubit," *Nature Physics*, pp. 1–7, Oct. 2021.
Bandiera_abtest: a Cg_type: Nature Research Journals Primary_atype: Research Publisher: Nature Publishing Group Subject_term: Quantum dots;Quantum information;Quantum optics;Quantum physics Subject_term_id: quantum-dots;quantum-information;quantum-optics;quantum-physics.

[206] C. Y. Hu, A. Young, J. L. O'Brien, W. J. Munro, and J. G. Rarity, "Giant optical Faraday rotation induced by a single-electron spin in a quantum dot: Applications to entangling remote spins via a single photon," *Physical Review B*, vol. 78, p. 085307, Aug. 2008.
Publisher: American Physical Society.

[207] C. Y. Hu, W. J. Munro, J. L. O'Brien, and J. G. Rarity, "Proposed entanglement beam splitter using a quantum-dot spin in a double-sided optical microcavity," *Physical Review B*, vol. 80, p. 205326, Nov. 2009.
Publisher: American Physical Society.

[208] R. M. Stevenson, R. J. Young, P. See, D. G. Gevaux, K. Cooper, P. Atkinson, I. Farrer, D. A. Ritchie, and A. J. Shields, "Magnetic-field-induced reduction of the exciton polarization splitting in InAs quantum dots," *Physical Review B*, vol. 73, p. 033306, Jan. 2006.
Publisher: American Physical Society.

[209] V. P. Krainov, H. R. Reiss, and B. M. Smirnov, *Radiative processes in atomic physics*.
Wiley Online Library, 2005.

[210] N. Khaneja, R. Brockett, and S. J. Glaser, "Time optimal control in spin systems," *Physical Review A*, vol. 63, no. 3, p. 032308, 2001.

[211] J. P. Palao and R. Kosloff, "Optimal control theory for unitary transformations," *Physical Review A*, vol. 68, no. 6, p. 062308, 2003.

[212] N. Khaneja, T. Reiss, C. Kehlet, T. Schulte-Herbrüggen, and S. J. Glaser, "Optimal control of coupled spin dynamics: design of nmr pulse sequences by gradient ascent algorithms," *Journal of magnetic resonance*, vol. 172, no. 2, pp. 296–305, 2005.

[213] D. Rowe, "Practical group theory with applications," *University of Toronto Press, Toronto*, 1997.

[214] R. N. Zare and W. G. Harter, "Angular Momentum: Understanding Spatial Aspects in Chemistry and Physics," *Physics Today*, vol. 42, pp. 68–70, Dec. 1989.
Publisher: American Institute of Physics.

[215] H. F. Jones, *Groups, representations and physics*.
CRC Press, 1998.